https://theses.gla.ac.uk/

Theses Digitisation:

https://www.gla.ac.uk/myglasgow/research/enlighten/theses/digitisation/

This is a digitised version of the original print thesis.

Copyright and moral rights for this work are retained by the author

A copy can be downloaded for personal non-commercial research or study, without prior permission or charge

This work cannot be reproduced or quoted extensively from without first obtaining permission in writing from the author

The content must not be changed in any way or sold commercially in any format or medium without the formal permission of the author

When referring to this work, full bibliographic details including the author, title, awarding institution and date of the thesis must be given

Enlighten: Theses
https://theses.gla.ac.uk/
research-enlighten@glasgow.ac.uk

# On The Luminescence Intensity of Quantum Dots, Dashes, and Wires

Thesis by

William Edward Leitch

Submitted for the degree of Doctor of Philosophy to the
Department of Electronics and Electrical Engineering
The University of Glasgow
September 1993

© William E. Leitch, 1993

ProQuest Number: 10992184

All rights reserved

INFORMATION TO ALL USERS
The quality of this reproduction is dependent upon the quality of the copy submitted.

In the unlikely event that the author did not send a complete manuscript
and there are missing pages, these will be noted. Also, if material had to be removed,
a note will indicate the deletion.

ProQuest 10992184

Published by ProQuest LLC (2018). Copyright of the Dissertation is held by the Author.

All rights reserved.
This work is protected against unauthorized copying under Title 17, United States Code
Microform Edition © ProQuest LLC.

ProQuest LLC.
789 East Eisenhower Parkway
P.O. Box 1346
Ann Arbor, MI 48106 – 1346

Thesis
9717
copy 1
copy 1

GLASGOW
UNIVERSITY
LIBRARY

**Abstract**

As part of the current interest in the optical properties of low dimensional structures, the fabrication of these structures by deep mesa etching of quantum well material has been investigated by a number of groups. In approaching the quantum régime, the effect of the etched surfaces on the structure emission efficiency must be well known in order to derive meaningful results on the luminescence, and the measurements of this effect have been subject to a degree of controversy.

This thesis presents results on attempts to quantify the emission efficiency of low dimensional structures down to 0.1 μm, by the technique of low-temperature photoluminescence.

The technique of quantifying the emission efficiency of a quantum structure array relative to a control mesa on the same piece of material relies on the assumptions that the the quantum well material is uniform, and that the measurement of emission intensity is highly reproducible.

Measurements of the uniformity of the quantum well material have revealed wide variations in emission intensity across the wafer, and poor reproducibility of measurement of emission intensity from alignment to structure arrays. Attempts were made to reduce these variations by selecting material with high wafer uniformity, and by batch-production of structures on such material to reduce the effects of structure variation during the fabrication process. On such structures, the behaviour is more consistent.

On such good material, the structures show a uniform reduction in emission efficiency with the smallest structure dimension. On poorer material, the quasi-quantum wires show a uniform reduction in emission efficiency with wire width again, but the quasi-quantum dots show little reduction in emission efficiency with dot diameter.

This behaviour was fitted with models of the effects of surface recombination and trapping on the carrier population in the material, and a fit was deduced with a novel qualitative model. The data, however, cannot sustain any more detailed analysis due to the poor quality of the quantum well material.

The qualitative results must be regarded with a degree of suspicion because of the limited success achieved in the attempts to improve the consistency of the data. Further progress in this particular methodology is unlikely until the material uniformity is improved, and fabrication volume is greatly increased.

*I dedicate this thesis to my parents and friends who gave me the support and encouragement to enable me to complete this thesis*

**Acknowledgements**

At this point, it is only fitting that I try to acknowledge the support that I have received during the last few years, which has made this thesis possible.

In the first place, I must thank my parents, who have encouraged and supported me, both financially and otherwise, throughout the course of my undergraduate and postgraduate studies, and without whose help I would have gone under long ago.

I would also like to thank my comrades-in-arms in the Ultra Small Structures and Laser Spectroscopy Laboratories, who endured the trials and tribulations of fabrication and experimental work with me; in particular I must mention Hazel Arnot, Morag Watt, Alistair Kean, Martin Holland, Mark McElhinney, John Weaver, and the late Don Reid, who all did their bit to alleviate the loneliness of the short distance fabricator.

I am indebted, for the professional help and assistance I have received, to the technical members of the Group, especially to Doug Irons, who brought cryostats back from the dead, against all the odds, to Alex Ross, for imposing order on the potential chaos of the lab, to Dave Gourlay, for introducing me to the delights of fabrication, and to Ray Darkin, for the quiet confidence with which he assisted my attempts at dry etching.

I would like to thank my supervisor, Clivia Sotomayor Torres. I must pay tribute to her energy and enthusiasm, for without her infectious enjoyment and encouragement, I would have been hard pushed to reach this far. I am also extremely grateful for the support she has given me in participating in conferences, and in obtaining funds for me to observe research in four laboratories worldwide, which has given me a good introduction to the international science community.

Finally, without the sustenance provided by the Loon Fung and Balbir's Ashoka restaurants, and by the wonderful elixir from the now sadly defunct Dallas Dhu distillery, Moray, life in Glasgow would not have been half the pleasure.

This work was supported by the UK Science and Engineering Research Council.

## Contents

## List of Figures

## List of Tables

**List of Publications**

"Luminescence studies from wires of varying aspect ratio in GaAs / AlGaAs quantum wells"
Leitch W.E., Sotomayor Torres C.M., Lootens D., Thoms S., van Daele P., Stanley C.R., Demeester P., and Beaumont S.P.
*Surface Science.* **263** (1992) pp. 622-627

"Radiative Recombination in GaAs / AlGaAs Wires and Dots"
Sotomayor Torres C.M., Wang P.D., Leitch W.E., Benisty H., and Weisbuch C.,
in: "*Optics of Excitons in Confined Systems*",
eds. d'Andrea A., del Sole R., Girlanda R., and Quattropani A., Institute of Physics Conference Series No. 123, Institute of Physics Publishing, Bristol, 1992, pp. 127 - 130.

"Wires and Dots in GaAs / AlGaAs Quantum Wells : Luminescence Intensity Studies"
Sotomayor Torres C.M., Leitch W.E., Lootens D., Wang P.D., Williams G.M., Thoms S., Wallace H., van Daele P., Cullis A.G., Stanley C.R., Demeester P., and Beaumont S.P.
Proceedings of the International Symposium on Nanostructures and Mesoscopic Systems, Santa Fe, USA, 19-20 May 1991, in: "*Nanostructures and Mesoscopic Systems*", Kirk W.P. and Reed M.A., eds., Academic Press, New York, 1992, pp. 455 - 461

"Size Dependence of Electron-Phonon Coupling in GaAs / $Ga_{0.7}Al_{0.3}As$ Single Quantum Wells"
Qiang H., Pollak F.H., Sotomayor Torres C.M., Leitch W.E., Kean A.H., Stroscio M.A., Iafrate G.I., and Kim K.W.
*Applied Physics Letters* **61** (12), 1411 (1992)

"Spectroscopy of Etched Low Dimensional Structures"
Leitch W.E., Sotomayor Torres C.M., Kean A.H., and Beaumont S.P.
Extended Abstracts EA-26, Berger S.D., Craighead H.G., Kern D., and Smith T.P. III, eds.,
Proceedings of Symposium Y,
1990 Fall Meeting of U.S. Materials Research Society, Boston, MA, USA, pp. 127-130.

"Raman Scattering and Photoluminescence of GaAs-based Nanostructures",
Sotomayor Torres C.M., Watt M., Arnot H.E.G., Glew R., Leitch W.E., Kean A.H., Cusco Cornet R., Kerr T.M., Thoms S., Beaumont S.P., Johnson N.P., and Stanley C.R.
in: "*Science and Engineering of 1- and 0-Dimensional Semiconductors*",
eds. Beaumont S.P. and Sotomayor Torres C.M.,
NATO ASI Series B **214**, Plenum Press, New York, 1990, pp. 297-307.

*The experimental study of the optical properties of quantum wires and dots can be described as elusive and frustrating, by virtue of the difficulty in creating structures small enough to exhibit quantum confinement effects and in sufficiently uniform arrays of sufficiently high quality material.*

K. Kash, Bellcore, speaking at EP2DS-8 (1989)

---

"Then I began to notice strange things. There were the signs of an incipient longing for something else. Science had been oversold. The true scientific vocation is very rare, and in the high schools it was presented in a technical and uninspired fashion. The students apparently learnt what they had to learn, but boredom was not wholly compensated for by great expectations. The new mental activity and desire for achievement had not quite found their objects. I observed that many of the best students' dedication to science was very thin. The great theoretical difficulty of modern natural science-that it cannot explain why it is good-was having its practical effect. The *why* question was coming close to the surface. A little liberal learning easily attracted the most gifted away from natural science. They felt the alternatives had been hidden from them."

Allan Bloom, "The Closing of The American Mind", Penguin Books, London, 1988

# Chapter 1: Introduction

## 1.1 What is Nanoelectronics?

'Nanoelectronics' is the technology which has grown up in order to fabricate extremely small structures, less than 0.1 μm in size. The impetus for this development has been the interest in exploiting the optical and electronic effects resulting from the quantum behaviour of microstructured solids, particularly semiconductors.

The criterion for 'quantum effects' in the optical behaviour of a semiconductor, such as GaAs, may be taken to be that the dimensions of the structure should be comparable with the Bohr diameter of the bulk exciton.

In the electronic behaviour, the situation is more complex, but the most stringent requirement is that the dimensions of the structure are much less than the Fermi wavelength.

The benefits from this technology are beginning to emerge. The quantum well laser, exploiting one degree of quantum confinement, has shown significant advantages over double-heterostructure lasers, and the next generation of devices exploiting confinement to one- and zero-degrees of freedom, as discussed in the *Devices* section below, will build upon these benefits.

The interest in nanotechnology widened in the late 1960s [Challis, 1992; Reed, 1993; Reed, 1989; Weisbuch and Vintner, 1991] when the possibility of fabricating materials exhibiting quantum effects was demonstrated by Cho and Arthur at Bell Laboratories (1975), who developed the III-V semiconductor growth method of molecular beam epitaxy, which allowed the controlled growth of heterojunctions.

In 1974, Esaki, Chang, and Tsu at IBM demonstrated the oscillatory behaviour of the differential conductance from resonant tunneling across a potential barrier [Esaki and Chang, 1974], and Dingle et al. observed the absorption from excitons confined to a two-dimensional quantum well (1974). From that point, there has been rapid expansion of the field, and the properties of two-dimensional systems are now receiving much attention. Aside from the advances in the understanding of the fundamental physics, enormous progress has been achieved in the fabrication of devices such as the High Electron Mobility Transistor (HEMT) [Weisbuch and Vinter, 1991], and the Quantum Well Laser [Tsang, 1987; Burnham, 1984].

Following the improvements in device performance in two-dimensional systems, attention has now turned to the projected improvements possible in yet lower dimensional systems: the quantum well wires and the quantum well dots (or boxes), of one-dimensionality and zero-dimensionality, respectively. These structures are, however, much more difficult to fabricate, as they, in general, require lateral patterning of two-dimensional systems by lithographic means.

## 1.2 Electronic Properties of 1-D and 0-D Structures

The electronic behaviour of a quantum wire or dot depends not only on the length scale of the structure, but also on the Fermi wavelength, on the electron elastic mean free path between impurity scattering processes, and on the inelastic phase-breaking mean path between phonon scattering events [Weisbuch and Vinter, 1991; Beaumont and Sotomayor Torres, 1990]. The relative size of these lengths determines the conductance régime and thus the behaviour of the structure.

In the 'ballistic' régime, the dimensions of the structure are less than the electron elastic mean free path between impurity scattering processes and the inelastic phase-breaking mean path between phonon scattering events. In this situation, the electron behaviour is wave-like, and the electron properties resemble more those of waveguides than electronic circuits, with the termination of the wires and layout of connections having impact on the rest of the circuit.

In the 'quantum ballistic' régime, where the dimensions of the structure are less than the Fermi wavelength, the low field conductance is quantized in units of $e^2/h$. Quantum point contacts, lateral constrictions of a 2-D electron gas, act as filters in that they transmit only electrons with the energy of the sub-band, and are analogous to optical point sources.

### 1.2.1 1-D and 0-D Edge Channel States in High Magnetic Field

Due to the presence of trapped charge at the surface, or band-bending, the Landau levels of a two-dimensional electron gas in the presence of a high magnetic field are driven higher in energy, and one-dimensional states are formed at the intersection of these Landau levels with the Fermi level [Burnham et al., 1984]. When the Fermi level lies between Landau levels, these one-dimensional states are the only extended states available, and so the net current will be carried by these states alone.

These edge states may be used to form an interferometer exploiting the zero-dimensional states in a quantum dot [Burnham et al., 1984]. Closed loops of the edge channels form zero-dimensional states as the finite circumference of the dot gives rise to a second confinement arising from the rotational symmetry of the state. The zero-dimensional nature of the states is observed in peaks in the conductance as the magnetic flux is varied or the Fermi level is swept in energy.

### 1.2.2 Quantum State Spectroscopy in Wires and Dots

Reed et al. (1988) and Randall et al. (1988a,b) discussed the fabrication and characterization of zero-dimensional resonant tunneling diodes, which were fabricated by electron beam lithography and reactive ion etching. The confined electron states in the dots gave rise to a series of resonances in the transmitted current as a function of applied potential.

The calculation of the energy separation of the confined states in the 100 nm pillars of InGaAs / AlGaAs / GaAs quantum well material was correlated with the resonance peaks measured in the current-voltage characteristic, and evidence was provided for single electron trapping effects.

Lateral confinement of electrons to one- and zero-dimensional states was observed by Lee et al. (1988) and Smith et al. (1987) in the change in the differential capacitance with gate voltage in a patterned modulation-doped structure. The confinement results from the surface depletion and etch damage, and the change in differential capacitance with gate voltage is due to the emptying of sub-bands as the Fermi level moves. The differential capacitance is thus a direct probe of the density of states in the structure, and the peaks in the oscillations were correlated with the wire and dot size.

### 1.2.3 Lateral Surface Superlattices

As-grown superlattices exhibit confinement in only one dimension, and the minigaps thus formed are not tunable. In addition, these superlattices suffer from low mobility in the direction perpendicular to the layers. Thus attempts have been made to fabricate lateral surface superlattices by laying periodic gates on the surface of a two-dimensional electron gas, with the minibands arising from the depletion from the gate potential. These devices offer high mobility from the use of a high-mobility electron gas, the gate potential is tunable, and the use of dimensionality reduced to one or zero dimensions reduces the scattering into free electron states.

Antoniadis et al. (1990) showed evidence for one-dimensional confinement in the multiple parallel quantum wires in the drain-source current as a function of gate bias, and Kotthaus and Merkt (1990) demonstrated one- and zero-dimensional confinement in transport and infra-red excitation studies.

## 1.3 Optical Properties of 1-D and 0-D Structures

The literature on the optical properties of one- and zero-dimensional structures will be reviewed in Chapter 3, but a brief summary is required here to put the position of the project in perspective.

Fabrication of one- and zero-dimensional structures lies at the limits of the lateral patterning techniques available, and hence it has not been easy to produce reliable evidence for quantization. There have been particular problems with the deep-etched fabrication of such structures in GaAs / AlGaAs quantum wells, as there is controversy over the behaviour of the etched surface in etched techniques, and further work is required into the damage induced into the structures as a result of etching and lithography. In the structures fabricated by ion implantation, there is concern over ion penetration of the mask, lateral straggling, and the shape of the potential resulting from the annealed ion bombardment.

Thus the interpretation of the data requires great care, and potentially the behaviour of a set of one- and zero-dimensional devices may be a property of the starting material or the fabrication process rather than of the structures themselves.

No direct evidence has been provided yet for optical quantization to zero-dimensions by a lateral patterning technique, other than a report of optical confinement of electrons through the use of surface stressors, although there is a growing evidence for structures fabricated by direct growth, such as microcrystals and GaAs droplets [see Chapter 3]. Progress has been made in one-dimensional fabrication, and a number of groups report the successful fabrication of quantum wires.

An overview of the radiative properties of etched nanostructures is still lacking, however, and thus this project was intended to help elucidate their behaviour.

Vahala et al. (1987) simulated the effects of quantum confinement on the lasing characteristics of a semiconductor laser. A large magnetic field of up to 19 T was applied perpendicular to a commercial quantum well laser, and the dependence of spectral linewidth on magnetic field was measured. The carriers confined in Landau states in the conduction and valence bands simulated the effect of confinement on the carriers in a quantum dot array. At 165 K, the spectral linewidth narrowed as the magnetic field was increased.

## 1.4 Potential 1-D and 0-D Device Applications

### 1.4.1 Electron Devices

The opportunities for the application of the properties of one- and zero-dimensional systems in devices is divided into two main areas: the continuation of progress in the field of reducing device size for increased speed and integration, and the exploitation of the properties unique to one- and zero-dimensional systems, such as Granular Electronics, Electron Phase Control, and Ballistic Electron Devices [Weisbuch and Vinter, 1991; Sols et al., 1989; Sollner et al., 1983; Capasso, 1987]

### 1.4.2 Optical Devices

In the field of optical devices, progress has already been made in the realization of quantum wire lasers [Kapon, 1989], although they are similar to quantum well lasers save for an improvement in the temperature dependence and enhanced modulation bandwidth [Arakawa and Sakaki, 1982; Arakawa et al., 1985].

The change in the density of states from the bulk to one- and zero-dimensional is from a $E^{1/2}$ dependence to a $E^{-1/2}$ and $\delta$ dependence, and this should result in an increase in spectral gain. As a result, it has been predicted [Weisbuch and Vintner B, 1991] that quantum dot lasers should have threshold currents 10 to 100 times smaller than quantum well lasers, and with increased modulation speed and lower spectral width.

Predictions have also been made for III-V lasers grown on silicon, where the carrier localization prevents the carriers from reaching non-radiative centres on dislocations.

## 1.5 Context of This Work

### 1.5.1 Scope of Project

Prior to the start of this work, considerable experience had been acquired in the Nanoelectronics Research Centre in the fabrication and optical spectroscopy of low dimensional structures. Early work by Arnot (1990) in the fabrication and photoluminescence characterization, complemented by the work of Watt (1988) on the study of phonons in etched semiconductor dots, had established a reputation in the field.

In order to observe quantum effects by photoluminescence, such as a shift in the exciton ground state with confinement, or a polarization dependence of the emission, it had to be determined whether or not there would be a sufficient emission signal from the structures fabricated. Data from other laboratories had suggested that the effect of surface recombination on the etched GaAs well surface would dominate over the intrinsic radiative recombination for small structures, and thus an attempt to study these structures by their luminescence would be futile. This was, however, contradicted by the work of Arnot [Arnot, 1990], which showed that, for some samples, no appreciable decrease in luminescence relative emission intensity was noted as the structure size was reduced. Serious questions then needed to be answered in respect of the difference in behaviour of structures fabricated in the Nanoelectronics Research Centre as compared with those fabricated elsewhere. In addition, experiments by Arnot [Arnot, 1990] had suggested a substantial difference in the behaviour of the dots as opposed to the wires.

In order to clarify the contradictory measurements reported in the literature, it was deemed necessary to assess the results of Arnot on the behaviour of the radiative efficiency of the quantum wires and dots, and to elucidate the behaviour of structures intermediate between the dots and the wires - the 'quantum dashes'.

During the course of the project, the main technique available was that of photoluminescence spectroscopy. Considerable facilities were available for the fabrication of etched wires and dots, and thus the project was biassed in favour of sample fabrication in order to try to elucidate the photoluminescence properties of the dot and wire structures.

The approach consisted of three main angles of attack: to simplify the number of fabrication steps to reduce the opportunities for run-to-run variation; to fabricate a large number of identical samples simultaneously in order to reduce the potential variations in the fabrication method; and to fabricate structures which were intermediary in size between dots and wires, thus allowing a definable trend from dot to wire to allow a more accurate interpretation of the data.

The implications of the method were that a large number of patterns had to be defined to cover the variations in size and aspect ratio required, and that a large amount of material was consumed due to process failure of complete batches of material chips.

A number of samples of wires and dots of various aspect ratios were fabricated and characterized by low temperature photoluminescence. The spectra showed no trend in the ground state heavy hole free exciton transition suggestive of quantum confinement, and on good material, the structures showed a uniform reduction in emission efficiency with the smallest structure dimension. On poorer material, the quasi-quantum wires showed a uniform reduction in emission efficiency with wire width again, but the quasi-quantum dots showed little reduction in emission efficiency with dot diameter.

### 1.5.2 Outline of Thesis

The thesis is structured as follows:

After the introductory chapter, a brief outline of the theoretical considerations behind the structures is given in Chapter 2, followed by a review of the literature on the optical properties of one- and zero-dimensional structures in Chapter 3. In Chapter 4 the fabrication process is outlined, and in Chapter 5 there is a discussion of the experimental apparatus. Following this, Chapter 6 describes the photoluminescence characterization of the material processed, and an attempt is made to quantify the uncertainty surrounding the measurement of photoluminescence intensity.

In Chapter 7 the results of the characterization of the structures are laid out; in Chapter 8 four models are presented for the radiative efficiency of etched quantum dots and wires. These data from the characterization of the structures is analysed with reference to these models in Chapter 9, and the findings are summarized in Chapter 10, together with the conclusions from the work and some recommendations for future research.

# Chapter 2: Theoretical Aspects

## 2.1 Electronic Properties

### 2.1.1 Oscillator Strength

The oscillator strength of a general quantum mechanical system may be considered as a measure of the strength of an electromagnetic transition between two quantum states, and so it is useful in calculating the probability of a particular transition [Woodgate, 1980; Kittel, 1986].

The oscillator strength for a particular electromagnetic transition between a group of states $n$ and a group of states $m$ may be calculated as follows:
The perturbation introduced into the Hamiltonian, $H_v$, at $\mathbf{k}=0$ is:

$$H_v = \frac{e}{m}\mathbf{A}.\mathbf{p} \qquad (2.1)$$

where **A** is the electromagnetic vector potential, and **p** is the matrix element between an initial quantum state $|n_0\rangle$ of energy $E_{n0}$ characterized by quantum number $n_0$ and a final quantum state $|m_0\rangle$ of energy $E_{m0}$ characterized by quantum number $m_0$, defined by:

$$p_{mn} = \langle m_0 | \mathbf{p} | n_0 \rangle \qquad (2.2)$$

The oscillator strength $f_{mn}$ is then defined as:

$$f_{mn} = \frac{2|p_{mn}|^2}{mH_v} \qquad (2.3)$$

One can derive an expression, from **k.p** theory [Ridley, 1988], for the matrix elements in terms of the effective mass,

$$\frac{m}{m^*} = 1 - \frac{2}{m}\sum_{m \neq n} \frac{|\langle m_0|\mathbf{p}|n_0\rangle|^2}{E_{n0} - E_{m0}} \qquad (2.4)$$

where m is the rest mass of the electron, and $m^*$ the effective mass. Thus it is possible to obtain the oscillator strength of direct interband transitions from the conduction band to different valence bands by summing the oscillator strengths over all the participating bands, calculating

$$\sum_{m \neq n} f_{mn} = 1 - \frac{m}{m^*} . \qquad (2.5)$$

As the valence bands interact weakly with each other, to a good approximation the oscillator strength for a given valence band of effective mass $m_v^*$ is:

$$f_{cv} = 1 + \frac{m}{m_v^*} . \qquad \{2.6\}$$

The ratio of the strengths of the transitions from valence bands to the conduction band thus depends on the ratio of the effective masses of the holes in the bands. More importantly, however, the strength of the transition depends on the overlap of the wavefunctions of the initial and final states, and in quantum confined systems this overlap is greatly enhanced, giving rise to a much greater oscillator strength.

### 2.1.2 Densities of States

The densities of states for a set of quantum particles in a continuous medium may be obtained by imposing periodic boundary conditions on the particles, thus giving the volume of k-space occupied by each of the states. The density of states for a particular system may then be derived by calculating the number of such states which will fit into the total available k-space, as is performed in elementary solid state texts [Kittel, 1986].

The results for particles of effective mass $m^*$ and spin 1/2 in a system of lower dimensionality are derived in a similar manner to the bulk density of states, and the relevant results are tabulated below.

| Number of Dimensions | Density of States $\rho \equiv \frac{dN}{dE}$ |
|---|---|
| 3 | $\frac{(2m^*)^{\frac{3}{2}}}{2\pi^2\hbar^3} . (E-E_n)^{\frac{1}{2}}$ |
| 2 | $\frac{m^*}{\pi\hbar^2}$ |
| 1 | $\frac{(2m^*)^{\frac{1}{2}}}{\pi\hbar} . (E-E_n)^{-\frac{1}{2}}$ |
| 0 | $\delta(E-E_n)$ |

Table (2.1): Densities of States in Low Dimensional Systems

As may be noted from Table (2.1), as the dimensionality is reduced, the state density at the bottom of each band is increased, and for 1-dimensional and 0-dimensional systems, there are singularities in the densities of states at the bottoms of the bands.

Although in real systems the singularities are smoothed out by residual effects, the change in the density of states as the dimensions of the system are reduced gives rise to a concentration of carriers at the bottom of the bands. It is this property, combined with the increase in oscillator strength arising from the confinement, which offers the possibility of increased quantum well laser performance in a quantum wire (1-dimensional) or quantum dot (0-dimensional) laser over that of the current quantum well (2-dimensional) laser.

### 2.1.3 Semiconductor Bulk Structure

#### 2.1.3.1 Gallium Arsenide (GaAs)

The gallium arsenide crystal is of the zinc-blende type, consisting of two interpenetrating face centred cubic sublattices displaced along the <111> axis by one bond length.

The degenerate valence band is split by spin-orbit interaction, and result in two bands degenerate at **k**=0, the heavy-hole (hh) and light-hole (lh) bands, and one band separated by an energy gap $\Delta_0$ at **k**=0, the split-off-hole (soh) band. The holes have different masses determined by the energy gap, and momentum matrix element between the conduction band Bloch function |s> and the valence band |p> states. The fundamental gap is 1.420 eV at room temperature [Thomas et al., 1986].

The lowest excited states of a perfect direct-gap semiconductor crystal are given by the promotion of a single electron **k**=0 from the top of the valence band to the bottom of the conduction band, creating an electron-hole pair bound by their Coulomb attraction. The exciton is stable, as the Coulomb attraction is balanced by an increase in the kinetic energy, which results from the spatial localization of the electron-hole pair through the Heisenberg Uncertainty Principle.

As the electron and hole must move with the same velocity to remain bound, an additional requirement to **k** conservation is that the excitons can only be found at the 'critical points' in **k** space, where the the particle velocities are the same [Pankove, 1971].

Assuming spherical bands at **k**=0, the solution to the exciton Hamiltonian is given by products of hydrogenic wavefunctions $\phi(\mathbf{r})$, of energy levels $E_n$, where R is centre of mass of the pair, **K** is the eigenvalue of the momentum operator of the exciton, $\mu$ is the reduced mass of the electron-hole pair, and $\Omega$ is the volume [Ridley, 1988; Pankove, 1971]:

$$\psi(r,R) = \frac{1}{\sqrt{\Omega}} e^{i\mathbf{K}.\mathbf{R}} \varphi(r) \qquad \{2.7\}$$

the total energy of the exciton system in level n is:

$$E_n = E_g + \frac{\hbar^2 K^2}{2(m_c^* + m_v^*)} - \frac{(e^2/4\pi\varepsilon)^2}{2(\hbar^2/\mu)n^2} \qquad \{2.8\}$$

The effective Bohr radius of the exciton is given by $a_{0exc}=(m\varepsilon/\mu\varepsilon_0).a_0$, where $a_0$ is the Bohr radius of 0.528 Å, giving in GaAs values for exciton Bohr radius of 200 Å and ground state binding energy of approximately 5 meV.

#### 2.1.3.2 Aluminium Arsenide (AlAs)

Aluminium arsenide has been subject to less investigation than gallium arsenide, or about aluminium gallium arsenide. This is due to the considerable difficulties in preparing the pure single crystals of the compound, associated with its high melting point (1740 °C), high decomposition pressure at the melting point, and its high reactivity.

The lowest indirect gap ($\Gamma$-$X_{1C}$) transition occurs at 2.16 eV at room temperature [Stukel and Euwema, 1969], and the direct gap transition ($\Gamma$-$\Gamma$) at 2.9 eV. [Jaros, 1985].

#### 2.1.3.3 III-V Alloys

Due to the random distribution of atoms on the zinc-blende sites in a III-V alloy, there is no translational invariance, the alloy is not an idealized crystal, and there is no reason to expect a well defined energy-gap between occupied valence states and empty conduction states [Philips, 1973].

As experimentally the alloys have energy bands similar to perfect crystals, the Virtual Crystal Model has been devised, where the random cation potential is replaced by a weighted average of the potential. This restores translational invariance, and allows the definition of Bloch waves, whilst still giving rise to disorder effects such as band tailing and the scattering of Bloch waves.

In general, however, it is not possible to obtain the properties of a ternary III-V semiconductor compound $A_xB_{1-x}C$ by linear interpolation between the properties of the compounds AC and BC [Ridley, 1988,Watt, 1988]. Linear behaviour of the band-gap requires that AC and BC have similar band structures and lattice constants, and so the band-gap is usually bowed, reflecting its dependence on the lattice constant (through the ionic and homopolar energy-gap dependencies on the lattice constant [Ridley, 1988]), and on the degree of disorder in the lattice.

The disorder in the lattice gives rise to fluctuations in the crystal potential, and as a result, the band states are mixed, reducing the band-gap when the disorder is maximized at x = 0.5. The disorder is attributed to the difference in the electronegativities of the competing cations.

The band-gap thus shows, in general, a bowing in the middle of the composition range, dependant on the difference in the electronegativities, and on the difference in the lattice constants.

Although the lattice constants of AlAs and GaAs are approximately the same, and the difference between the Philips electronegativities of Al and Ga are small, the band structures of AlAs and GaAs differ in that AlAs is indirect.

As a result, the band-gap of $Al_xGa_{1-x}As$ is a piecewise linear function of aluminium composition. Between x = 0 and x = 0.37, the gap is direct, and $E_g = 1.512 + 1.455\ x$ (eV) at 2 K [Kuech et al., 1987]. At x = 0.37, the lowest energy transition changes from a direct $\Gamma$–$\Gamma$ transition to an indirect $\Gamma$–X transition, and the gradient of energy gap against Al composition reduces.

The $E_0$ transition at 297 K may be approximated by the quadratic expression:

$E_0(\Gamma) = 1.424 + 1.594\,x + x(1 - x)(0.127 - 1.310\,x)$ (eV) [Aspnes et al., 1986] {2.9}

In order to ensure maximum barrier height whilst maintaining the direct gap, the mole fraction x for the barriers used in this project was kept to approximately 0.3.

### 2.1.4 Semiconductor Heterojunctions

A heterojunction is formed by the joining of two dissimilar semiconductors such that the interface is abrupt, and the plane of interface is smooth.

The heterojunction properties depend crucially on the size of the band-gaps, the lattice constants, and the energy band structure of the constituent semiconductors, and on the line-up between the band-gaps - the heterojunction band-offset.

In the case of GaAs-$Al_{0.3}Ga_{0.7}As$, the lattice constants of GaAs and AlAs are very similar ( 5.660 Å and 5.654 Å ) [Wolfe et al., 1989], and at 30% Al concentration the lowest AlGaAs transition is direct $\Gamma$-$\Gamma$, as in GaAs. The band-gaps of GaAs and $Al_{0.3}Ga_{0.7}As$ at 297 K are 1.420 eV and 1.846 eV [Thomas et al., 1986].

#### 2.1.4.1 The Band Offset

The band-offset, defined as the ratio of the offsets at the conduction and valence bands, is of great importance in determining the character of the heterojunction.

The effect of varying the band-offset may be seen especially clearly in a quantum well, where two heterojunctions, of the same two materials, are placed within a a few tens of nm of each other. The confinement results in quantized states which are discussed in later section.

The band-offset for doped heterojunctions is determined by the position of the Fermi level, and charge will flow until thermodynamic equilibrium is reached with the Fermi levels on either side of the junction equal.

In undoped junctions, the 'common anion rule' according to Harrison [Ridley, 1988] stipulates that if the two semiconductors have the same anion, crystallographic structure, and lattice constant, the valence band offset should be zero. This does not hold to better than several tens of meV, and so in general the band-offsets are obtained by fitting to experimental data.

There is a great deal of controversy on the subject of GaAs-$Al_{0.3}Ga_{0.7}As$ band-offsets; recent determinations favour a conduction band offset to valence band offset ratio of 65:35 [Duggan et al., 1985], or 60:40 [Ridley, 1988], but this is not significant for the interpretation of the data in this study.

#### 2.1.4.2 The Envelope Function Model

To enable calculations of states and wavefunctions in a heterostructure, one must overcome the problem that the heterostructure is not a perfect crystal due to the differences in atomic species, band-gap, band structure, and lattice constant.

The envelope function model [Ridley, 1988; Altarelli (1986); Bastard and Brum (1986)], derived from the effective mass formalism, enables one to solve an effective Schrödinger equation in which the rapidly varying terms (on the scale of a unit cell) are expressed through effective parameters, such as the band-gap and interband p matrix elements, and the differences between the heterojunction and an ideal crystal are felt only by the slowly varying 'envelope functions'.

The envelope function model gives simple analytical results close to points in **k** space of high symmetry such as the Γ, X, L points. It assumes that the constituent semiconductors are lattice matched and that the periodic parts of the Bloch functions of the semiconductors are taken to be equal.

By solving a coupled second-order 8 x 8 differential system, maintaining the continuity of the wavefunctions and the conservation of the average probability current, one can obtain a framework for deriving the expressions for wavefunctions and states in heterostructures.

### 2.1.5 Semiconductor Surfaces

The abrupt cessation of crystal structure at a semiconductor surface results in a change in a number of properties of the crystal [Many et al., 1965; Wallis and Sébenne, 1980]. The interruption of the crystal lattice leaves free bonds which are then able to combine together to form a surface lattice, or to include atoms from the ambient onto the surface of the crystal. The abrupt ending of lattice periodicity, the relaxation of the surface, and the adsorbed species all give rise to new energy levels which may lie in the band-gap of the bulk semiconductor:- the 'surface states'. The mid-gap states can provide efficient non-radiative recombination sites.

The presence of such surface states generates a layer of charge at the surface which is balanced by an electrostatic field extending into the bulk of the crystal, which bends the conduction and valence bands near the surface. The range of the field depends on the bulk carrier concentration, and its strength will depend on the position of the Fermi level in the bulk, and its position at the surface, which depends on the densities and energy levels of the surface states.

#### 2.1.5.1 Surface Recombination

At a temperature T, each carrier in the valence or conduction band moves, on average, with a thermal velocity $v_T$ [Aspnes, 1983]:

$$v_T = \sqrt{\frac{3\,kT}{m^*}} \qquad \{2.10\}$$

where $m^*$ is the effective mass of the carrier in the band. $v_T$ is of the order of $10^5$ $ms^{-1}$ at room temperature. At equilibrium, the total current density of either holes or electrons is zero, but if the equilibrium is disrupted, and recombination occurs at surfaces or interfaces, the net flow of carriers to the surface is $J_s = n\,q\,v_s$, where a velocity, $v_s$, is the natural form to describe the carrier recombination.

The *Surface Recombination Velocity*, S, is defined as the number of excess bulk carriers recombining on the surface per unit area per unit time per unit volume at the boundary between the quasi-neutral and space-charge regions. The surface recombination velocity can vary up to an appreciable fraction of the thermal velocity $v_T$, but only has meaning when it takes values (at room temperature) above $10^3$ cm $s^{-1}$, below which the volume recombination dominates the surface recombination, and below $10^8$ cm $s^{-1}$, the thermal velocity when surface recombination is limited by the transfer of carriers by the thermal velocity.

In a simple model, the *Stevenson-Keyes* expression for the surface recombination velocity in terms of the carrier concentrations, carrier velocities, and empirical values for carrier capture cross-sections.may be derived from models of the recombination in the bulk semiconductor and at volume defects. The model assumes that an equilibrium exists between the space-charge region and the bulk, and that the bulk is electrically neutral.

For a distribution of traps j,

$$S = \sum_j N_s^j \frac{\sigma_n^j \sigma_p^j v_n v_p (n_0 + p_0)}{\sigma_n^j v_n (n_s + n_T^j) + \sigma_p^j v_p (p_s + p_T^j)} \qquad \{2.11\}$$

where:

| | |
|---|---|
| $N_s$ | density of surface traps |
| $\sigma_n, \sigma_p$ | carrier capture cross-sections |
| $n_0, p_0$ | bulk carrier concentrations |
| $v_n, v_p$ | bulk carrier velocities |
| $n_T, p_T$ | carrier density if the Fermi level lay at the trap level $E_T$ |

From this Stevenson-Keyes expression, it is possible to observe that the surface recombination is maximized if the trap levels $E_T$ lie in the middle of the band gap, if the surface trap density is high, if the trap capture both carriers, and if they have a large capture cross-section.

In order to reduce the effects of surface recombination, two processes are believed to passivate the surface: reduction of the total surface trap density, and the movement of the surface Fermi level nearer one of the band-edges.

#### 2.1.5.2 GaAs Surface

The GaAs surface has been investigated in detail by such methods as photoluminescence, photoreflectance, X-ray photoelectron spectroscopy, and surface current transport [Aspnes et al., 1986, Korinfskiĭ and Musatov 1985; Wieder, 1983].

When the air-exposed GaAs surface is considered, the surface Fermi-level is pinned by the high concentration of half-filled states arising from lattice vacancies, either at 0.5 eV above the valence band, at the Ga vacancy level, or at 0.8 eV above the valence band, at the As vacancy level. Measurements of the surface recombination velocity S at room temperature yield values of the order of $10^6$ $cms^{-1}$ [Korinfskiĭ and Musatov, 1985].

#### 2.1.5.3 Surface Passivation Techniques

A number of techniques have been developed for surface passivation (i.e. reduction of surface recombination velocity by a reduction in surface state density, or by re-pinning the Fermi level away from mid-gap). Discussion of the effects of the passivating techniques reveals controversy over which of the two processes is responsible for the reduction in surface recombination.

The techniques exploited include ruthenium washes [Nelson et al., 1980), photochemical oxidation [Offsey et al., 1986; Ives et al., 1987], sodium sulphide deposition [Skromme et al., 1987; Besser and Helms, 1988; Hasegawa et al., 1988; Spindt et al., 1989; Yablonovitch et al., 1987; Sandroff et al., 1987], exposure to ammonia and hydrogen chloride gases [Wallis and Sébenne, 1980], and deposition of amorphous phosphorous overlayers [Olego et al., 1984; Olego et al., 1985].

Particular interest has been focussed on sodium sulphide deposition, due to the large reduction in surface recombination, as evidenced in room-temperature epilayer photoluminescence emission and the improvement in gain of a heterostructure bipolar transistor [Aspnes, 1983]. The mechanism was attributed to strong sulphur bonding producing an efficient electronic termination of the GaAs surface. The sulphur bonding does not, however, result in a reduction of the band bending, but rather shifts the Fermi level closer to the valence band maximum. Recent studies [Spindt and Spicer, 1989] suggest that this result can be explained in terms of a mid-gap state due to a double donor, compensated by an acceptor close to the valence band maximum. The sulphur reduces the number of donor states, thus shifting the Fermi level pinning closer to the valence band. Sodium sulphide deposits also exhibit good temporal stability.

Selenium / ruthenium washes, resulting in chemisorbed ruthenium, are reported [Nelson et al., 1980] to reduce the surface recombination of an etched GaAs surface. The ruthenium is incorporated at 1/3 monolayer coverage in nonsubstitutional sites of the GaAs crystal, and does not migrate during ageing.

The beneficial effect of Ru is attributed to the scavenging of free As on the surface which removes the As levels out of the band-gap, although repinning of the Fermi level closer to the valence band cannot be ruled out.

Photochemical oxidation [Offsey et al., 1986; Hasegawa et al. 1988] results in increased growth of $Ga_2O_3$, with a reduction in elemental As and $As_2O_3$. The Fermi-level is re-pinned closer to the valence band, giving increased photoluminescence intensity, but a reduction surface conductivity.

Exposure to $NH_3$ [Hasegawa et al. 1988] improved the surface conductance during exposure, but no effect was noted after the removal of the gas.

Exposure to HCl in air [Hasegawa et al. 1988], however, was noted to improve the photoluminescence emission, and the surface current transport indicated a reduction of band bending, though only during the exposure to the gas. This is attributed to a reduction in surface state density, perhaps from absorption of chlorine atoms onto surface gallium.

In order to test the theory that the Fermi level is pinned by surface lattice defects, particularly the arsenic vacancies, Olego et al. [Olego et al, 1984; Olego et al, 1985] have attempted to maintain the lattice continuity by the deposition of amorphous phosphorus, which closely mimics the atomic pattern of the GaAs surface. Investigation of the effects of the overlayers by Raman and photoluminescence spectroscopy reveal a reduction in the surface recombination velocity of one order of magnitude, and a re-pinning of the surface Fermi level from 0.7 to 0.18 eV, away from mid-gap.

#### 2.1.5.4 Low Temperature GaAs Passivation

Few measurements have been made of the surface recombination velocity of GaAs at low temperature. Low temperature photoluminescence measurements of GaAs treated by hydrated sodium sulphide were performed by Skromme et al. [Skromme et al., 1987], and it was noted that there was no significant increase in the luminescence intensity, suggesting that recombination with the bare surface was not a limiting factor on the lifetime, unlike the behaviour at room temperature.

### 2.1.6 2D-Confinement: Quantum Wells

#### 2.1.6.1 Electronic Structure

A quantum well is a double-heterostructure system where carriers are confined between barriers whose thicknesses exceed the penetration depth of the confined wavefunction, and whose separation is comparable with the bulk wavelength of the carriers.

The energy levels of such a system may be calculated using a Kane model [Weisbuch and Vinter, 1991] for the electron and hole states in the two materials in the approximation of the envelope wavefunction. The approximation assumes a strongly localized interface, and that the band-edge wavefunctions are not mixed, but only shifted.

The solutions for electron energy levels may be derived [Weisbuch and Vinter, 1991] for both an infinite and finite well depth; in the case of an infinite square well of width $L_z$ the energy levels $E_n$ are given by:

$$E_n = \frac{\hbar^2}{2\,m^*}\left(\frac{n\pi}{L_z}\right)^2 \qquad n = 1, 2, 3, \ldots \tag{2.12}$$

Considerable difficulties arise in the calculation of the hole energy levels in the quantum well due to the quadruple degeneracy of the valence bands at $\mathbf{k}_\perp=0$ in the bulk in the Kane model. The levels may be derived by a successive perturbation method [Weisbuch and Vinter, 1991], and show a behaviour differing considerably from that of the bulk, including a lifting of the degeneracy at $\mathbf{k}_\perp=0$ between light and heavy hole states, a well-width dependendent band structure with highly non-parabolic behaviour, strong anti-crossing behaviour, and the states exhibiting 'heavy' hole properties perpendicular to the interface exhibit 'light' hole behaviour parallel to the interface, and vice versa.

#### 2.1.6.2 Excitons in Quantum Wells

In the bulk semiconductor, the exciton energy levels are given by [see above in bulk semiconductor section]:

$$E_n = \frac{2\,\mu e^4}{(8\,\pi\varepsilon)^2 \hbar^2 n^2} \tag{2.13}$$

In an infinitely deep quantum well of negligible thickness, the energy levels are given by:

$$E_{n,2D} = \frac{E_{3D}}{\left(n-\frac{1}{2}\right)^2} \tag{2.14}$$

and the lowest energy level is at $E_{0,2D} = 4\,E_{0,3D}$.

For a finite well depth and finite well thickness, variational calculations [Bastard et al., 1982; Greene et al., 1984; Sanders and Chang, 1985] have shown that the energy levels are lower than these extreme values, because the exciton wavefunction leaks into the barriers under these conditions.

The lateral extent of the exciton reduces as the quantum well width is reduced; calculations [Bastard et al., 1982] show a minimum value of the lateral radial extent $\rho$ as:

$$\rho \rightarrow a_\infty \sqrt{\frac{3}{8}} \tag{2.15}$$

where $a_\infty$ is the bulk Bohr radius in GaAs.

The increase in exciton binding energy over that of the bulk implies that excitonic effects may be observed at room temperature.

### 2.1.6.3 Shallow Impurities in Quantum Wells

The energy levels associated with shallow impurities depend critically on the positions of the impurities with respect to the well interfaces [Pearah et al., 1985); Masselink et al., 1984)], because of the effect of the imposition of differing symmetry requirements on the wavefunctions localized at the impurities.

In a wide quantum well, of width tending to infinity, the well impurity levels may be separated into two groups; those associated with impurities close to the well barriers have p-type symmetry and $E_{imp2D} = E_{imp3D} / 4$, and those associated with impurities near the centre of the well have s-type symmetry and $E_{imp2D} = E_{imp3D}$.

As the well width is reduced, the binding energies for all impurities increases, and for a negligibly thin well, the well impurity levels converge on $E_{imp2D} = 4\ E_{imp3D}$ for all positions.

### 2.1.6.4 Quantum Well Interfaces

In early studies of layer-to-layer thickness reproducibility by excitation luminescence spectroscopy, it was observed that the increase in luminescence linewidth with reducing well thickness could be accounted for by a variation in the confinement energy due to well thickness variations of the order of half a monolayer. The model assumes an island size greater than the lateral extent of the exciton, and this was later corroborated by comparison with measurements of the island size.

In some more perfect crystals, almost atomically-flat layers were deduced from luminescence measurements, and the method of interrupted growth was developed to grow layers with large island size, giving rise to luminescence with discrete exciton lines corresponding to atomic layer variations.

Studies of excitation spectra linewidth have allowed the optimization of substrate growth temperature, and monolayer fluctuations associated with large island size may be observed routinely without growth interruption.

In an infinitely deep square quantum well of width $L_Z$, the energy levels $E_n$ of carriers of effective mass $m^*$ may be given as:

$$E_n = \frac{\hbar^2}{2\,m^*}\left(\frac{n\pi}{L_z}\right)^2 \qquad n = 1, 2, 3, \ldots \qquad \{2.16\}$$

The fluctuation in well width by a monolayer gives rise to an energy splitting of [Bimberg et al., 1986]:

$$\Delta E = \left(\frac{\hbar^2\pi^2}{m^* L_z^3}\right).\ \Delta L_z \qquad \{2.17\}$$

which is of the order of several meV for an electron in a 10 nm well.

The effects of these monolayer fluctuations on the luminescence spectrum is discussed more fully in the section on the photoluminescence of quantum wells below.

### 2.1.7 1-D Confinement: Quantum Wires

Calculations of the binding energy of hydrogenic states in GaAs-AlGaAs quantum well wires have been performed by Bryant (1984), and these can be extended to calculate the binding energies of excitons in these structures. In very small wires, the carriers leak out and behave as 3-D carriers in AlGaAs. As the wire width increases, the carriers are confined to one dimension, and the exciton binding energy increases greatly. This confinement behaviour extends out to wire widths of 1000 times the bulk Bohr radii. In addition to the enhancement of binding energy, one would also expect a broadening in the luminescence, due to an increased sensitivity to exciton lateral location relative to well wall.

Due to the importance of the wall boundary in determining the effects of one-dimensional confinement, one might expect the cross-sectional shape of the wire to have influence on the properties of the wire. In fact, for the same cross-sectional area, the binding energies of excitons in the wires are independent of the shape [Bryant, 1985].

### 2.1.8 0-D Confinement: Quantum Dots

Calculations of the binding energies and oscillator strengths of excitons confined in zero-dimensional quantum boxes [Bryant, 1988] show that for large boxes, the exciton binding (correlative) effects dominate over the confinement effects. As the box decreases in size, the excitons are unbound in that the confinement energy dominates over the Coulomb energy, and the carriers occupy the lowest single-particle states. The confinement increases the exciton kinetic and Coulomb energies, reduces the electron-hole separation, and the normalized oscillator strength increases rapidly.

## 2.2 Optical Properties

### 2.2.1 Bulk GaAs

#### 2.2.1.1 Photoluminescence Characterization

A sensitive method for observing both the intrinsic and extrinsic transitions in semiconductors is photoluminescence (PL) [Stradling and Klipstein, 1990], where the carriers are excited by a monochromatic light source, usually a laser, and the resultant luminescence dispersed by a spectrometer.

The transitions observed are usually the lowest energy transitions, as the carriers relax by phonon emission and other non-radiative processes to these levels before recombining, and thus the PL spectrum can be dominated by transitions with low density of states, which would be weak in absorption spectra. In addition, luminescence from a particular energy level may have a number of competing non-radiative channels which reduce the emission.

The advantages of PL over absorption lie in the sample preparation, as PL can be measured from the front surface of the sample, whereas an absorption measurement may require thick layers of the material investigated, with very thin substrate material.

Illumination of GaAs with 2.55 eV radiation from a 488 nm Ar ion laser gives rise to highly excited electron-hole pairs which rapidly relax non-radiatively to form electron-hole pairs and excitons. These may occur either as free particles, or excitons bound to impurities and defects. This gives rise to a wide variety of possible luminescent transitions [Stradling and Klipstein, 1990; Bishop, 1990]; the actual transitions observed depend on the impurity and defect concentration, the lattice temperature, and the exciting laser power density.

In the low temperature (1.8 K), low power (typically $P < 0.1$ W $cm^{-2}$) regime, the photoluminescence spectrum of high purity MBE GaAs is dominated by bound-exciton luminescence, in particular an acceptor bound exciton complex at 1.5121 eV and a donor bound exciton complex at 1.5137 eV.

The free exciton transition in bulk GaAs at 1.5155 eV, the highest energy excitonic feature, is broader than the bound exciton transitions, and is usually weak because, to first order, the free exciton transition is forbidden by k-conservation, only allowing excitons with exactly the photon k vector to radiate [Weisbuch and Vinter, 1991]. This is usually relaxed by polariton effects in the bulk.

Free-to-bound transitions occur when an electron at the bottom of the conduction band recombines with a hole on a neutral acceptor. A broad band between 1.480 and 1.495 eV is attributed to these transitions, in particular Zn in Vapour Phase Epitaxy (VPE) material, and C, Si, Ge in Liquid Phase Epitaxy (LPE) material.

### 2.2.2 GaAs Quantum Wells

#### 2.2.2.1 Photoluminescence Characterization

The low temperature (PL) emission of a GaAs single quantum well is completely different from the spectrum of high purity GaAs material [Weisbuch et al., 1981b], consisting of a single narrow line from the 1S free exciton recombination, or a superposition of such lines from parts of the well varying in thickness (see section on monolayer fluctuations below), as opposed to the multiple-transition impurity-dominated behaviour described in the bulk. The position of the line is dependent on the binding energy of the exciton, which is defined by the exciton confinement in the well, and the line is much more intense than bulk transitions.

These properties are due to efficient carrier capture in the wells, the large binding energy of the 2-D exciton, and the gettering of impurities on well interfaces. Transitions associated with bound excitons, electron-neutral acceptor, hole-neutral donor, and donor-acceptor pair transitions are weaker by ~2 or 3 orders of magnitude.

#### 2.2.1.1 Free Exciton Transitions

The k-conservation rule for free exciton recombination is relaxed in quantum wells by exciton scattering due to fluctuations in confining energy from well thickness variations, and so the 1S heavy hole free exciton luminescence in high quality material dominates PL emission. The light-hole free exciton luminescence can be seen at low temperatures if the well width ≥ 15 nm [Dawson et al., 1986], and higher levels can be observed at higher temperatures and excitation powers, subject to the selection rules below.

The magnitude of the nS exciton absorption transition varies as $(2n-1)^{-3}$ [34], and thus the dominant transition is the 1S heavy hole exciton recombination, although the 2S transition has been reported [Dawson et al., 1986; Moore et al., 1986].

#### 2.2.1.2 Free Exciton Selection Rules

From the calculation of the transition probability in an electromagnetic field in the envelope function approximation [Weisbuch and Vinter, 1991], one obtains selection rules for the excitonic transitions which are of three types:

i) Polarization selection rules arising from the dipole matrix element

ii) Quantum number selection rules arising from the overlap integral between the envelope functions of the initial and final states.

iii) Angular momentum selection rules: L=0

The polarization selection rules derivable from band-to-band absorption are the same as those fulfilled by excitons [6] :

The polarization selection rules give rise to a 3:1 hh:lh absorption ratio for propagation in the z direction [Weisbuch and Vinter, 1991].

For an exciton with initial state principle quantum number $n$, and final state quantum number $m$, there are two restrictions: $n+m$ even, and $\Delta n = n - m = 0$. Due to the symmetry of a quantum well, there is a well defined parity for the envelope functions, and so $n+m$ must be even to give a non-zero overlap integral. This is only broken when the symmetry is lifted, for example by an electric field. The $\Delta n = 0$ restriction is only valid for an infinitely deep rectangular quantum wells, where the envelope functions are orthogonal; in finite wells the functions are slightly mixed, and so this restriction is relaxed, although $\Delta n = 0$ transitions are much stronger than $\Delta n \neq 0$.

Because the transition probability depends on the amplitude of the wavefunction of the exciton at the origin of the coordinate system [Weisbuch and Vinter, 1991], only states with orbital angular momentum L=0 (S states) can participate in optical transitions.

#### 2.2.1.3 Oscillator Strength

The oscillator strength per electron-hole pair for band-band transitions is not increased in a quantum well over the oscillator strength in the bulk [Weisbuch and Vinter, 1991], but for excitonic transitions in narrow wells ($L_Z << a_B$) the oscillator strength is increased over that in the bulk by a factor [Rorison and Herbert, 1985]:

$$\frac{1}{L_z} \frac{|\phi_{x2D}(0)|^2}{|\phi_{x3D}(0)|^2} \qquad \{2.18\}$$

where $\phi_{x2D}$ and $\phi_{x3D}$ are the excitonic wavefunctions at k=0 in 2D and 3D respectively and $L_Z$ is the quantum well width.

This has been evaluated [Weisbuch and Vinter, 1991] as $\approx 8 . (a_B / L_Z)$, where $a_B$ is the bulk Bohr radius of the exciton.

The oscillator strength for bound excitons is found to be decreased slightly from the bulk value [Rorison and Herbert, 1985].

#### 2.2.1.4 Temperature Dependence of Exciton Transitions

Variation of temperature affects the exciton energies, the exciton linewidths, the exciton population of areas differing in well width by fractions of a monolayer, and the trapping of excitons on defects and impurities [Chen et al., 1987].

The exciton energies, in the main, follow the temperature dependence of the bulk, but at low temperatures the effects of trapping and population exchange shift the exciton emission lines in a sample- and site-dependant fashion.

The linewidth of the exciton emission below 150 K can be expressed as:

$$\Gamma = \Gamma_0 + \Gamma_A T + \Gamma_{LO} (\exp ( \hbar\omega / kT) -1)^{-1} + \Gamma_{imp} \exp ( -E_b / kT) \qquad \{2.19\}$$

[Lee et al., 1986; Hong and Singh, 1986]

where $\Gamma_0$ is the linewidth due to inhomogeneous fluctuations of the well width present at 0 K, $\Gamma_A$ is due to acoustic phonon scattering, $\Gamma_{LO}$ is due to optical phonon scattering (with LO phonon energy $\hbar\omega$), and $\Gamma_{imp}$ is due to ionized impurity scattering.

The luminescence intensity as a function of temperature has received less attention. The intense free exciton emission lines at low temperature fall off dramatically as the LO phonon population rises above 100 K, but it is exactly at these high temperatures that one would expect free exciton luminescence to dominate over any impurity-related transitions.

The identification of transitions is assisted by the use of a technique such as photoluminescence excitation spectroscopy, but it is believed that the best material currently available has such a low concentration of impurities that the photoluminescence spectra is dominated by free exciton emission. This free exciton emission has been observed up to room temperature [Dawson et al., 1983].

#### 2.2.1.5 Power Dependence of Photoluminescence

Studies of the power dependence of the photoluminescence emission [Xu et al., 1983] reveal that the lowest allowed band-band transitions were observed up to the highest excitation powers; the exciton related peaks were not observed due to the high excitation power.

The shift of the photoluminescence spectra to increasing energy with increasing excitation power, and the increasing linewidth, were attributed to band-filling effects.

#### 2.2.1.6 Interface Roughness in Quantum Wells

Following the observation of a systematic increase in photoluminescence linewidth with decreasing well with [Weisbuch et al., 1981a], Weisbuch et al. suggested a model for the broadening resulting from fluctuations in the interfaces of a monolayer; this model was expanded by Singh et al. [Singh et al., 1984]. This model was supported by experiments on growth interruption [Voillot et al., 1986; Wilson et al., 1986; Tanaka and Sakaki, 1987; Fujiwara et al., 1989], and the observation of fine structure in excitonic transitions [Bastard et al., 1984; Bimberg et al., 1986], attributed to emission from areas of the quantum well of different thickness.

This model of was confirmed by investigations with X-ray diffraction [Deveaud et al., 1984] which demonstrated a correlation between the interface disorder and the luminescence effects.

Later observations [Deveaud et al., 1986)] demonstrated that it was possible to observe luminescence from extended areas of well without the ordering effect of growth interruption, but by optimization of the growth process.

Recent measurements have demonstrated, in continuously grown material, a longer lifetime and greater exciton mobility than in interrupted growth material [Fujiwara et al., 1989; Zhou et al., 1989; Hillmer et al., 1990].

#### 2.2.2.2 Photoreflectance Characterization

Modulation techniques are particularly attractive for the characterization of the material properties of semiconductors due to their ease of use and the large amount of information which can be obtained without the need for low temperatures [Aspnes, 1980]. In these techniques, one applies a periodic perturbation to the sample under investigation, and investigates the resulting change in the reflectivity.

In ease of sample preparation, and simplicity of apparatus, photoreflectance, in which the perturbation takes the form of light modulation, is perhaps the most useful for the characterization of quantum wells, but the data is requires further analysis than the more direct methods of photoluminescence and photoluminescence excitation spectroscopy.

The measurement of relative change of reflectance ( $\Delta R / R$ ) as a function of the reflected light wavelength $\lambda$ gives information on the energy band transitions available in the sample investigated, through the effect of the modulated pump beam on the dielectric function. Initially, there was some dispute as to the mechanism involved in the technique, with one group asserting that the change in $\varepsilon$ measured by Wang et al. (1968) arose from a change in the effective density of states produced by the photoexcited carriers through the Pauli principle (band-filling) [Gay and Klauder, 1968], and others disputing whether, if the change is due to an electric field, the origin of the field is due to the difference in the mobilities of the electrons and holes (the Dember effect), or the neutralisation of the surface electric field.

Experiments by Nahory and Shay and comparison of results with electroreflectance resolved in favour of the surface electric field [Nahory and Shay, 1968].

The electric field in the material is modulated by the creation of electron-hole pairs by the pump beam which lower the surface field. The reduction in the field changes the dielectric function $\varepsilon$, which is observed by the change in reflectivity.

The calculation of the change in reflectivity ( $\Delta R / R$ ) as a function of the change in the complex dielectric function $\Delta\varepsilon$ may be expressed as follows:

$$\frac{\Delta R}{R} = \mathrm{Re}[(\alpha - i\beta)\Delta\varepsilon] \qquad \{2.20\}$$

where $\alpha$, $\beta$ are the Seraphin coefficients [Seraphin and Bottka, 1965]. The Seraphin coefficients have a characteristic variation for semiconductors, but differ in detail from semiconductor to semiconductor. Near the fundamental gap of bulk materials, $\beta = 0$, but in multilayer structures, interference effects are important, and so both $\alpha$ and $\beta$ must be considered.

The general expression for the dielectric function $\varepsilon$ in the one-electron approximation for a semiconductor described by Bloch states $\Psi_n(k, r)$ with energy of band index n and wavevector **k** is [Petroff, 1980]:

$$\varepsilon(E,\Gamma) = 1 + \frac{4\pi e^2\hbar^2}{m^2E^2}\sum_{k,c,v}\left|\hat{\underline{e}}.\underline{P}_{cv}(k)\right|^2\left[\frac{1}{E_{cv}(k) - E - i\Gamma} + \frac{1}{E_{cv}(k) + E + i\Gamma}\right] \qquad \{2.21\}$$

where

| | |
|---|---|
| n=c,v | conduction and valence bands respectively |
| e | polarisation vector of the photon electric field |
| P | momentum matrix element |
| E | interband energy |
| $\Gamma$ | a phenomenological broadening parameter |

For a given band pair c,v for which $\nabla_k E_{cv}(k) = 0$, ε has a singularity for all k; the points which satisfy this requirement, called *critical points*, are of extreme importance in modulation spectroscopy, because it is the regions around these points which give rise to the structure in modulation spectra, through these singularities. As the structure is associated only with narrow regions around the critical points, it is possible to replace the complicated E(k) dependence with a superposition of local functions around these critical points.

Any single parabolic critical point in the dielectric function has an empirical variation of the form:

$$\varepsilon(E,\Gamma) = A\Gamma^{-n} e^{i\theta}(E - E_g + i\Gamma)^n \qquad \{2.22\}$$

where:

| | | |
|---|---|---|
| A | amplitude |
| θ | phase projection factor |
| Γ | broadening parameter |
| $E_g$ | threshold energy |
| n | exponent |

The exponent n is defined according to the dimensionality of the system considered:

| | |
|---|---|
| -1/2 | for 1-D critical points |
| 0 (ln) | for 2-D critical points |
| 1/2 | for 3-D critical points |
| -1 | for excitons |

The dependence of ε on the surface field **F** may be derived as follows.

In the case of excitons, impurities, confined states in quantum wells and uncoupled states in multiple quantum wells, the particles do not have translational symmetry and are confined in space.Their energy spectra are discrete, and the electric field modulates the shape of the binding potential, thus affecting the binding energy of the particle, and giving rise to a Stark shift. In addition, the electric field can vary the intensity of the transition or the lifetime of the state.

$$\Delta\varepsilon = \left[\frac{d\varepsilon}{dE_g}\frac{dE_g}{d|F|} + \frac{d\varepsilon}{d\Gamma}\frac{d\Gamma}{d|F|} + \frac{d\varepsilon}{dI}\frac{dI}{d|F|}\right]\Delta|F| \qquad \{2.23\}$$

where $E_g$ is the energy , Γ is the linewidth, and I is the intensity of the transition.

For the band states in a semiconductor quantum well, the electrons are strictly confined in potential wells. The electric field induced change in the dielectric function is dominated by the Stark effect, and thus gives rise to a first derivative lineshape. The modulation on Γ can be neglected, and the lineshape is determined by the first two terms. The effect of the electric field is to lift translation symmetry, and so the usual selection rules are lifted, and the expression for may be reduced to:

$$\Delta\varepsilon = \left[\frac{d\varepsilon}{dE_g}\frac{dE_g}{dF} + \frac{d\varepsilon}{dI}\frac{dI}{dF}\right]\Delta F \qquad \{2.24\}$$

Thus the expression for ( ΔR / R ) can be derived:

$$\frac{\Delta R}{R} = \mathrm{Re}\left[C\, e^{i\theta}(E - E_g + i\Gamma)^{n-3}\right] \qquad \{2.25\}$$

or

$$\frac{\Delta R}{R} = \mathrm{Re}\left[e^{i\theta}(E - E_g + i\Gamma)^{-m}\right] \quad \text{where m=3-n} \qquad \{2.26\}$$

The value of m is dependent on the dimensionality of the critical points; for excitons in quantum wells m = 2.

$$\frac{\Delta R}{R} = \mathrm{Re}\left[e^{i\theta}(E - E_g + i\Gamma)^{-2}\right] \qquad \{2.27\}$$

The photoreflectance spectra can thus be fitted with a superposition of the equations above to derive the values of $E_g$ the energy , $\Gamma$ the linewidth, and I the intensity.

#### 2.2.2.3 Low Temperature GaAs Quantum Well Surface Passivation

No measurements have been reported of the surface recombination velocity of GaAs quantum wells at low temperature. Measurements have been reported, however, of the surface recombination velocity in quantum structures fabricated in quantum wells; these are discussed in Chapter 3.

### 2.2.3 GaAs Quantum Wires and Dots

As the number of allowed states is reduced drastically in quantum wire and box systems, scattering into different k-states is restricted. This is predicted to lead to enhanced spectral gain in injection lasers.

The effect of the change in the density of states from quantum well to wire and dot results in an enhancement of non-linear and electro-optic effects.

### 2.3.1 Oscillator Strength

Current theoretical models of the oscillator strength of transitions in quantum wires and dots to be highly dependent on the degree of confinement in the structures [Weisbuch and Vinter, 1991; Bryant, 1984; Bryant, 1985; Bryant, 1988].

In highly confined systems (where the structure dimension, $L << a_B$, the bulk Bohr radius) the Coulomb attraction between electron and hole acts a perturbation on the confinement kinetic energy, and the oscillator strength per transition per unit surface area for a planar array of dots is $f / ( d_x . d_y )$ where f is the atomic oscillator strength and $d_x$, $d_y$ are the inter-box distances. As the oscillator strength per transition per unit surface area for a quantum well is $f / ( \pi . a_B . a_B / 8)$, the quantum dot array oscillator strength will only exceed that of the quantum well when $d_x < a_B . \sqrt{(\pi / 8)}$.

When $L >> a_B$, a 'giant' oscillator strength situation develops, giving rise to an oscillator strength enhanced by a factor $(V_{dot} / V_{exc})$, where $V_{dot}$, $V_{exc}$ are the dot and exciton volumes respectively.

For intermediate sizes, where $L \approx a_B$, the exciton binding energy may lie between the electron and hole confinement energies, but the oscillator strength is still larger than the $L << a_B$ case.

In quantum wires the behaviour of the oscillator strength is intermediate in behaviour between those of quantum wells and quantum dots.

## 2.3 Summary

The main theoretical points relevant to the study of the optical properties of low dimensional systems have been outlined. As the dimensionality of the system is reduced, the oscillator strength and density of states per unit volume increase dramatically. The surface recombination in GaAs would be expected to have a significant impact on the radiative recombination.

# Chapter 3: Literature Review

Despite the considerable interest in the properties of one- and zero-dimensional systems (Quantum Wires and Quantum Dots), there are considerable fabrication difficulties to be overcome before the properties can be usefully exploited in devices. This is evidenced by the array of fabrication methods which have been evaluated. The different approaches which have been tried in the past include deep mesa etching, ion implantation, and surface stressors, but the most promising currently are the techniques based on epitaxial growth on patterned substrates, although these are inappropriate for the production of integrated devices.

The main advantage of the direct growth of quantum wires is that the methods avoid damage from such fabrication processes as etching or ion implantation. These techniques are, however, more suited to the fabrication of quantum wires rather than dots.

Several laboratories have reported observation of optical properties due to 1-dimensional (1-D) confinement, but there has been no substantiated claim to observation of the optical properties of etched structures exhibiting 0-dimensional (0-D) confinement. This is due to the damage introduced during etching, and the difficulty in fabricating small enough structures. In addition, there is the controversy over the possible quenching of the emission from the dots at small sizes. To observe the effects of lateral confinement of electrons and holes in carriers vertically quantized in GaAs / AlGaAs quantum wells, one requires to fabricate structures of less than 25 nm [Bryant, 1990] compared with an exciton Bohr radius of approximately 20 nm in GaAs, but the minimum size currently obtainable is 40 nm.

The different methods of fabricating quantum wires and dots, and the results of such techniques, are outlined below. Other reviews of the literature have also been given recently by Forchel (1988), Kash (1990), and Sotomayor Torres (1992).

## 3.1 Effect of Lateral Quantization on Semiconductors

### 3.1.1 Coulomb Effects

As discussed by, for example, Bryant (1990), the confinement modifies the Coulomb interaction of the exciton, resulting in three régimes, of strong, intermediate, and weak confinement.

In the smallest structures, where there is strong confinement, the electron and hole zero-point energies dominate the Coulomb interaction, and the Coulomb interaction can be treated as a perturbation on the confined single particle states.

In both wires and dots, the binding energies [Brown and Spector, 1987; Degani and Hipólito, 1987); Bryant, 1988] and oscillator strengths for both free excitons and for impurities located in the centre of the structure are increased as the dot size is reduced [Bryant, 1984,1985; Osório et al., 1988], and diverge for infinite barrier heights. This occurs in GaAs for dots below 10 nm for infinite barriers, or, according to Austin (1988), the energies reach a maximum for finite wells at 3 nm dot radius.

In the intermediate range, up to 100 nm [Bryant, 1988], the particle correlation energies are comparable to the confinement energies, and the Coulomb interaction cannot be treated as a perturbation. In this situation, it may happen that the electron is strongly quantized, whereas the hole is not, and the hole as a result oscillates in the potential well of the field of the electron.

For weak confinement, the quantized motion is that of the centre of mass of the exciton. Correlation energies are greater than the confinement energies, but are less than the exciton binding energy. Apart from an increase in oscillator strength, the properties of this system are little changed from those of a quantum well.

### 3.1.2 Optical Properties of One- and Zero-Dimensional Structures

Particular interest has been expressed in the optical properties of one- and zero-dimensional structures such as an increased normalized oscillator strength and optical non-linearity, as explained by, e.g., Hanamura (1988a,b), Takagahara (1987), Banyai (1988), and Austin (1988). The theory of super-radiance requires, however, that the system emits coherent light, which is dependent on the control of size fluctuations in the wires and dots. The experimental evidence for enhanced oscillator strength is, therefore, still lacking.

### 3.1.3 Structure Uniformity

Wu et al. (1987) have calculated the effect of a size distribution on the absorption of an array of square quantum dots, and found that the emission broadening varied as the size non-uniformity, thus suggesting that fabrication of optical devices is not ruled out by the effects of size distribution. Vahala (1988) calculated that in high-gain operation, a quantum dot laser array does not offer advantages over a bulk semiconductor unless the size tolerances are tightly controlled, in low gain operation, however, the fabrication does not require such size tolerances, and offers the possibility of low threshold operation, though, as yet, this has not been demonstrated.

## 3.2 Device Implications

The successful operation of quantum wire lasers has been demonstrated by, among others, Kapon et al. (1989b) with MOCVD grown wires on grooved substrates, but this approach, as compared with wires fabricated by deep mesa etching, benefits from the efficient capture of carriers in the un-quantized well material, and this carrier capture is not possible in deep mesa etched wires. A recent study of the optical properties of the quantum wires grown in these V-grooves [Kapon et al., 1992] has shown that the photoluminescence excitation spectra exhibit enhanced absorption and increased sub-band separation, both in good agreement with a model for an effective wire width of 16 nm. Time-resolved studies [Christen et al., 1992] of the same material has revealed that the luminescence is dominated by one-dimensional carriers.

The prospects for quantum wire lasers fabricated by deep mesa etching are, however, less promising, because of the low capture of carriers, and the unresolved question of the effect of non-radiative processes arising from non-passivated free surfaces.

As a result of the modelling of the luminescence behaviour of one- and zero-dimensional structures discussed below, the optical yield for quantum dot lasers is predicted to be so small as to be rendered useless.

In the case of optical modulators, however, quantum dot devices are expected to yield advantages over quantum well devices, as the absorption between peaks may be minimized, and the possibility of multiple wavelength operation exists, if the dot size distribution were kept small [Wu et al., 1987].

## 3.3 Luminescence Efficiency of Nanostructures

### 3.3.1 Surface Diffusion (or 'Dead Layer') Model

As will be discussed in Chapter 8, the surface diffusion model, presented for the case of wires by Forchel et al. (1988) and later for dots by Clausen et al. (1989), relies on the luminescence efficiency of the structures being dominated by carrier diffusion from the bulk of the structure to the structure etched surface. Assuming a constant generation of carriers, it is possible to derive expressions for the normalized luminescence efficiency as a function of structure size. As illustrated in Chapter 8, and noted by Hamao et al. (1991), the dot expression is not analytic for the appropriate values of diffusion constant D and for the structure size-range of interest, but may be used to to provide additional information on the application of the wire expression to the limiting cases of such structures.

### 3.3.2 'Intrinsic' Bottleneck Model

Weisbuch et al. (1992) and Benisty et al. (1991) have developed a model to calculate the luminescence yield from dots and wires as a function of lateral dimension. This model has no free fitting parameters, such as surface recombination velocity or dead layer thickness, and is based only on intrinsic phenomena of the one- and zero-dimensional systems. As the dimensions of the structure approach one- and zero-dimensionality, the energy and momentum relaxation is predicted to be inhibited. This arises from the small energy separation of the energy levels of the electron one- and zero-dimensional sub-bands as the dimensions are reduced, which results in the suppression of LO-phonon scattering when the energy levels become separated by energies smaller than that of the LO-phonon. This leaves scattering by acoustic phonons as the main relaxation process for the electrons at low temperature.

In addition, scattering of electrons by acoustic phonons has been calculated by Bockelmann and Bastard (1990) to decrease substantially for wires of width, and dots of diameter, below 150 nm, compared to 2D confined carriers. The model takes into account size irregularities of the nanostructures, the modifications to the transition rates due to LA phonon scattering between all occupied levels, and the probability of the levels being occupied. It also assumes a typical non-radiative recombination lifetime of 0.1 ns.

As a result, when an electron-hole pair is photocreated, the hole thermalizes to the bottom of the valence band in a short time compared to the non-radiative lifetimes, but the electron is held in higher energy states because of the reduction in scattering mechanisms due to the quantization. The electron and hole are thus in orthogonal states for times long compared with the two-dimensional radiative recombination rate because of the conservation rules for energy and momentum, and thus, as a result, non-radiative recombination processes dominate over the radiative recombination. This reduces dramatically the luminescence yield. The model is supported by reference to magnetic confinement in quantum well lasers.

The effect has been reported in this group in dots by Sotomayor Torres et al. (1991), where the transition probability between the electronic states in the dot or wire has been calculated taking into account both the phonon and electron wavevectors. In a paper by Wang et al. (1992), the 'intrinsic model' is combined with the 'dead layer' model to provide an accurate fit to their data. The master equation on the occupation probabilities is iterated to obtain a steady state which allows the computation of fluxes and yields separately for the non-radiative and radiative recombination channels. The results obtained compare favourably with the experimental results for the best deep etched dot and wires.

The behaviour of the radiative efficiency of quantum box luminescence is tentatively explained in a model produced by Benisty et al. [Benisty et al., 1991]. In this model, the poor radiative efficiency is explained as an intrinsic effect due to the decreased relaxation rate in zero-dimensional systems in the 100-200 nm size range, and in quantum dashes, or 'pseudo-wires', the onset of the decay in radiative efficiency occurs for a much smaller dash width than for the same dot diameter.

### 3.3.3 Exciton Trapping along Wires

In Chapter 8, a model is presented in which the emission efficiency in the high quality material of our structures is governed by the trap density, following the suggestion by Kash et al. (1986). The removal of some 96% of the well area by etching, followed by a scaling of the remaining emission to a normalized level according to the remaining area coverage, leads to an increase of the calculated effective emission efficiency if the non-radiative areas within a diffusion length of a trap are removed. In certain cases, this could give rise to a calculated effective emission efficiency greater than that of a control mesa. This model gains plausibility as the MBE GaAs layers grown immediately prior to the series of quantum well layers used in this work exhibited record free carrier densities and mobilities, suggesting less than 4 x $10^{13}$ $cm^{-3}$ free carriers, corresponding to a sheet donor density of 10 ionised donors per $\mu m^2$. For wires of 1 μm long by 0.1 μm wide this would suggest one ionised donor per wire.

## 3.4 Quantum Well Exciton-Polaritons in Wires

In periodically-modulated microstructured surfaces fabricated by Kohl et al. (1988), Demel et al. (1988) and Heitmann et al. (1990), a strongly polarized feature was observed indicating the existence of quantum well exciton polaritons formed by the coupling between the periodic quantum well excitons and photon emission. The nature of the feature was confirmed by the presence of a sharp dip in the reflectivity spectrum at the same wavelength. A later study by Kohl et al. (1990) investigated the exciton polariton emission as a function of wire width down to 150 nm, and in this range the exciton polaritons behave as free particles, but below 150 nm wire width, the polariton features disappear suggesting that the excitons are confined in the wires of this width. This hypothesis is supported by the luminescence excitation spectra which show a blue-shift of the ground-state luminescence, and the appearance of wire-width dependent sub-band transitions.

## 3.5 Photoluminescence of Wires and Dots

### 3.5.1 Microcrystallites

Quantum dots can be realized in the semiconductor microcrystallite system, where microcrystallites of size between ~2 and 10 nm are precipitated in liquids, glasses and dielectrics, and show three dimensional electron quantum confinement effects in the optical spectra [Brus, 1986], including spectral shifts from the confinement of up to 1 eV. In an unstrained heterojunction, such as the

GaAs / $Al_{0.3}Ga_{0.7}As$ system, the interface merely changes the crystal potential with minimum disruption to the bands, but in the microcrystallite system the lattice is interrupted at the semiconductor-matrix interface, and the surface contains 'dangling bond' states which may give rise to mid-gap states, surface reconstruction, or chemical bonding to foreign atoms. The smallest crystallites behave as atomic clusters with discrete molecular bond energy levels, rather than an energy band structure.

Commercial glass filters contain many small crystallites of cadmium selenium sulphide. Warnock and Awschalom (1985) demonstrated, in some filters, that the crystallites were of the order of 10 nm in size, and luminescence spectroscopy revealed energy shifts from the bulk CdSeS which allowed the confinement energy of the localized electrons to be calculated. The microcrystallite size could be controlled by annealing the filter glass, but the distribution, size and shape of the microcrystallites are poorly controlled. The emission has been attributed to donor-acceptor pair recombination from deep traps, strongly coupled to lattice phonons, rather than 1S free excitons.

Schmitt-Rink et al. (1987), and Nair et al. (1987) analyze in detail the theory of the optical properties of semiconductor microcrystallites showing that for cluster size very much smaller than the bulk exciton diameter, the Coulomb interaction can be treated as a perturbation on the single particle confined states, and suggesting that the oscillator strength would increase dramatically, and that bistability effects could be exploited in these structures.

Hodes et al. (1987) demonstrate, by absorption and photoluminescence experiments, that the optical band-gap is increased by up to 0.5 eV by confinement in crystallites of 4-8 nm deposited as films.

These investigations have been augmented by work in this group by Rodden (1993).

### 3.5.2 Direct Growth of Wires

#### 3.5.2.1 Growth of Microcrystals

Yazawa et al. report the direct growth of InAs wire crystals on GaAs substrates partially masked with $SiO_2$ (1991), and by the same method, Hiruma et al. (1991) and Morgan et al. (1991) report the fabrication and luminescence characterization of GaAs wires. The wires are air-exposed whiskers 10-200 nm wide, and 1-5 μm long, with an increase in width towards the base of the whisker. Photoluminescence characterization at low temperature reveals a spectrum dominated by free carrier-acceptor transitions, but the free exciton emission is more intense than in a control material, and the free- and acceptor-bound excitons are blue-shifted by up to 0.5 meV, resulting supposedly from quantum confinement in the widest parts of the whisker near the base. The most intense emission would be expected from the most confined states in the narrowest parts of the whisker due to the increased oscillator strength, and so the interpretation is doubtful.

#### 3.5.2.2 Growth on Tilted Superlattices

The method of growth on Tilted Superlattices or Fractional Layer Superlattices, that is surfaces which are cut a few degrees off the [001] crystal axis towards the [110] axis, was first reported by Petroff et al. (1984), although these first attempts by molecular beam epitaxy (MBE) failed due to non-uniform lateral growth at the step-edges. The series of steps allows preferential growth, and the growth direction is in the plane of the surface. By adjusting the composition it is possible to grow quantum wires. The advantages of the technique include the avoidance of damage-inducing fabrication stages, and the possibility of a large packing factor for the wires. This process has not yet, however, been demonstrated to produce quantum dots. Fukui and Saito (1989) successfully fabricated wires less than 10 nm in diameter by MOCVD for tilt angles $1° \leq \alpha \leq 3°$, and Gaines et al. reported the successful fabrication by MBE on surfaces cut towards the [110] axis, but not towards the [1$\bar{1}$0] axis [Fukui and Saito, 1989].

This technique was exploited by Tsuchiya et al. (1989b) to produce an array of quantum well wires of width ~ 5 nm. Polarized photoluminescence spectroscopy revealed a strong polarization dependence arising from the lateral confinement of the carriers. A more recent paper by Tsuchiya et al. [Tsuchiya et al., 1989a] has reported the fabrication of a quantum wire laser using the tilted superlattice technique, and the technique has been investigated more fully in a paper by Nakamura et al. (1991).

Kanbe et al. (1991) report the observation of optical anisotropy in a GaAs / AlAs 4 nm wire array grown on a vicinal substrate.

A development of the tilted superlattice is the Serpentine Superlattice (SSL), obtained when the natural meandering of the growth on a tilted superlattice is deliberately exaggerated [Weman et al., 1991], resulting in areas of shallow confinement. These SSLs were characterized by low temperature photoluminescence and excitation spectroscopy, and the strong anisotropy of the emission was attributed to one-dimensional localization.

#### 3.5.2.3 Growth on Non-Planar Substrates

The difference in growth rate on different crystal planes for ternary alloys [Demeester et al., 1988] may be utilized to reduce the size of structures grown on a substrate patterned with grooves, mesas, or mask windows.

Kapon et al. (1987) reported MBE growth on V-grooves wet-etched in a GaAs substrate, and Bhat et al. (1988) have studied the MOCVD growth in etched channels. Galeuchet et al. (1988) have used this technique to fabricate GaInAs wires on InP substrates patterned with [011] and [01$\bar{1}$] orientated grooves and mesas. Bhat et al. (1991) have fabricated InGaAsP wires in grooves etched in InP substrates. Kapon et al. (1989a) report the observation of stimulated emission from quasi-one-dimensional semiconductor wires fabricated by selective growth in V-shaped grooves.

The emission spectra exhibit fine structure which may be attributed to transitions between laterally confined states; the fine structure splitting corresponding to the calculated sub-band separations in a wide parabolic well. A subsequent paper [Kapon et al., 1989b] reveals improved laser characteristics with a threshold current reduced from 18 mA to 3.5 mA for uncoated devices at room temperature. The improvement in threshold current is attributed to the increase in optical confinement resulting from use of cladding with a higher Al mole fraction.

Lebens et al. (1990) have utilised grooves and mesas patterned by dry etching through a $Si_3N_4$ mask to act as growth sites for GaAs wires and dots. The structures have a uniform size, although facetted, and a size régime of 70 to 300 nm for dots and 90 to 200 nm for wires was possible. The cathodoluminescence shows a series of blue shifts consistent with the reduction in size for both the dots and wires, but this was attributed to stress resulting from the mask. A recent paper by Tsai et al. (1992) has developed the technique of facet modulation selective epitaxy which produces crescent-shaped wire doublets of 140 nm wire width, with a thickness of 14 nm.

Galeuchet et al. (1990) have used a similar technique with wet-etching through a photolith $SiO_2$ mask on InP substrates. MOVPE over-growth on the subsequent structures produced quantum wires. In the case of the grooves, however, the nucleation was irregular. Growth on a ridge and in selectively patterned areas resulted in a facetted structure with buried quantum wells. The facetting results in a decrease in wire width towards the top of the structure. Investigation of the wires by low temperature cathodoluminescence revealed high quality material, although with no evidence of confinement. Subsequent development produced facetted dots varying in size from 150 to 500 nm [Galeuchet et al., 1990a,b; 1991]. These dots were characterized by low temperature cathodoluminescence, and revealed that the spectra from the dots was red-shifted, possibly due to lack of control of the In content. The luminescence intensity from these structures was, however, greatly increased over control areas, by up to 420 %. This was attributed to the lack of air-exposed or damaged surfaces, and carrier transfer from under the mask to the dots.

Tsukamoto et al. (1993) report the fabrication of 'arrowhead' quantum wires using selective growth using the difference in growth rates between GaAs and AlGaAs. A systematic change in the quantum wire width results in a consistent blue-shift of the photoluminescence peak, which was attributed to confinement to one dimension. Wire widths of down to 14 nm with thicknesses of 25 nm were achievable. The blue-shift of the photoluminescence peak of the 30 nm wire at 8.5 K was blue-shifted by 60 meV.

Fukui et al. (1991) have reported the growth of tetrahedral quantum dot structures using selective growth through square windows in a $SiO_2$ masked substrate.

Kojima et al. (1990) report similar results with the growth of wires of width 60 and 90 nm with thicknesses of 3 and 7 nm respectively. The photoluminescence at 77 K reveals strong anisotropy in amplitude and peak energy in the plane of the substrate.

#### 3.5.2.4 Superstep Growth

A development of the tilted superlattice method is the 'superstep' technique, where off-axis growth is initiated on a substrate previously patterned by wet-etching through a photolith mask [Clausen et al., 1990; Cox et al., 1989a,b,c; Colas et al., 1989]. The principle of the growth is based on macrosteps; it has been shown by Vermeire et al. (1991) that it is possible to obtain macrosteps with up to $2^{\circ}$ off-orientation of the substrate. These are used to generate large fluctuations in well thickness, producing a type of superlattice with alternating sizes of quantum well. Colas et al. (1990a,b) have shown that it is possible to obtain a quantum wire structure by using the appropriate layer structure, and showed that the the luminescence emission could be resolved from areas of different thickness of well [Colas et al., 1990a].

#### 3.5.2.5 T-Junction Growth

Observation of GaAs / AlGaAs quantum wire formation has been reported recently by Gofii et al. (1992). The wires were fabricated at the T-junction between intersecting quantum wells grown perpendicularly. The presence of confined carriers was confirmed by the polarization dependence of the emission. Quantum wires of 5 nm were observed to have confinement energies of 28 meV.

#### 3.5.2.6 Gallium Droplets

Microcrystals of GaAs have been produced by As reaction with Ga droplets on a ZnSe surface [Chikyow and Koguchi, 1991]. The droplets of Ga form because of the large surface tension of Ga liquid and low Ga inter-diffusion at 200 °C. A distribution of pyramidal microcrystallites of base 35 nm separated by an average distance of 250 nm is formed when the droplets are exposed to As. As this process is very difficult to control, the droplets are irregular in size and distribution, and thus the technique suffers from the same limitations as the growth of semiconductor glasses, not being useful for systematic studies of the size dependence or for the fabrication of structure arrays suitable for device fabrication.

A recent development of this technique [Chikyow and Koguchi, 1992] has reported the growth of GaAs microcrystals on a Se-terminated GaAlAs surface. The mean size of the crystals was 860 nm, with a mean separation of 1.5 μm.

#### 3.5.2.7 Induced Growth of Wires

Takahashi et al. (1992) have reported the use of electron beams to induce MOCVD growth of 300 nm quantum wires.

### 3.5.3 Planar Modulation by Ruling

Xie et al. (1990) have used a ruling machine to fabricate wires from 200 nm to 1.6μm in width, and dots of 1.2 μm x 1.6 μm and 1.2 μm x 1.2 μm. The structures were characterised by low temperature photoluminescence, and show blue shifts compared with unpatterned areas. The shifts are conflicting and confused, and, in the case of the wires, independent of the width. This method is expected to contribute a significant amount of surface damage to the well, and no evidence, such as micrographs of the etch profile, was given to disprove this.

### 3.5.4 Wet Chemical Etching

Miyamoto et al. (1987) exploited the anisotropy of the wet etching process to undercut lithographically defined dots to reduce their size, resulting in a blue shift of the photoluminescence signal from the processed areas. The quantum dot structure thus formed was exploited in the fabrication of a p-n junction and optical guide structure. Lasing was not achieved due to the large separation, and hence poor optical confinement, between the dots.

Subsequently, lasing action from a wire-like active region was reported [Cao et al., 1988], where the wires were 120 nm wide and 30 nm thick. CW lasing was achieved at 77 K, demonstrating the low damage of the wire fabrication procedure.

### 3.5.5 Ion Implantation Induced Inter-diffusion (IIID)

In order to avoid the quenching effect ascribed to dry-etched GaAs structures from damaged sidewalls, Cibert et al. [Cibert et al., 1986,1987; Gossard et al., 1987] fabricated quantum wires and dots by 210 keV Ga ion implantation through a Ti / Au-Pd mask patterned by electron beam lithography, followed by rapid thermal annealing at 900 °C. The aluminium in the barriers diffuses into the vacancies caused by the ion bombardment. This alters the band gap, creating parabolic wells of approximate quantum wires of widths between 40 and 200 nm. The resultant structures were characterized by low temperature cathodoluminescence, and the spectra reveal a width dependant series of transitions, for wires from 450 to 140 nm, which was attributed to transitions between 1-dimensional states. Similar results were obtained from the quantum dots. The transitions were fitted [Cibert and Petroff, 1987] with a model of the potential profile resulting from the bombardment.

Forchel et al. (1988) and Leier et al. (1989) have used the same technique. For 100 and 130 nm wire widths, a width-dependent photoluminescence shift is observed, and this is identified as one-dimensional confinement, although this may be due to changes in well thickness instead. A later paper

[Leier et al., 1990] describes a consistent blue-shift with wire width varying from 310 nm down to 40 nm, with a blue-shift of 11 meV for 50 nm wires.

A similar technique was used by Hirayama et al. (1988), this time with focussed ion beams rather than electron beam lithography and ion bombardment. The luminescence characterization of the 200 nm quantum wire revealed fine structure which was attributed to quantum confinement in the parabolic lateral quantum well. A later report by Notomi et al. (1991) on 10 nm InGaAs / InP wires shows a clear blue-shift, attributed to confinement.

Yu et al. (1991) report the effect of Ga ion beam implantation on a GaInAs / InP superlattice, and the low temperature photoluminescence showed that the luminescence peak energy followed the quantum levels associated with one-dimensional confinement from the inter-diffusion.

Zarem et al. (1989) report similar 310 and 370 nm wire microstructures fabricated by diffusion selective disordering by Zn in-diffusion. Cathodoluminescence measurements reveal consistent blue-shifts of 21 to 30 meV, but these are inconclusive and may be due to Al diffusion rather than quantum confinement.

### 3.5.6 Strain Confinement

A review of the use of strain confinement is given in [Kash, 1990]. Kash et al. (1988) initially proposed the use of surface stressors to confine laterally carriers in a semiconductor quantum well. The stressors are formed by patterning a uniformly strained layer, with the resulting structures altering the volume dilation in the quantum well. The variation in dilation results in a lowering of the band edges, particularly in the conduction band, resulting in extra confinement of the electrons, but, in a first approximation, the holes are two-dimensionally confined in the quantum wells only.

Maile et al. (1987) and Forchel (1988, 1990) investigated the effects of ion milling and reactive ion beam etching (RIBE) on the luminescence efficiency of quantum wires down to 30 nm in both the GaAs / AlGaAs and InGaAs / InP systems. There is a steep decrease of three orders of magnitude in the integrated emission as the wire width is reduced from 6 μm to less than 1 μm in the GaAs / AlGaAs system for both ion beam milling and reactive ion etching, whereas in the InGaAs / InP system, the luminescence efficiency decrease is less than an order of magnitude over the same width range. In a later paper, Maile et al. (1988) report a very strong dependence of the emission efficiency of quantum wires on the GaAs / AlGaAs etched surface, but a weaker dependence in the case of InGaAs / InP, attributing this to a difference in the the surface recombination velocity between the two materials rather than a difference in surface recombination velocity due to the etch process used. GaAs / AlGaAs dots were also fabricated, but none of the dots luminesced.

The patterning of a pseudomorphic InGaAsP overlayer by electron beam lithography and reactive ion etching resulted in the lateral confinement of carriers in a GaInAs / InP, with a red-shift in the exciton emission arising from the stressors [Kash et al., 1989]. The arrays of wires and dots exhibited exciton confinement resulting from the strain, but the confinement was insufficient to give rise to any observable quantum effects. Amorphous carbon was used to pattern GaAs / AlGaAs wells [Kash et al., 1990a], giving rise to a 31 meV red-shift in the photoluminescence emission from the lateral confinement to 400 nm wires. The photoluminescence excitation characterization of these structures is reported in Kash et al. (1990b), and the excitation spectrum shows an isotropy in the optical selection rules, which is due to valence band mixing by the strain rather than any one-dimensional effect.

In a similar process, Tan et al. (1991, 1992) report the effect of lateral confinement in a GaAs / AlGaAs well resulting from patterning a pseudomorphic InGaAs stressor layer. As in the results published by Kash et al., the luminescence is consistently red-shifted, by up to 20 meV for 75 nm wires. The integrated luminescence intensity is not reduced after the processing.

Ismail et al. (1991) report the patterning and characterization of large-area quantum-wire arrays of 30 - 80 nm width. The luminescence revealed a blue-shift due to a combination of strain and quantum confinement. Polarization effects due to the confinement were observed in the wires, but not in the well emission. Shubnikow-de Haas measurements on modulation–doped material patterned in an identical way showed one-dimensional quantum confined behaviour.

Xu et al. (1992) report the successful fabrication of surface stressors.

### 3.5.7 Laterally Patterned Modulation Doped Heterostructures

Confinement to spatially indirect Type II quantum wells was reported by Weiner et al. (1989, 1990), using modulation doped material depleted by ion milling through a periodic wire mask. Inelastic light scattering revealed inter-sub-band excitations of the one-dimensional gas, and luminescence measurements allowed the calculation of sub-band occupancy.

### 3.5.8 Confinement in Lightly Etched Structures

Gréus et al. (1992) report the fabrication of 35 nm quantum wires by lightly etching the top barrier. For wire widths below 100 nm, the emission efficiency is at least an order of magnitude greater than that of deeply etched structures. For wires of below 70 nm width, a systematic blue-shift is observed, which is attributed to quantum confinement.

### 3.5.9 Confinement in Deeply Etched Structures

Reed et al. (1986) reported the first attempt to fabricate quantum dots in GaAs / AlGaAs by electron beam lithography and reactive ion etching, and characterize them by low temperature photoluminescence. The decrease in signal strength reduction was attributed to the filling factor, with no evidence of sidewall damage. The luminescence from the 0.25 μm dots was observed to show enhanced light hole exciton recombination over the quantum well and 0.25 μm quantum wires, and this was attributed to a bottleneck arising in the relaxation mechanism from light hole to heavy hole; this bottleneck was due to the confinement in the 0.25 μm dots. As these results were not reproducible either by this group or by others, the validity of these data must be in question, and could perhaps be attributed to poor sample fabrication.

Worlock et al. (1986) and Kash et al. (1986) report the fabrication, photoluminescence and luminescence excitation spectra from 40 nm wires and 45 nm dots in GaAs /AlGaAs. The structures were fabricated by electron beam lithography and reactive ion etching. The structures are reported to luminescence more efficiently, by factors of up to 30 for the wires and up to 100 for the dots, than the original quantum wells, and so the etched surfaces are not contributing significantly to the non-radiative recombination. This is tentatively attributed to inhibition of non-radiative recombination at traps and surfaces by the lateral confinement of the carriers.

Temkin et al. (1987) report the fabrication of 30 nm wires and dots in InGaAs / InP, and the structures exhibit blue-shifts of the luminescence of 8-14 meV, consistent with lateral quantum confinement. The luminescence emission efficiency does not scale with the filling factor, and this is attributed to the shadowing effects of an incompletely removed mask rather than surface recombination.

Gershoni et al. (1988) fabricated wires in InGaAs / InP down to 35 nm in width.The intensity of the wire emission can be accounted for by the area filling factor, thus discounting the possibility of significant non-radiative recombination in the sidewalls. The luminescence emission is blue-shifted by 11 meV, consistent with the quantum confinement in the wires, and the electron-heavy hole n=1 transition is split due to lateral confinement in the low temperature photoluminescence excitation (PLE).

Arnot et al. (1989a) reported the first use of MOCVD overgrowth after reactive ion etching of GaAs / AlGaAs quantum dots. Dots of diameter 75, 110 and 350 nm were fabricated on MOCVD material, and dots of diameter 75, 110 and 300 nm on MBE material, and all the dots were found to luminesce in the MBE material before re-growth, but none were found to luminesce in the MOCVD material. After re-growth, it was found that only the 300 nm dots on the MBE material luminesced, but luminescence was recovered from the 350 nm dots on the MOCVD material. The emission was found to blue-shift after re-growth at 750 °C, and this was attributed to Al inter-diffusion into the well through the vacancies introduced during etching. Arnot et al. (1989b) also reported a study of overgrown quantum dots fabricated by two different etch processes in MOCVD material.

None of the dots (of size 70, 110, 350 nm) luminesced with either etch process prior to overgrowth, but, after overgrowth, emission was obtained from the 350 nm dots etched in $SiCl_4$, but no emission was obtained from the $CH_4$ / $H_2$ etch. The emission efficiency of the dots scaled with the material remaining after etching. A study of the photoluminescence properties of quantum dots [Arnot et al., 1989c] showed no significant decrease in the normalized emission efficiency for either $SiCl_4$ or $CH_4$ / $H_2$ etch processes as the dot diameter is reduced from 400 to 40 nm, no difference in behaviour was noted between the etch processes, or in the choice of metal or organic mask. The results are reviewed in Sotomayor Torres et al. (1990a,b).

Andrews and Arnot (1990a) find that the luminescence from free-standing GaAs/AlGaAs quantum dots below 20 K scales with the emitting volume down as far as 40 nm dots, whereas the luminescence from InGaAs/GaAs dots, a strained system, quenches below 500 nm diameter dots. This is attributed to carriers thermalizing rapidly in the GaAs / AlGaAs system, and being localized in fluctuations in the well thickness. This effect is assumed to be less important in the InGaAs / GaAs system. In a later paper, Andrews et al. (1990b) compare the radiative emission from free-standing wires and dots. At low temperature, the dot emission is found to scale with the volume of material remaining, whereas the emission from the wires falls off rapidly with decreasing wire width. The emission from the wires is recovered by overgrowth with indium tin oxide; this may be due to the relaxation of strain in the wires from the overgrown layer. The narrowest overgrown wires exhibit anisotropy in the polarization dependence of the excitation spectrum: this is attributed to a combination of strain and quantum confinement effects.

Clausen et al. (1989) performed cathodoluminescence on 60 nm to 200 μm dots to model the surface recombination velocity and 'dead layer' in GaAs/AlGaAs. The luminescence from the dots is found to be dependent on the etch time, and cuts-off at a dot diameter of 600 Å with an etch depth of 150 nm. The dot luminescence is found to be best modelled by a diffusion equation with a dead layer thickness dependent on etch time. The luminescence intensity is found to be insensitive to the surface recombination velocity when the dot is smaller than the exciton diffusion length of 1 μm. This model is, however, dependant on the assumption that the higher order terms in the expression can be neglected, and, as considered in Chapter 8, the diffusion constant applicable for quantum wells under these conditions rules this assumption invalid. The surface recombination velocity could be varied from $10^6$ to $10^{10}$ $cms^{-1}$, compatible with Forchel's estimate [Forchel, 1988].

Izrael et al. (1990) fabricated wires in InGaAs / InP and GaAs / AlGaAs down to 30 nm width, and characterised them by low temperature time resolved photoluminescence. The smallest GaAs wires do not luminesce in the as-etched state, but do so after overgrowth. Overgrowth leads to a significant increase in carrier lifetime in GaAs / AlGaAs wires, and the surface recombination velocity falls from $10^5$ to $10^4$ $cms^{-1}$ after overgrowth. A 5 meV shift in the smallest 40 nm wires may be due to confinement. A recent report [Birotheau et al., 1992] gives optical data on GaAs / AlGaAs quantum wires of widths down to

15 nm, showing lateral confinement energies of up to 23 meV and one-dimensional polarization effects. Comparison of the observations with calculations of the absorption spectra indicate wire width fluctuations of ± 5 nm.

Mayer et al. (1990) report time-resolved investigations of the sidewall recombination in dry-etched GaAs quantum wires. The etch damage was found to be the same in Ar assisted $CCl_2F_2$ as in $SiCl_4$. Measurements of the surface recombination velocity S at 30 K gave values of $10^6$ $cms^{-1}$, with a recombination time of 292 ps and a diffusion constant of 3 $cm^2s^{-1}$. At 50 K these values were 2 . $10^6$ $cms^{-1}$, 552 ps and 6.5 $cm^2s^{-1}$ respectively.

Hornischer et al. (1992) report the overgrowth of deep-mesa-etched AlGaAs / GaAs 500 nm quantum wires by LPE. The overgrowth is reported to reduce the surface state density and lateral edge depletion in modulation doped quantum wires, and resulted in a one-dimensional system which was observed by FIR spectroscopy.

A study by Maile et al. (1990) of dry-etched wires subsequently overgrown has revealed a dramatic decrease of the dead layer thickness. After overgrowth, the original values for 40 nm wires etched in $CCl_2F_2$ / Ar for a surface recombination velocity S of $8.10^5$ $cms^{-1}$ and dead layer thickness $W_d$ of 65 nm were reduced to $5.10^5$ $cms^{-1}$ and 14 nm respectively. The photoluminescence spectra of the overgrown wires shows a consistent blue-shift of up to 3 meV in the smallest wires, but this may be due to effects other than the quantum confinement.

Patillon et al. (1991) report the large enhancement in the luminescence from InGaAs / InP quantum wires of 50 nm width, together with a blue shift of 2.5 meV attributed to the quantum confinement. The wires were fabricated by an etch process relying on the reversal of the equilibrium in a vapour phase epitaxy reactor.

Hamao et al. (1991) report the use of annealing under a $SiO_2$ cap to reduce the surface recombination velocity from 8 x $10^6$ to 4 x $10^4$ $cms^{-1}$ in GaAs / AlGaAs quantum well mesa structures. The disordering introduced by the annealing of the $SiO_2$ forms a shallow potential at the surface which reduces the surface recombination.

Lage et al. (1992a,b) report the use of luminescence techniques to probe the effects of quantum confinement in 150 nm wires, with an active width of 60 nm. The characterization by luminescence excitation reveals quantization of the centre of mass of the exciton, and high intensity excitation spectroscopy of the electron-hole plasma reveals transitions between one-dimensional sub-bands, although the wire widths are too great for single-particle quantization at low excitation density. Kohl et al. (1989) demonstrate one-dimensional confinement effects in etched GaAs / AlGaAs wires of 70 nm width. The confinement is evidenced by the appearance of two sub-band heavy hole transitions, separated by 2.5 meV, and by the strong polarisation dependence of the photoluminescence excitation spectrum. The magnetic field dependence of the sub-band transitions indicated an increase in the heavy hole exciton binding energy of 15 %. Heitmann et al. (1991), in reviewing excitonic excitations in wires, provide additional evidence for the one-dimensional confinement in a wire-width dependent series of luminescence excitation transitions. These agree with the exciton binding energies of quantum confined one-dimensional exciton sub-bands.

excitation transitions. These agree with the exciton binding energies of quantum confined one-dimensional exciton sub-bands.

## 3.6 Summary

Considerable effort in recent years has resulted in a much greater understanding of the necessary fabrication procedures and optical properties of low-dimensional structures. Both one- and zero-dimensional optical devices have been made, in the form of optical modulators and lasers, but the full exploitation of the potential of these devices remains limited by the problems in the fabrication of such devices.

Investigations of the optical properties of one- and zero-dimensional systems have reported varied behaviour for the structures, discussed in this chapter. Of particular interest are the works of Andrews et al. (1990), Kash et al. (1990), and Qiang et al. (1993), which have investigated the effect of strain on these structures.

The effect of strain on the recombination rate of the structures fabricated in this work is discussed in Chapters 8 and 9.

# Chapter 4: Sample Fabrication

## 4.1 Sample Design

The method of electron beam lithography and dry etching was ideally suited to the fabrication of structures of differing size and aspect ratio. This flexibility was exploited in making a range of structures varying from small circular dots to long, thin wires, by way of intermediate structures called 'dashes', which could be regarded as either elongated dots or shortened wires.

The fabrication of such structures allowed the investigation of the radiative properties of wires and dots, and, in particular, the discrepancy in the reported luminescent behaviour of wires and that of dots, as reported by Arnot (1990).

The method of fabrication, that of electron beam lithography using negative resist, and dry etching in a reactive ion etch plasma, has been previously reported by a number of authors.

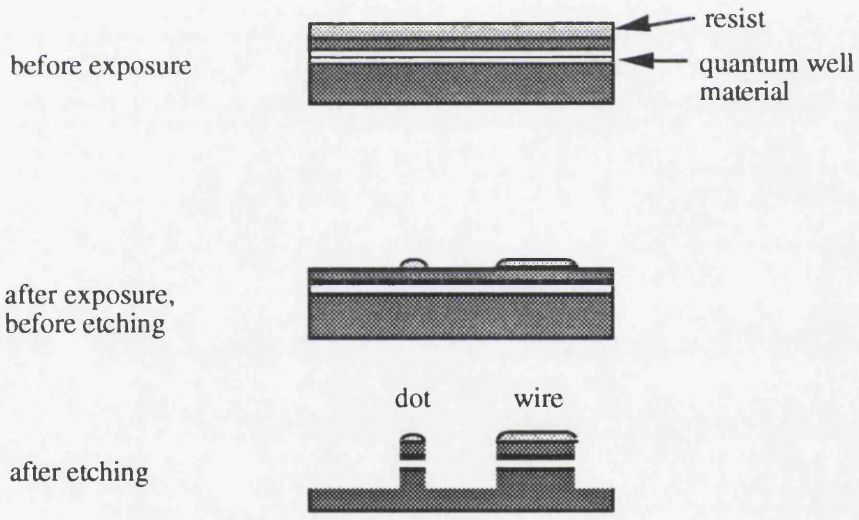


Figure (4.1): Schematic of Fabrication Process

Throughout the project, the emphasis was on simplifying the fabrication techniques in order to concentrate on one process. This allowed one to attempt to correlate the behaviour of a number of samples prepared under nominally the same conditions, differing solely in the pattern written to the mask.

Following this rationale, negative resist was chosen to define the structures, because its use reduced the number of processing steps. The use of positive resist and a metal mask was rejected because this ruled out any contribution to strain in the structures at low temperature due to the difference in thermal expansion coefficients of mask and material.

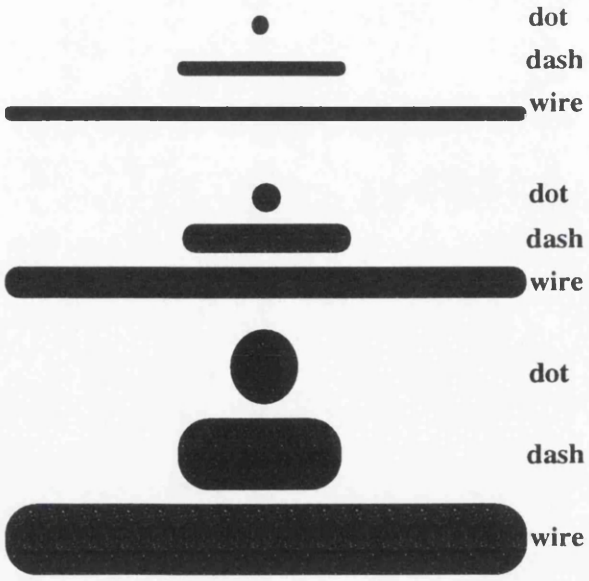


Figure (4.2) : Schematic of dots, wires, and dashes

### 4.1.1 Sample Layout

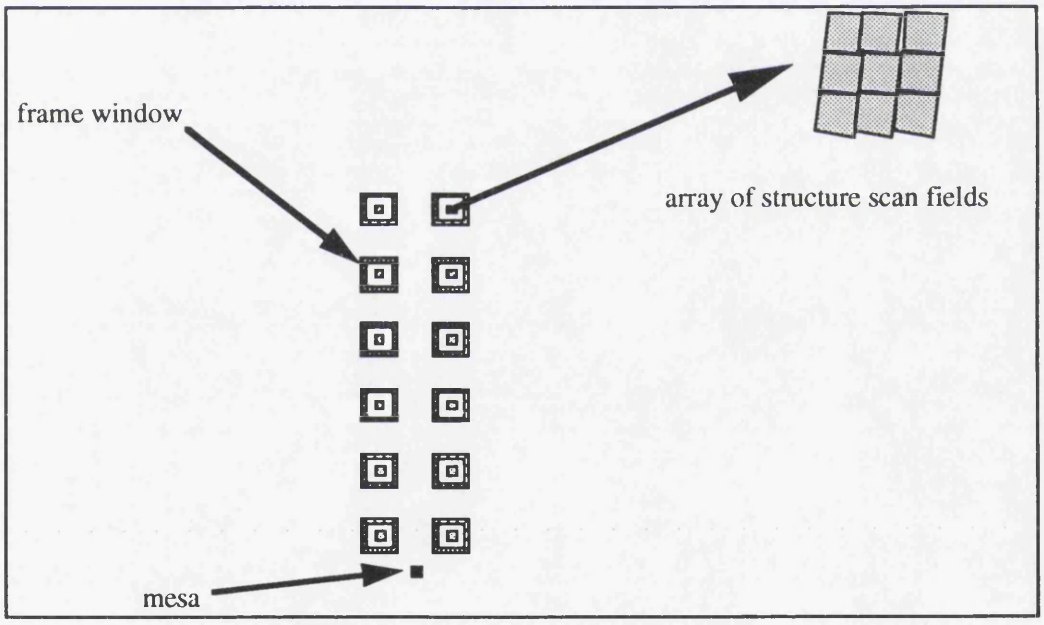


Figure (4.3): Schematic of Sample Layout

### 4.1.2 Frame Windows

Initial attempts required that the patterned areas were surrounded by a frame, to enable easy alignment of the laser beam on the structure array under investigation in the cryostat, and to ease fine focussing of the electron beam for structure lithography. These frame arrays were fabricated initially by evaporation of germanium / gold, but this method was superseded by a wet-etching technique which allowed greater contrast on under the electron microscope, and reduced the fabrication time by avoiding metal evaporation.

Improvements in the observation of the sample in the cryostat rendered the fabrication of these etch windows unnecessary, thus simplifying the fabrication process in the Philips. The Jeol required focussing at the four corners of the chip allowing interpolation of the focus at sites across the chip, and thus ruling the etch windows redundant in this case as well.

## 4.2 Lithography

### 4.2.1 Electron Beam Lithography Microscopes

Two electron beam lithography microscopes were available for use during the course of this project: a modified Philips PSEM500 scanning electron microscope, and a modified Jeol 100CXII scanning / transmission electron microscope.

Preliminary structures were fabricated on the Philips electron microscope, because of the unreliability of the scan generation software implemented on the Jeol electron microscope, but the Philips microscope was later abandoned because improvements in the Jeol microscope software allowed the exploitation of its greater speed and higher resolution due to its 100 keV beam. The Jeol could write similar patterns several times faster than the Philips microscope, thus saving several hours per sample. The advantages in speed and resolution were, however, counterbalanced by difficulties in focussing and poor reliability.

### 4.2.2 Negative Resist

The preferred resist for the small structures was Philips High Resolution Negative (HRN) resist, thinned to a concentration of 8 % in Microposit thinner.

The resist was spun on at 7 000 rpm for 60 s, and baked at at 120 °C for 1hr, giving a thickness of 280 nm. Typical doses for the 100 keV beam of the Jeol are illustrated in Figures (4.6) and (4.7).

Following development in undiluted MIBK at 23 °C for 15 s, the samples were rinsed in IPA for 15 s, and then the development and rinsing were repeated.

### 4.2.3 Stitching

The scan generation software had fixed the number of individually addressable pixels in a scan frame at (4096,4096). In order that adjacent pixels connect to form a smooth pattern, the spot size was chosen to be comparable with the pixel size, and thus for the highest resolution lithography, the smallest pixel size dictated the smallest structure which could be written. Because the number of pixels in a scan frame was fixed as mentioned above, the choice of pixel size defined the size of the scan field.

The stages on the electron microscopes had significant backlash and were accurate only to a few μm. Thus a number of scan fields laid next to each other exhibited a degree of overlap and separation dependent on the size of the scan field and the accuracy of the microscope stage. Pattern overlap leads to over-exposure and malformed structures, whereas field separation introduced inaccuracy into the calculation of filling factor for the array under investigation. It was decided to use the maximum scan field size possible which gave the smallest pixel size needed, in order to minimize the field stitching.

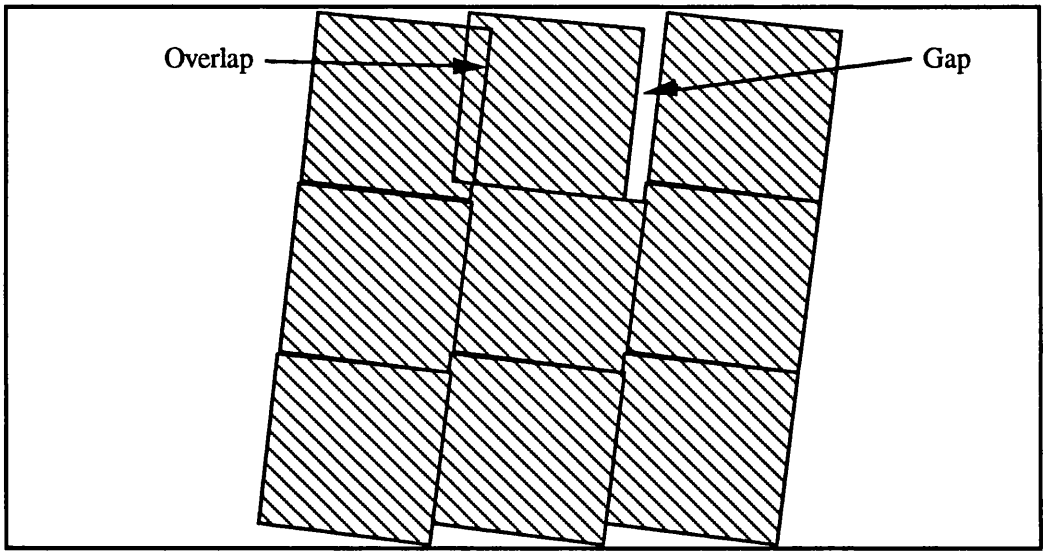


Figure (4.4): Stitching Scan Fields

### 4.2.4 Exposure Testing

A considerable effort was devoted to obtaining the correct exposure for the structures required for this project. The exposure was obtained empirically because of the proximity effect, where the exposure at one site is directly affected by the average exposure in the area surrounding the site. Thus small features had to be spaced far apart to ensure resolution, whereas bigger structures could be placed closer together. One needs to maximize the area coverage of the structures to maximize the luminescence intensity recorded in the photoluminescence, and so there is a payoff between the proximity effect and the filling factor.

By fabricating a large number of variations on a structure by changing the exposure and separation between the structures in an array it was possible to devise a suitable scan file. The mask was inspected under the scanning electron microscope to ensure that the resist had cleared and that the mask was intact. After dry-etching, the mask was checked again in case the mask had disintegrated in the etching.

The exposure patterns had to be derived for both the Philips and Jeol microscopes as the accelerating potentials of the electron beams were different, and thus the proximity effect behaviour differed in the two cases.

### 4.2.5 Mask Fabrication on the Philips PSEM500

It was necessary to re-focus the microscope at every area to be patterned on the chip, in order to compensate for the variation in height across the chip. This arose from its position in the sample holder. On a smooth resist surface insufficient features were present to set the focus, but the large frame windows fabricated on the surface as a first process level allowed finer focussing for the smaller structures. It was possible then to focus on the corner of the frame window, and align the array of patterned areas along the side of the frame window.

#### 4.2.5.1 Philips PSEM500 Software

The pattern exposure was generated from files run on the EBSS program on the Philips; the data consisted of Go Files (see Table AI.5), which were batch routines for the exposure, Position Files (see Table AI.4), which determined the layout of the scan frames on the chip, and Scan Files, which specified the structures to written in each scan frame.

The key parameters of the Philips PSEM500 electron microscope are summarized in Tables (AI.6) and (AI.7).

The size of the scan frame on the Philips is defined as (0-4096, 0-4096) pixels, and elements outside this range will 'wrap round' causing spurious exposure. An exposure may be defined for each pixel, but for patterns consisting of a large number of identical small elements, such as the dots, wires, and dashes fabricated in this project, the scan files make use of the 'step-and-repeat' command, thus avoiding the specification of the exposure of every pixel in the frame. For a pattern defined by exposing the black squares of size [(x1,y1),(x2,y2)], one divides the field into box intervals of size X,Y. The number of repeats is calculated as Int (4096/X) and Int (4096/Y).

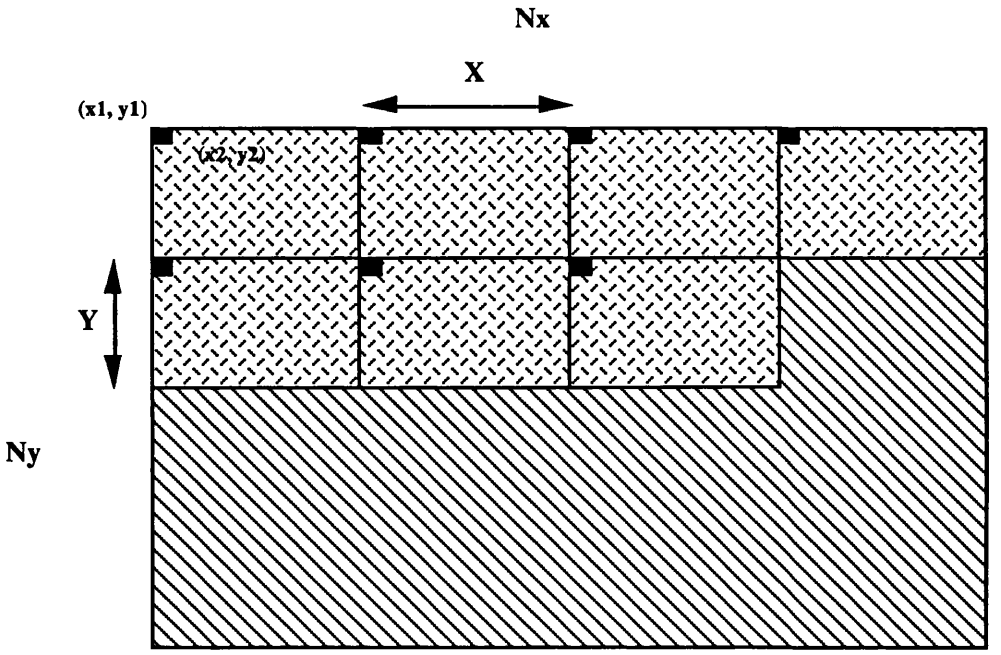


Figure (4.5): Layout of elements in a scan-frame in step-and-repeat file

The form of the scan files is shown in Table (A1.2) in Appendix A.1.

### 4.2.6 Mask Fabrication on the Jeol 100CXII Microscope

#### 4.2.6.1 Jeol Microscope Software

The software on the Jeol microscope could use the same scan-files as the Philips microscope, but the running of the routine was performed by a job-file, which set up the focus, controlled the stage movement, and determined the scan files.

A variation of spot size was observed across the scan field of the Jeol. This is attributed to de-focussing of the beam, and increased the spot size at the corners of the scan field by approximately 50% over that in the centre of the field. As the structures were exposed above the minimum threshold, the de-focussing resulted in a slight increase in structure size at the corners. This could have been avoided by restricting the area scanned to the centre of the frame and increasing the number of frames stitched, but this was deemed to introduce more uncertainty into the calculation of filling factor than neglecting the variation of structure size across the frame.

In Figure (4.6), it can be seen that the exposure in the smallest structures had to be increased dramatically over that of the larger areas; this was a consistent trend for structures of all widths. In addition, it may be noted that the actual fraction of the scan field covered by the structures (the inverse of the 'filling factor') fell dramatically as the structure size was reduced. This was as a result of the proximity effect: small structures had to be spaced relatively further apart as the proximity scattering became more important. Measurements of the most interesting structure sizes were thus subject to the

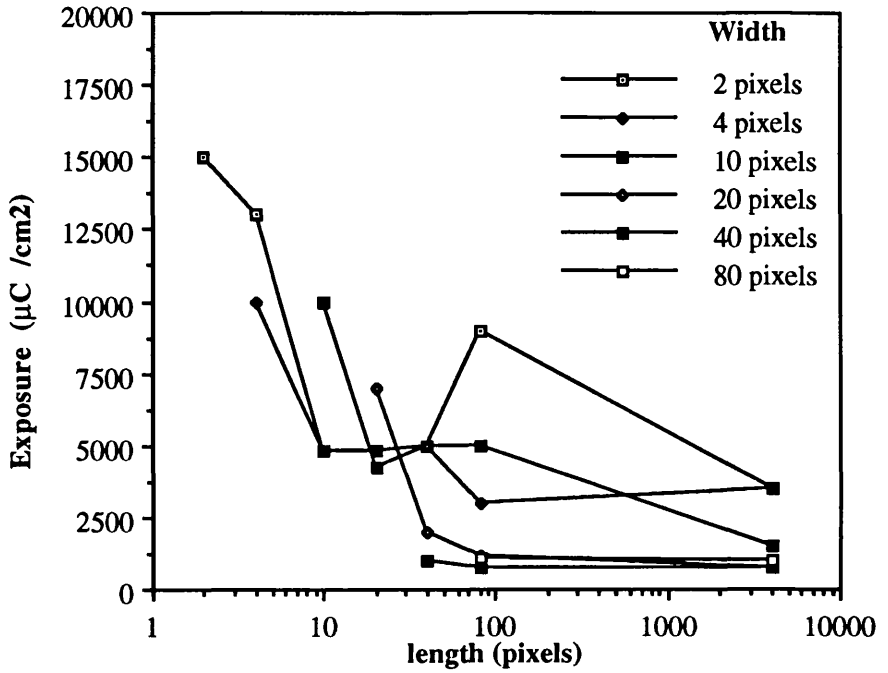


Figure (4.6): Jeol Microscope Exposures against Structure Size

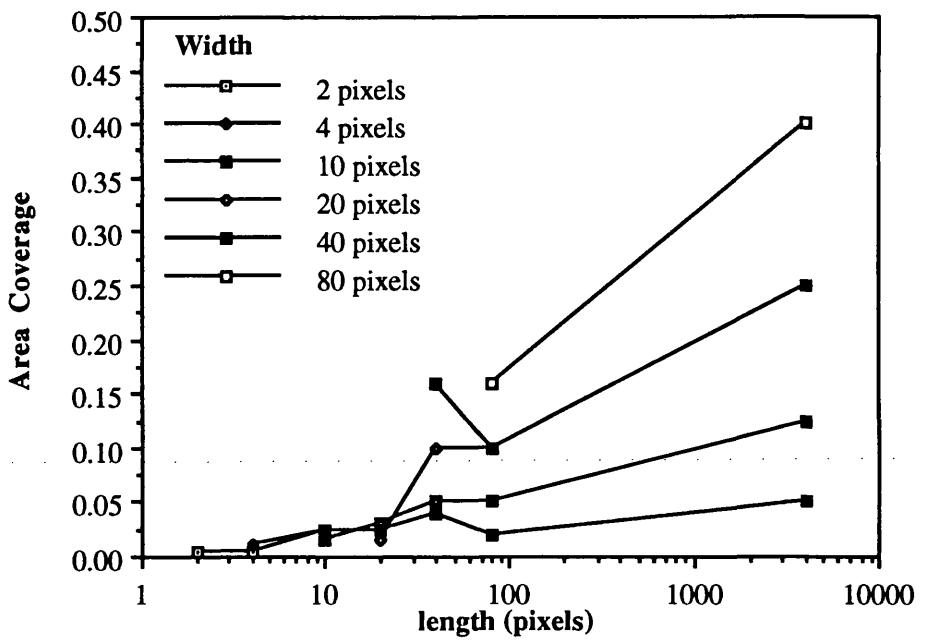


Figure (4.7): Jeol Microscope Area Coverage against Structure Size

largest errors, as in these cases the total emission intensity of the structure area was weak, and the normalization of the emission intensity to the equivalent of complete area coverage resulted in small intensity variations being amplified greatly.

### 4.2.7 Mask Fabrication Focus

On the Jeol electron microscope, the focus for the whole chip was achieved by measuring the coil current required to achieve focus at the four corners of the chip. The the best fit focus plane was then calculated for the whole chip, and the size of the deviations from this plane at the four corners indicated the consistency of the focus. Unfortunately, the size of the deviations does not necessarily indicate the accuracy of the mean focus, and so samples were lost due to poor focus leading to insufficient exposure.

The focus was determined by accurate choice of focus points, and by reduction of the reported focus deviations.

## 4.3 Etching

### 4.3.1 Definitions

#### 4.3.1.1 Edge Profiles, Isotropy and Resolution in Etching

The resolution of an etching process is crucially determined by the etch bias, which is a measure of the under-cut or over-cut between the mask and the resulting etched image. In the figure below, the bias is defined to be (B-A). A zero-bias etch process transfers the mask pattern faithfully, producing a vertical etch profile, and is referred to as *anisotropic*. When the etch rate is uniform in all directions, the etch is known as *isotropic*, and the bias is twice the film thickness.

The anisotropy $A_f$ is defined as:

$$A_f = \frac{v_l}{v_f}$$

where $v_l$ and $v_f$ are the lateral and vertical etch rates, respectively.

Some particular etch processes are orientation dependent, which etch some crystal planes faster than others. In zinc-blende lattices, the (111) plane is more closely packed than the (100) plane, and thus the etch rate is lower on the (111) plane than the (100).

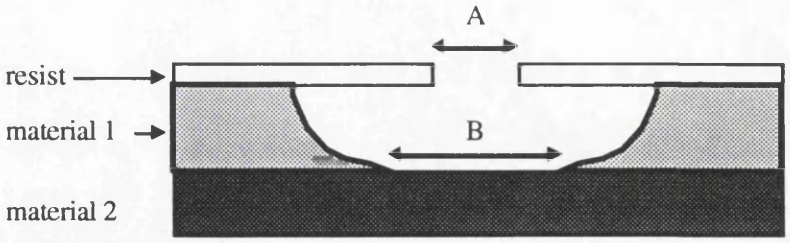


Isotropic

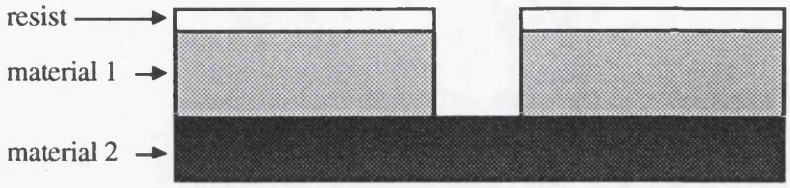


Anisotropic

Figure (4.8): Etching Profiles

The ultimate resolution of the etch process is dependent on the anisotropy of the process and the thickness of the mask.

#### 4.3.1.2 Selectivity

All materials exposed to the etchant have a finite etch rate, and an important parameter of etch process is the *selectivity*,which is the ratio of etch rates between different materials. The selectivity with respect to the mask affects the resolution and tolerance of the final structure.

### 4.3.2 Wet Etching

In semiconductor materials, wet chemical etching [Thomas et al., 1986] usually proceeds by oxidation, followed by dissolution of the oxide by chemical reaction [Shaw, 1981]. The etch mixture must thus contain an oxidizing agent (usually hydrogen peroxide or a halogen), and a solvent to dissolve the amphoteric oxides (either an alkali or an acid).

In the particular case of GaAs, the (111)-As planes etch much faster than the (111)-Ga planes, resulting in trapezoidal and dove-tailed etch profiles in certain orientations [Tarui et al., 1963]. Because of the difference in activity of the (111)-Ga and (111)-As planes, few GaAs etches are isotropic. The As faces generally have a polished appearance, but the Ga faces are pitted and show crystallographic defects [Iida and Ito, 1971].

Typical etches for GaAs combine an acid with hydrogen peroxide and water; the relative composition determines the etch rate, surface finish and selectivity. The acids used include $H_2SO_4$ and $H_3PO_4$ [Thomas et al., 1986], but, as detailed below, in this project HCl was used.

#### 4.3.2.1 Frame Window Wet Etch

To form the large feature frame windows, trenches of ~ 500 μm in length by ~ 30 μm in width were etched using a HCl / $H_2O_2$ (30 %) / $H_2O$ mixture in the ratio of 80 : 4 : 1. At room temperature, this gives an isotropic etch rate of 1.1 μm / min [6] with little evidence of GaAs / AlGaAs selectivity, and a 2 minute etch was found to give a trench of sufficient depth to be observable on the electron microscope when overlaid by the second layer of resist. This was necessary to allow the accurate focussing and alignment of the structure arrays.

HCl was considered appropriate rather than $H_2SO_4$ or $H_3PO_4$ because of the need to reduce contamination by other chemical species, and HCl would be appropriate as the sample would be subsequently etched in $SiCl_4$.

### 4.3.3 Dry Etching

Dry etching was originally developed for resist stripping in oxygen plasma, and subsequently gained favour in stripping silicon nitride, for which no wet chemical etch was available. The major disadvantage of wet chemical etching, however, is the impossibility of obtaining etching with $A_f$ close to unity, and the ability of certain dry etching methods to overcome this has resulted in intense study of this technology [6].

In this project, the etching process used was reactive ion etching in $SiCl_4$. This combines the benefits of *Sputter Etching* and *Plasma Etching*, in order to maximize the anisotropy and minimize the damage introduced into the material.

One distinguishes between *sputter etching* and *ion beam milling*, where the material is removed by 'physical' effect of bombardment of the target, and *plasma etching*, where the material is removed by the 'chemical' effect of a reaction of the target with the plasma resulting in a volatile product, even though a plasma may be used in both cases. The method in which one exploits both the 'physical' and the 'chemical' aspects of the plasma is known as reactive sputter etching or *reactive ion etching* .

#### 4.3.3.1 'Physical' Etching

Sputter etching is used widely in sputter deposition systems to eject material from a target before deposition on the substrate. The process can also be used to etch material, and as the material is removed by bombardment by ions moving along electric field lines, a high degree of anisotropy may be obtained.

There is little selectivity between the mask and the material, and so it is not suitable for high aspect ratio structures, but the most important consideration is that of damage. Degradation of the characteristics of the material such as photoluminescence intensity is observed, although these can be reduced by using smaller ion energies and heavier ions. Thermal annealing can ameliorate the damage, although this is ineffective for ion bombardment above 500 eV.

#### 4.3.3.2 'Chemical' Etching

In contrast to the physical nature of the sputter etching process, plasma etching relies on the chemical reaction of the substrate with active species in a plasma to produce a volatile product. To minimize the physical effects of ion bombardment, the operating pressure is higher than in reactive ion etching, and the electrodes are of closely similar size.

As a result of the increase in reacting species, the etch rate is higher than in reactive ion etching, but the etching is more isotropic, with aspect ratios of less than 2:1. In addition, the etch is preferential, with

(111)-As > (100) > (110) > (111)-Ga.

The absence of high-energy ion bombardment results in little ion-related damage.

#### 4.3.3.3 Reactive Ion Etching

Reactive ion etching (RIE) uses apparatus similar to that used for sputter etching, but the plasma employed is the same as that used in plasma etching, rather than the noble gas plasma used in sputter etching.The combination of chemical and physical effects is thought to produce anisotropic etching with low damage.

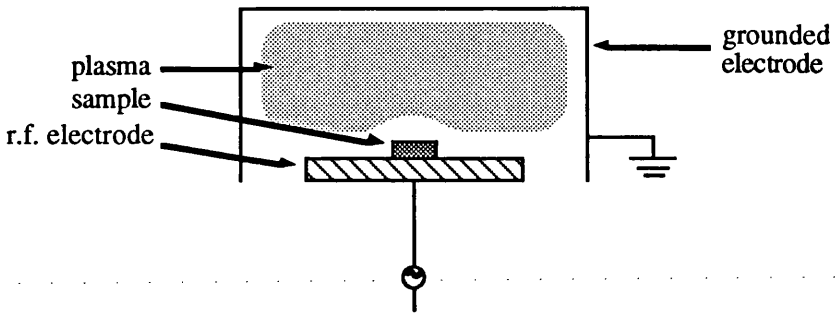


Figure (4.9): Schematic of a reactive ion etch unit

When an insulator is introduced into a d.c. discharge tube, the full potential is developed across the insulator, and the glow is extinguished.

In order to excite a discharge across an insulator, the d.c. potential must be replaced with a.c. excitation, so that the charge built up in one half-cycle is discharged in the next half-cycle. At low frequencies, the discharge can only be maintained periodically, and the frequency must be increased to maintain a continuous discharge. An order of magnitude calculation of the time taken to discharge a

parallel plate capacitor gives a typical value of 1 μs, suggesting an excitation frequency of 1MHz. In addition, the use of radio frequency excitation promotes ionization at lower applied potentials, because the electrons gain higher energies whilst oscillating in the plasma, and at lower gas densities, due to the increased likelihood of a collision when an electron makes multiple traverses of the gas.

Experimentally, a continuous discharge can be maintained above 100 kHz, but the frequency is generally chosen to be 13.56 MHz, the ISM frequency allocated by the U.S. Federal Communications Commission for Industrial, Scientific and Medical (ISM) use. The generation of intense harmonics of the fundamental frequency results in more stringent emission requirements, so the choice of 13.56 MHz is largely convention, and recent studies indicating the dependence of ion energy on frequency have resulted in other exciting frequencies being chosen.

In order to maximize the etching at the target, the potential drop across the sheath must be maximized.

According to the Koenig model [Koenig and Maissel, 1970], the ratio of the potentials $V_1$, $V_2$ at electrodes of areas $A_1$, $A_2$ satisfy the relationship:

$$\frac{V_1}{V_2} = \left(\frac{A_2}{A_1}\right)^4$$

The larger potential difference appears at the smaller electrode, and the fourth power dependence exaggerates the effect of the difference in areas.

The r.f. power generator is matched to the loading of the chamber to ensure maximum transmission with a reactive impedance.

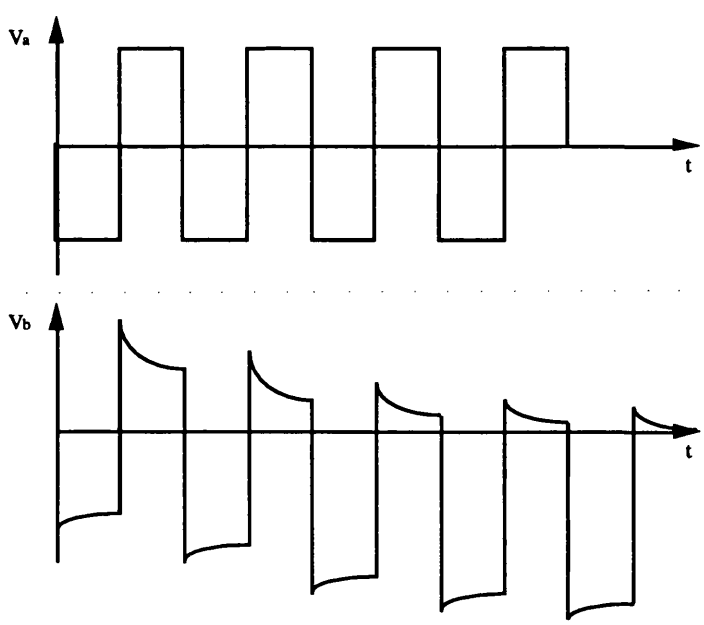


Figure (4.10): Development of d.c. bias

As a result of the difference in mobility of the electrons and ions in the plasma, at high frequencies a net negative potential is developed on the insulated electrode. This can be considered in a simplified fashion using square-wave excitation of the system. When the insulated electrode is driven negative by the r.f. source, the positive ions slowly discharge the insulated electrode, and when the electrode is driven positive, the electrons discharge the electrode. Due to the difference in mobility between the species, the discharging by the electrons is more effective, and over several cycles the insulated electrode develops a net negative potential, which rises to half the peak-to-peak voltage. Similar behaviour occurs with sine wave excitation. This potential is known as the d.c. bias.

The d.c. bias results in the ions being accelerated in the same sense during the non-zero-potential half cycle, and thus increasing their momentum towards the substrate.

#### 4.3.3.4 RIE with $SiCl_4$

A number of gases have been used successfully to reactive ion etch gallium arsenide; these include $Cl_2$ [Hu and Howard, 1984], $BCl_3$ [Sonek and Ballantyne, 1984], $CCl_2F_2$ [Klinger and Greene, 1981], $CCl_2F_2/Ar/O_2$ [Hu and Howard, 1980], $Cl_2/CH_4/H_2/Ar$ [Vodjdani and Parrens, 1987], $CH_4/H_2$ [Cheung et al., 1987], and $SiCl_4$ [Stern and Liao, 1983].

**Choice of $SiCl_4$ for Project**

In order to choose a suitable etch gas for the semiconductor system of GaAs / AlGaAs multiple quantum wells, a number of considerations have to be taken into account.

1) Halocarbons, such as $CCl_4$, and hydrocarbons, such as $CH_4$ / $H_2$, can give rise to polymer films which can contaminate the sample and etch chamber [Stern and Liao, 1983]. The use of etchants such as $Cl_2$, $BCl_3$, $CH_4$ / $H_2$ and $SiCl_4$ avoids this problem.
2) One requires that the etch rates of the $Al_{0.3}Ga_{0.7}As$ and GaAs be very similar, to avoid preferential etching of the quantum well and the distortion of the etch profile. $CCl_2F_2$ [Seaward et al., 1987], and $SF_6$ / $SiCl_4$ [Salimian and Cooper, 1987, 1988; Cooper et al., 1987] reactive ion etching can exhibit extreme selectivities for use in etch-stop reactions, and were not used in this project.
3) The etch must have high resolution; gases proved to have etched small features include $SiCl_4$ [Stern, 1984; Thoms 1988], $BCl_3$ [Randall 1988a,b], Ar / $BCl_3$ [Scherer, 1986], $O_2$ [Kubena, 1987], $CCl_2F_2$ / Ar [Maile, 1988], $CCl_2F_2$ / He [Lee, 1988], $CH_4$ / $H_2$ [Thoms, 1988].
4) In the Department, facilities are available, and considerable experience has been gained in etching with the gases $SiCl_4$ [Thoms, 1988] and $CH_4$ / $H_2$ [Thoms, 1988; Cheung et al., 1987].

Earlier work by in this laboratory by Arnot [1] has shown that the fabrication of wires and dots is possible using either $SiCl_4$ or $CH_4$ / $H_2$, but that the sidewall etch profile is considerably smoother with $SiCl_4$ than with $CH_4$ / $H_2$. Although some work [Cheung et al., 1987, 1988] has shown that $CH_4$ / $H_2$ creates less damage than $SiCl_4$, the problems of feature control for the intermediate structures and hydrogen incorporation due to the etch process were sufficient to justify $SiCl_4$ rather than $CH_4$ / $H_2$.

**GaAs / AlGaAs Selectivity in $SiCl_4$ Plasma**

The etch rate depends on the volatility of the chemical reaction products in reactive ion etching [Seaward et al., 1987], and in chloride etching of the GaAs / AlGaAs system, the selectivity depends on the volatility of the Group III chloride products.The volatility of the Group V chlorides is much greater.

$SiCl_4$ has been shown to be an effective etchant of Al [Sato and Nakamura, 1982)], but it might be thought that the low volatility of $AlCl_3$ would mean a preferential etch of GaAs over AlGaAs in the chlorinated gas plasma. Nevertheless, $SiCl_4$ reactive ion etching of GaAs / AlGaAs shows no evidence of preferential etching [Salimian and Cooper, 1987, 1988], indicating that the additional mechanism of physical sputtering may play a role in rendering the difference in volatility of the chlorides unimportant. The evidence of a 1:1 GaAs : AlGaAs etch rate is important as the preferential etch of the quantum well would not be easily observed under normal inspection using the scanning electron microscope.

| Etch Product | Volatility at 25°C (Torr) |
|---|---|
| $AsF_5$ | > 60 000 |
| $AsF_3$ | > 200 |
| $AsCl_3$ | ~ 40 |
| $GaCl_3$ | ~ 0.08 |
| $AlCl_3$ | 0.000 2 |

Table (4.1): Volatility of Halogen Etch Products [Seaward et al., 1987]

**Etching of oxide layer**

Results from plasma etching in chlorinated gases [Smolinsky et al., 1981] have indicated that the etch rate of the oxide layer can be much lower than that of the GaAs, and for $Cl_2$ and $COCl_2$, the oxide does not etch at all. In reactive ion etching, however, the oxide layer can be sputtered [Hu and Howard, 1984], and thus no pre-etch is required to allow the reactive ion etching of the rest of the material. The etching of the oxide layer is, however, considerably slower than the reactive etching of the AlGaAs, and is observed as an 'inductance' time in the etch process.

**Effect of Parameters on Etch Process**

The temperature affects the etch process through its effect on the chemical reaction rates; the etch rate generally increases with temperature through an Arrhenius dependence, and the selectivity may be affected due to the material-dependent activation energies [Mogab, 1983]. To ensure etch reproducibility and etch uniformity across the sample, the substrate was cooled with water to a temperature of 39 °C, sufficiently above ambient to aid the desorption of water vapour during the chamber evacuation.

The flow rate is chosen to supply the minimum reactant species sufficient to remove material; for a given system, the flow rate is intimately connected with the etch pressure, and is set to maintain the chamber pressure against the full suction of the vacuum pump. As the etch pressure is increased, ion-ion scattering results in a lower ion directionality, and thus the anisotropy of the etch process falls. For the etch processes used on the Plasma Technology RIE 80 etcher, the gas flow was set at 9 standard cubic centimetres per minute, to give a gas pressure of 12 mTorr.

The d.c. bias is determined by the r.f. power and the gas pressure, and so for a fixed pressure, variation of the applied power results in a variation of the d.c. bias. Increasing the d.c. bias results in an increased etch rate, and more anisotropic etching, but increases the damage [Stern and Liao, 1983]; this is because the energy of the sputtering ions is increased. The d.c. bias chosen depends on the etch profile required, the effect of bias on selectivity, and the extent of damage which can be tolerated. At low d.c. bias in $SiCl_4$, AlGaAs etches faster than GaAs, and GaAs achieves the same etch rate only above 100 V d.c. bias, and so despite the risk of serious damage, it was decided to perform the etching with a d.c. bias of 300 V, which resulted in conditions optimized for selectivity and structure profile. Using the Plasma Technology RIE-80 reactive ion etcher used in this project, with a graphite base-plate of 15 cm radius, and an applied r.f. power of 100 W, the power density is 0.14 W $cm^{-2}$.

The etch time was chosen bearing in mind the etch rate at the d.c. bias and minimum flow rate, to give an etch depth sufficient to isolate the quantum wells in the structures for a given material. Under standard conditions, the etch rate was ~ 0.2 μm / minute, and so the etch time was set at 1 minute. Although a prolonged etch at low power causes less overall damage than a prolonged etch at high power, the depth of sidewall damage increases with etch time in reactive ion etching, and so in order to reduce the damage on the sidewalls of the quantum wells, a fast etch with high d.c. bias was more preferable than a slow etch with low d.c. bias.

### RIE Damage

The environment of the dry-etching is rich in species which can contribute to the degradation of the substrate material beyond the intended etching. The plasma contains high-energy ions, neutrals, electrons and photons, which can all penetrate the surface and change the properties of the crystal [Mogab, 1983].

Under energetic ion or neutral impact, the surface atoms can be displaced. This form of damage is limited to a region within 10 nm of the surface. Deep UV and soft X-rays generated in the plasma create energetic electron-hole pairs in the crystal, breaking bonds, and the electrons created by atomic displacement or by primary ionization interact with defects and traps in the material.

Of particular concern for thin conducting channels, quantum wires, and quantum dots, is the damage to the sidewalls of the structures fabricated. In strongly anisotropic etch processes, greater sidewall damage than surface damage can result due to the lower sidewall etching rates. As the etch front progresses, the surface damage is etched away, but the sidewall area exposed to damage resulting from back-scattered ions progressively increases, and remains vulnerable throughout the etch run.

This sidewall damage is minimized by using heavier ions, by reducing the ion energy, or by increasing the chemical contribution to the etching. For a given etch gas, the ion energy may be reduced by reducing the d.c. bias, and the chemical contribution may be increased by increasing the etch pressure.

As a result, one may choose a particular etch process in an attempt to minimize the damage, but the actual etch operating conditions are chosen to give the optimum etch selectivity, profile and depth.

### 4.3.4 Summary of Etch Parameters Used

| | |
|---|---|
| r.f. Power (Forward) | 100 W |
| r.f. Power (Back) | 0 |
| d.c. bias | 300 V |
| Gas Flow | 9 sccm |
| Chamber Pressure | 11.6 mTorr |
| Etch Time | 60 s |

Table (4.2): $SiCl_4$ Etch Parameters on Plasma Technology RIE 80 etcher

Figure (4.11): Micrograph of Typical Wires
(approximately 0.1 μm by 100 μm)

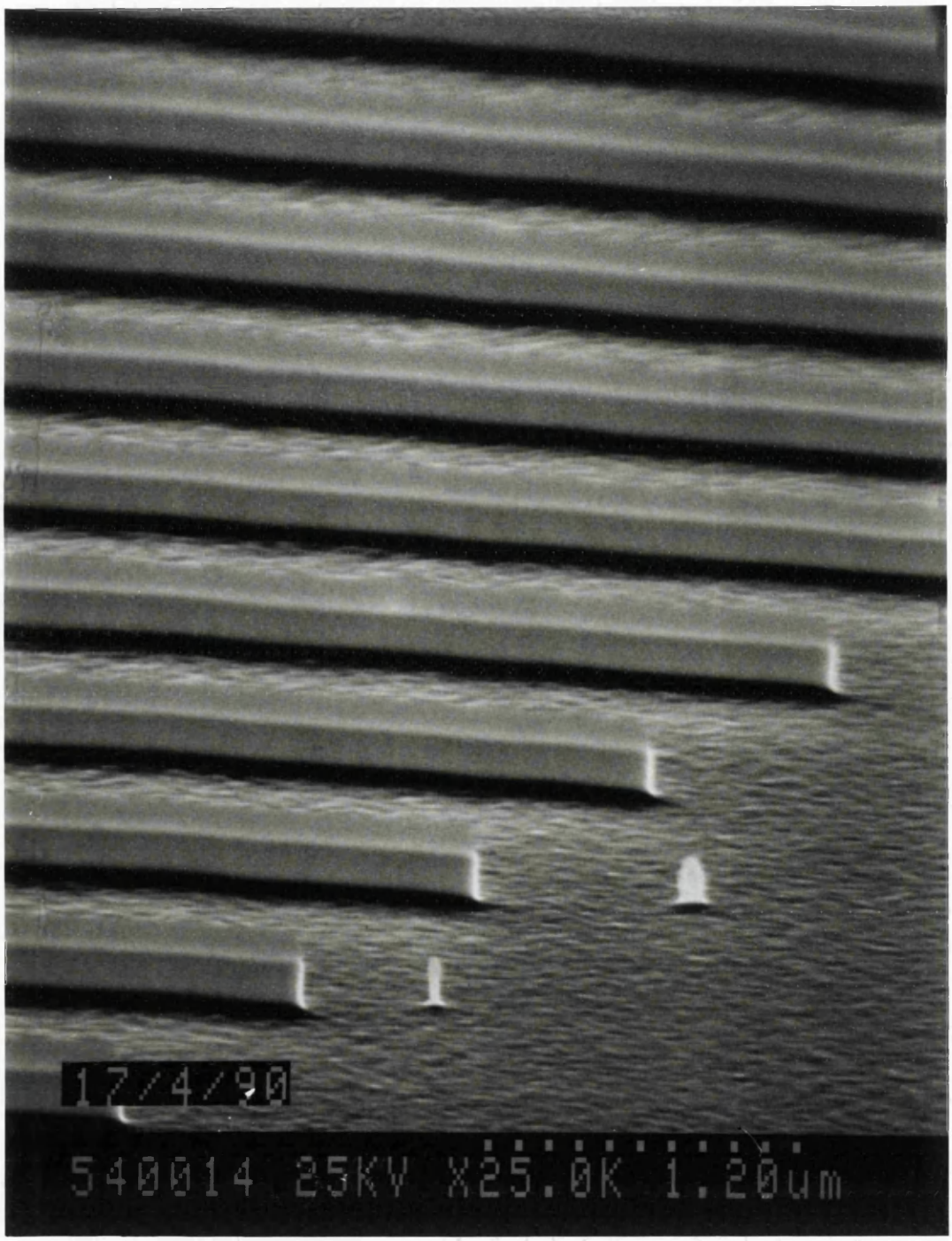

Figure (4.12): Micrograph of Typical Dots
(approximately 0.1 μm diameter)

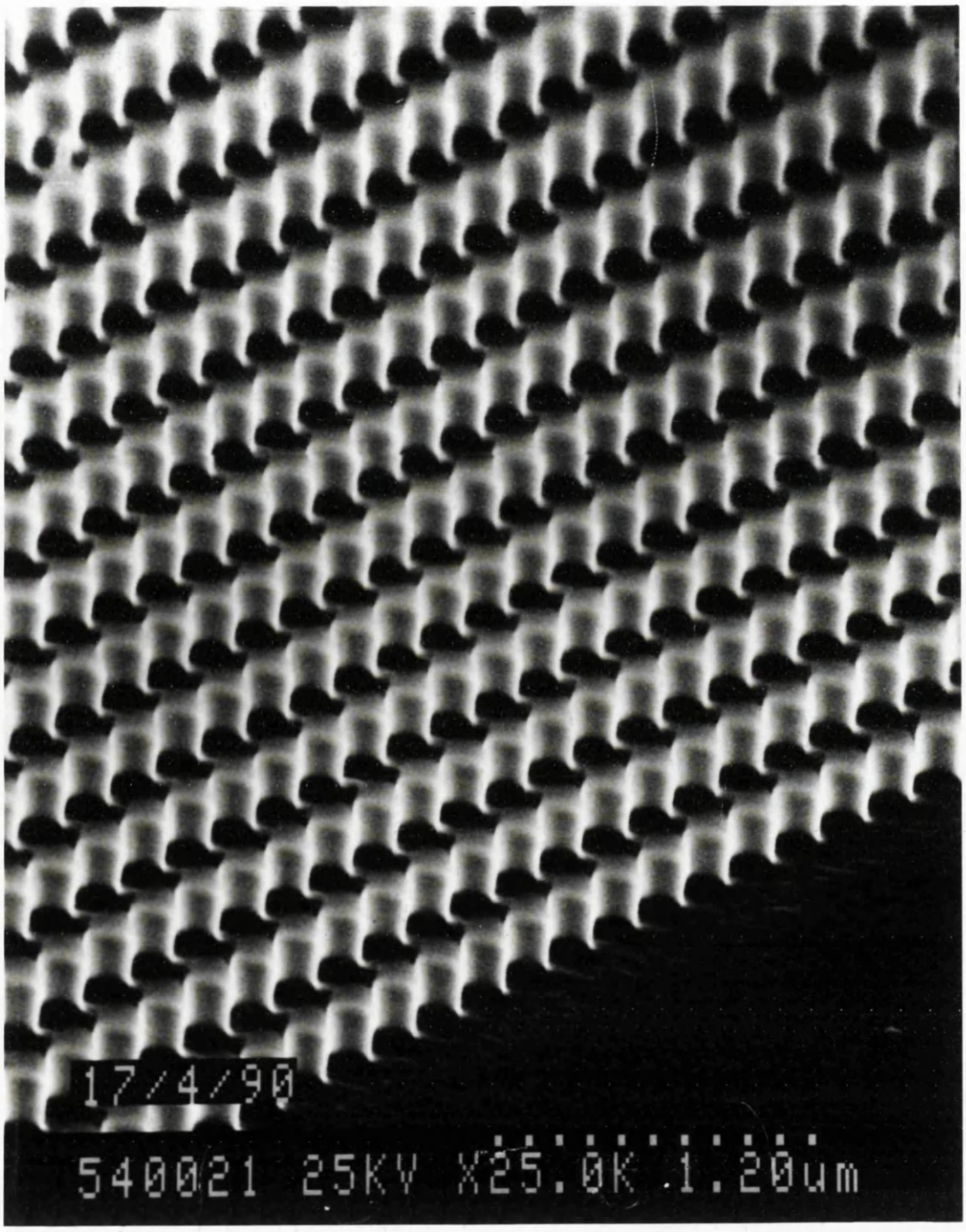

Figure (4.13): Micrograph of Typical Dashes
(approximately 0.1 μm by 1 μm)

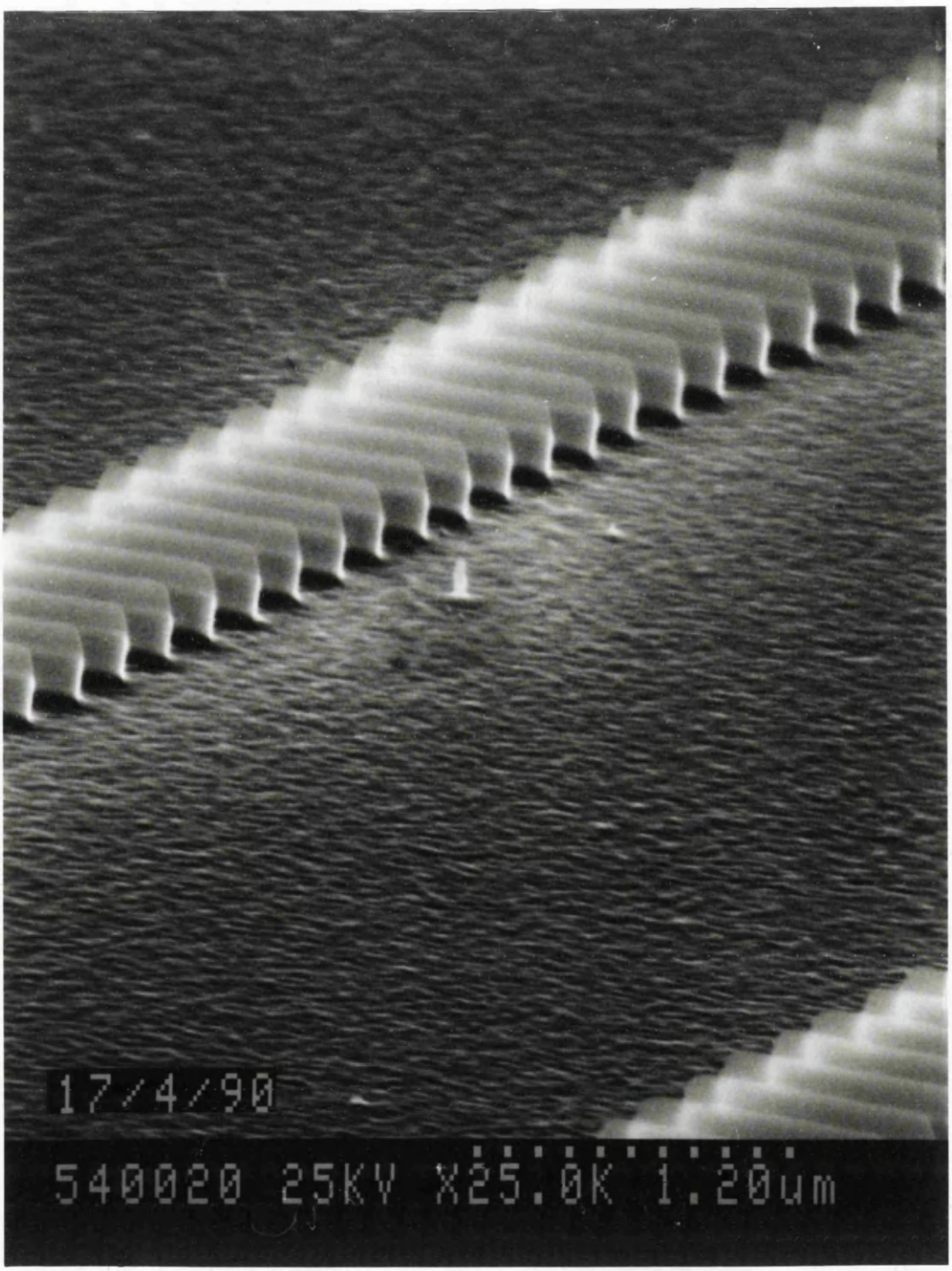

# Chapter 5: Optical Spectroscopy Apparatus

## 5.1 Photoluminescence

### 5.1.1 Discussion of Technique

Standard low temperature photoluminescence methods were used in the course of this project, save for the adaptation of the technique to characterizing small (100 μm square) areas with low signal intensity. The etched structures were difficult to observe, emitted weakly, and were in close proximity to strongly emitting control areas (mesas).

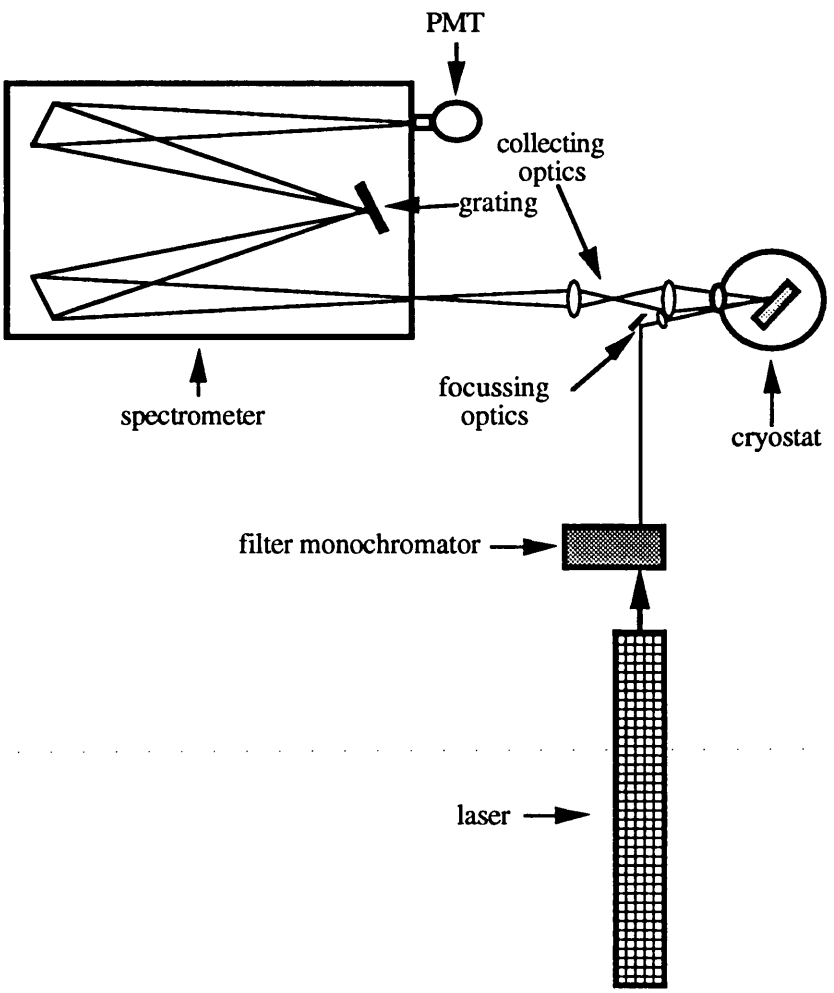


Figure (5.1): Backscattering Photoluminescence Apparatus Layout

The laser beam was focussed onto the surface of the sample using a microscope objective, mounted on an XYZ micrometer stage. The beam was then aligned onto the relevant structure area using the focussing stage. Care was necessary to establish that the laser beam was aligned accurately onto the structure to be investigated, and the scattered light had to be focussed visually onto the entrance slits of the spectrometer.

Once the light had been aligned by eye, the signal from the quantum wells was located, and the alignment of the collecting optics optimized to maximize the signal. If no quantum well emission could be located, the laser beam intensity was increased, and if there were still no signal, the alignment of the laser beam to the structure area was checked in both the focussing optics and collecting optics. Some areas were seen not to emit after processing. Care had to be taken during the optimization technique in order not to maximize the signal on a more efficient emitting area nearby.

### 5.1.2 Apparatus Layout

In the initial apparatus layout, the near back-scattering configuration, it proved to be extremely hard to align the emitted light into the entrance slits of the spectrometer, and to make sure that the laser beam had indeed been focussed on the correct sample area. This was because it was impossible to project an image of the chip with the structure areas and laser spot visible onto the plane of the slits.

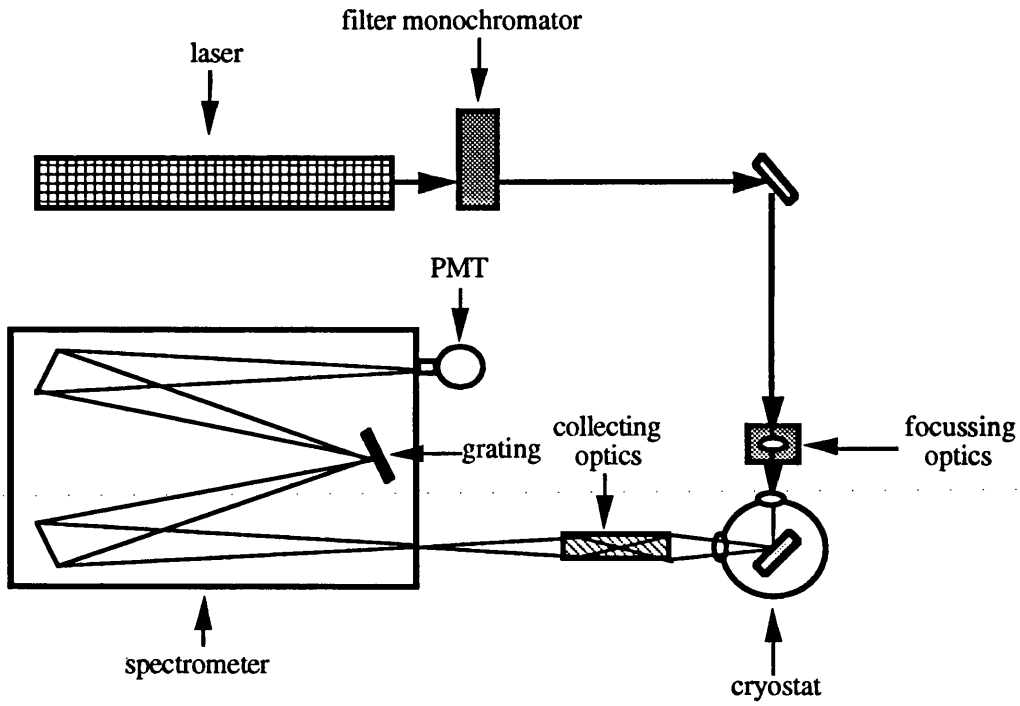


Figure (5.2): Modified Photoluminescence Apparatus Layout

The small focal length of objective and collecting optics prevented illumination from a 'swan-neck' light source, and the laser beam reflection left off-axis, preventing the signal being optimized by 'walking' it down the reflected beam axis.

In the modified apparatus layout, the laser beam was aligned at 45° to the plane of the sample, thus enabling the image of the laser spot on the sample to be projected through the collecting optics onto the entrance slit plane. In addition, the reflected laser beam ran along the emitted light axis, and thus it was possible to maximize the emission intensity once the collecting optics had been aligned with the aid of this beam.

### 5.1.3 Photodetectors

#### 5.1.3.1 Photomultiplier Tube 1: Hamamatsu R943-02 Photon Counter

The R943-02 photon counter [Watt, 1988; Arnot, 1990] used in the early stages of the project, although extremely sensitive up to 930nm because of its GaAs(Cs) photocathode [Hamamatsu, 1988], was limited in this application of photoluminescence because of its imposed small signal to noise ratio of 100:1. The photoluminescence of the quantum wells was relatively bright, and easy comparison of the differences of the relative emission intensity was made difficult because of the dark count level of approximately 20 counts per second (cps) and the self-imposed upper limit of 2000 cps to prevent deterioration of the photocathode for Raman scattering work. The photon counter was operated at 1.5 kV and cooled to -23 °C with a Peltier effect chiller, and the pulses fed into either an amplifier / discriminator circuit, or the acquisition (ACQ) board of a modular spectrometer control system (SPECTRALINK®).

#### 5.1.3.2 Photomultiplier Tube 2: Hamamatsu R928

The main features of interest in the photoluminescence characterization of GaAs / $Al_{0.3}Ga_{0.7}As$ quantum wells at low temperature lie between a broad band of AlGaAs emission at 650nm and the transitions of the GaAs cap and substrate from 818nm to 850 nm. The R928 side-on photomultiplier tube (PMT) was chosen for the light detection because of its extended spectral response into the near infra-red at 900nm [Hamamatsu, 1988] and its high sensitivity, both of which are due to its Na-K-Sb-Cs multi-alkali photocathode.

Using the SPECTRALINK® modular control system, it was possible to supply the 1 kV supply voltage from the High Voltage (HV) card, and measure the current from the R928 on the ACQ card. No PMT cooling to -20 °C was thought necessary as the realized signal to noise of 1500:1 at 25 °C was deemed sufficient.

The maximum average anode current for the photomultiplier was 100 μA, and this was set to full range deflection on the ACQ card of 500 000 'counts per second'. The typical anode dark current according to the specification was 2 nA at 25 °C, corresponding to 10 cts, but as the background count

was ranged from 100 - 300 cps in the dark, it can be seen that the anode dark current contribution to the background was insignificant compared to that from electrical noise in the acquisition circuitry.

### 5.1.4 Spectrometers

#### 5.1.4.1 Spectrometer Details

During the course of this project, two 1 m asymmetric Czerny-Turner grating spectrometers were used: the Ramanor U1000 double spectrometer and a THR1000 single spectrometer; both were supplied by ISA Jobin-Yvon and several gratings were available for use in the visible and near infra-red.

#### 5.1.4.2 Resolution of a Spectrometer

The spatial dispersion of light by a grating spectrometer at a wavelength $\lambda$ is quantified by the *angular dispersion*, defined as $d\theta/d\lambda$ [Hamilton et al., 1978], where $\theta$ is the grating angle. The *linear dispersion* available at the exit slit of the spectrometer, where f is the focal length of the spectrometer focussing mirror and dl is measured across the exit slit, is defined as $dl/d\lambda$, and as $\Delta l = f\Delta\theta$, $dl/d\lambda = f\, d\theta/d\lambda$.

But the resolution, or *bandwidth*, is the sum of a *static* bandwidth, determined by the angular dispersion and the width of the slits, and a *dynamic* bandwidth arising from the movement of the grating.

| | Spectrometer | |
|---|---|---|
| | U 1000 | THR 1000 |
| Grating used | 1800 gr / mm | 1200 gr / mm |
| Resolution | 0.15 cm-1 @ 579.1 nm | 0.008 nm @ 564 nm |
| Aperture | f/8 | f/8 |
| Dispersion specified | 9.2 $cm^{-1}$ / mm @ 514.5 nm | |
| Stray Light | $10^{-14}$ @ 20 $cm^{-1}$ from the Rayleigh line | < $10^{-5}$ @ 1 nm from 514.5 nm laser line |
| Repeatability | ± 0.1 $cm^{-1}$ while ± 1 °C | ± 0.02 nm while ± 1 °C |
| Precision | ± 1 $cm^{-1}$ over 5000 $cm^{-1}$ | ± 0.05 nm (0-1500 nm) |
| Grating size | 110 x 110 $mm^2$ | 110 x 110 $mm^2$ |

Table (5.1): Spectrometer Specifications

Angular dispersion $$\frac{d\theta}{d\lambda} = \frac{n}{L\cos\theta} \quad \{5.1\}$$

Static bandwidth $$W\frac{d\lambda}{dl} = \frac{W}{f}\frac{d\lambda}{d\theta} \quad \{5.2\}$$

where W is the slit width, n the diffraction order, L the grating groove separation, $\theta$ the grating angle, and f is the spectrometer focal length.

For a f = 1 m single spectrometer in air ($n_r$=1), and a grating of 1200 lines / mm, of area 102x102 mm, such as the THR1000 [ISA Jobin-Yvon, 1985], we can calculate the bandwidths and resolution, given that at $\lambda$ = 500 nm, the linear dispersion is 0.8 nm / mm:

| | | |
|---|---|---|
| Angular dispersion | = 1/L for small $\theta$ | |
| (Angular dispersion)$^{-1}$ | = L ; L | = $(1.2\text{x}10^{6})^{-1}$; |
| | | = $1.2\text{x}10^{-6}$ m$^{-1}$ |
| | | ≈ 800 nm / rad |
| (Linear dispersion)$^{-1}$ | = (1/f) . (Angular dispersion)$^{-1}$ | |
| | | ≈ 800 nm / m |
| | | = 0.8 nm / mm |
| *Static* bandwidth | = linear dispersion x slitwidth | |
| | | = W . 0.8 nm / mm |
| For 10 μm slits, i.e. 0.01 mm slits, this gives: | | |
| Static bandwidth | | = 0.01 . 0.8 |
| | | = 0.008 nm |
| but for 200 μm slits, | | |
| Static bandwidth | | = 0.16 nm |
| *Dynamic* bandwidth | = scanning rate x system time constant | |
| | | ~ 0.5 nm s$^{-1}$ x 1 ns |
| | | ~ $5\text{x}10^{-10}$ nm (negligible) |
| *Resolution* | = Static + Dynamic bandwidths | |
| | | = 0.16 nm |

For the spectrometers used, the time response is dominated by the time response of the photomultiplier tube, as the motor moves the spectrometer to the correct position before measuring the intensity, and the measurement was made of direct photomultiplier current rather than by use of a lock-in technique. The time interval between stopping and measuring, and the decay time of the photomultiplier tube, are both considerably greater than the transit time for light in the system in current mode, and so the system is effectively at rest for each measurement. Thus the dynamic bandwidth has a negligible effect on the resolution of the system, which is ~1 Å for 200 μm slits. Most features of interest in the

photoluminescence spectra are much broader than this, and so this choice of spectrometer and grating is sufficient for this purpose.

#### 5.1.4.3 Stray Light Rejection

Stray light in a spectrometer system arises both from scattering inside the spectrometer, and from stray light entering the spectrometer together with the signal. The effect of the stray light on the detector for a given spectrometer may be reduced by variation of the entrance and exit slit heights and widths, and coupling a number of gratings together can greatly reduce the stray light.

For a continuous spectral source, such as the photoluminescence emitted by a quantum well, the signal to stray light ratio in a single spectrometer is independent of slit width, but depends linearly on the slit height [ISA Jobin-Yvon, 1985], whereas for a double spectrometer, the signal to stray light ratio is proportional to the slit widths and the square of the slit heights.

The stray light level is a major problem in front-surface photoluminescence characterization, as the laser light reflected off the sample is much more intense than the well luminescence, especially for patterned structures. This is not a serious problem in the double spectrometer, which has a much higher stray light rejection, but for a single spectrometer the laser light scatters inside the spectrometer giving an unacceptable stray light level. The stray light level was reduced using band-pass filters at the entrance of the spectrometer to block the laser light.

#### 5.1.4.4 Grating Response

The spectrometer grating used was 1200 gr / mm blazed at 500 nm for maximum efficiency in the 330-1000 nm range. There is a strong dependence of the grating efficiency on polarization, but although the laser beam is 100 % vertically polarized on leaving the tube, this polarization disappears

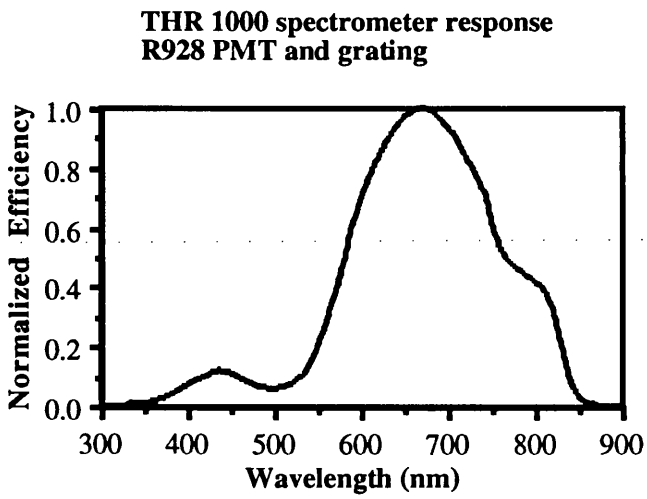


Figure (5.3): Combined Spectral Response of THR1000 spectrometer and R928 PMT

after the beam has passed through the prism monochromator, and thus no polarization of the emission from the wells is produced.

Due to the optical apparatus arrangement, no polarization dependence of the emission would to be detected in the emission from the structures. The combined photomultiplier and grating response is shown in Figure (5.3) above.

#### 5.1.4.5 Spectrometer Light Flux Throughput

The light throughput of the spectrometer is controlled by a number of factors including grating efficiency, mirror quality. Those which are can be varied easily are the choice of grating, the filling of the angular aperture of the spectrometer, and the settings of slit width and slit height.

The collecting optics of the system must be chosen such that the aperture of the system matches that of the spectrometer. If the collected light does not fill the entrance mirror, the throughput and resolution will be reduced. If, however, the collected light overfills the mirror, the level of stray light will be increased.

Variation of slit width can affect the resolution and stray light rejection, as well as the throughput (see above), and variation of slit height also affects the stray light rejection.

#### 5.1.4.6 Slit Settings

A suitable choice of slit settings must be made to minimize the stray light and maximize the throughput and resolution of the system.

On the THR1000, it was possible to use minimum slit heights (1 mm), without reducing the signal strength . The slit widths were set to 200 μm, giving a resolution of 0.16 nm and reasonable signal intensity of (100 000 - 400 000) cps for 10 nm quantum well emission at 6 K, for HeNe 633 nm laser intensity of 50 μW into a 100 μm spot.

On the U1000, because of the reduced light flux and increased dispersion, and the restricted dynamic range of the photon counter, it was decided to use slit heights of 1 or 2 mm, and slit widths of 300 μm, and this proved satisfactory.

#### 5.1.4.7 Spectrometer Control System

##### 'Old' U1000 system

In the initial U1000 configuration, the spectrometer motor movement was controlled by a microcomputer via an RS232 link to the SPECTRALINK® console.

As described in [Watt, 1988], the current pulses from the photon counter were passed through a Thorn EMI Gencom AD-100 remote amplifier / discriminator and integrated using a C-10 counter / display unit. The output was passed through a digital I/O board to the microcomputer. The AD-100 had a threshold sensitivity of 1 mV across an input impedance of 50 Ω, with a signal output time of 50 ns. The maximum count rate was, however limited by the digital counter dead-time of 120 ns to 8 x $10^6$ cts, although as noted above, the count rate was restricted to below 3000 cps to prevent saturation of the photocathode.

The signal acquisition was performed by the 'PLSCAN' program written by Morag Watt in Turbo Pascal 4, and run on an IBM PC [Watt, 1988].

#### 'New' U1000 system

In the new implementation of the spectrometer system, a greater part of the control was devolved to the SPECTRALINK® console, so that as well as motor control, it performed the data acquisition through an amplification / discrimination / integration card.

The 'Enhanced PRISM Software' spectroscopy package, supplied by Jobin-Yvon Instruments S.A. superceded the PLSCAN program, and offered a number of additional features such as signal search and scan abort, but its main advantage was in increased acquisition speed. The data could be dumped in ASCII format: a typical file structure can be seen in Appendix A.2.

#### THR1000 system

As in the U1000 implementation, the SPECTRALINK® console controlled the spectrometer motor movement and performed the data acquisition. The current from the photomultiplier tube (0 - 100 μA) was measured on the ACQ card without the need for lock-in techniques.

The THR1000 used the same PRISM spectroscopy software.

### 5.1.5 Lasers

#### 5.1.5.1 Spectra-Physics Model 2035 High Power Ion Laser

The 2035 high power Ar ion laser offers cw multi-line lasing from 275.4 to 514.5 nm in the UV and visible, with up to 9 W on the 488 nm line. On the light stabilized operational mode, the noise was 0.3 % rms and the stability < 0.5 % , with 100:1 vertical polarization.

#### 5.1.5.2 Spectra-Physics Stabilite® 2016 Ion Laser

The cw 2016 lases, in the multi-line mode, on a number of lines in the VUV range, the most intense being those at 514.5 nm and 488 nm, corresponding to the transitions from J=5/2 $4p^4D^0$ and

J=5/2 $4p^2D^0$ to J=3/2 $4s^2P$ argon ion states respectively. The laser was operated, however, on the single line $TEM_{00}$ 488 nm, where up to 9 W was measured. The polarization of the lasing light is 100:1 vertical, because of the Brewster polarizing window. More importantly, in the power stabilized mode, the variation in light output was less than ± 0.5 %.

#### 5.1.5.3 NEC HeNe

The Helium-Neon laser operates on the 633nm line, with a fixed power output of 18 mW.

### 5.1.6 Optical Elements

#### 5.1.6.1 Monochromators

In addition to the intense lasing lines, a number of background 'plasma' lines are also emitted, which lie in the visible range. These may overlap features in the photoluminescence spectrum of quantum wells at low temperature, and are often much more intense than the features of interest.

To remove these plasma lines, the laser beams were passed through a prism monochromator, which allows through only a narrow band around the laser line. The monochromator reduces the laser power by 50%.

#### 5.1.6.2 Power Meters

The power meter used in the latter stages of the project was the Coherent LABMASTER® Laser Measurement System with the detector heads LM-2 Silicon Sensor and LM-45 high power detector head, with a specified power accuracy of ± 1%.

#### 5.1.6.3 Focussing Stage

The laser beam was focussed to a 100 μm spot using a microscope objective lens, on an XYZ stage with a nominal resolution of ~ 100 μm. The size of the spot was measured by projecting an image of the spot on a piece of material, patterned with a calibrated scale, onto a screen placed at the entrance slits of the spectrometer.

#### 5.1.6.4 Collecting Optics

The requirements for the collecting optics for the photoluminescence system are that they should project a focussed image of the sample in the cryostat into the entrance slits of the spectrometer, and that the f-number of the optics should match the f-number of the spectrometer for optimum light collection.

At the start of the project a pair of biconvex lenses were used to collect the light from the cryostat, but the lenses were subsequently replaced by a camera zoom lens, because of the higher quality of the lenses for minimal cost, and the closer matching of the aperture requirements.

The smallest f-number available on the zoom lens was f=4, compared with the f=8 aperture of the spectrometer, and so the light will overfill the collecting mirror in the spectrometer. The principle disadvantage of the commercial camera lens system is the 'blooming', which maximizes light transmission at ~ 500 nm, for human eye response, by use of anti-reflection coatings. The coating will result in poor transmission at the edges of the visible spectrum, and so one would expect the zoom lens system to attenuate near infra-red signals considerably.

This spectral response would have a significant impact only on the temperature-variation data, like the spectral responses of the gratings and photomultiplier, where the peak well luminescence positions move. All other data were normalized to mesa intensities at the same emission wavelength, and so the spectral responses were cancelled out.

The collecting optics were mounted on an XYZ stage of resolution 100 μm, to allow the collected light to be projected onto the entrance slits of the spectrometer.

#### 5.1.6.5 Measurement of Intensity

Using the structure arrays described in Chapter 7, a series of measurements was made to calculate the effect of slight adjustments of the focussing and collecting optics on the measured intensity.

A lateral movement in the collecting optics of only 140 ± 10 μm was sufficient to lose the intensity completely, as was a lateral movement of 100 ± 10 μm in the focussing optics. As these lateral movements are of comparable size to the resolution of the XYZ stages, it can be seen that the aligment of the optics had a critical effect on the intensity measured.

### 5.1.7 Cryogenic Apparatus

#### 5.1.7.1 Cryostats

Two cryostats were used in the course of the project: a Quantum Production wide bore optical cryostat [Watt, 1988], especially modified for a pressure cell, and an Oxford Instruments CF1204 Cryostat [Arnot, 1990].

The Quantum Production cryostat had serious problems with the temperature stability, and was unreliable. This resulted in the use of short runs with large periods in between to refill the sample space with helium from the reservoir. The cryostat did, however, have a large aperture of f / 1.6, and a 12 mm diameter central window, and so alignment to samples in the insert was easy. The windows were of spectrosil WF® material, which gave excellent transmissivity through visible, UV, and IR.

The Oxford Instruments CF1204 optical cryostat, when used in conjunction with the ITC4 temperature controller, allowed the sample temperature to be maintained at any temperature from 4.2 K to 300 K in the continuous flow mode, stable to within 0.1 K. The temperature was maintained by balancing the gas flow of cold helium against the heat produced by a 80 W heater in the base of the cryostat, which was controlled by the ITC4.

Because of the continuous flow nature of the process, temperatures can be maintained until the helium dewar is empty, which can allow runs of 12 hours or more, as at a temperature of 4.2 K, and a pump pressure of 0.24 bar, the boil off rate was 0.7 litres / hour.

In the bath mode, obtained by filling the sample space with liquid helium and then using a rotary pump to reduce the pressure, temperatures as low as 1.3 K can be achieved.

**Temperature Controller**

Using an Oxford Instruments ITC4® Temperature Controller, the temperature of the sample could be held stable to within 0.1 K across the range 4.2 - 300 K, by balancing the cooling effect of the gas flow through the cryostat sample space against the heat produced by an element in the base of the cryostat. The temperature in the cryostat was measured using Rhodium-Iron (Rh-Fe) sensors, mounted on the insert and cryostat body, calibrated at 77 K and 300 K. The resolution of the sensors was limited by the analogue to digital conversion to 0.001 % , which gave an error of ± 0.3 K at 300 K.

**Calibration of Sensors**

Three temperature sensors were used: the Rh-Fe sensor mentioned above, an Allen Bradley resistance sensor, and a silicon diode.

The Rh-Fe sensor operated as a four-wire resistance measurement, drawing a constant current of 10 μA from the ITC4 or a current source. The voltage drop was recorded by the ITC4 or a multi-meter, and the temperature calculated using the calibration data at 77 K, and at 4.2 K in the cryostat bath mode.

| Temperature (K) | Resistance (Ω) |
|---|---|
| 273.15 | 27.018 |
| 77.3 | 6.9170 |
| 4.2 | 2.012 |

Table (5.2): Calibration of the Rh-Fe sensor
(Oxford Instruments No. 21716) 3636

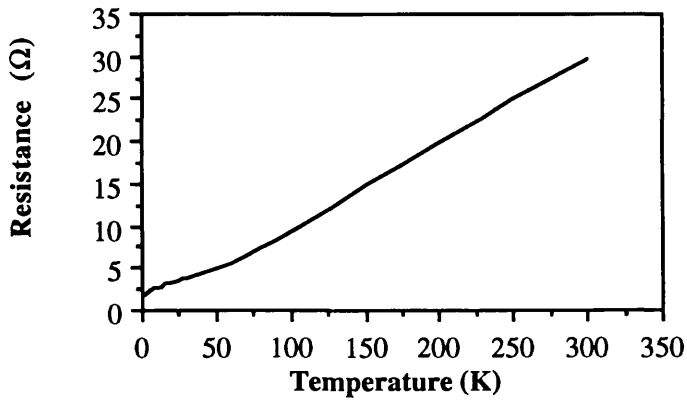


Figure (5.4): Rh-Fe Calibration Curve

The Allen Bradley resistor is most useful below 20 K, but the temperature-resistance relationship differs slightly each time the resistor is cooled down. After measurement of the resistance at two temperatures, a calibration curve may be derived.

The Allen-Bradley 1/8 W BB carbon resistors have an empirical behaviour [Rose-Innes, ]:

$$\log_{10}(R) = a + b\sqrt{\left(\frac{\log_{10}(R)}{T}\right)} \qquad \{5.3\}$$

where a,b constants

T temperature (K)

R resistance (Ω)

The relationship is not easily solved for R, but can be solved for T. Choosing a range of R corresponding to the range of temperatures found empirically, one can calibrate the resistor.

It was not possible to determine the exact temperature of the Allen-Bradley resistor when it was not immersed in superfluid He. The sole fixed points are at room temperature (300 K), liquid nitrogen boiling point (77 K), and superfluid helium transition (2.2 K).

| Temperature (K) | Resistance (Ω) |
|---|---|
| 295 | 126.9 |
| 77 | 159.8 |
| 2.2 | 1099 |

Table (5.3): Calibration of the Allen-Bradley Resistor

A linear fit to the values at these three points yields, using the relationship log R against [(log R)/T]1/2, one can deduce values for the constants a=2.046, and b=0.848.

The values compare badly with values interpolated from data for 1/8 W resistors [Rose-Innes, ]:

a=1.979 b=1.508

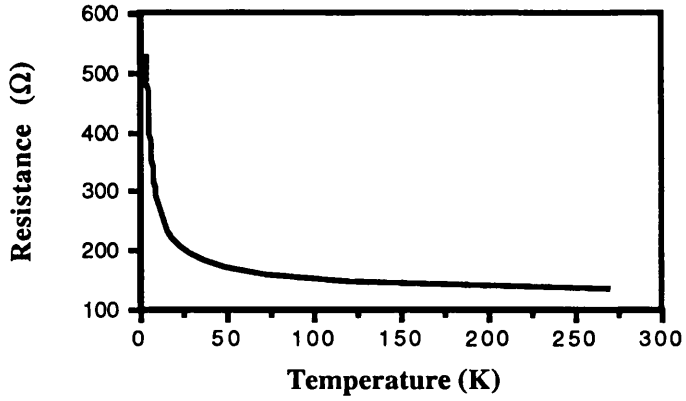


Figure (5.5): Allen Bradley Calibration Curve

The Si diode was not suitable for use in the lowest temperature régime as it ceased to operate below 19 K, and so it was calibrated at 20.0 K and at 325 K.

| Temperature (K) | Voltage (V) |
|---|---|
| 20.0 | 1.4922 |
| 325 | 0.3038 |

Table (5.4): Calibration of the Silicon Diode

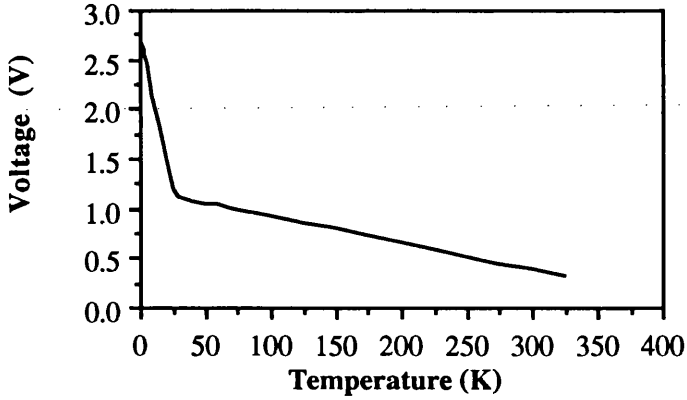


Figure (5.6): Si diode Calibration Curve
at 10 μA current for DT-500DRC (E1)

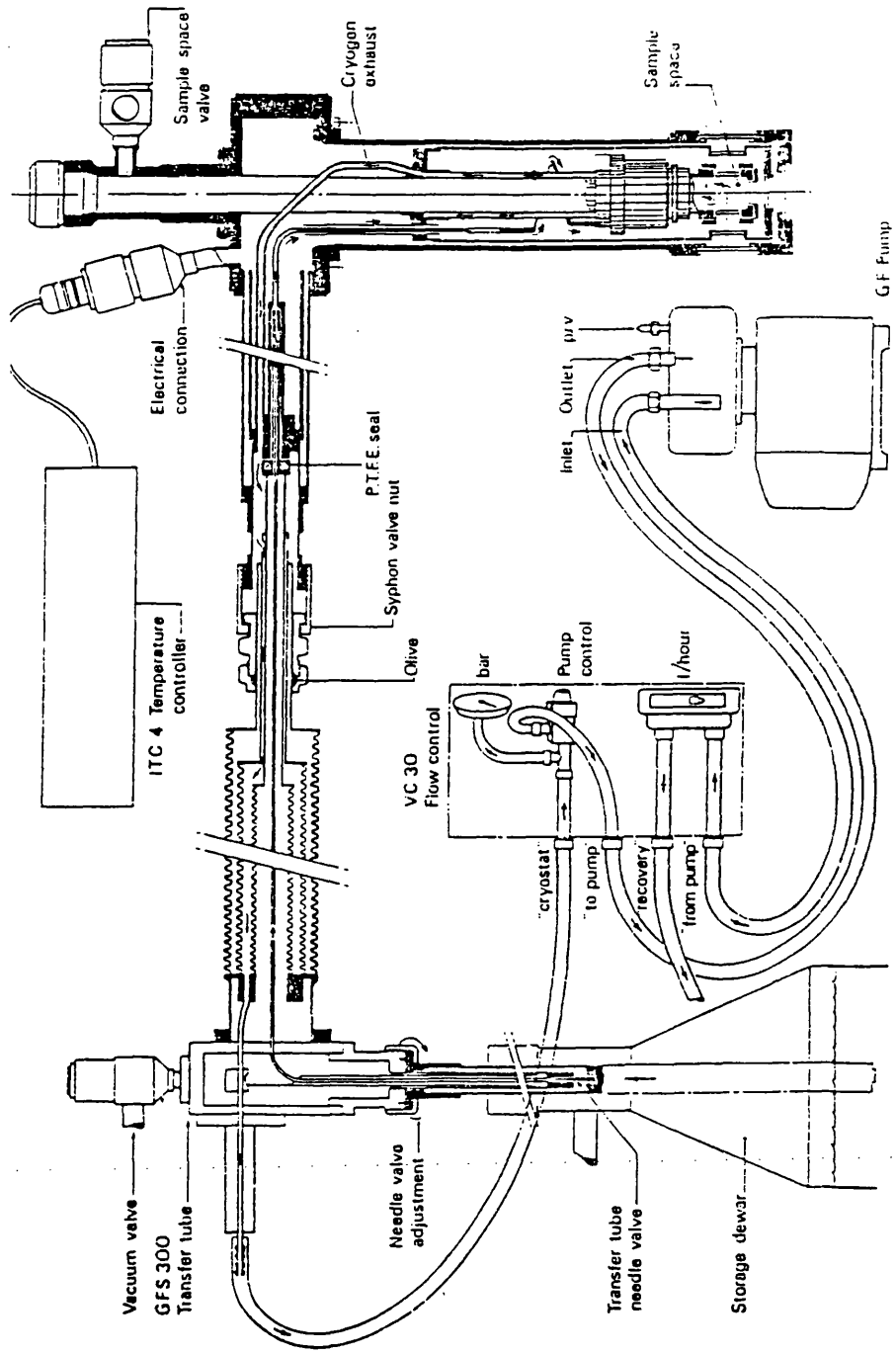


Figure (5.7): Cryogenic Apparatus

### Sample Mounting

Samples were mounted on 1" square thin copper sheets screwed to the cryostat insert tail. The samples were affixed to the centre of the sheets with a thin layer of Bostik All Purpose Clear Gel diluted in ethanone (acetone). The glue made a flexible mount which allowed for differences in the thermal contraction, and was easily removed again after characterization by soaking in ethanone.

## 5.2 Photoreflectance (†)

### 5.2.1 Apparatus Layout

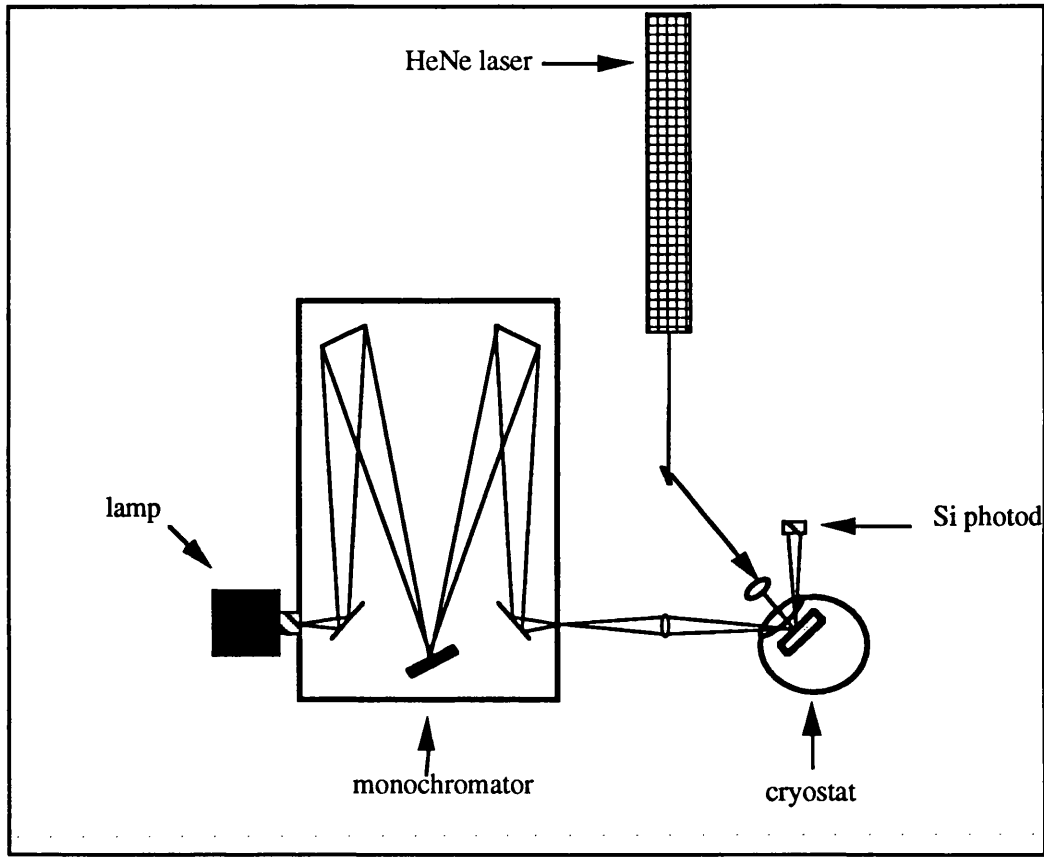


Figure (5.8): Photoreflectance Apparatus Layout

(†) The photoreflectance measurements on quantum wells were performed at the laboratory of Professor Fred Pollak at the Physics Department, Brooklyn College, City University of New York, USA.

### 5.2.2 Description of Apparatus

As described in [Pollak and Glembocki, 1988; Qiang et al., 1992], the apparatus consists of a small He-Ne laser, a tungsten lamp source, a single 0.25 m monochromator, and a silicon PIN diode. The laser beam is chopped to modulate the surface field, and the difference in reflectivity is measured as a function of the monochromator wavelength. The signal from the silicon photodiode is sampled through a lock-in amplifier fixed to the chopping frequency, and the results normalized and recorded on a computer.

# Chapter 6: Characterization of Material

## 6.1 Introduction

This chapter is concerned with a description of the starting material used to fabricate the one- and zero-dimensional structures, and its characterization by low temperature photoluminescence and photoreflectance. In addition, attempts are made to quantify the uncertainty in a measurement of the luminescence peak, with the effect of material variation, apparatus drift, and measurement methodology being considered for their impact on the luminescence peak position, peak linewidth, and peak intensity.

Following material characterization by photoreflectance, preliminary attempts were made to measure the effect of quantum confinement on the electron-LO phonon coupling as evidenced in the dependence of photoreflectance linewidth, and these are discussed in the light of subsequent developments.

## 6.2 Growth of Material

### 6.2.1 Material Structure

The material consisted of a number of quantum wells of different sizes grown with the narrowest wells on top of the wider wells. The optical absorption of a quantum well is independent of the well thickness under high energy excitation, but narrow wells were grown later because the impurities during growth are deposited at interfaces and the wavefunction of the narrowest well penetrates the barriers most, thus being most influenced by remaining impurities deposited at the interfaces. This also has the advantage that it reduces the effect on the structure size of a preferential etch of GaAlAs over GaAs.

Growth of a superlattice buffer between the substrate reduces the impurity distribution and improves the wall smoothness of the quantum wells, because the GaAs on AlGaAs inverted heterojunction is notoriously rough and impurities are preferentially deposited at this interface. The disadvantage of the superlattice is that the luminescent emission is very broad and can dominate the emission over the weak emission of structures etched in the quantum wells.

The growth parameters such as substrate temperature, source / cracker temperature, atomic flux and substrate rotation speed have influence on the smoothness of the interfaces and impurity distribution in the quantum wells produced. The requirement was to maximize the free exciton luminescence from the quantum wells, and to minimize the gradient and wall roughness.

## 6.3 Photoluminescence of Quantum Well Structures

The low temperature photoluminescence spectrum from quantum well material consists, in the direction of increasing wavelength (decreasing in energy), of a broad emission due either to the AlGaAs or superlattice emission, depending on the material structure, followed by a number of peaks arising from the lowest quantum well transitions, corresponding to transitions in confined GaAs, followed by a broad structure due to emission from the unconfined GaAs material of the cap and spacer layers. The emission from the superlattice, depending on the period and aluminium concentration, may overlap the emission from the narrower quantum wells.

### 6.3.1 AlGaAs or Superlattice Barrier Emission

The AlGaAs emission was not investigated extensively in the material structures used, although the emission could have given information on the aluminium concentration of the barriers of the quantum wells, and so have an impact on the calculation of the energy levels of the quantum wells, but this was not deemed of major importance in this study.

Sun et al. (1984) have studied the emission from quantum well AlGaAs barriers as a function of growth substrate temperature $T_S$, and find that the emission is dominated by excitons bound to neutral acceptors ($X,A^0$), with contributions from donor-acceptor pair (DAP) and free-to-bound transitions associated with carbon on arsenic sites ($e,A^0$). The dependence on substrate temperature is believed to arise from the reduction in adhesion of $H_20$ and CO with increased substrate temperature, which are believed to give rise to non-radiative recombination centres. Their optimum substrate temperature of 720 °C contrasts with the value of 690 °C of Weisbuch et al. (1981), and this is attributed to the use of $As_4$ cracker by Weisbuch et al., which increases As mobility on the surface and may reduce contamination arising from the As source.

The superlattice emission energy had a major impact on detecting the emission of the fabricated structures in that the broad emission could lie over that from the quantum wells, preventing accurate measurement of the peak intensities. This was exacerbated after etching, as the quantum well material area could be reduced by two orders of magnitude, and the etch stopped in the superlattice, allowing much more intense emission from the superlattice as it was no longer covered by absorbent quantum wells. This problem was avoided by careful choice of the effective aluminium concentration in the superlattice to reduce its emission wavelength.

### 6.3.2 Quantum Well Emission

The quantum well emission consisted of several intense peaks, which could be split by several meV. A crucial question to be answered in the justification for the method employed to fabricate one- and zero-dimensional structures is whether or not the quantum well emission is intrinsic or extrinsic, and, of

equal importance, whether the emission arises from free excitons, or excitons localized in potential fluctuations of the well width.

**Intrinsic or Extrinsic Luminescence?**

In photoluminescence excitation spectroscopy of GaAs quantum wells, the transitions which dominate the spectrum are those with the largest oscillator strength, which favours the intrinsic transitions associated with free excitons, and allows the measurement not only of the lowest n=1 electron-heavy hole transition, but also higher transitions involving light holes and larger confinement energies.

In contrast, however, the low temperature photoluminescence spectrum of bulk GaAs is dominated by extrinsic transitions, as the carriers thermalize to the lowest energy levels before recombining. Obtaining the intrinsic transitions is difficult by photoluminescence alone, although by varying the power and temperature it is possible to identify the intrinsic exciton peak and even its excited states.

Considerable effort has been expended in attempting to decide whether or not the predominant photoluminescence emission from quantum wells arises from free or bound excitons. The current state of belief may be surmised as that in 'good' quality material, as described subjectively by low impurity content, narrow linewidth and high luminescence intensity, the emission is predominantly from free excitons [Sun et al., 1984], but in 'poorer' material, or in material grown with long periods of growth interruption, the emission may have significant contributions from bound exciton transitions.

The reduction in relative importance of bound exciton transitions in quantum wells was attributed by Weisbuch et al. (1981) to a segregation of the impurity centres away from the centre of the well, resulting in a reduction of the bound exciton transition rate from symmetry considerations. The confinement smears out the impurity binding energy, and the symmetry of the impurity ground state wavefunction depends on the impurity position in the quantum well, and thus the oscillator strength of the impurity transitions varies across the well, and is reduced compared with the bulk materials.

Reynolds et al. (1984), in studies of wide (10-40 nm) quantum wells in the excitation range $10^{-3}$ to 10 W $cm^{-2}$, find that the dominant transitions are donor-related, being ($D^0$,$X_h$), ($D^0$,$X_l$), and ($D^0$,h), although the free exciton recombination of both sets of holes may also be observed, much reduced compared with the donor-related transitions.

Juang et al. (1985), however, suggest that, in the excitation range $10^{-2}$ to 10 W $cm^{-2}$, although the dominant emission is from light- and heavy-hole free exciton emission, some features can be described by bound exciton emission, in particular light- and heavy-hole bound excitons ($D^0$,X) and free-to-bound heavy hole transitions ($D^0$,h), and weak acceptor-bound heavy-hole excitons ($A^0$,$X_h$).

Koteles et al. (1986) show that the bound-exciton peak may dominate the emission even in narrow quantum wells

**Interface Roughness**

During investigations into the effect of substrate temperature $T_S$ on the quality of quantum wells grown by molecular beam epitaxy [Weisbuch et al., 1981], it was suggested that the variations in the quantum well thickness, as measured by optical microscopy, and the variations in photoluminescence and photoluminescence excitation linewidth, could be attributed to variations in the heterointerface topology. Islands of height of the order of monolayers, and of lateral extent $\geq 30$ nm, were believed to give rise to a variation in the confinement energy of the excitons in the quantum well, and by varying the substrate temperature one could vary the size of the islands, and hence the luminescence linewidth was minimized when the heterointerface was smooth [Hermann et al., 1991].

Later investigations by Deveaud et al. (1984) showed that the individual transitions corresponding to one-monolayer size fluctuations in the quantum well could be resolved, and the peaks fitted calculations of the confinement energies of the excitons in the quantum well. The early model was developed by Singh et al. (1984), who derived expressions for the variation of luminescence halfwidth as a function of island height and lateral extent.

Transitions arising from differences in well thickness of half monolayers were observed by Weisbuch et al.(1981), but these were attributed to interlayer fluctuations in a multiple quantum well structure, rather than intra-layer fluctuations. Hayakawa et al. (1985) observed transitions which could not be attributed to whole monolayer fluctuations, and explained their results in terms of variations in the aluminium content in the heterointerface arising from clustering of the Al in the well barriers. Bimberg et al. (1986) also observed fractional monolayer fluctuations.

Voillot et al. (1986) observed that although it was not always possible to observe monolayer fluctuations under normal growth conditions, the effect could be enhanced by interrupting the growth for up to 100 s at each interface. The effect of growth interruption was explained in terms of Group III atom migration across the surface, to reduce the islands formed by multinucleate growth. The stabilization of the surface was observed by Reflection High Energy Electron Diffraction (RHEED). Bimberg et al. (1986) observed that the surface stabilization was obtained at the expense of greater incorporation of impurities, such as carbon, and deep traps.

The reduction of surface roughness also resulted in a change in lineshape, according to Bimberg (1986). Uninterrupted growth luminescence peaks could be fitted with a Gaussian lineshape, but for interrupted growth, a Lorentzian lineshape was found to give a better fit. This was attributed to the reduction in the random nature of the islands evidencing itself as a change in the statistics of the transition.

In some wells, the number of monolayer-related peaks in a luminescence well emission envelope is not the expected three or more, but only two. This is attributed either to a difference in the relative smoothness of the upper and lower heterointerfaces, perhaps because of differences in the aluminium and gallium migration rates at a particular substrate temperature, or because of differences in the relative populations of the sections of the well after carrier thermalization.

In the latter case, if the mean well thickness $L_z$ is shown to occur over approximately 90 % of the well area, then at low temperatures and excitation densities, the transitions occur at $L_z$ and at $L_z+a/2$, corresponding to a well width increase of one monolayer, and sometimes wells wider by several further monolayers. The transition $L_z-a/2$ and thinner wells are depopulated at low temperatures by carrier thermalization. At higher temperatures and excitation densities, these thinner well transitions may be observed.

If the heterointerfaces have widely differing properties, as suggested by [Tanaka and Sakaki, 1987; Bimberg et al., 1986], then the lower GaAs on AlGaAs surface may have extremely small island size, to which the exciton is insensitive. The surface roughness then acts as a pseudosmooth surface with a reduced aluminium concentration. The number of transitions is then far more likely to be two, as the fluctuation at each heterointerface is most likely to be of one monolayer.

Hillmer et al. (1990) compared the exciton mobility as a function of interface roughness from data obtained from space- and time-resolved spectroscopy, finding that the exciton mobility was maximized when the interface roughness was minimized.

Koteles et al. (1986) found that in a single spectrum obtained from low temperature photoluminescence, it was possible to confuse monolayer fluctuations with impurity transitions, necessitating temperature dependent photoluminescence coupled with photoluminescence excitation spectroscopy to confirm peak assignment. This may have been exacerbated by the growth interruption, which may have increased the impurity incorporation.

### Dependence of Luminescence Peak Position on Growth

The luminescence peak position is dependant on the well width. The width can be controlled to a few monolayers, but of particular concern in this project is the variation of peak position across the wafer. These can arise from the effects of the substrate temperature gradient, as the desorption of gallium from the surface is critically dependant on the substrate temperature. Gallium desorption from the edge of the wafer can lead to a widening of the quantum well at the periphery of the wafer. Reduction of growth temperature reduces the gallium desorption.

### Dependence of FWHM ($\Gamma$) on Growth Parameters

The choice of substrate temperature also impinges on the resultant full width at half maximum of the luminescence peak. Weisbuch et al. (1981) find that the luminescence width is minimized for a particular choice of substrate temperature, and this also corresponds to a maximum for the luminescence peak intensity. This is attributed to the effects of interface roughness. An additional concern must be that of the incorporation of impurities, as the contamination from the arsenic source can be reduced by growth at high temperature.

The use of an $As_4 \rightarrow As_2$ thermal cracker reduces the temperature at which the material may be grown, and reduces the impurity emission from the arsenic source, thus allowing one to minimize the

gallium desorption and impurity distribution, whilst choosing the optimum temperature for a good linewidth, limited by the alloy distribution scattering in the barrier and impurity distribution in the well, rather than by interface roughness.

### Dependence of Luminescence Intensity on Growth

Weisbuch et al. (1981) have studied the dependence luminescence peak intensity on substrate temperature and find that it reaches a maximum at the same temperature as the linewidth is minimized. This suggests that non-radiative recombination is minimized when the potential fluctuations, which separate the carriers are minimized, thus allowing more efficient trapping.

Bimberg et al. (1986) record a decrease in luminescence efficiency on growth interruption, which is attributed to the incorporation of deep traps during the growth interrupt.

## Spectral Linewidth

### Photoluminescence Linewidth

The linewidth of an exciton peak in a quantum well photoluminescence spectrum arises from a number of considerations [Weisbuch et al., 1981], including interactions with polar optical phonons, acoustic phonons, ionized impurities, and interface roughness.

Lee et al. (1986) express the half-width at half-maximum (HWHM) $\Gamma$ as:

$$\Gamma(\text{meV}) = \Gamma_0 + (1.47 \times 10^{-3})T + \frac{4}{\left(e^{\frac{\hbar\omega_0}{k_B T}} - 1\right)} + \Gamma_{imp}\, e^{-\frac{(E_b)}{k_B T}} \qquad \{6.1\}$$

where $\Gamma_0$ is the intrinsic linewidth, neglecting interface roughness, $\Gamma_{imp}$ is the linewidth due to fully ionized impurity scattering in the well, and $E_b$ is the impurity binding energy. The second term represents the linewidth due to acoustic phonon scattering, while the third term represents the contribution from optical phonon scattering.

Their model assumes negligible penetration of the carrier wavefunction into the barrier, neglects the effective mass mismatch between GaAs and AlGaAs, and assumes an infinite square well. These assumptions would be less valid for narrow wells, but the model fits the experimental dependence of linewidth on temperature for the heavy and light hole excitons in a 10 nm quantum well.

Above 150 K, the dominant contribution is from LO-phonon scattering.

Below 25 K, however, the linewidth is dominated by the contribution of the interface roughness, with small contributions from acoustic phonon and ionized impurity scattering.

**Photoreflectance Linewidth**

Above 100 K, the dominant thermal broadening mechanism for photoreflectance peaks is LO-phonon scattering [Qiang et al., 1992],and the linewidth $\Gamma$ in this temperature range can be expressed as:

$$\Gamma(meV) = \Gamma_0 +$$

$$\Gamma(meV) = \Gamma_0 + \frac{\Gamma_1}{\left(e^{\frac{\hbar\omega_0}{k_B T}} - 1\right)} \qquad \{6.2\}$$

where $\Gamma_0$ is the intrinsic linewidth, neglecting nterface roughness, and $\Gamma_1$ is the electron-LO phonon coupling constant.

Qiang et al. (1992) derive that the matrix element $\Gamma_1$ is proportional to the well width $L_z$, and thus by measuring the photoreflectance linewidth as a function of temperature and well width, it is possible to derive values for the electron-phonon coupling constant.

**Gaussian or Lorentzian fit ?**

Bimberg et al. (1986) have found that the peaks resulting from uninterrupted growth by molecular beam epitaxy are best fit with Gaussian lineshapes, whereas the peaks resulting from interrupted growth must be fit with Lorentzian lineshapes. This is explained in terms of a re-ordering of the growth terraces which results in a change in the statistics governing the occurrence of the peaks.

The photoluminescence data recorded in the course of this project, from material grown without interruption, are best fit with Gaussian lineshapes (see below).

**Gaussian fit to Luminescence Peaks**

A number of luminescence peaks were broadened due to monolayer fluctuations in the well thickness, and as the individual peaks could not be resolved, the lineshapes were fitted with Gaussian profiles to derive the intensities and positions of the constituent peaks.

The best fit was chosen by eye, and at low temperatures and intense peaks, there was good agreement with the sum of Gaussian profiles, as seen in Figure (6.1). At the higher temperature of 125 K in Figure (6.2), however, the sum of Gaussian profiles gave a much poorer fit.

In weak emission, a distinctive low energy tail is observed which could not be fitted with Gaussian profiles appropriate to monolayer fluctuations, and this was attributed to the transitions of excitons bound to impurities in the quantum wells and of confined electrons to acceptors.

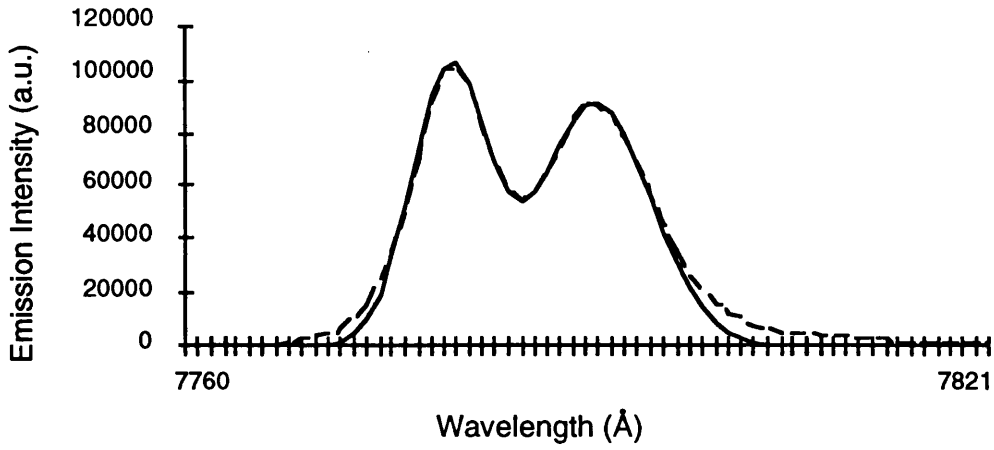


Figure (6.1): Gaussian fit to 5.8 nm well of B33 at 5 K

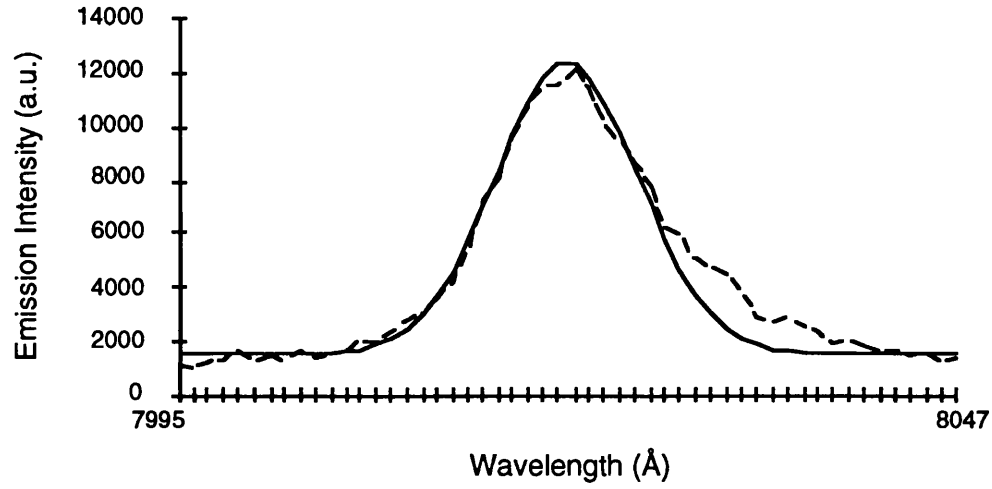


Figure (6.2): Gaussian fit of 5.8 nm well of B33 at 125 K

**Impurities**

In the data obtained from the material investigated, no prominent peaks were observed which could be attributed to impurity transitions, although the residual low energy tails of the peaks can be explained in terms of a distribution of impurity related transitions.

### 6.3.3 Substrate and Cap Emission

In addition to the emission from the quantum well, AlGaAs barriers, and superlattice, if present, emission could also be detected from transitions arising in the GaAs cap or substrate.

In mesas and unetched material, the emission arises from the cap layer, which was grown by molecular beam epitaxy, whereas the emission from etched material arises from the substrate, which was

grown from the melt. In both cases, however, the emission from the GaAs tended to be much weaker than that from the quantum wells, and was due to bound exciton and carrier-impurity transitions.

## 6.4 Measurement of Experimental Precision

The method of recording the luminescence emission from a particular structure area, and comparing it with the emission from a control mesa nearby, depended for its validity on the assumption that the effect of fabricating a structure out of the quantum well material would have greater influence on the luminescence behaviour of the resultant structure than the difference in luminescence behaviour between the area of material to be patterned with a structure and the area of material to be protected with a mesa pattern.

The extent of the validity of the assumption that the material properties could be approximated by uniform values across the wafer had to be verified, and estimates had to be derived of the precision with which one could measure the important variables: the luminescence peak position ($\lambda$), the peak full-width-at-half-maximum ($\Gamma$), and the peak intensity (I). The measurements of precision were undertaken under the same conditions as the subsequent measurements of luminescence from fabricated chips, but the results derived here are merely typical of the method involved, as the measurements were not repeated for each chip fabricated, nor were structure luminescence intensity measurements available from the material examined in this section, due to its loss in a fabrication process.

### 6.4.1 Precision of Static Measurement

In order to clarify the reproducibility of measurements of intensity, width, and peak position, it was decided to measure repeatedly the emission from areas of B33 quantum well material. Spectra were obtained for consecutive scans in time, with no changes made to the apparatus during this period. The 5 scans of 12 minutes duration were recorded consecutively, with the same spectrometer sense of movement, thus giving results averaged over a 80 minute period.

The possible factors contributing to variation in the intensities of these spectra include the effects of sample temperature stability, excitation laser stability photomultiplier noise, physical drift of the optical elements, and the drift of the photomultiplier tube potential supply.

Contributions from drift and noise in the electronics performing the analogue-to-digital conversion and signal acquisition are expected to be insignificant.

The contributions from each of these sources was considered in turn. As the temperature controller could maintain the temperature of the sample under continuous laser excitation within 0.1 K of its set temperature at 6 K, the luminescence spectrum is only weakly dependent on the temperature in the range 5.8 - 6.2 K. When operating in light-stabilized mode, the argon laser power varies by less than 0.5 %, and once warmed up, the drift in laser power is negligible. The sample temperature would thus be

expected to have stabilized under such conditions, and thus the sample temperature stability and excitation laser stability are expected to have contributed negligibly to the variations in the spectra recorded.

Although the noise in a photomultiplier tube is extremely dependent on the applied potential, variations in this noise level would be measurable over the lowest signal areas of the spectra as well as in the peaks and as this is not observed, it is concluded that this is not a significant factor over the time interval studied. The noise level in the spectrum, arising from both the dark noise and the scattered light in the spectrometer, is not seen to vary in the spectra, and so the main factor in the change of the luminescence intensities must be attributed to drift in the alignment of the optical components.

When the variation in peak positions of the spectra is considered, although the factors mentioned above will have some impact, these are insignificant when compared to the resolution due to the 200 μm slit widths of 1 Å, which corresponds to a resolution of 0.2 meV over the energy range of interest.

| Well Width (nm) ±0.2nm | λ (eV) | | Γ (meV) | |
|---|---|---|---|---|
| | (mean of 5) | σ | (mean of 5) | $\sigma_{n-1}$ |
| 4.0 | 1.647 1 | ($3 \times 10^{-5}$) | 5.9 | 0.3 |
| 5.8 | 1.595 3 | ($1 \times 10^{-5}$) | 1.6 | <0.1 |
| 8.3 | 1.567 6 | ($< 1 \times 10^{-5}$) | 1.2 | 0.1 |

Table (6.1): Precision of Static Measurement of B33 (i)

| Well Width (nm) ±0.2nm | Intensity (a.u.) | |
|---|---|---|
| | (mean of 5) | $\sigma_{n-1}$ |
| 4.0 | 23 000 | 800 |
| 5.8 | 105 000 | 2 000 |
| 8.3 | 177 000 | 2 000 |

Table (6.2): Precision of Static Measurement of B33 (ii)

The precision of an experiment [Barford, 1985] to measure z is given by σ(z), the standard deviation of the limiting frequency distribution. This relies on the notion of an infinitely repeated experiment, and so for a finite number of measurements, one calculates the root mean square(or standard) deviation $\sigma_n$ which gives σ as $n \to \infty$. When n is small, however, it is possible to define an 'adjusted' root mean square deviation $\sigma_{n-1}$ (or $s_n$), as $\sqrt{(n / (n-1))} \cdot \sigma_n$, which vanishes for n=1. The value $\sigma_{n-1}$ may be taken as the 'best estimate' of the precision of the apparatus.

As the value of n is extremely small, it is unlikely that the values of best estimate of precision reflect the true precision of the method. It is, however, indicative of the accuracy with which one should treat a single measurement of the luminescence variables.

The methodology used in characterizing the photoluminescence of the etched structures is highly subjective in that one assumes that the most 'accurate' spectrum is recorded when the intensity of the luminescence is maximized. This is neither a large number of repeats of an identical experiment, nor is it a random choice of luminescence spectrum, nor is it even the maximum luminescence intensity possible

from the structure area, as this depends on the spatial resolution of the movement of the optics, and on an infinite perseverance to produce the maximum intensity.

Given, however, a single measurement of a spectrum from one area, maximized subjectively, it is possible to say that the *minimum* error in the peak position energy is ± 0.01 %, the minimum error in the peak width (Γ) is ± 5 %, and the minimum error in the peak intensity (I) is ± 3 %. These values are, however, insignificant when compared with those considered in the next section.

### 6.4.2 Precision of Re-Aligned Measurement

After moving the focussing and collecting optical components, and re-maximizing the signal, the precision of the spectra thus recorded vary partly because of the factors measured in the section above, but these are seen to be negligible compared with the variations due to differences in the alignment after the alignment has been disrupted.

The methodology used, in which the laser beam is moved away, and then back to approximately the same position on the chip, before maximizing the signal, is the same used in the characterization of the structures, and so gives a measurement of the best precision which can be expected from measurements on these structures. The signal is maximized because the emitted light in the near infra-red will have a different optical path from the reflected laser beam, and because of the narrow acceptance angle of the spectrometer with 200 μm slits, the position of the collecting optics is critical to the collection of the light.

The factors contributing to the variation in spectra measured are the difference in alignment of the collecting optics, occurring whilst optimizing the signal, and the difference in alignment of the focussing optics, giving rise to emission from a different area of the material, and a different optical path to the entrance slits of the spectrometer.

Wet-etched frame-windows act as alignment marks and allow the laser spot to be re-positioned each time within ~ 20 μm. The differences in the spectra due to variation in material properties across the wafer cannot be derived independently of the variation due to the collecting optics alignment; it is possible to note, however, that the peak position is unaffected by the alignment of the collecting optics, whereas the intensity measured is critically affected by the alignment.

The graphs illustrate the variation with repeated measurement, and indicate that there is variation in peak position, FWHM, and in the relative intensity of the five peaks. This shows that different areas of the quantum well are being sampled in different scans, although the laser beam was aligned within ~ 20 μm. In addition, it may be noted, from the collective variation of the peak intensities, that the major contributor to the variation in peak intensity is seen to be the alignment of the collecting optics.

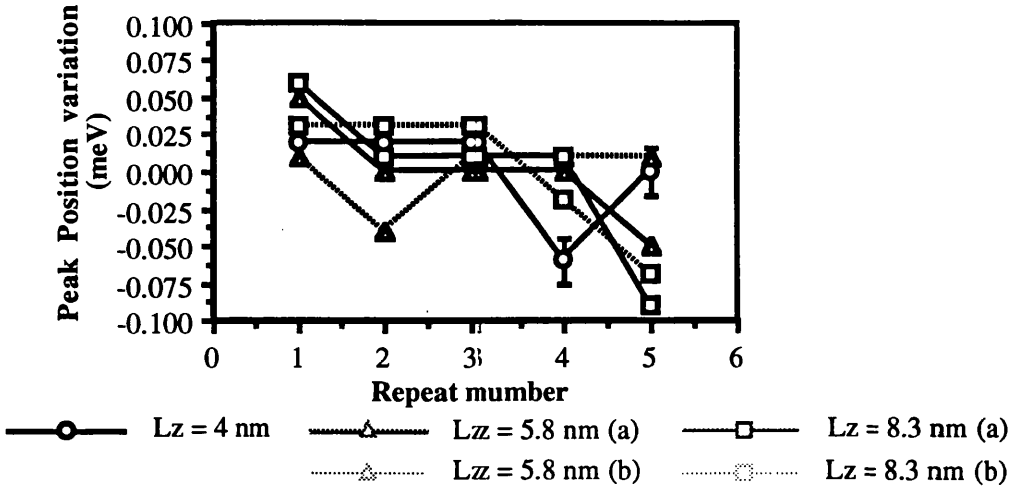


Figure (6.3): Reproducilbility of Peak Position of B33
(after realignment)

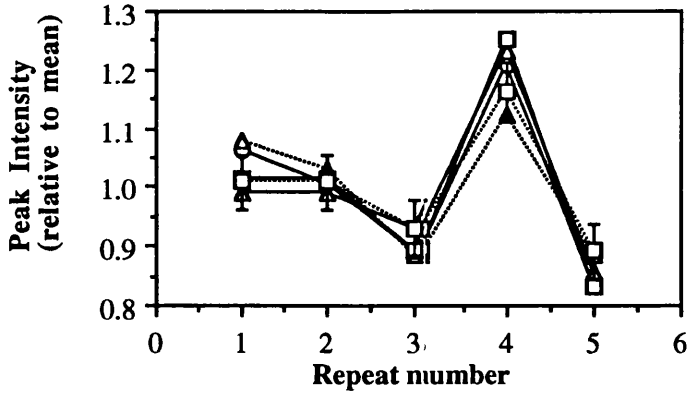


Figure (6.4): Reproducibility of Peak Intensity of B33
(after realignment)

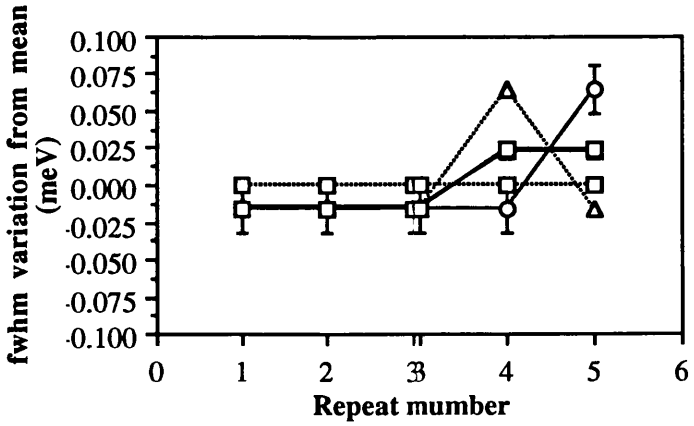


Figure (6.5): Reproducibiility of FWHM of B33
(after realignment)

| Well Width | λ (eV) | | Γ (meV) | |
|---|---|---|---|---|
| (nm) ±0.2nm | (mean of 5) | $\sigma_{n-1}$ | (mean of 5) | $\sigma_{n-1}$ |
| 4.0 | 1.6473 | (2.88 x$10^{-5}$) | 3.15 | 004 |
| 5.8 | 1.5976 | (3.11 x$10^{-5}$) | 1.16 | 002 |
| | 1.5953 | (2.22 x$10^{-5}$) | 2.34 | 004 |
| 8.3 | 1.5699 | (4.44 x$10^{-5}$) | 1.19 | - |
| | 1.5683 | (5.99 x$10^{-5}$) | 1.61 | 0.02 |

Table (6.3): Precision of Re-Aligned Measurement of B33 (i)

| Well Width | Intensity (a.u.) | |
|---|---|---|
| (nm) ±0.2nm | (mean of 5) | $\sigma_{n-1}$ |
| 4.0 | 355 000 | 5 000 |
| 5.8 | 622 000 | 16 000 |
| | 422 000 | 5 000 |
| 8.3 | 1310 000 | 13 000 |
| | 841 000 | 13 000 |

Table (6.4): Precision of Re-Aligned Measurement of B33 (ii)

From a single measurement of a spectrum from one area, maximized according to he method described above, the *minimum* error in the peak position energy is due to the slit width precision, and gives ± 0.01 %; the minimum error in the peak wiidth (Γ) is ± 2 %, and the minimum error n the peak intensity (I) is ± 26 %.

These estimates of error are, however, only for repeated measurement of the same area. In practice, where different areas are compared with the behaviour of the control mesa, the assumption is made that the material properties of the wafer are uniform. This gives rise to a sizable error in addition to those considered above, and the size of this error is dependent on the uniformity of the material used.

This could perhaps be avoided by making multiple measurements of the intensites of each area to be patterned, and then making multiple measurements of the same areas after patterning. The best estimates of error so obtained would not then reflect the wafer dependence of the properties, but at the cost of considerable increase in the workload. In addition, the errors would contain a substantial element from the re-alignment uncertainty, and so the overall measurement might not be reduced.

The alternative method of reducing the uncertainty in the data, adopted here, was to compare a number of identical specimens fabricated under the same conditions in order to increase the number of measurements of different structure areas, thus averaging over the behaviour of a number of identical structure areas. This avoids the problem of multiple measurements of a freak sample.

### 6.4.3 Precision of Measurement Averaged over Wafer

The luminescence peak position, linewidth, and emission intensity need not vary in a random fashion across the wafer: the growth parameters can produce gradients in the quantum well thickness, in the concentration of aluminium in the well barriers, and in the distribution of impurity atoms. But there is an additional random element due to the random distribution of impurities, and to the monolayer islands in the quantum well.

**B33 Material**

| Well Width (nm) | Energy †(eV) | | Γ (meV) | |
|---|---|---|---|---|
| | (mean of 5) | $\sigma_{n-1}$ | (mean of 5) | $\sigma_{n-1}$ |
| 4.0 | 1.6464 | (2 x $10^{-4}$) | 3.2 | 0.1 |
| 5.8 | 1.5968 | (2 x $10^{-4}$) | 1.61 | 0.05 |
| | 1.5946 | (1 x $10^{-4}$) | 2.4 | 0.2 |
| 8.3 | 1.5692 | (1 x $10^{-4}$) | 1.4 | 0.2 |
| | 1.5676 | (1 x $10^{-4}$) | 1.6 | 0.1 |

Table (6.5): Precision of Whole Wafer Measurement of B33 (i)

† Spectrometer Calibration Error of 0.3 nm

| Well Width (nm) | Intensity (a.u.) | |
|---|---|---|
| | (mean of 5) | $\sigma_{n-1}$ |
| 4.0 | 60 000 | 20 000 |
| 5.8 | 60 000 | 20 000 |
| | 110 000 | 30 000 |
| 8.3 | 200 000 | 40 000 |
| | 100 000 | 30 000 |

Table (6.6): Precision of Whole Wafer Measurement of B33 (ii)

When compared with the data in Tables (6.6 and 6.7), the assumption of wafer uniformity can be seen to degrade the precision of measurement of the peak intensity and peak FWHM considerably, but to have no effect on the precision of the peak position, as this is determined by the slit width precision.

Thus the best measurement of precision that we should expect would be ± 0.01 % in transition energy, ± 14 % in FWHM, and ± 31 % in intensity. The worst precision occurs for the intensity, which is of crucial importance when comparing the emission from different structures, but the intensity is still within an order of magnitude.

Compared with B33, the assumption of wafer uniformity in PD880 gives rise to significantly worse values for the precision, in all three parameters, and in the cases of IM13a and IM13b, the errors are much larger than in B33. Of especial concern is the fact that the precision of the intensity measurement of IM13b is of the order of ± 100 %, and this would render any measurement of emission intensity of a structure almost meaningless, but also the peak position precision is dominated by the wafer uniformity, rather than being due to the slit width precision.

| Well Width (nm) | Energy †(eV) | | Γ (meV) | |
|---|---|---|---|---|
| | (mean of 4) | $\sigma_{n-1}$ | (mean of 4) | $\sigma_{n-1}$ |
| 11.5 | 1.550 | 0.006 | 7 | 1 |
| 8.9 | 1.566 | 0.011 | 14 | 5 |
| 3.5 | 1.667 | 0.008 | 13 | 8 |

Table (6.7): Precision of Whole Wafer Measurement of PD880 (i)

| Well Width (nm) | Intensity (a.u.) | |
|---|---|---|
| | (mean of 4) | $\sigma_{n-1}$ |
| 11.5 | 90 000 | 20 000 |
| 8.9 | 240 000 | 80 000 |
| 3.5 | 11 000 | 7 000 |

Table (6.8): Precision of Whole Wafer Measurement of PD880 (ii)

| Well Width (nm) | Energy †(eV) | | Γ (meV) | |
|---|---|---|---|---|
| | (mean of 4) | $\sigma_{n-1}$ | (mean of 4) | $\sigma_{n-1}$ |
| 12.0 | 1.549 | 0.008 | 4.39 | 0.08 |
| 7.5 | 1.578 | 0.009 | 6.0 | 0.5 |
| 4.5 | 1.629 | 0.013 | 8 | 0.2 |

Table (6.9): Precision of Whole Wafer Measurement of IM13a (i)

| Well Width (nm) | Intensity (a.u.) | |
|---|---|---|
| | (mean of 4) | $\sigma_{n-1}$ |
| 12.0 | 20 000 | 10 000 |
| 7.5 | 8 000 | 4 000 |
| 4.5 | 4 000 | 2 000 |

Table (6.10): Precision of Whole Wafer Measurement of IM13a (ii)

| Well Width (nm) | Energy †(eV) | | Γ (meV) | |
|---|---|---|---|---|
| | (mean of 3) | $\sigma_{n-1}$ | (mean of 3) | $\sigma_{n-1}$ |
| 13.1 | 1.544 | 0.007 | 4.7 | 0.7 |
| 8.4 | 1.570 | 0.009 | 6 | 1 |
| 5.0 | 1.618 | 0.012 | 7.3 | 0.9 |

Table (6.11): Precision of Whole Wafer Measurement of IM13b (i)

| Well Width (nm) | Intensity (a.u.) | |
|---|---|---|
| | (mean of 3) | $\sigma_{n-1}$ |
| 13.1 | 60 000 | 60 000 |
| 8.4 | 40 000 | 40 000 |
| 5.0 | 30 000 | 30 000 |

Table (6.12): Precision of Whole Wafer Measurement of IM13b (ii)

In order to quantify the precision of the measurement of the well thickness, one should take into account the combined precision of the measurement of transition energy, and the precision involved in the calculation of well width from the transition energy, obtained by graphical means. This is considered in the next section.

**Calculation of Combined Precision of Measurement of Well Width**

The precision with which one can measure the quantum well width arises both from the precision of the measurement of the emission energy, and the precision with which one can calculate the well width from a graph of well width against emission energy.

The best estimate of the precision is calculated as:

$$\sigma_{n-1} = \sqrt{\sigma^2_{n-1,a}(L_z) + \sigma^2_{n-1,b}(L_z)}$$

where:

$$\sigma_{n-1,a}(L_z) = \frac{\partial L_z}{\partial E}\sigma_{n-1}$$

$\sigma_{n-1,a}$ is the precision associated with the measurement of the energy, and $\sigma_{n-1,b}$ is the precision with which one can read the well size from the graph.

In the region of interest, $\partial/\partial E\ (L_Z)$ is $\approx$ 55 nm $eV^{-1}$, and $\sigma_{n-1,b}$ is estimated at 0.2 nm.

For the case of Glasgow MBE B33 material, the value of an accuracy of $\sigma_{n-1,a}$ is estimated at 0.0002 eV, and so $\sigma_{n-1}$ is estimated to be 0.2 nm, dominated by the precision with which one can read the graph.

For the Ghent MOCVD material, the value of $\sigma_{n-1,a}$ is estimated at 0.011 eV, and this gives a value of 0.63 nm, dominated by the precision with which one can measure the material.

**Summary**

Measurements of precision on several samples of different material have indicated that, at best, the measurement at a single point will yield errors of the order of ± 0.2 nm for the well width, ± 2 % for the peak FWHM, and ± 26 % for the peak intensity. If the assumption is made that the wafer is uniform, these values deteriorate, in the case of most uniform material, to: ± 0.2 nm , ± 14 %, and ± 31 % respectively, and, in the case of poor material uniformity, to: ± 0.7 nm, ± 80 %, and ± 100 % respectively.

This suggests that the choice of material will have significant impact on the validity of the measurement of the structure emission.

| Material | Well Width Precision (±nm) | Peak Width (Γ) Precision (± %) | Intensity (I) Precision (± %) |
|---|---|---|---|
| B33 | 0.2 | 14 | 31 |
| PD 880 | 0.6 | 58 | 64 |
| IM 13a | 0.7 | 79 | 54 |
| IM 13b | 0.7 | 19 | 100 |

Table (6.13): Summary of Precision of Wafer Measurement

## 6.5 Low Temperature Photoluminescence of Material

The full analysis of the low temperature photoluminescence of all the material characterized is detailed in Appendix IV; a brief summary of the data is contained in this section in order to elucidate the choice of material for the fabrication of structures.

### 6.5.1 Gent Material

The material was grown by Metal-Organic Chemical Vapour Deposition (MOCVD) by the Universiteit Gent and consisted of sets of three quantum wells.

Samples of materials PD880, IM13a, and IM13b were made available. Characterization at 2.2 K revealed that the emission from the quantum wells was so broad that peaks from different wells overlapped. The material was poor in terms of the large variation in peak intensity, emission wavelength, and peak width as a function of position on the wafer.

A typical spectrum of the material is shown in Figure (6.6). The material was designated PD880, and consists of three quantum wells of width 12, 9, and 4 ( $\pm$ 1) nm.

### 6.5.2 Glasgow Material

The material was grown by Molecular Beam Epitaxy (MBE) by the MBE group at Glasgow University. The wafers characterized were A122, B33, A275, A315, A362, A363, A364, A365.

A typical spectrum of the material B33 is shown in Figure (6.7). It consists of three quantum wells of width 8, 6, and 4 ( $\pm$ 1) nm.

### 6.5.3 STL Material

The material was grown by Metal-Organic Chemical Vapour Deposition (MOCVD) by STL.

The low temperature photoluminescence spectrum of material A1995A is shown in Figure (6.9). The material consists of two quantum wells of width 3.5 nm and 7.5 nm.

Figure (6.6): Photoluminescence Spectrum of Gent PD880

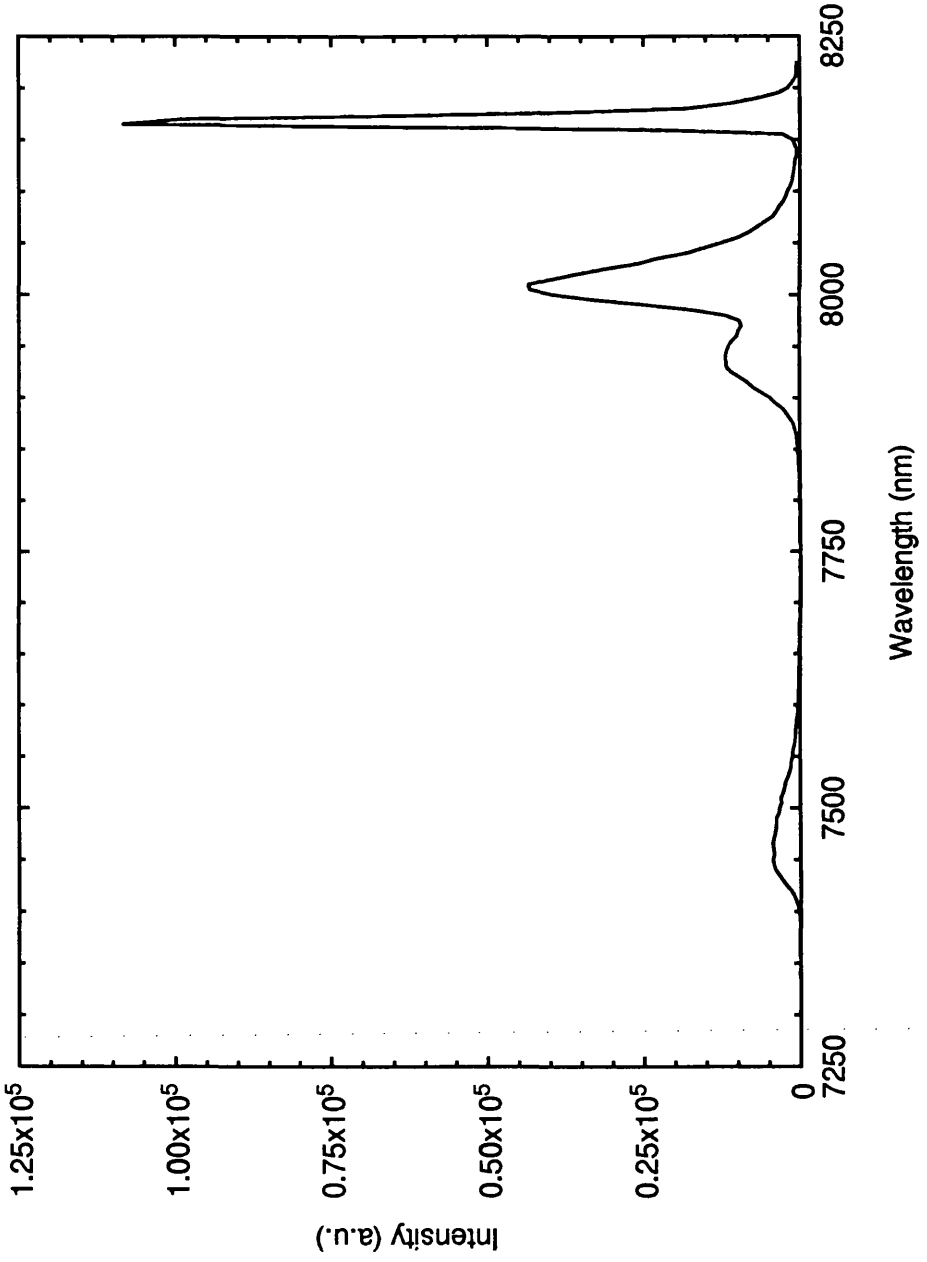

Figure (6.7): Photoluminescence Spectrum of Glasgow B33

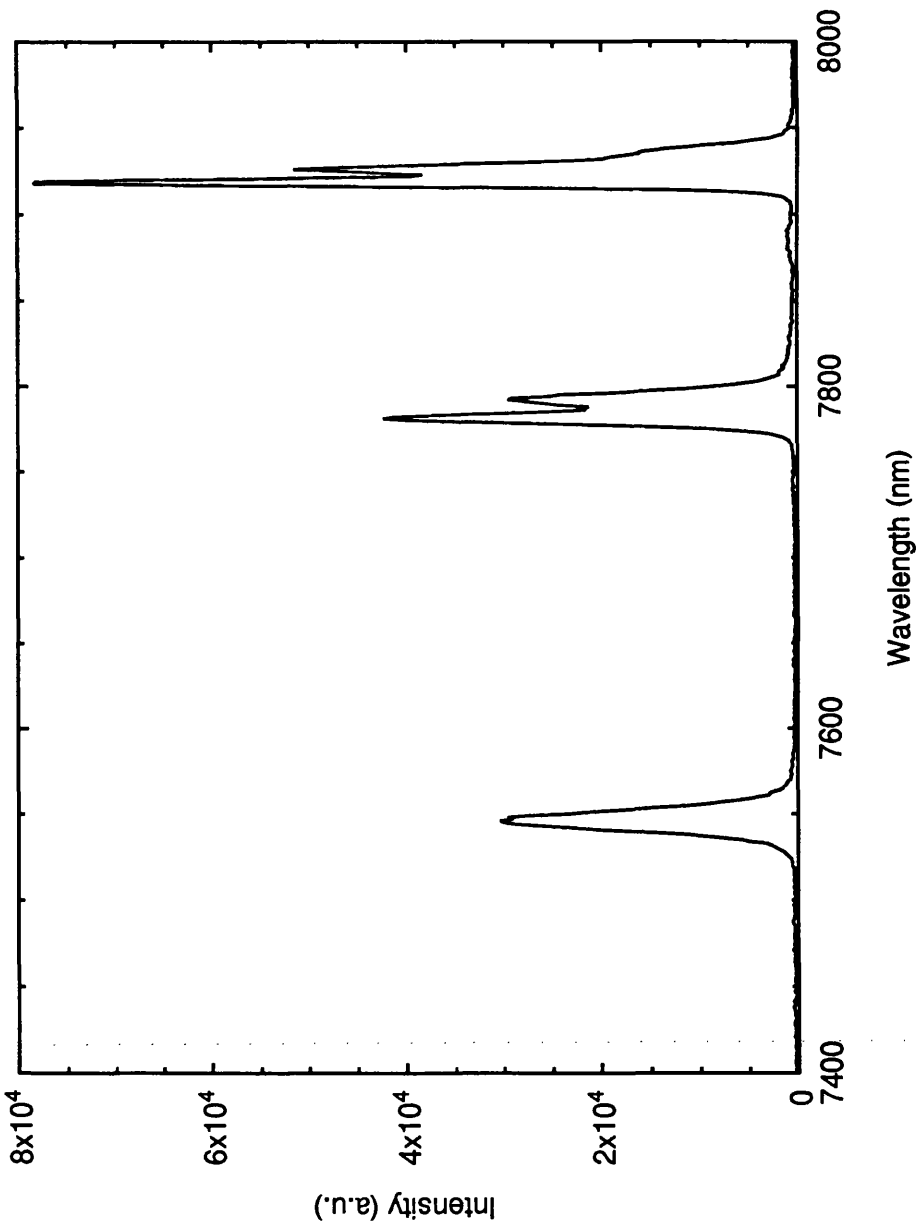

Figure (6.8): Photoluminescence Spectrum of Glasgow A362

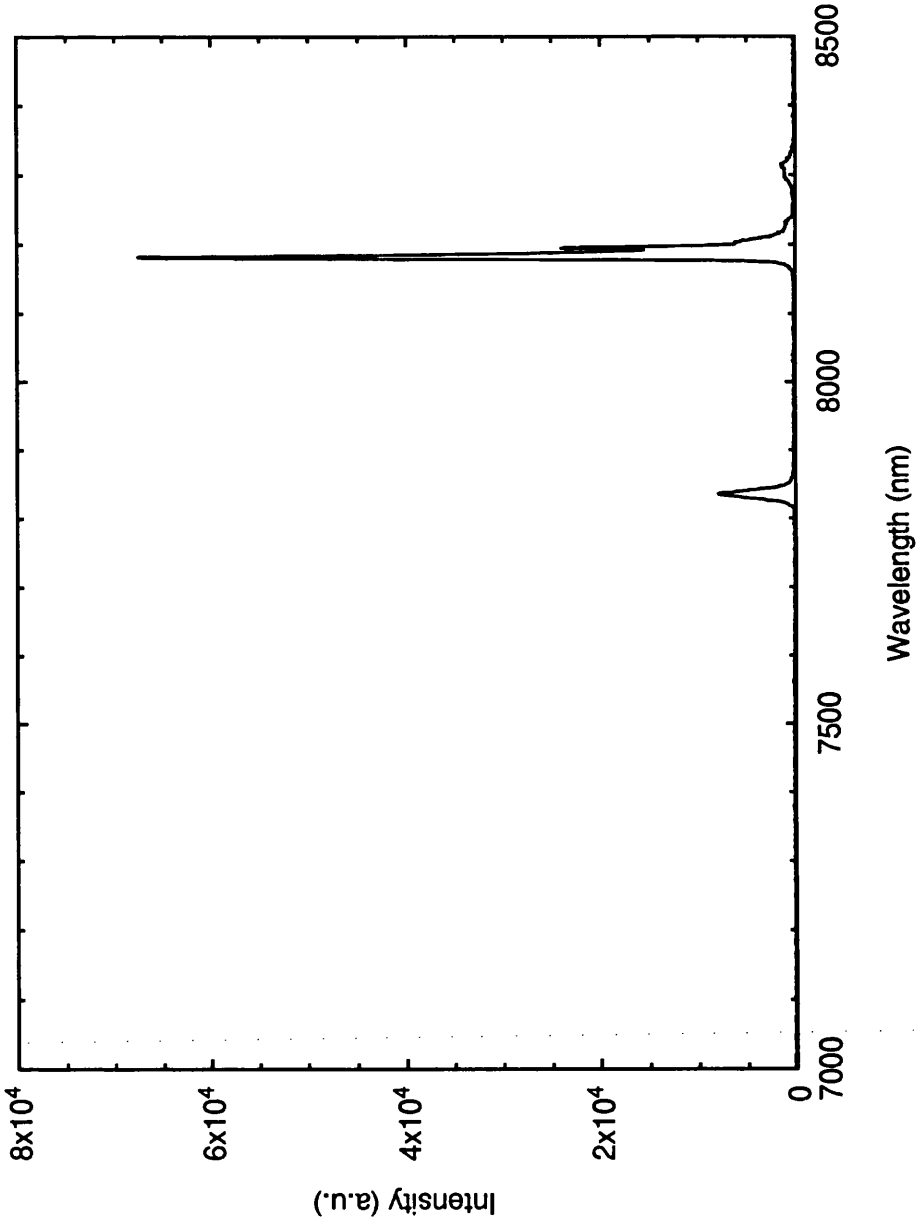

Figure (6.9): Photoluminescence Spectrum of STL A1995A

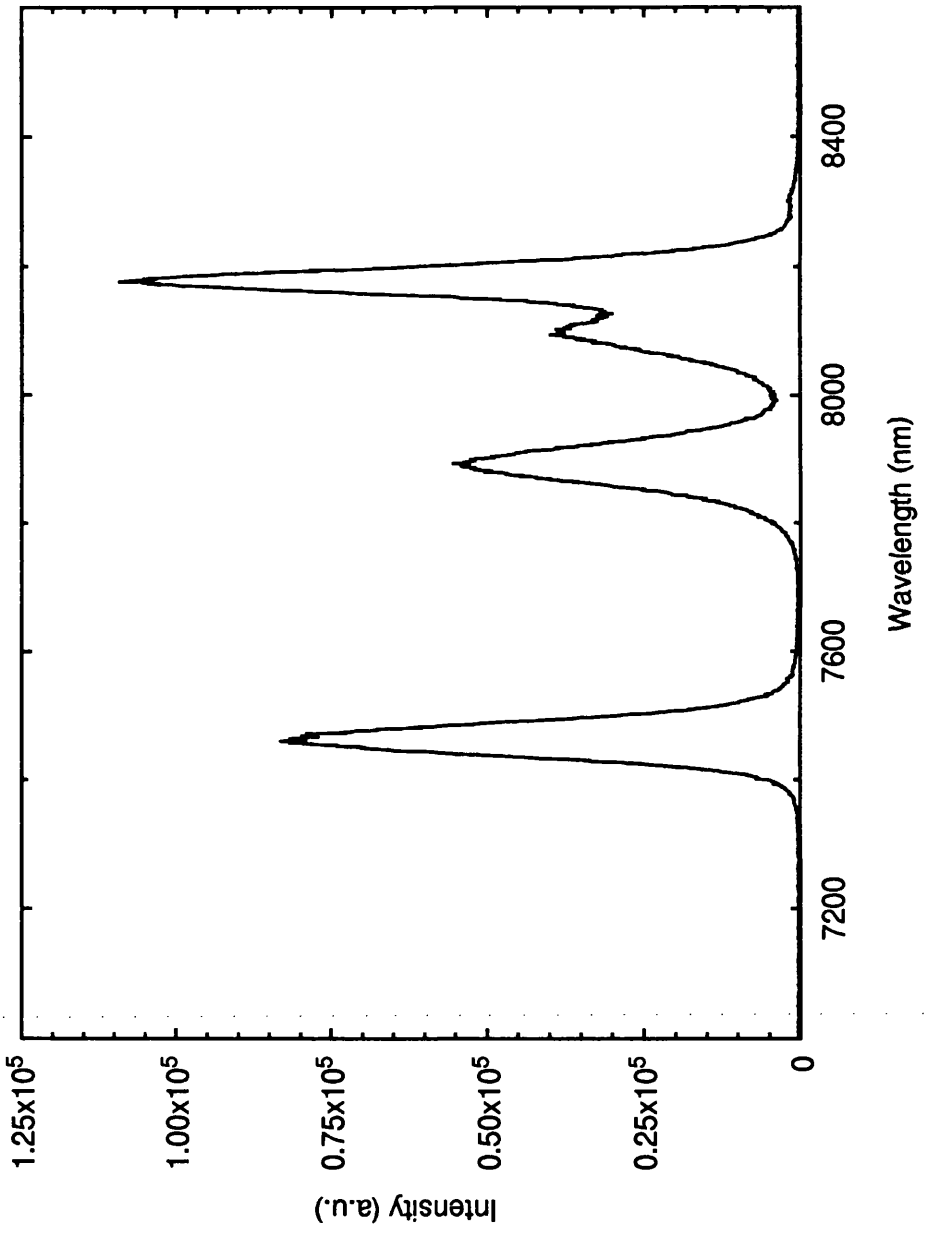

## 6.6 Assessment of Trends on Material B33

### 6.6.1 Variation across wafer

Measurements were made of the emission spectra of B33 at 8 points over a wafer of size 5x10 mm, which had had wet etch windows fabricated on it, to enable accurate calculation of position (Figure (6.10)). The spectra were compared to deduce the behaviour of the luminescence across the wafer.

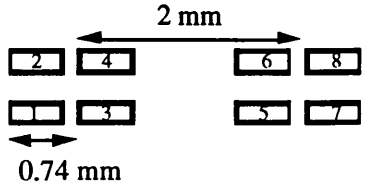


Figure (6.10): Area Layout for Wafer Characterization of B33

Comparison of the behaviour of two parallel sets of four data points allows one to deduce trends associated with the material separately from poor precision of measurement. It can be seen from Figures (6.11) and (6.12) that the peak position measurements reflect a gradient in the well thickness across the sample, perhaps arising from an uneven growth rate due to a substrate temperature gradient.

The measurements of peak intensity at the odd positions closely mirror those at the even positions Figures (6.9) and (6.10), and must be attributed to a combination of factors such as trap distribution and oscillator strength dependence on well width, but the exact causes are unclear from this data alone.

The measurements of fwhm illustrated in Figures (6.11) and (6.12) seem to vary in a random fashion, perhaps reflecting the surface topology of the quantum well, but, as this would have affected the peak position as well, a more likely explanation is the variation in the best fit by Gaussian to the experimental data.

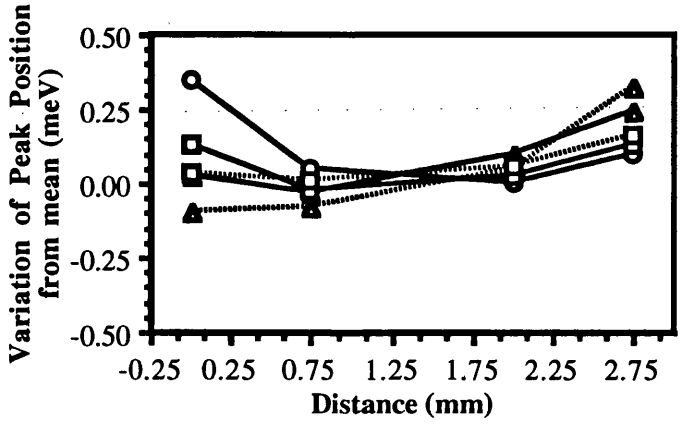


Figure (6.11): Variation of Peak Position across B33 (odd positions)

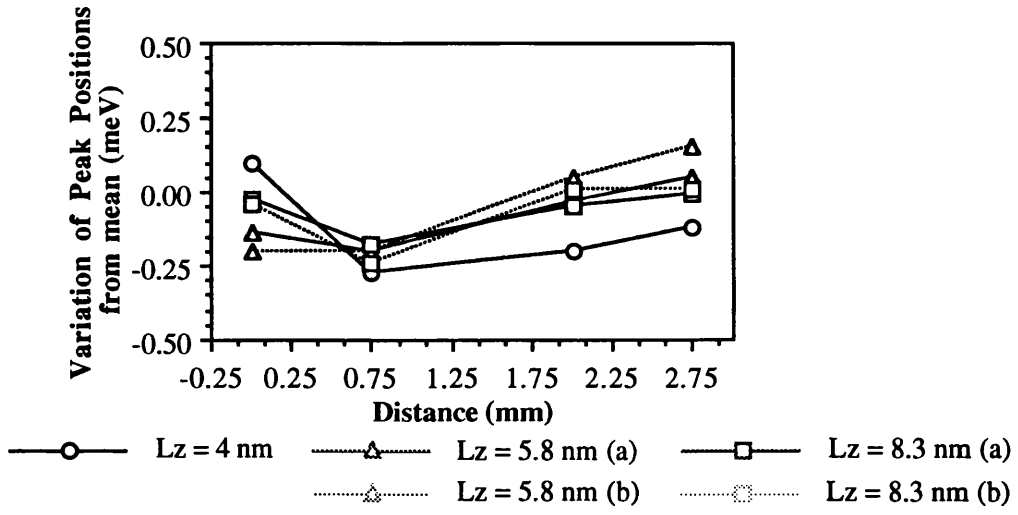


Figure (6.12): Variation of Peak Position across B33 (even positions)

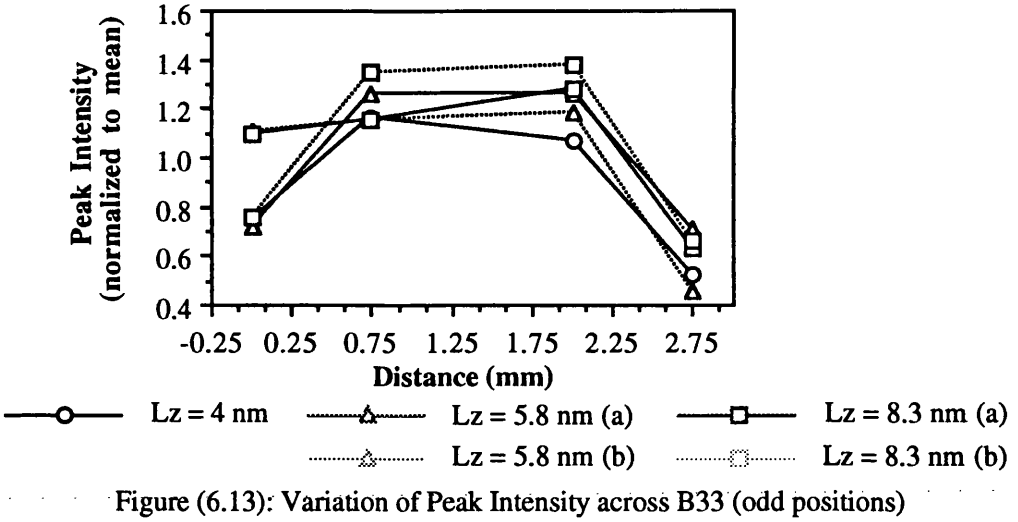


Figure (6.13): Variation of Peak Intensity across B33 (odd positions)

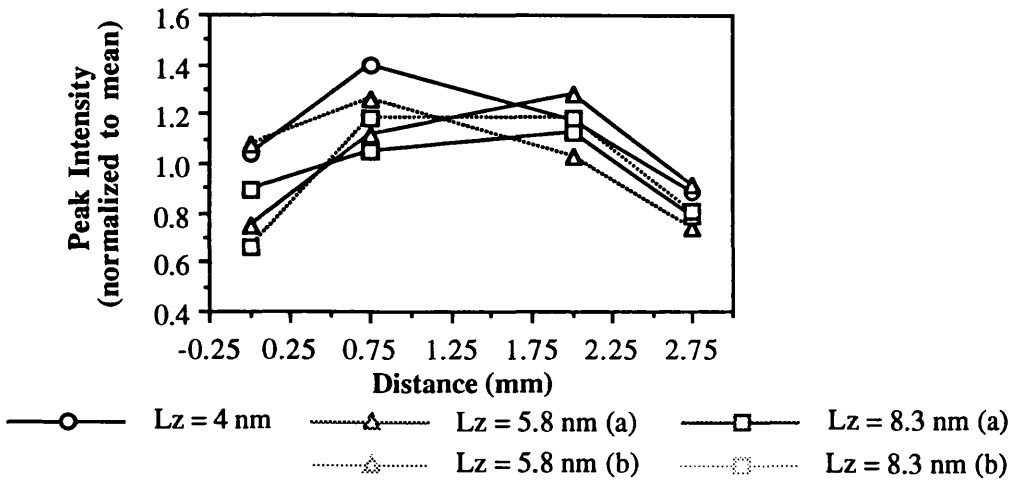


Figure (6.14): Variation of Peak Intensity across B33 (even positions)

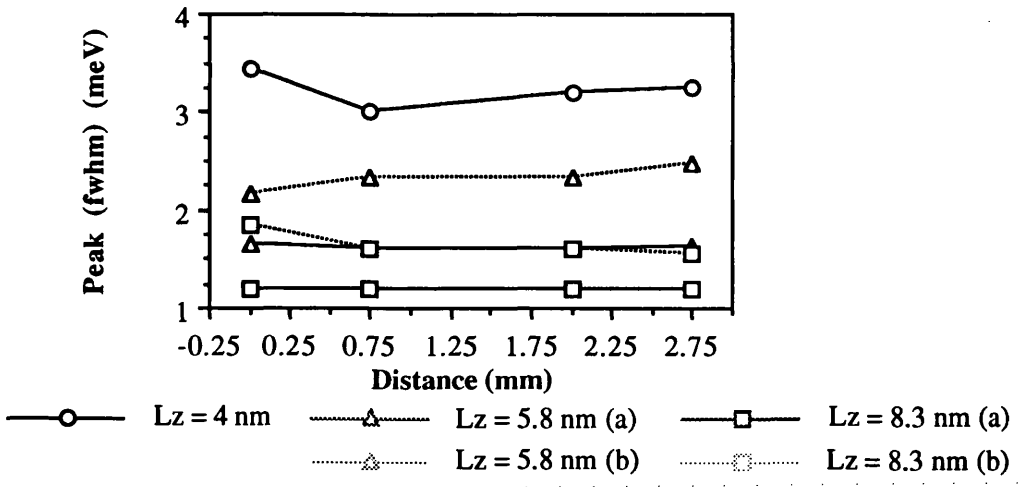


Figure (6.15): Variation of Peak fwhm across B33 (odd positions)

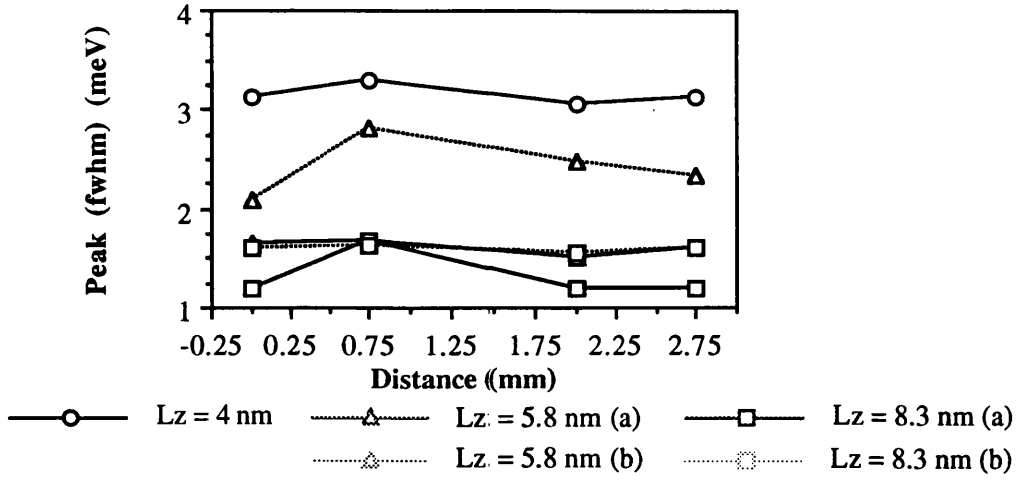


Figure (6.16): Variation of Peak fwhm across B33 (even positions)

### 6.6.2 Variation with Temperature

The temperature dependence of the peak position is seen to follow the band gap at high temperature, but at low temperatures a small shift to higher energy is seen between 5 and 10 K. This has been discussed as a thermalization between wider parts of the wells and those parts narrowed by a monolayer fluctuation.

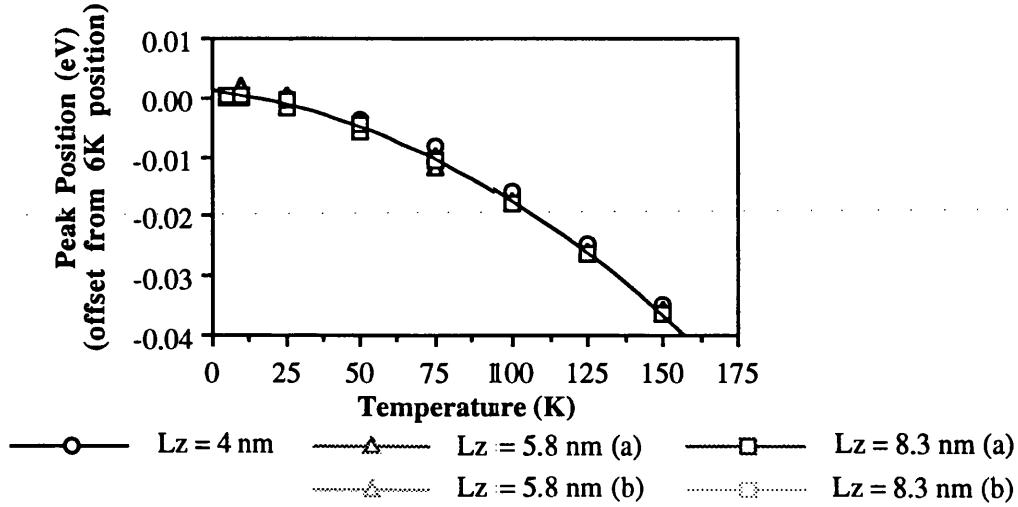


Figure (6.17): Variation of Peak Position of B33
with Temperature

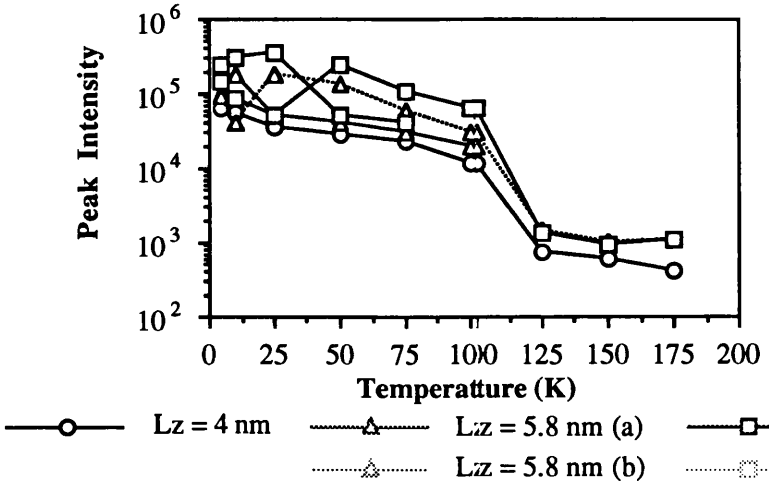


Figure (6.18): Variation of Peak Intensity of B33 with Temperature

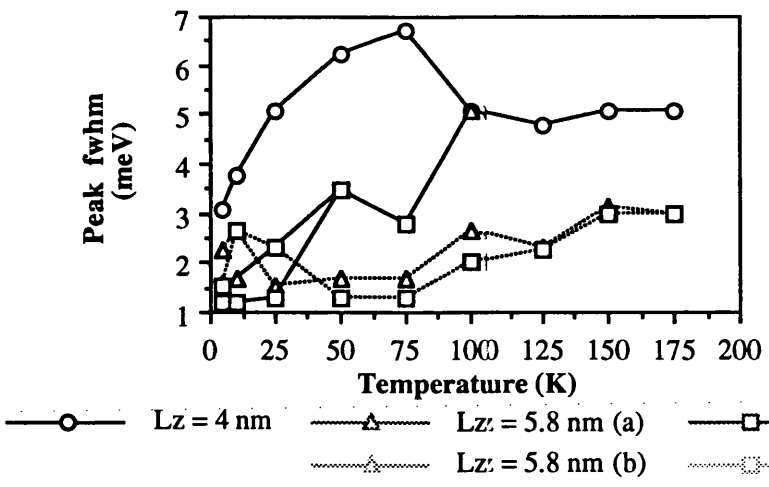


Figure (6.19): Variation of Peak FWHM of wafer B33 with Temperature

Similar exchange of excitons between different well widths is seen in the change in relative intensity of peaks 2 and 3 at ~ 10 K, and between peaks 4 and 5 at ~ 40 K, although in both cases the temperature dependence of the transitions may be due to some impurity de-trapping phenomenon. The fact that the 8 nm well de-trapping occurs at a higher temperature than the 6 nm well de-trapping, and the

indications that the emission is free-excitonic, lend support to the theory of exciton thermalization to areas of well differing in width by monolayers.

As seen in Figure (6.19), the FWHM of the quantum well emission peals 1,3 and 5, corresponding to the dominant transitions in the wells, reach a maximum at a particular tenperature, fall off, and then increase again with a much smaller rate with temperature. The other peaks, corresponding to emission from areas of the nm wells which differ by a monolayer in thickness, are seen to increase monotonically with the temperature.

This behaviour can be understood as a combination of the effect of a decrease in signal strength, giving rise to a more important contribution from the noise, and the intrinsic broadening of the linewidth due to the increase in phonon population with temperature.

### 6.6.3 Variation with Excitation Power

From Figures (6.16) and (6.17), the luminescence peak position has negligible dependence on the excitation power, and the integrated peak intensity has a linear dependence on the exctation power. The continuous broadening of the FWHM Γ can be attributed to band-filling effects.

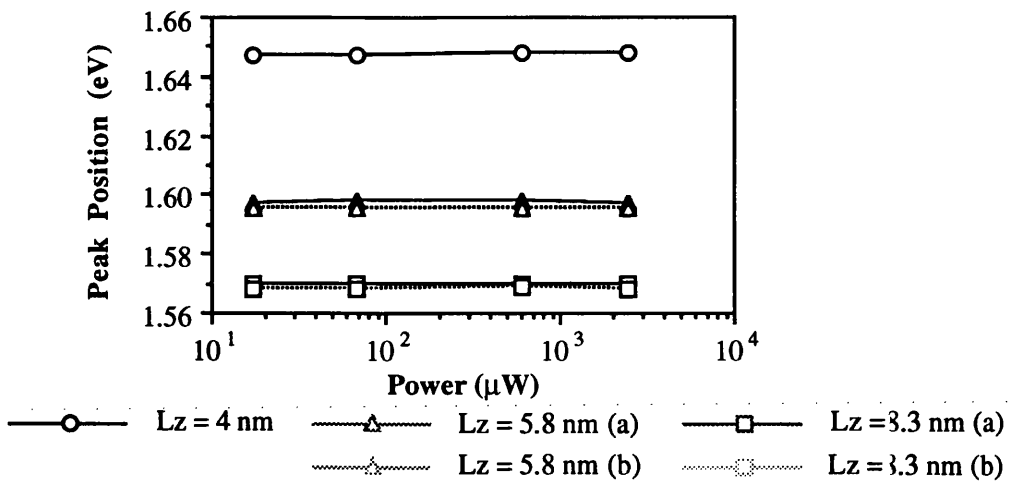


Figure (6.20): Variation of Peak Position of wafer B33 with excitation Power

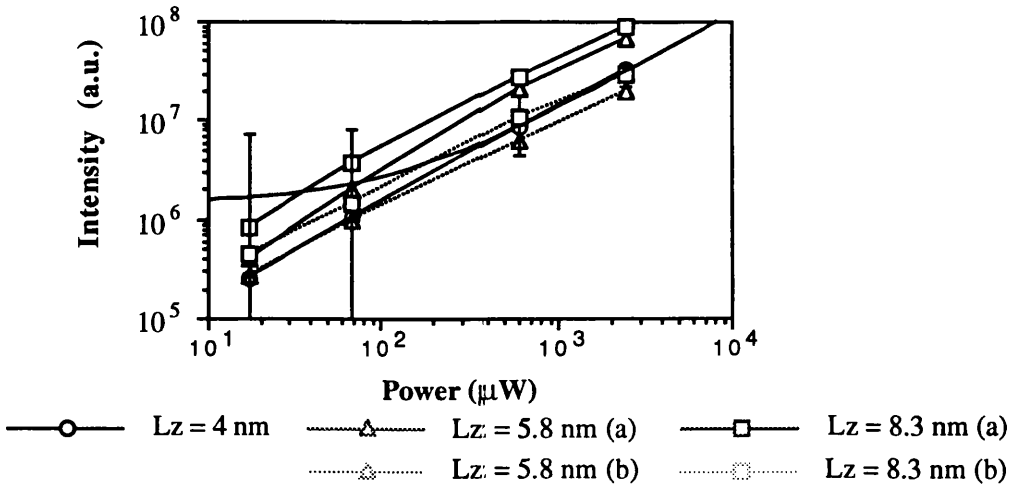


Figure (6.21): Variation of Peak Intensity of wafer B33 with excitation Power

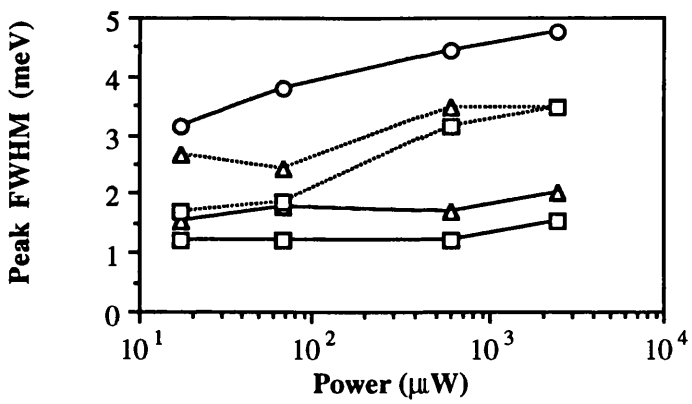


Figure (6.22): Variation of Peak FWHM of wafer B33 with excitation power

## 6.7 Temperature Variation of A275

The variation in luminescence from material A275 was recorded from 5 K to 100 K, when the luminescence became too weak to measure at the excitation power used. The temperature dependence could then be compared with that of B33.

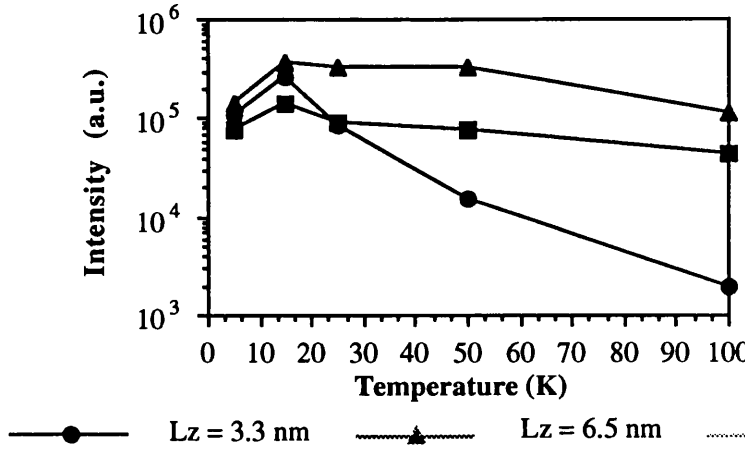


Figure (6.23): Variation of Peak Intensity of wafer A275 with Temperature

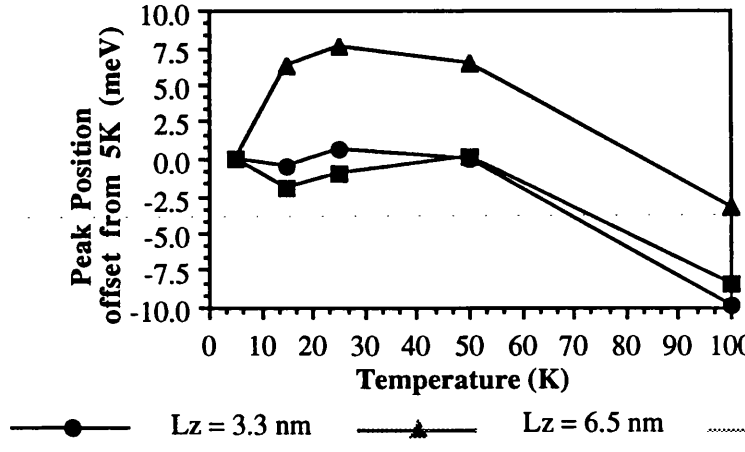


Figure (6.24): Variation of Peak Position of wafer A275 with Temperature

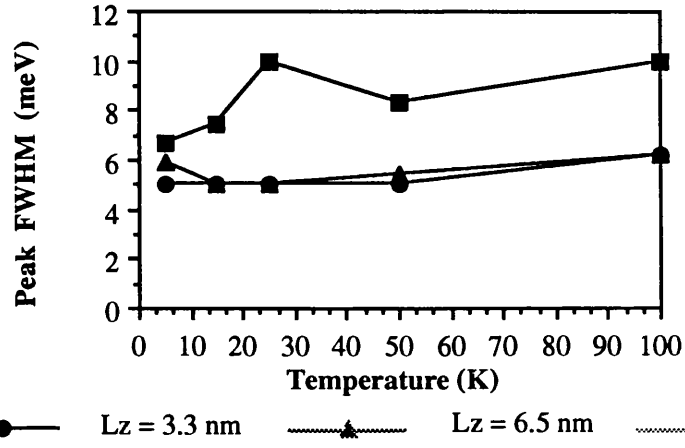


Figure (6.25): Variation of Peak Width of wafer A275 with Temperature

Compared to the behaviour of material B33, reported in a previous section, material A275 is much more temperature dependant. The peak integrated intensity rises sharply between 5 K and 15 K, this is may be attributed to the thermalization of carriers bound to impurities which then contribute to quantum well free exciton emission. The intensity decreases with temperature with a comparable rate of decrease to that of B33.

The temperature dependence of the peak position for A275 shows a much larger swing from the 5 K peak positions than B33; this is also due to the fact that the 5 K emission is dominated by emission from excitons bound to impurities in the well. As the temperature is increased, the free exciton emission dominates, at a higher energy than that from the impurity bound emission. From the ionization energy of ~8 meV in a 100 nm quantum well, the temperature dependence may be due to excitons bound to acceptors, where the dominant impurity is carbon.

The FWHM ($\Gamma$) is seen to show a slight temperature dependant increase, apart from the anomalous peak in the emission from peak 3. This is due to the decrease in signal intensity.

### 6.7.1 Monolayer Well Fluctuations

The emission spectra of a number of materials show monolayer well fluctuations, detected by their behaviour as a function of temperature and power, and their small separation from the dominant quantum well free emission.

An example of the monolayer fluctuations recorded in the material B33 is illustrated in Figures (6.22) and (6.23) below.

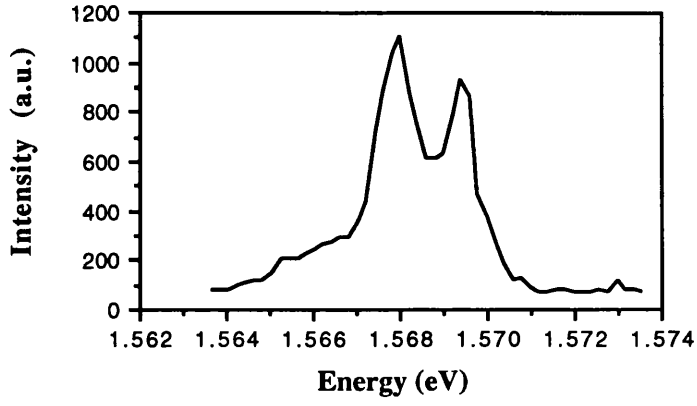


Figure (6.26): Monolayer Fluctuations in B33

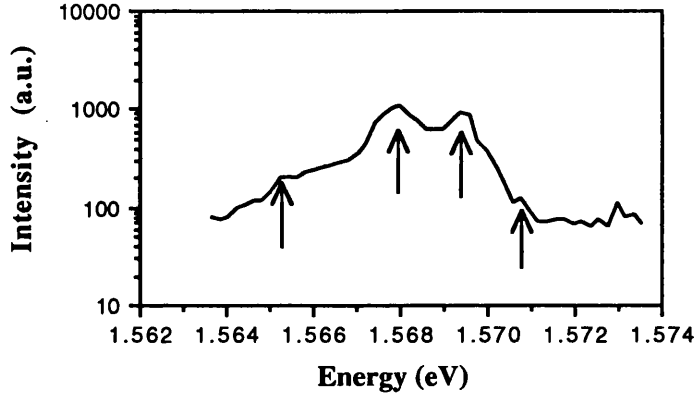


Figure (6.27): Monolayer Fluctuations in B33 (ln scale)

At least five equally separated transitions may be observed in Figure (6.23), with an mean separation of 1.4 (± 0.2) meV, corresponding to monolayer fluctuations in a well of ~ 13 nm.

## 6.8 Photoreflectance of Quantum Well Material

### 6.8.1 Photoreflectance of Glasgow A275 material

A photoreflectance spectrum of A275 material was obtained at room temperature, and Gaussian fits to the spectrum yielded the following values for quantum well heavy hole transitions:

| Feature | Position (eV) | FWHM (Γ) (meV) |
|---|---|---|
| 40Å well heavy hole | 1.5886 | 6.427 |
| 70 Å well heavy hole | 1.4958 | 6.442 |
| 100 Å well heavy hole | 1.472 | 4.689 |

Table (6.14): A275 photoreflectance heavy hole transitions

Although the transitions in the photoreflectance spectrum of A275 were much better resolved than in the case of B33, and the modulation of the reflectance was of similar intensity, more attention was paid to the characterization of B33 because of its suitability for structure fabrication.

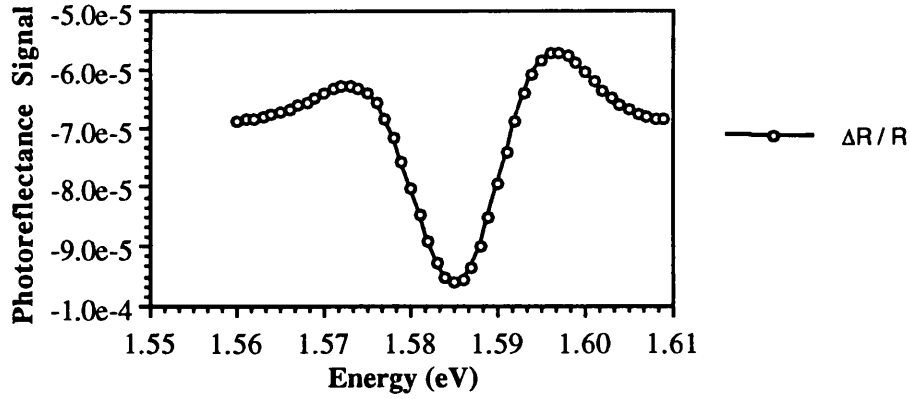


Figure (6.28): 300 K Photoreflectance of 40Å well of A275

### 6.8.2 Photoreflectance of Glasgow B33 material

The photoreflectance spectra from B33 material were confused by the overlap of signals from the quantum wells. Higher order transitions of the wide wells could not be resolved due to the modulation of the thinner wells, and the overlap of signals from well widths differing by one monolayer fluctuations in the two wider wells prevented accurate determination of the positions and widths of these features, especially at higher temperatures.

Photoreflectance spectra were recorded from 77 K to 300 K. At 77 K, the features were sufficiently well resolved for accurate fits to be made to light and heavy hole n=1 transitions for all three wells, but at higher temperatures it was only possible to fit the profile of the 40 Å well.

By measuring the temperature dependence of the width of the 40 Å heavy hole transition, and assuming the dominant broadening mechanism in the temperature range from 77 K to 300 K is LO phonon scattering, it was possible to derive a value for the electron—LO-phonon coupling.

The temperature dependent contribution to the linewidth ($\Gamma$) of the photoreflectance from LO-phonon scattering, with other broadening effects included in $\Gamma_0$, is given by:

$$\Gamma = \Gamma_0 + \frac{\Gamma_1}{\left(e^{\Gamma_2 / kT} - 1\right)}$$

A plot of the linewidths against temperature gives rise to a widely scattered graph, and a $\chi^2$-fit to the data using the expression above with the LO-phonon energy ($\Gamma_2$) = 36 meV, gives:

$\Gamma_0$ = 2.94 meV

$\Gamma_1$ = 1.68 meV,

but as $\chi^2$ = 0.54, the fit is poor.

The possibility of deriving the dependence of the electron—LO-phonon coupling on quantum well width from the temperature dependence of $\Gamma_1$ for a series of quantum wells of different widths is investigated in the next section.

| Feature | Peak Position (eV) | FWHM ($\Gamma$) (meV) |
|---|---|---|
| superlattice | 1.6969 | 3.171 |
| 40 Å heavy hole | 1.6398 | 2.877 |
| 40 Å light hole | 1.6693 | 3.466 |
| 60Å heavy hole | 1.5862 | 2.071 |
| 60Å light hole | 1.6100 | 2.311 |
| 80Å heavy hole | 1.5597 | 2.172 |
| 80Å light hole | 1.5752 | 2.216 |

Table (6.15): B33 77K Photoreflectance data

| Temperature (K) | Peak Position (eV) | Width ($\Gamma$) (meV) |
|---|---|---|
| 77 | 1.6398 | 2.881 |
| 100 | 1.6373 | 2.668 |
| 120 | 1.6298 | 3.066 |
| 150 | 1.6191 | 3.107 |
| 200 | 1.5998 | 3.426 |
| 250 | 1.5813 | 3.424 |
| 300 | 1.5585 | 3.477 |

Table (6.16): Temperature dependence of 40Å quantum well

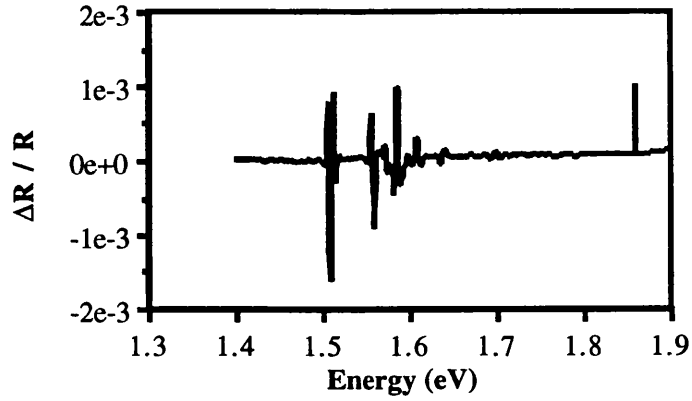


Figure (6.29): PR of B33 at 77 K

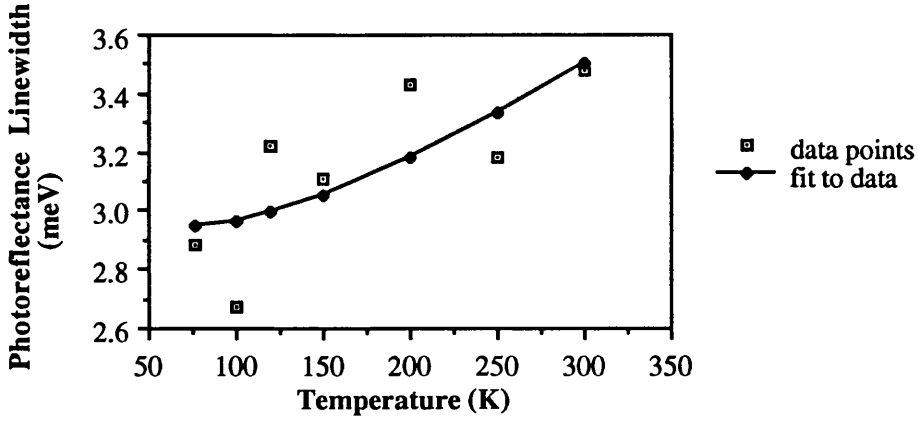


Figure (6.30): Temperature dependence of 40Å quantum well

### 6.8.3 Single Quantum Well Electron-Phonon Coupling

As reported in [Qiang et al., to be published], following the observation of the linewidth dependence of the photoreflectance of B33 material on temperature reported above, it was postulated that it might be possible to measure the electron-phonon coupling as a function of the quantum well width.

A series of quantum wells of varying well width was grown, and the linewidth of the photoreflectance measured as a function of temperature and quantum well width. The data allowed a calculation of the electron-phonon coupling in quantum confined structures, and found a linear dependence of $\Gamma_{ep}$ on $L_z$.

## 6.9 Comparison of Photoluminescence and Photoreflectance Data

### 6.9.1 Peak Positions

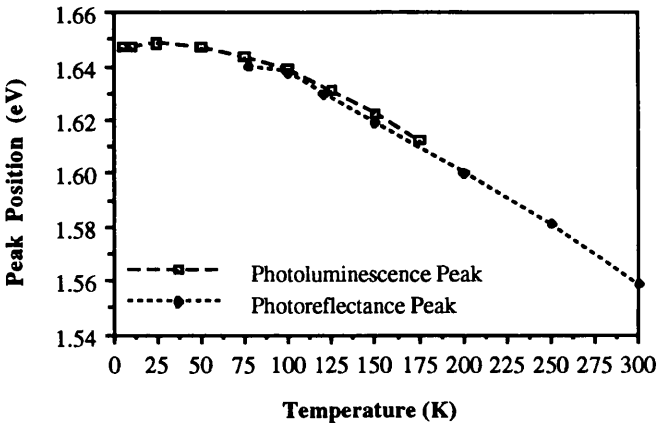


Figure (6.31): Comparison of PL and PR peak positions for 4 nm quantum well of B33 material

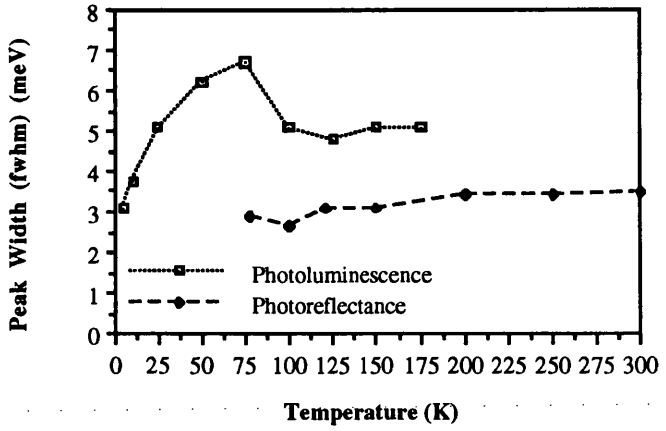


Figure (6.32): Comparison of PL and PR peak fwhm for 4 nm quantum well of B33 material

| Well Width | Photoreflectance (77 K) | | Photoluminescence (75 K) | |
|---|---|---|---|---|
| nominal (nm) | Peak Pos (eV) | Width (meV) | Peak Pos (eV) | Width (meV) |
| 4 | 1.6398 | 2.877 | 1.6435 | 6.691 |
| 6 | 1.5862 | 2.071 | 1.5912 | 1.676 |
| | | | 1.5923 | 2.808 |
| 8 | 1.5597 | 2.172 | 1.5636 | 1.271 |
| | | | 1.5640 | 2.808 |

Table (6.17): Comparison of peak data of B33 material obtained by photoreflectance and photoluminescence

The difference in peak position between the photoreflectance and the photoluminescence data may be attributed to a difference of 10 K in the measurement of the temperature in the cryostats, perhaps from the difference in the separation of the temperature sensor and the sample in the two cryostats.

The difference in peak width, in Figure (6.27), is due to the difference in excitation powers used in the luminescence and reflectivity measurements.

## 6.10 Choice of Material for Fabrication

### 6.10.1 Material Supply

The choice of material used for the fabrication of structures was heavily influenced by the quantity of material available, as it was necessary to fabricate a large number of structures, in order to enable individual structure-to-structure variations to be averaged out over a large number of structures. Due to the large failure rate of the fabrication process, however, a substantial quantity of material was lost in this way, and several times as much material was required as was necessary for the minimum number of chips to be fabricated for comparisons.

### 6.10.2 Peak Linewidth

The peak linewidth of the free exciton emission is an important criterion for assessing material quality. The linewidth of a quantum well emission peak is smallest for the widest wells, and for a well of 10 nm thickness, the smallest fwhm obtainable was 1 meV, on material B33.

### 6.10.3 Intensity Variation

Measurements of the variation in intensity across the wafer were crucial in the choice of material. As the structure intensities were compared with that of the control mesa, wide variations across the wafer would give rise to large errors in the interpretation of the variations in structure intensity.

Material which exhibited essentially flat intensity across the wafer was thus chosen for structure fabrication.

### 6.10.4 Actual Choice of Material

The wafers chosen after considering the factors outlined above were B33, A315, A362, A363, A364, and A365. In order to compare the data with the results obtained by Arnot et al. [op. cit.], structures were also fabricated on material A1995A, which showed extremely poor luminescence, wide fwhm, and wide intensity variation across the wafer.

It was hoped that the properties of the structures would dominate over those of the materials, but if this were not the case, and a choice had to be made between samples fabricated on different material, the behaviour of the structures on B33 would be more plausible.

# Chapter 7: Photoluminescence of Nanostructures

## 7.1 Spectroscopy Considerations

### 7.1.1 Alignment to Nanostructure Array

Unlike the case of quantum well spectroscopy reported in Chapter 6, the alignment of the laser beam to the patterned structure arrays is crucial in recording any signal from the material. The etch process was chosen in order to remove all the quantum well material from the chip save what was protected from the etching by a resist mask. Thus the quantum well emission may only occur from the control mesa and the structured areas.

If the signal from a particular quantum well is recorded from a structure illuminated by the laser beam, the signal may, however, include significant contributions from scattered light in the cryostat exciting the mesas or largest structures. These areas emit strongly, as they have the highest filling factors. One has to take care that the signal is from the structures in question, and this may be checked by two methods.

Firstly, the recorded emission intensity is maximized in signal strength by adjusting the position of the focussing and collecting optics stages. A signal which arises from a nearby structure array or mesa will be maximized at the position of the nearby structure array or mesa, and so the laser beam will wander off the array initially chosen.

Secondly, as the emission from a well broadens considerably as the laser intensity is increased (See Chapter 6, Section 6), the mesa emission from a scattered beam is considerably narrower than the emission from the directly excited array, and can thus be distinguished clearly.

In addition, as there is a residual trend in well thickness across the wafer, emission from the mesa can be discriminated against.

By these methods, it is possible to detect the low level emission from the patterned structure arrays, although it may not be possible always to detect emission from the weakest areas.

### 7.1.2 Choice of Array Size

The main factor in the choice of array size is in the need to minimize stitching between frames. The laser beam was focussed typically down to 70 μm in diameter, thus requiring frames of the order of 100 μm, to maximize structure excitation. Frames larger than 100 μm would have increased the minimum structure size possible on the electron microscope, as the scan field has a fixed number of pixels.

### 7.1.3 Choice of Laser Line

The laser lines available were those of a high power Ar ion laser, with strong emission in the visible and ultra-violet, and a dominant line at 488 nm, and a HeNe laser with main line at 633 nm. The Ar ion laser was capable of driving a dye laser with a range of dyes, but the main use of the lasers was on the single lines mentioned above.

The 488 nm line was sufficiently high in energy to stimulate emission from the AlGaAs barriers as well as the quantum wells, but the 633 nm line lay in the AlGaAs régime, and could not allow study of the barriers.

### 7.1.4 Sample Temperature

The structures were characterized at a sample temperature of 6 K, maintained within ± 0.1 K by heater control. The choice of 6 K was made to reach a sufficiently low stable temperature: below 6 K the condensation of liquid He in the cryostat made temperature control more time consuming; above 6 K, the n=1 free exciton photoluminescence intensity diminishes, and the emission from arrays of structures with low filling factors becomes weak.

### 7.1.5 Choice of Excitation Laser Power

In order to choose the best laser intensity to use, it was necessary to consider the effect of power variation on the photoluminescence from the material. At low excitation densities, the emission consists of contributions from bound-exciton luminescence, but at high excitation densities the scattered light from one structure array can excite emission from other areas, giving rise to false readings for the intensity measurement.

A compromise choice of power was made, involving the power available on the laser and the luminescence of the material.

The laser power could be attenuated with neutral density filters to give sufficient emission firstly from the brightest structure array to allow full-scale to be recorded on the spectrometer. If the weakest areas did not luminesce, the power was increased to investigate whether luminescence was possible, the optical alignment was improved, and then the power reduced to that of the other arrays. In this way it was possible to be consistent about the excitation level of a given array, without recording contributions from light scattered off other areas.

## 7.2 Causes of Sample Failure

### 7.2.1 Mask Failure

Some samples were unable to be characterized due to the failure of the mask. This was due in the main to poor mask adhesion, but in a few cases poor focussing led to insufficient exposure. Ion penetration during the etch process led to unreliable results.

### 7.2.2 Insufficient Etch Depth

In some cases the standard etch process failed to remove sufficient material, and residual luminescence was observable from quantum wells even in the unmasked areas. The signal from these unmasked areas swamped the emission from the structure arrays, and so in these cases the samples were redundant.

The cause of the etch failure was not isolated but could be corroborated with contamination of the etch chamber by previous use of alternative gases.

### 7.2.3 Weak Light Emission

In some cases the emission intensity of the wells under standard laser excitation intensities was insufficient to allow observation of the emission from any but the largest structures.

This did not yield sufficient information to allow worthwhile exploitation of the material.

### 7.2.4 Surface Contamination

In one material, PD880 from Gent, surface residue tentatively assigned to aluminium and arsenic oxides, prevented good mask adhesion and resisted the etch. This produced arrays of structures which were not fully isolated from one another, and data from these structures were ignored.

### 7.2.5 Tweezer scratches

The structures formed by the fabrication process were extremely fragile, and incautious treatment using tweezers during the mounting process could give rise to serious damage to the structures. In order to prevent this having a spurious effect on the luminescence intensity measurements, the samples were observed in a scanning electron microscope immediately after characterization. Pre-characterization observation was precluded by concern over the effects of electron bombardment on the structures, and also the potential sample mortality in the microscope.

## 7.3 Size of Nanostructures

The size of the nanostructures fabricated is controlled by the choice of substrae, resist, resist thickness, beam spot size, and dry etching.

For a given substrate, and a given resist, the resist thickness required is determined by the difference in etch rate between the resist and the substrate. The free parameters are then given by the beam spot size and the etch processing.

The hypothetical minimum structure size exposed on an isolated, infinitely thin film of resist is given by the finite spot size of the electron beam in the electron beam microscope. This is the geometrical image of the cathode, limited by the effects of beam diffraction and aberrations in the lenses. The choice of spot size affects the magnitude of the beam current, and hence the time required to scan the entire sample. As one had to be considerate of other electron microscope users, the scan time was restricted to 4-6 hours, and spot sizes of 8 nm on the Jeol 100CXII and 8 and 16 nm on the Philips PSEM500 were chosen.

After development and etching, the fabrication process resulted in a minimum structure size of approximately 0.1 μm, small variations arising from variations in the focal plane of the electron beam.

This limit of 0.1 μm could be reduced still further by the use of a positive resist and metal masks, by the use of smaller spot sizes, and by using much smaller scan fields to control the depth of focus.

For a given field size of 100 μm, and for the range of sizes chosen up to 100 μm to be fabricated at the same time on the same sample, 0.1 μm was the fabrication limit.

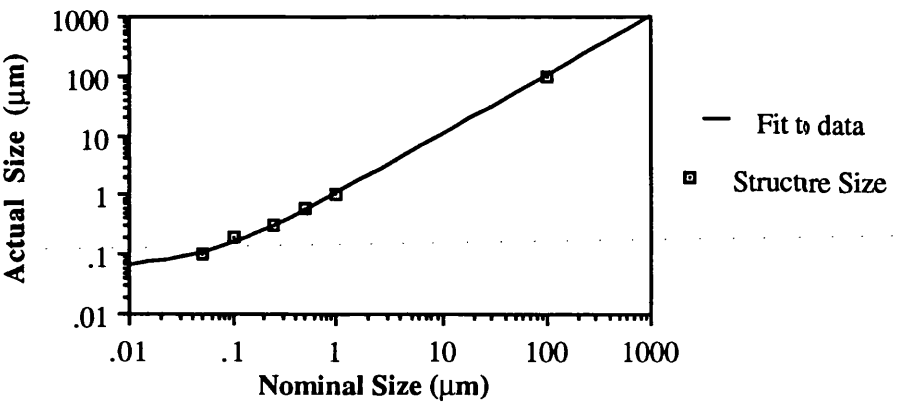


Figure (7.1): Actual Size Of The Structures Fabricated

Because of the inability to stitch the exposure frames with an accuracy better than 5 μm, the maximum structure size is the frame size of 100 μm. The limits to the structure size are thus 0.1 μm and 100 μm, and two structures were fabricated per decade of size from 0.1 μm and 100 μm.

In order to minimize the pattern scan time, the structures were fabricated with the long axis along the X-axis of the frame. Although the full permutations of the structures possible were not exploited, the benefits gained by increasing the number of structures were outweighed by the increase in fabrication time and the necessity of testing the exposures required. The fabrication of structures rotated by 90° might have contributed new information on the effects of a change in crystal orientation, but insufficient time was available for the fabrication of these structures.

### 7.4 Noise Level in Photoluminescence Measurement

The use of the concept of filling factor results in small variations in the weak emission from small structures being exaggerated in the final data. In the Figure (7.2), it may be observed that the emission intensity from the smallest structures is subject to large variations because of the magnifying effect of the filling factor. Coupled with the uncertainty in the luminescence intensity of 30 % in the previous chapter, it may be deduced that the interpretation of any results obtained by this method must be considered carefully, and are uncertain within an order of magnitude.

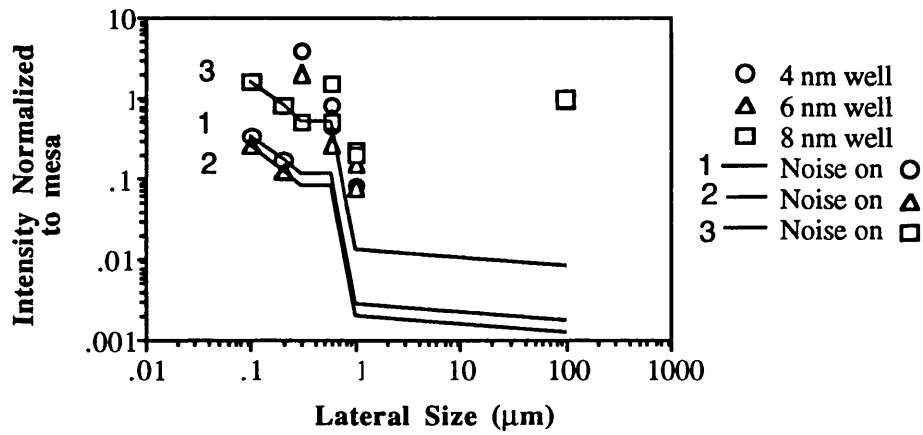


Figure (7.2): Effect of Noise Level and Filling Factor on 6K Photoluminescence Emission of Wires

### 7.5 Reproducibility of Luminescence Measurement

Repeated optimized measurements of the structure emission intensity revealed a similar variation to that of the material reported in Chapter 6. The major factor in the variation in the intensity was due to the alignment of the laser beam to the structure array, but careful optimization of the alignment reduced the variation to factors close to unity.

Variation in the emission efficiency across the starting material contributed to the scatter of the measurements of the structures.

## 7.6 Use of Integrated Intensitty Measurement

The integrated intensity was measured by calculating the area under the spectrum linearized in wavelength. Consistent use was made of this method, justified by the fact that the variation in emission peak position from material to material was insignifiicant compared to the separation betweei the quantum well emission peaks of the same material.

## 7.7 Photoluminescence of Dot,, Dash, and Wire Structure Arrays

A number of observations may be made about the normalized emission intensity neasurements of all of the structures.

In general, the normalized emission intensity is approximately the same for he different quantum wells in the same structure array. This indicates that the behaviour is not very sensitive to variations in well width, and also that reductions in luminescence intensity are not due to the destruction of the upper quantum wells in the etch process, nor to a well-dependent distribution of traps.

The lack of luminescence from a particular structure array or whole sample is not due to physical destruction, as may be assertained by examination under an electron microscope. It is difficult to identify the exact cause for the lack of luminescence; this may be due to poor control of the etch processing chemistry, resulting in a non-uniform surface chemistry from array to array and a dramaticaly increased rate of non-radiative recombination.

The behaviour of the structures is not very reproducible; this is believed to be due to the combined effects of a material-dependent emission, and an etch process which is non-unform across individual samples and from run-to-run.

### 7.7.1 Emission Intensity Measurements in Dots

Five samples of small dots were fabricated as follows: one on material A1995A figure (7.5), two on A365 (one failed, one in Figure (7.6)) and two on A315 (Figures (7.3, 7.4)). The dot sizes utilized were 0.1, 0.2, 0.3, 0.6, 1 μm in diameter, and eight patterned areas were fabricated on each chip, allowing duplication of three areas, 0.1, 0.6, 1 μm.

On four of the samples, most of the arrays luminesced, but one of the A365 sampes failed to luminesce at all, save for the mesa. The results of the measurements of normalized photoluminescence intensity at 6 K are presented in the following figures. Figures (7.3) and (7.4) show the resuts on A315 material, whereas the results from the A365 material are shown in Figure (7.5), with the behaviour of each quantum well of the materials graphed separately for clarity.

By comparing Figures (7.3) and (7.4), it is apparent that identical structures fabricated from the same material and etched at the same time exhibit a considerable variation in behaviour, thus rendering the detailed investigation of the size-dependence of the structures difficult.

For the four sample results illustrated above, however, one may observe that the efficiency lies within one to two orders of magnitude of unity for all the points recorded. Points lying above unity efficiency may be due to luminescence from the mesa material being weaker than the luminescence from the rest of the wafer, or from one particular well at a wafer site being particularly bright.

The scatter within one sample may be attributed to variations in the measurement of well intensity as discussed in Chapter 6, where the best estimate of error in intensity was ± 30 %, and, in the measurements here, may be considerably greater, as discussed in Section (7.5) above.

In these samples, however, it may be noticed a distinct trend in the luminescence efficiency, especially in Figure (7.4), which is that the efficiency of the small dots increases by one order of magnitude as the dot size is reduced from 1 μm to 0.1 μm, approaching the efficiency of the mesa. Thus the efficiency of the larger dots is smaller than either the mesa or the smaller dots. This behaviour is seen to be independent of the quantum well material used.

In summary, the all of the dots luminesce with an efficiency close to unity, and they show no dramatic reduction in efficiency with size: on the contrary, the efficiency of the smaller dots increases relative to the larger dots in the 0.1 μm to 1 μm régime.

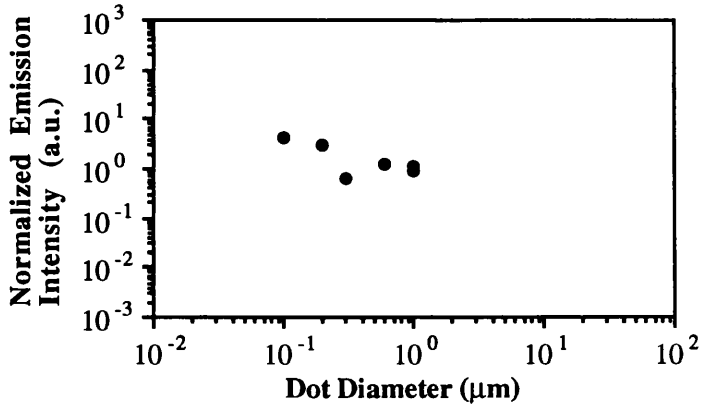


Figure (7.3i): Luminescence Intensity of the 4 nm well of Dot Sample 1

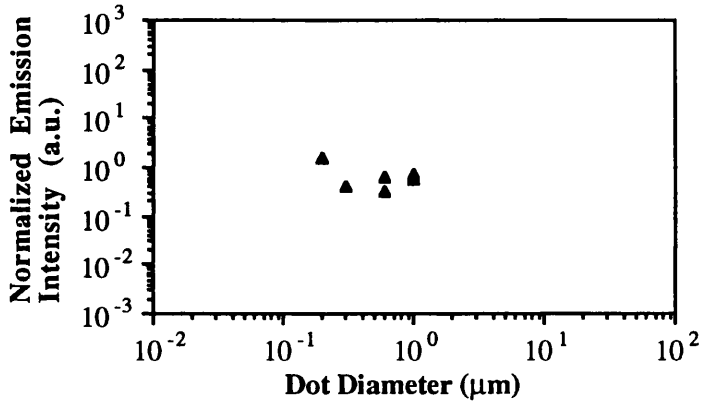


Figure (7.3ii): Luminescence Intensity of the 6 nm well of Dot Sample 1

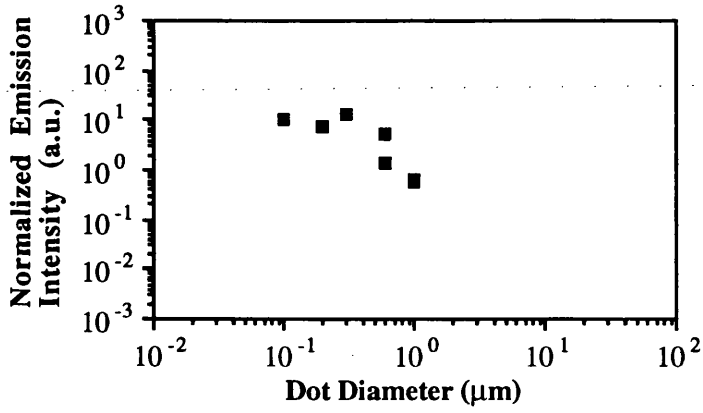


Figure (7.3iii): Luminescence Intensity of the 8 nm well of Dot Sample 1

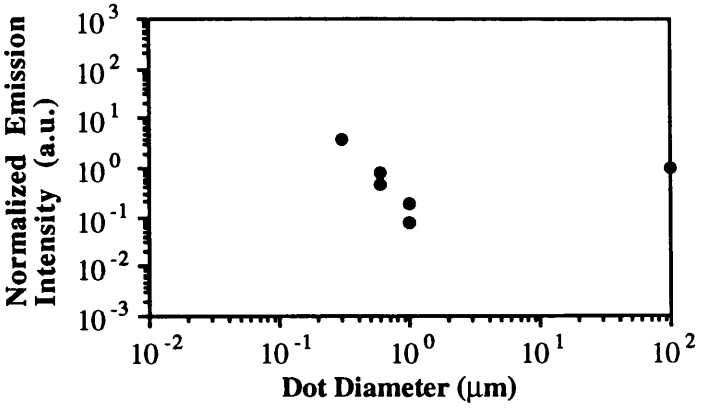


Figure (7.4i): Luminescence Intensity of the 4 nm well of Dot Sample 2

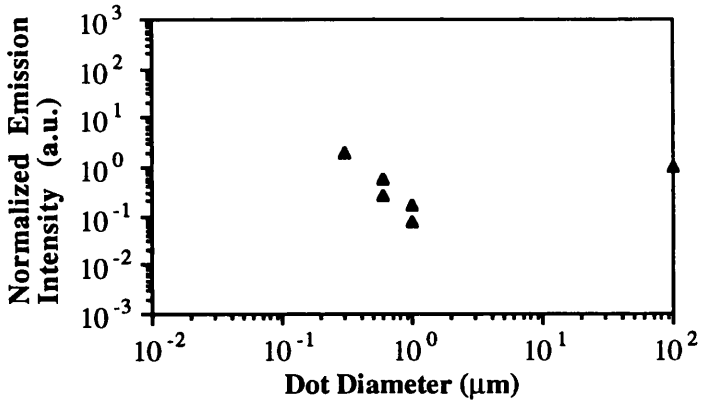


Figure (7.4ii): Luminescence Intensity of the 6 nm well of Dot Sample 2

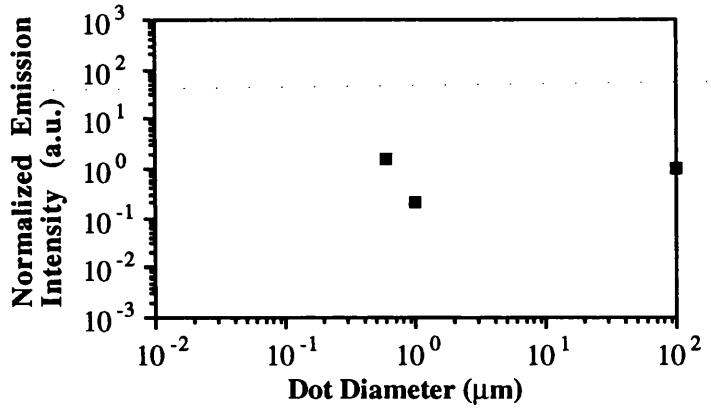


Figure (7.4iii): Luminescence Intensity of the 8 nm well of Dot Sample 2

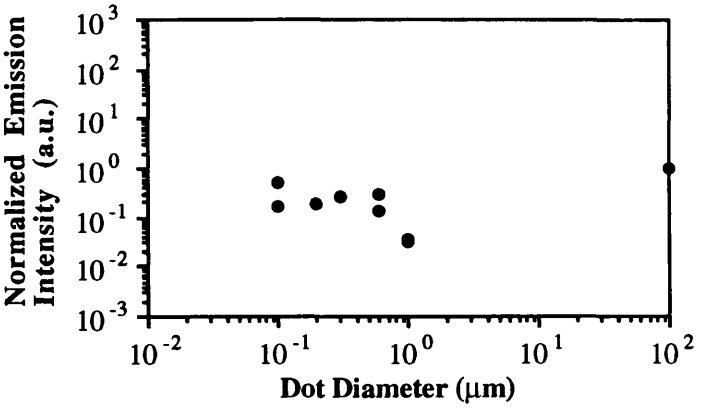


Figure (7.5i): Luminescence Intensity of the 3.5 nm well of Dot Sample 3

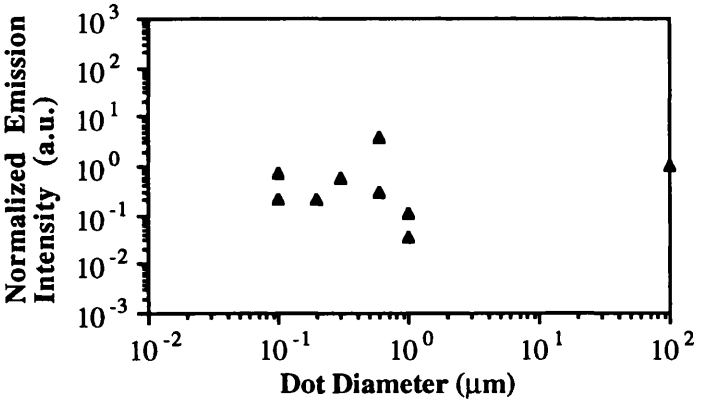


Figure (7.5ii): Luminescence Intensity of the 7.5 nm well of Dot Sample 3

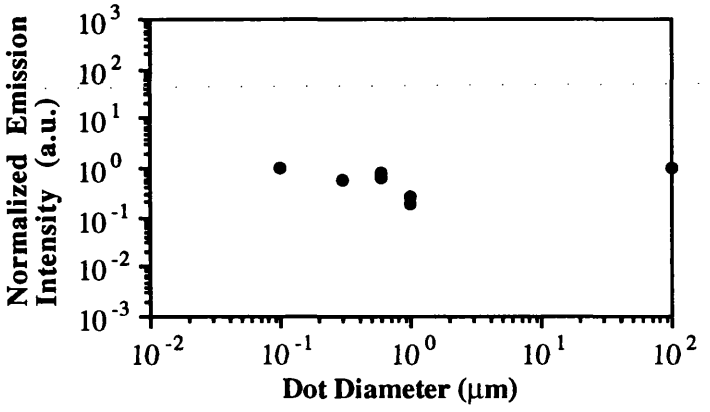


Figure (7.6): Luminescence Intensity of the 20 nm well of Dot Sample 4

### 7.7.2 Emission Intensity Measurements in Wires

Three samples of the wires were fabricated on A315 material, one on A1995A, and two on A365 material. These results are illustrated in Figures (7.7-7.9), (7.10), and (7.11-7.12) respectively. The length of the wires fabricated was fixed at 100 μm, and the wires were of width 0.1, 0.2, 1, 3 μm; in an attempt to reduce the uncertainty in the measurement of luminescence emission efficiency, structures were duplicated rather than using a wider range of size.

All the samples luminesced, with some 'dead' arrays, which did not luminesce, randomly distributed on the chips; the cause of the 'dead' arrays is assumed to be similar to that mentioned in Section (7.7.1) above. In addition, the emission from the 4 nm well of Wire Sample 2 did not luminesce for any of the structures, perhaps indicating penetration of the mask by ion in the etch process

In contrast to the results obtained from the dot structures, the results obtained from the wire structures, shown in Figures (7.7) to (7.12), showed no uniform trend. The results from Wire Sample 2 on A315 material, Figure (7.8), showed luminescence efficiency approximately independent of the wire width, whereas in Wire Sample 3, Figure (7.9), also of A315 material, the efficiency increases monotonically with the reduction in structure size, as in the case for the dots. In the remaining four samples, Wire samples 1, 4-6, shown in Figures (7.6), (7.10-12), however, there was a monotonic decrease in efficiency as the wire width was reduced, decreasing by up to two orders of magnitude on the efficiency of the mesa.

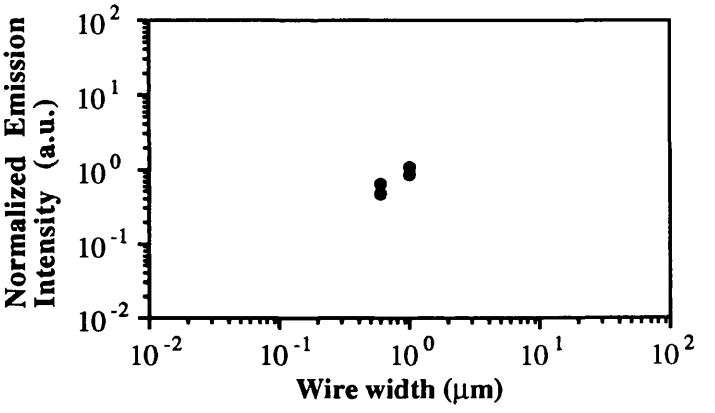


Figure (7.7i): Luminescence Intensity of the 4 nm well of Wire Sample 1

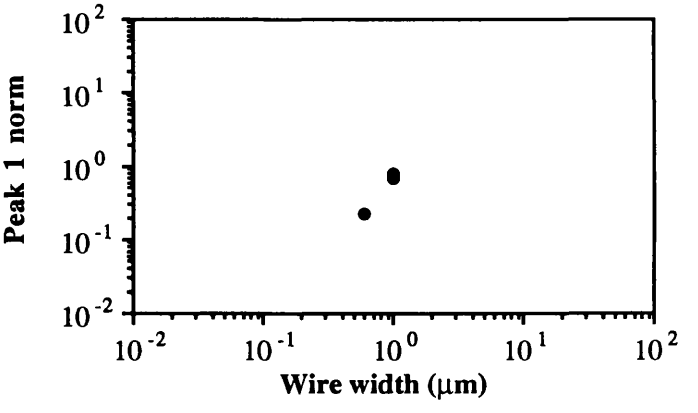


Figure (7.7ii): Luminescence Intensity of the 6 nm well of Wire Sample 1

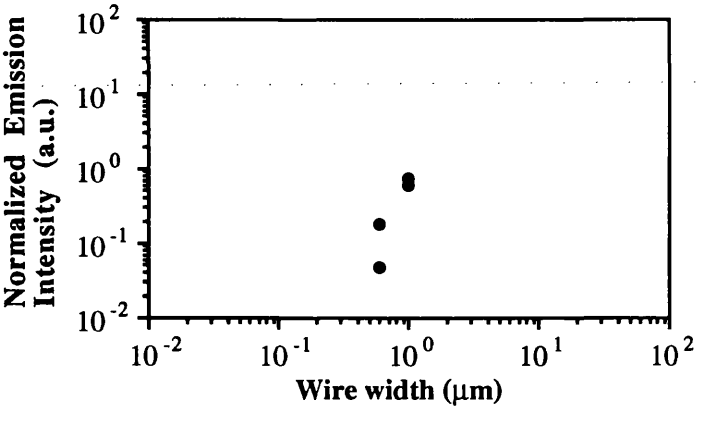


Figure (7.7iii): Luminescence Intensity of the 8 nm well of Wire Sample 1

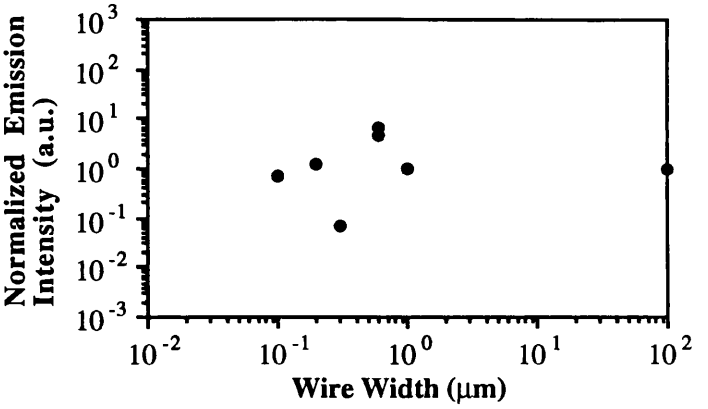


Figure (7.8i): Luminescence Intensity of the 6 nm well of Wire Sample 2

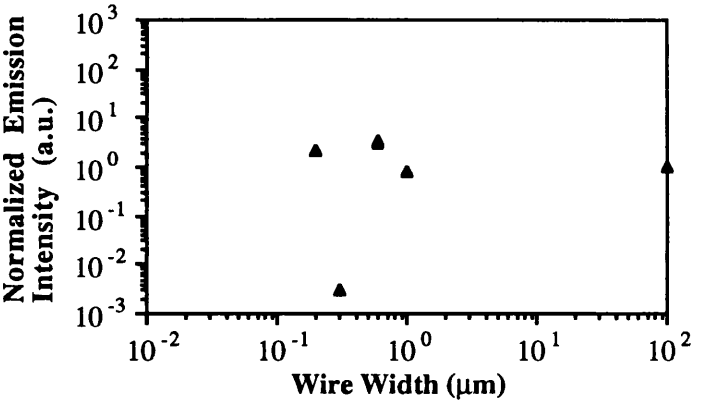


Figure (7.8ii): Luminescence Intensity of the 8 nm well of Wire Sample 2

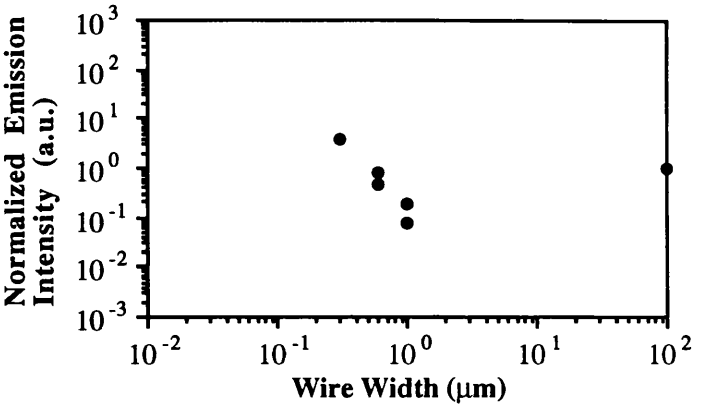


Figure (7.9i): Luminescence Intensity of the 4 nm well of Wire Sample 3

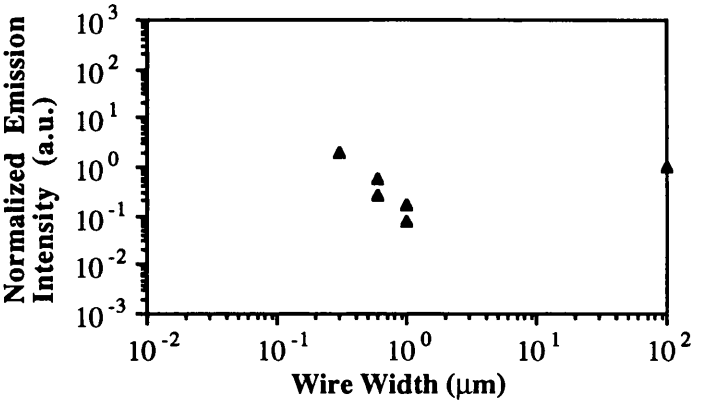


Figure (7.9ii): Luminescence Intensity of the 6 nm well of Wire Sample 3

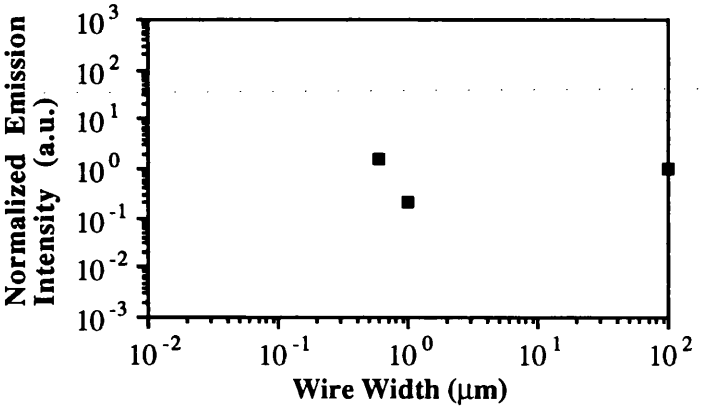


Figure (7.9iii): Luminescence Intensity of the 8 nm well of Wire Sample 3

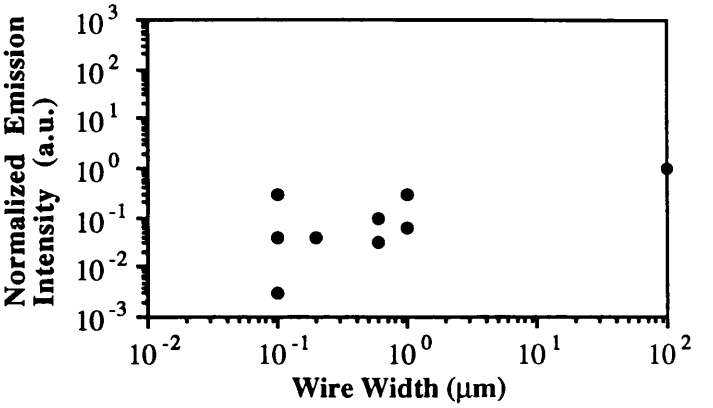


Figure (7.10i): Luminescence Intensity of the 3.5 nm well of Wire Sample 4

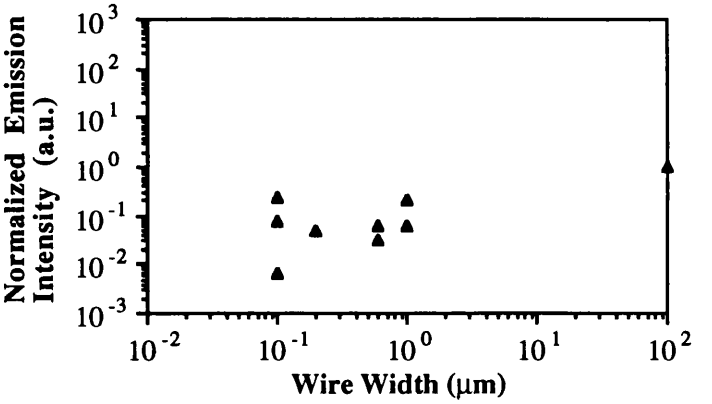


Figure (7.10ii): Luminescence Intensity of the 7.5 nm well of Wire Sample 4

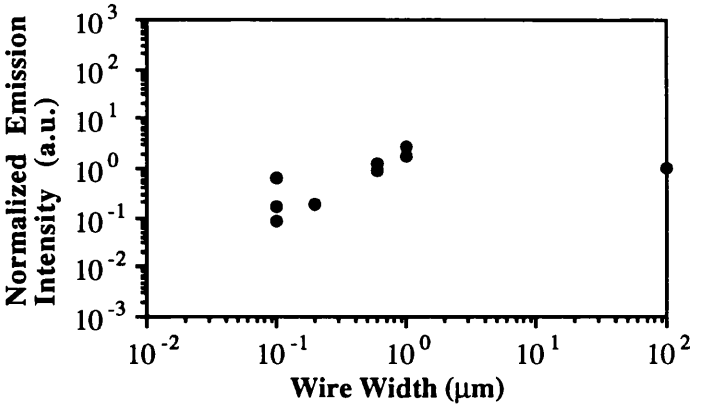


Figure (7.11): Luminescence Intensity of the 20 nm well of Wire Sample 5

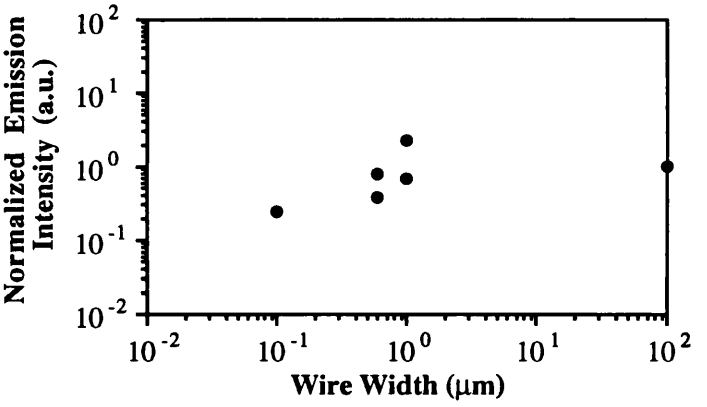


Figure (7.12): Luminescence Intensity of the 20 nm well of Wire Sample 6

### 7.7.3 Emission Intensity Measurements in Quantum Dashes

For large dashes of constant width of 3 μm (Dash Samples 8 and 12, Figures (7.20) and (7.24)), and for medium dashes of 1 μm wide (Dash Samples 9-11, Figures (7.21-7.23)): as the length is reduced, the efficiency remains approximately constant with large scatter, and within two orders of magnitude of that of the mesa.

For some narrow dashes of 0.1 μm wide there was no emission, and thus no comparison was possible. But for others (Dash Samples 1-3, Figures (7.13) and (7.15)), of material B33, combined results show that as the length is reduced, a small increase in intensity is observed.

In Dash Samples 4-6, Figures (7.16-7.18), it was observed that a decrease in structure width resulted in a decrease in luminescence efficiency, but that the efficiency also depended on the structure length. This was most clearly seen in Dash Sample 5, Figure (7.17) and Dash Sample 6, Figure (7.18), where, for a constant structure width, the efficiency increases as the structure length is reduced.

The most consistent results are observed in the behaviour of Dash Samples 5 and 6, particularly in the behaviour of the dots and wires on this sample, depicted in Figures (7.17(e,f) and 7.18 (e,f)). There is a consistent reduction in intensity in all the structures fabricated on these samples. There is little dependence of the intensity on the dash length for a given dash width, thus indicating that the emission efficiency is dominated by the smallest dimension. These samples were fabricated on material B33, whose characterization was described in Chapter 6. This material was shown to have the narrowest emission peak width for narrow well widths, indicating the high quality of the starting material. This will be discussed further in Section (7.7.4).

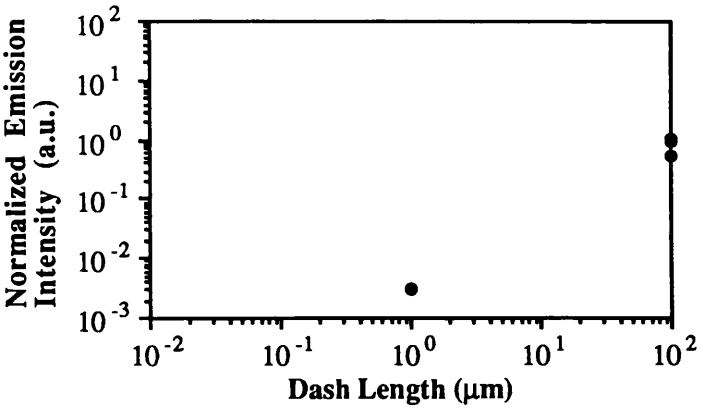


Figure (7.13i): 4 nm well of Dash Sample 1

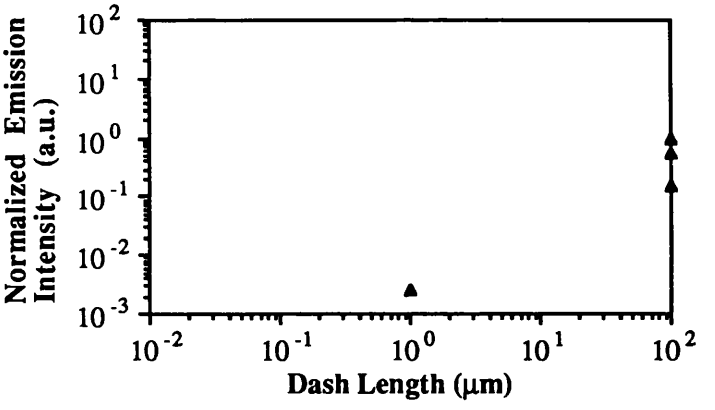


Figure (7.13ii): 6 nm well of Dash Sample 1

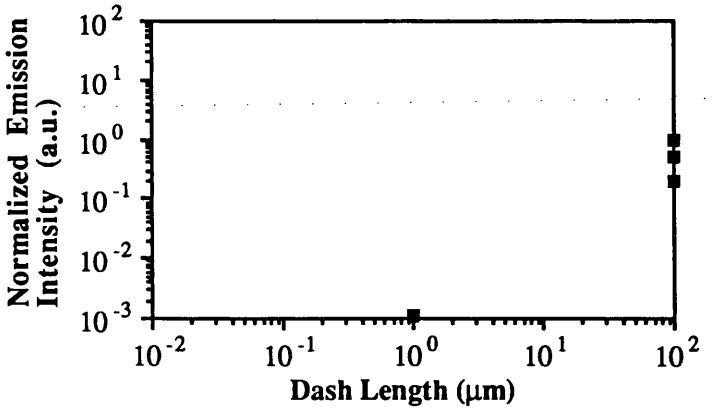


Figure (7.13iii): 8 nm well of Dash Sample 1

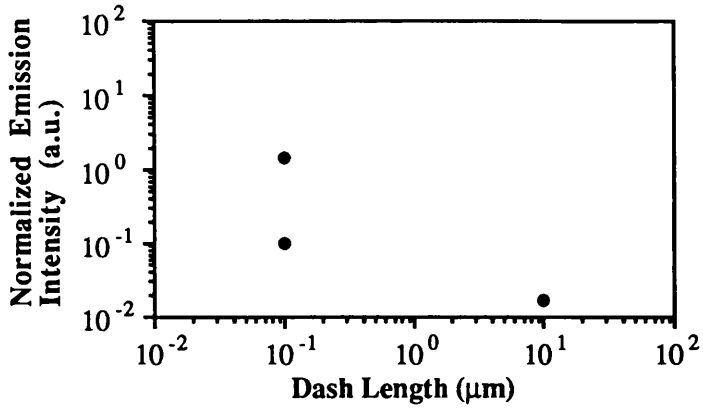


Figure (7.14i): 4 nm well of Dash Sample 2

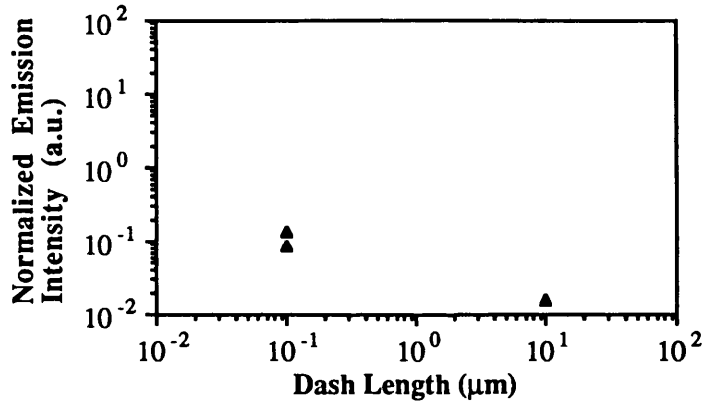


Figure (7.14ii): 6 nm well of Dash Sample 2

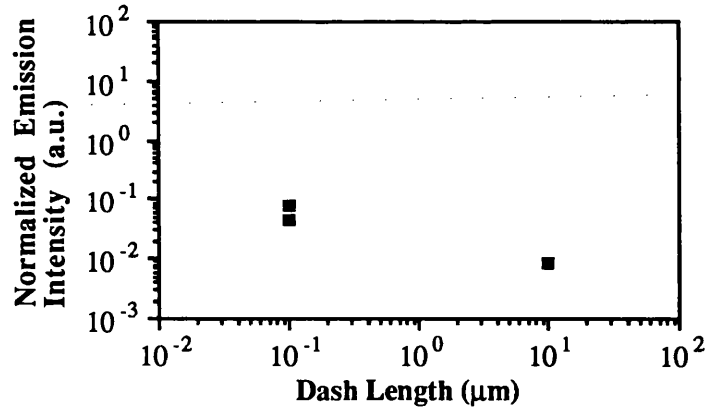


Figure (7.14iii): 8 nm well of Dash Sample 2

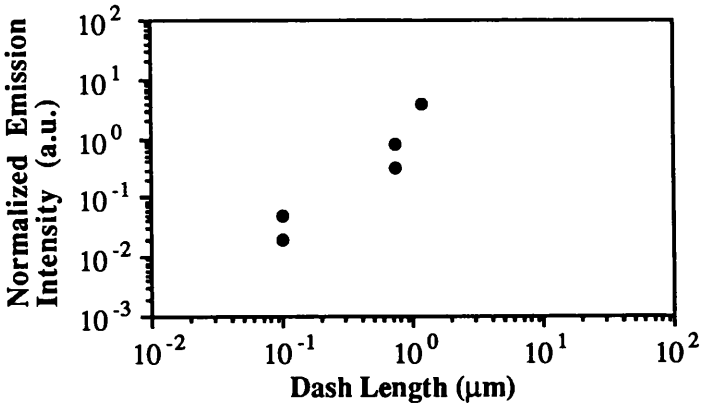


Figure (7.15i): 4 nm well of Dash Sample 3

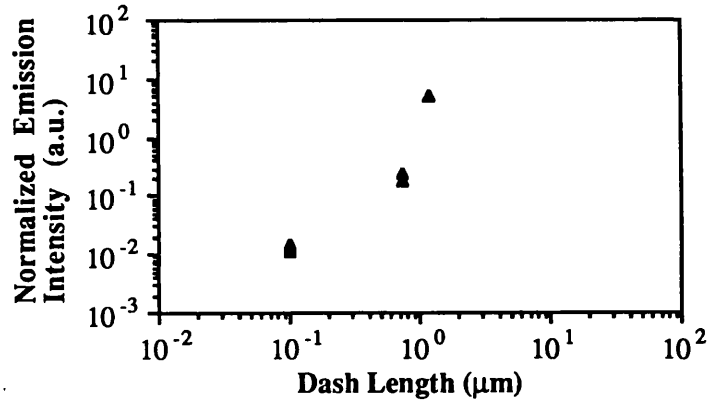


Figure (7.15ii): 6 nm well of Dash Sample 3

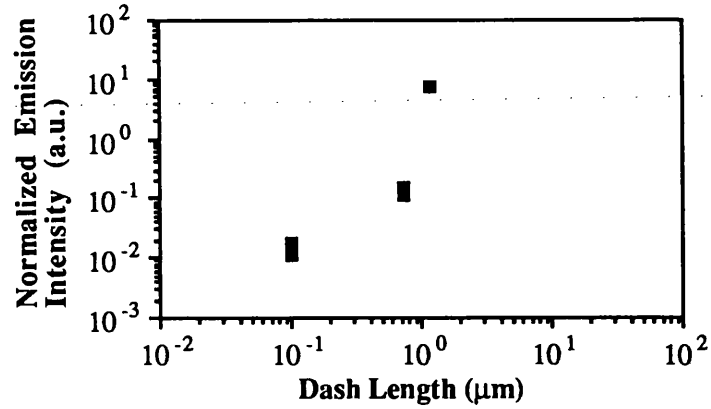


Figure (7.15iii): 8 nm well of Dash Sample 3

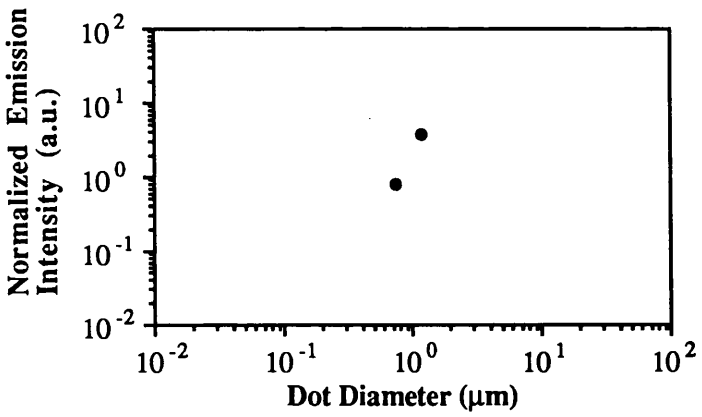


Figure (7.16ai): 4 nm well of Dots of Dash Sample 4

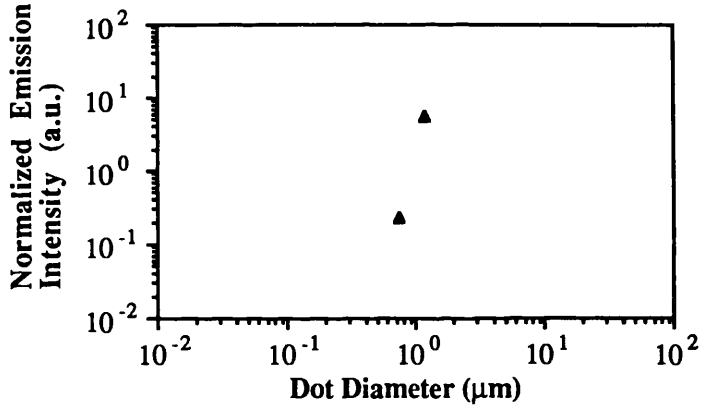


Figure (7.16aii): 6 nm well of Dots of Dash Sample 4

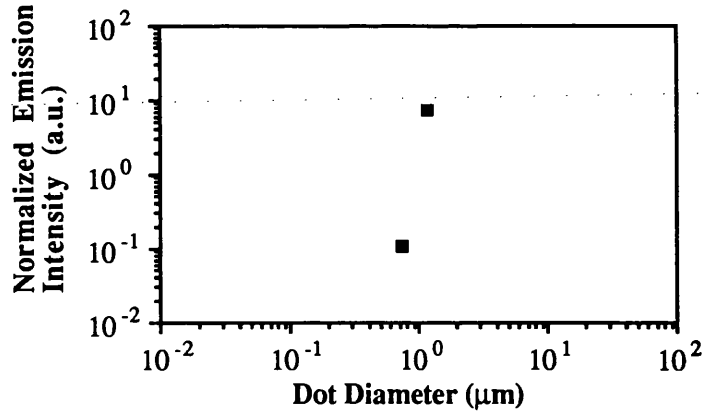


Figure (7.16aiii): 8 nm well of Dots of Dash Sample 4

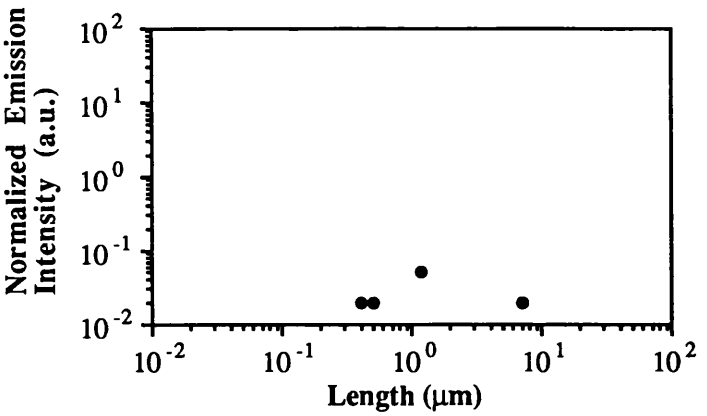


Figure (7.16bi): 4 nm well of dashes of Dash Sample 4

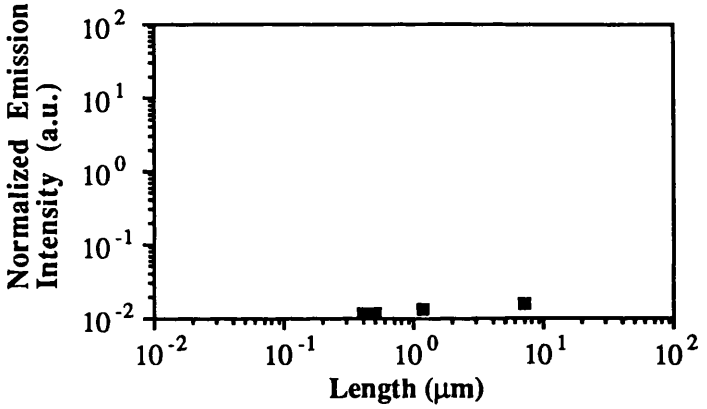


Figure (7.16bii): 6 nm well of Dashes of Dash Sample 4

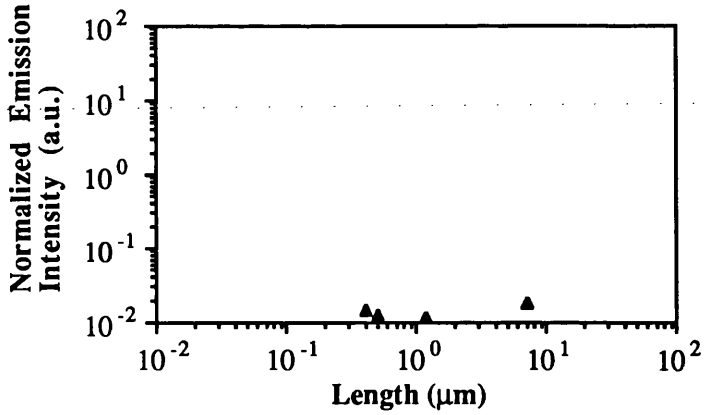


Figure (7.16biii): 8 nm well of dashes of Dash Sample

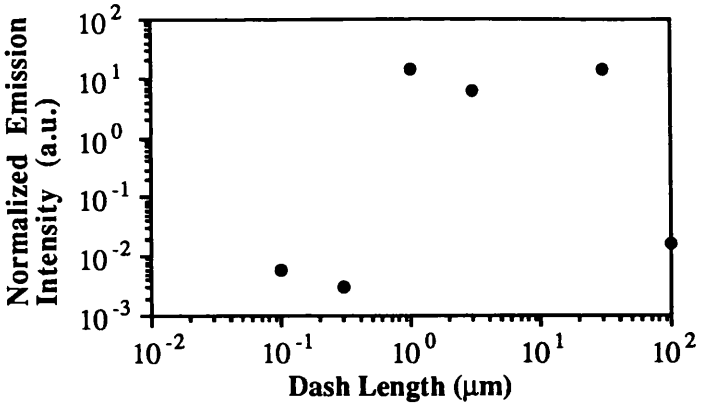


Figure (7.17ai): 4 nm well of 0.1 μm dashes of Dash 5

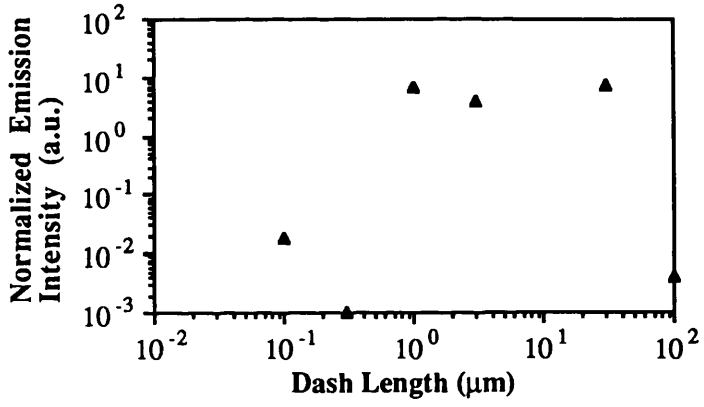


Figure (7.17aii): 6 nm well of 0.1 μm dashes of Dash 5

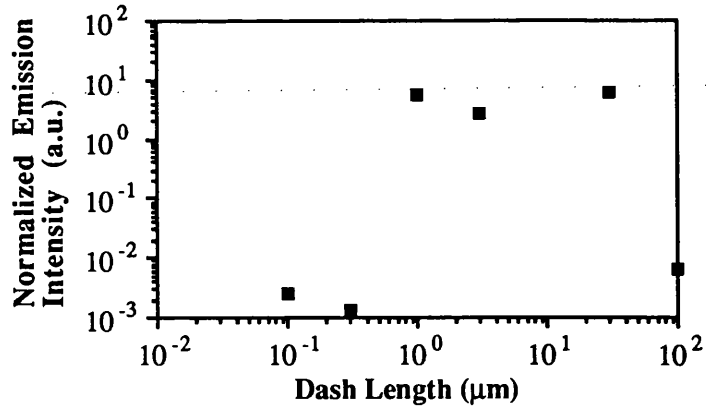


Figure (7.17aiii): 8 nm well of 0.1 μm dashes of Dash 5

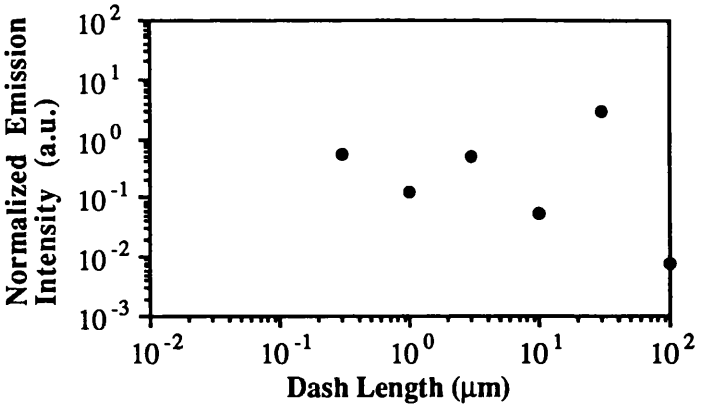


Figure (7.17bi): 4 nm well of 0.3 μm wide dashes of Dash 5

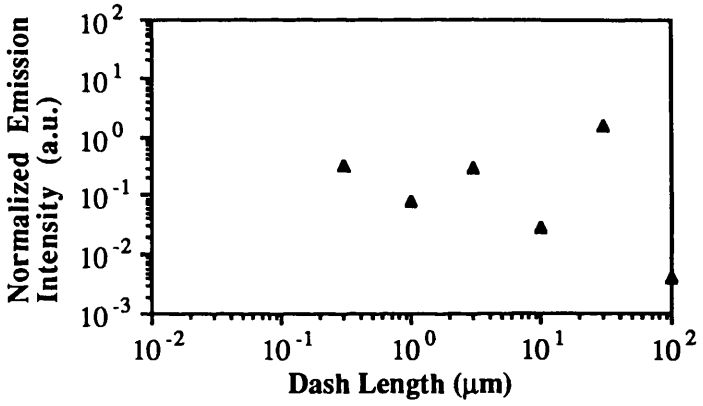


Figure (7.17bii): 6 nm well of 0.3 μm wide dashes - Dash 5

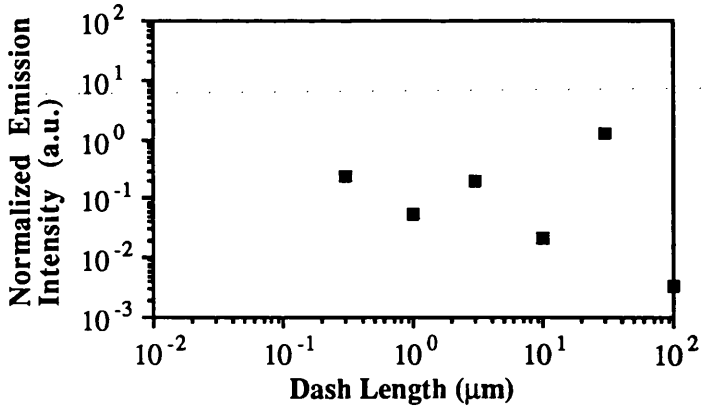


Figure (7.17biii): 8 nm well of 0.3 μm wide dashes Dash 5

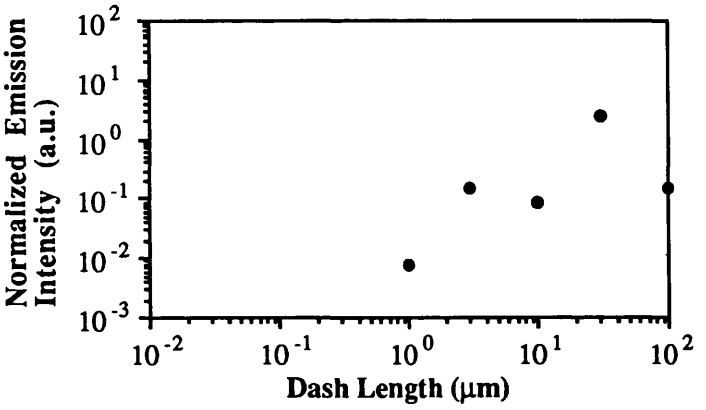


Figure (7.17ci): 4 nm well of 1 μm dashes of Dash 5

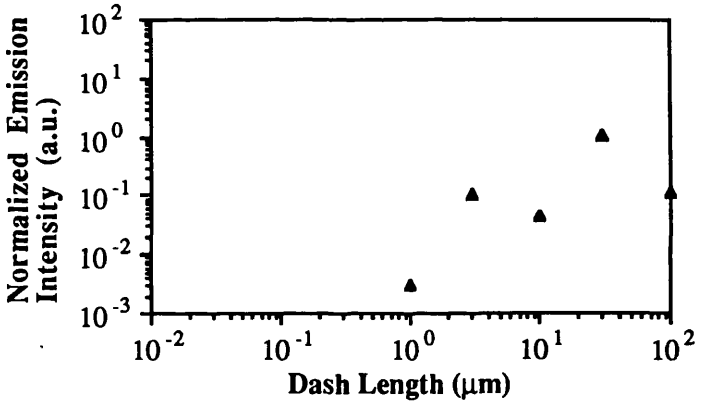


Figure (7.17cii): 6 nm well of 1 μm dashes of Dash 5

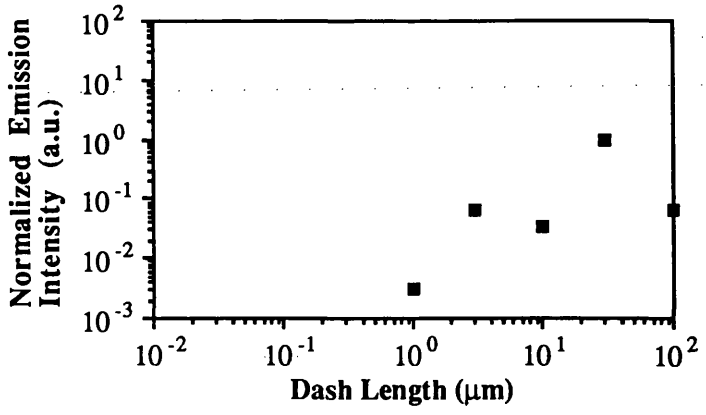


Figure (7.17ciii): 8 nm well of 1 μm dashes of Dash 5

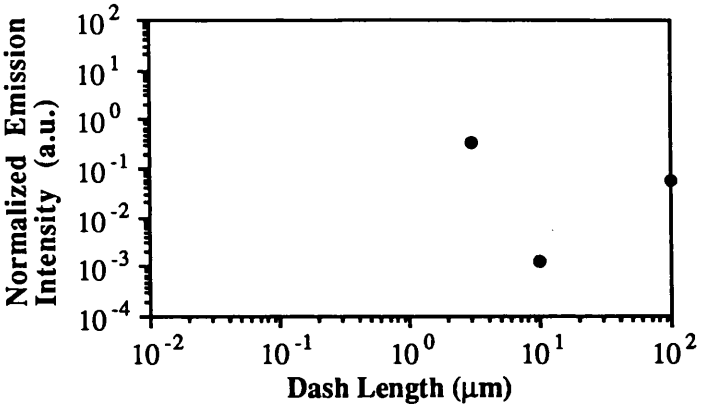


Figure (7.17di): 4 nm well of 3 μm dashes of Dash 5

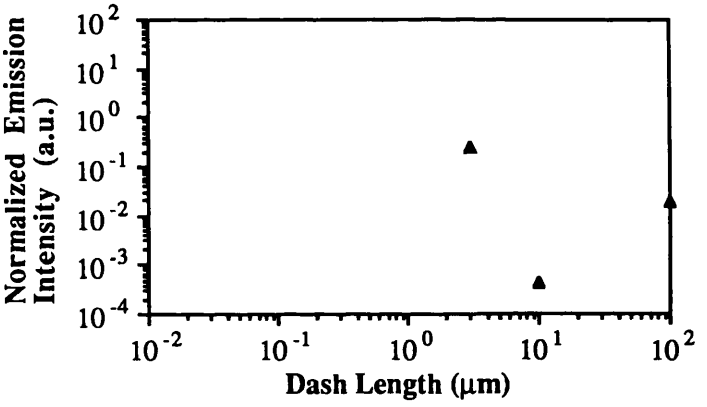


Figure (7.17dii): 6 nm well of 3 μm dashes of Dash 5

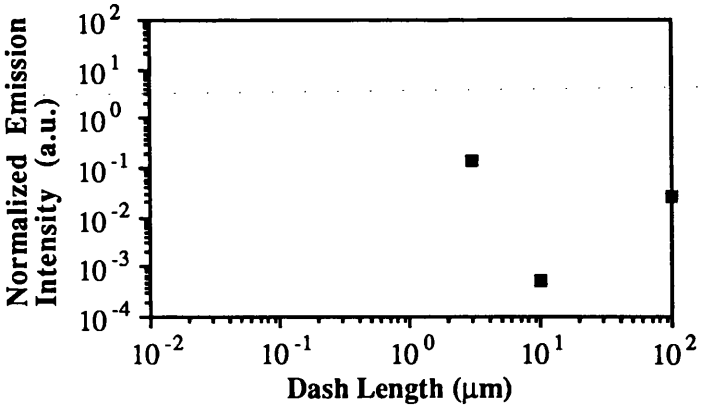


Figure (7.17diii): 8 nm well of 3 μm dashes of Dash 5

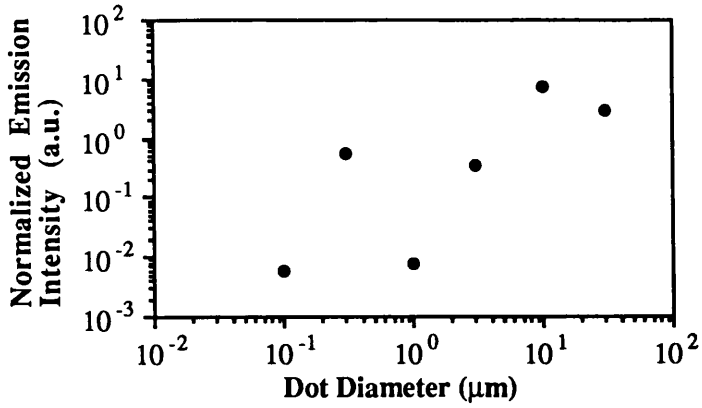


Figure (7.17ei): 4 nm well of dots of Dash 5

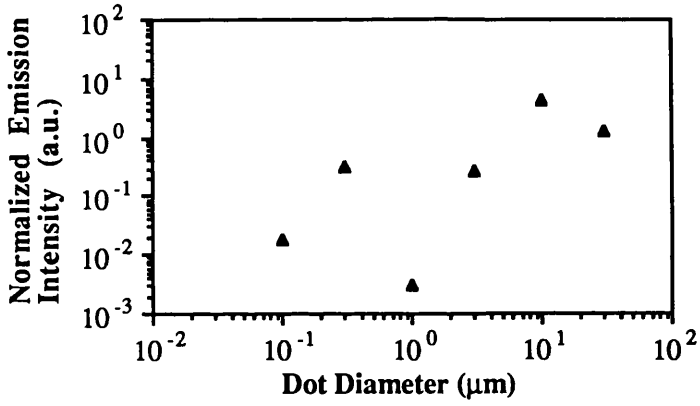


Figure (7.17eii):6 nm well of dots of Dash 5

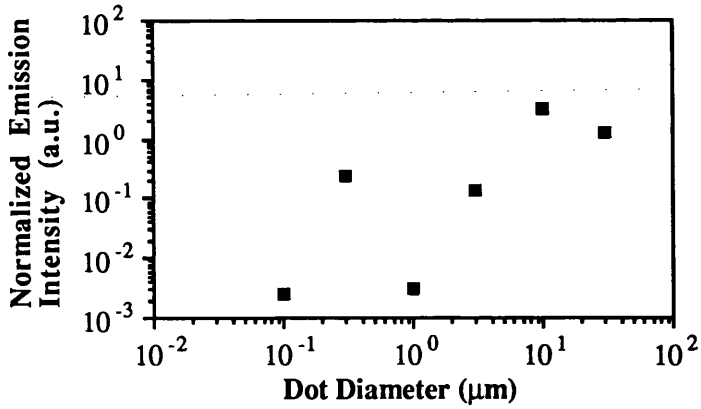


Figure (7.17eiii): 8 nm well of dots of Dash 5

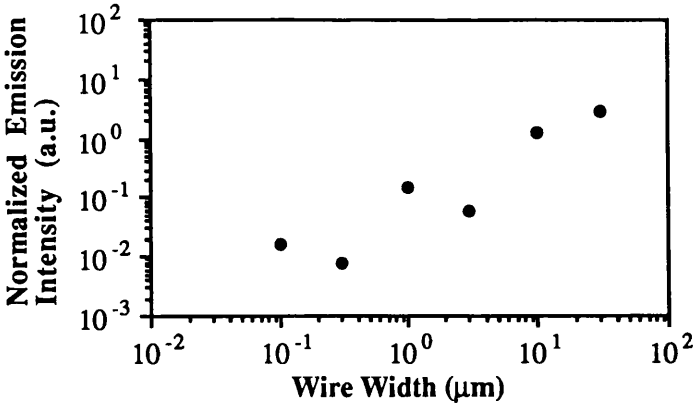


Figure (7.17fi): 4 nm well of wires of Dash 5

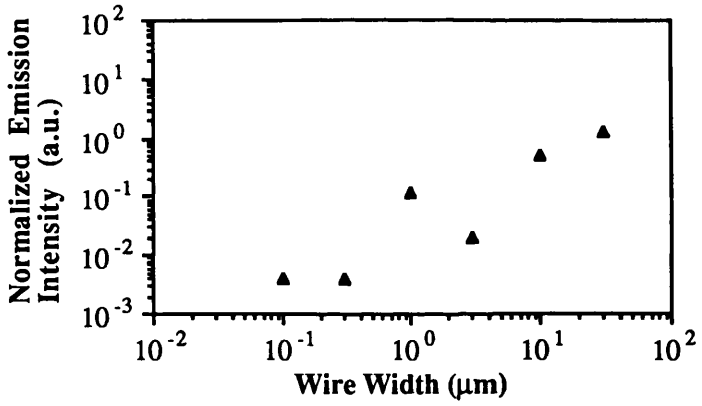


Figure (7.17fii): 6 nm well of wires of Dash 5

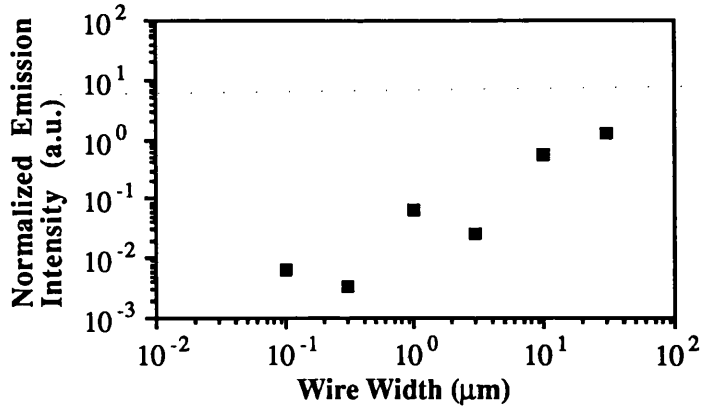


Figure (7.17fiii): 8 nm well of wires of Dash 5

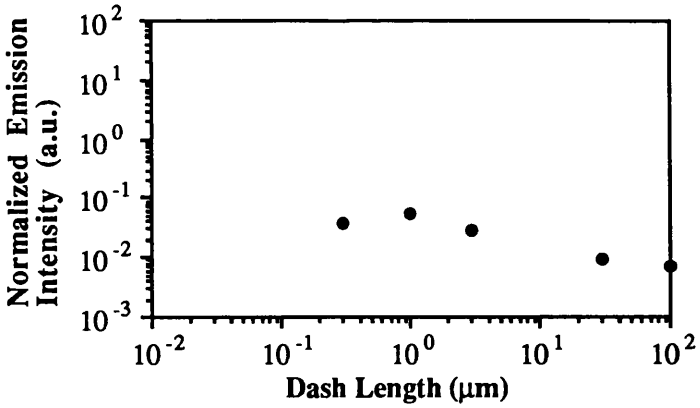


Figure (7.18ai): 4 nm well of 0.1 μm wide dashes of Dash 6

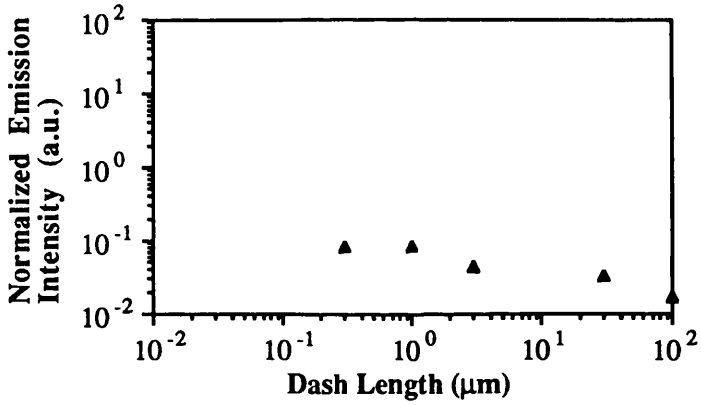


Figure (7.18aii): 6 nm well of 0.1 μm wide dashes Dash 6

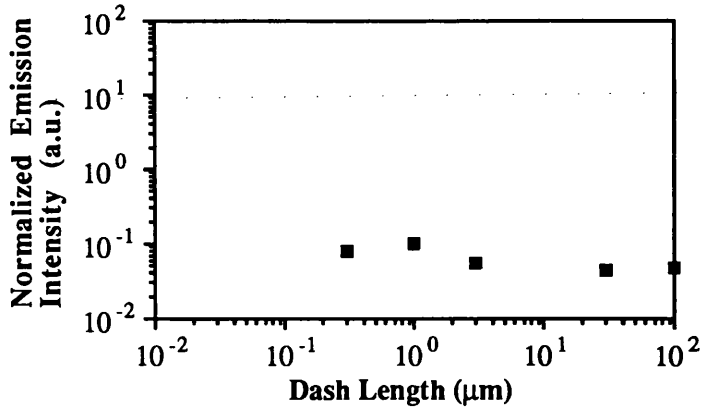


Figure (7.18aiii): 8 nm well of 0.1 μm wide dashes Dash 6

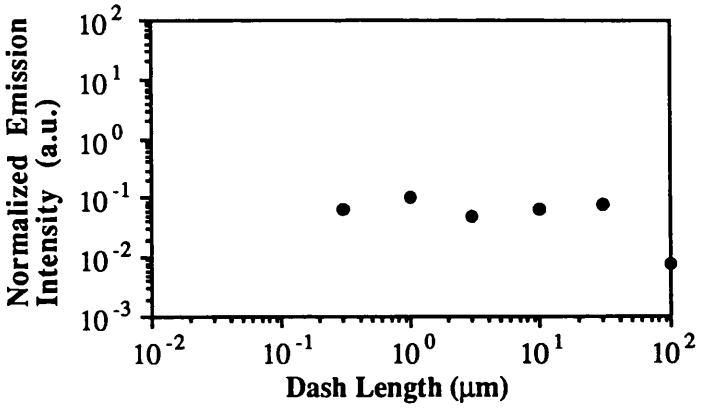


Figure (7.18bi): 4 nm well of 0.3 μm wide dashes of Dash 6

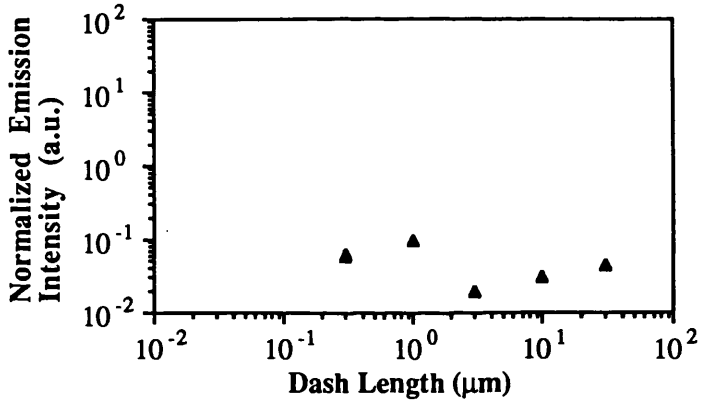


Figure (7.18bii): 6 nm well of 0.3 μm wide dashes Dash 6

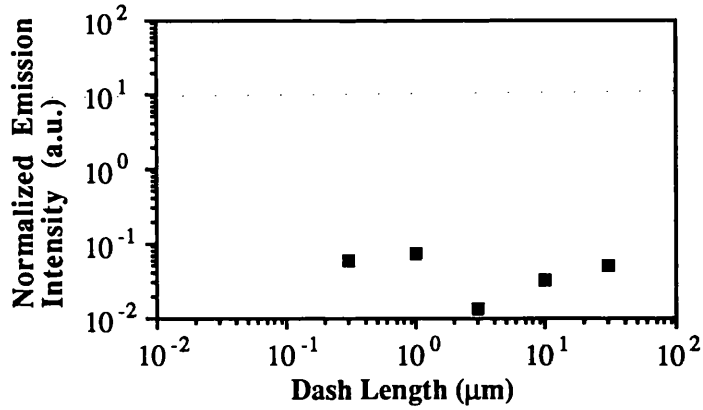


Figure (7.18biii): 8 nm well of 0.3 μm wide dashes Dash 6

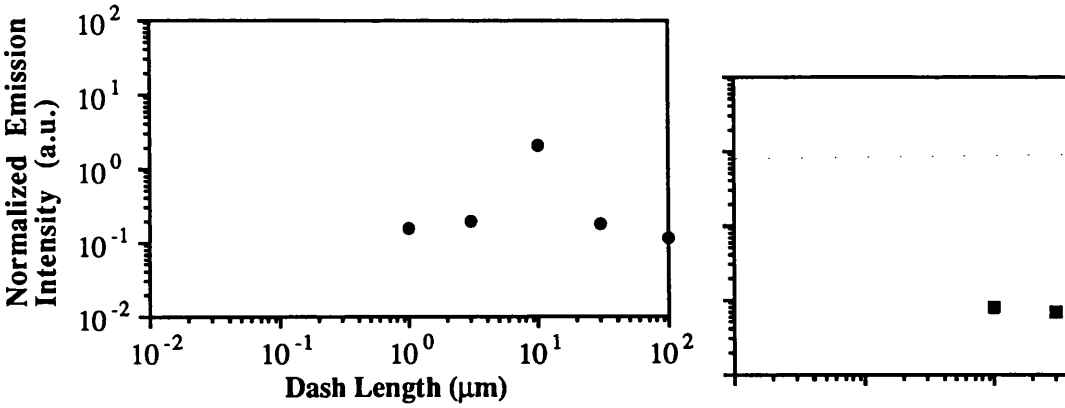


Figure (7.18ci): 4 nm well of 1 μm wide dashes of Dash 6

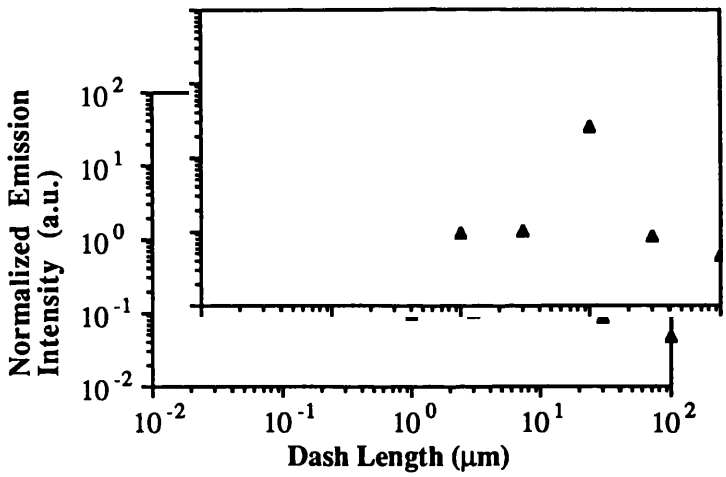


Figure (7.18cii): 6 nm well of 1 μm wide dashes of Dash 6

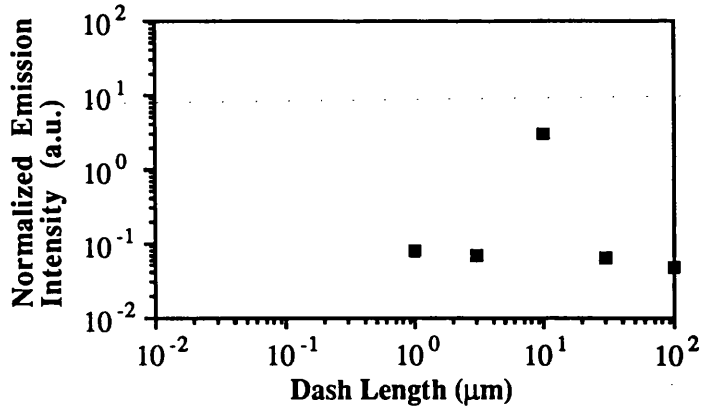


Figure (7.18ciii): 8 nm well of 1 μm dashes of Dash 6

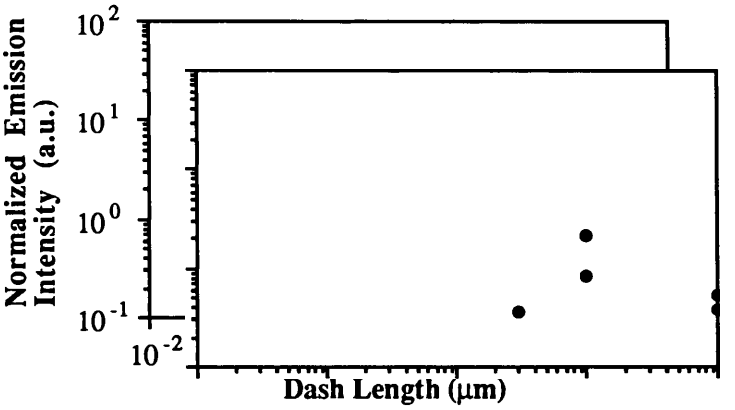


Figure (7.18di): 4 nm well of 10 μm dashes of Dash 6

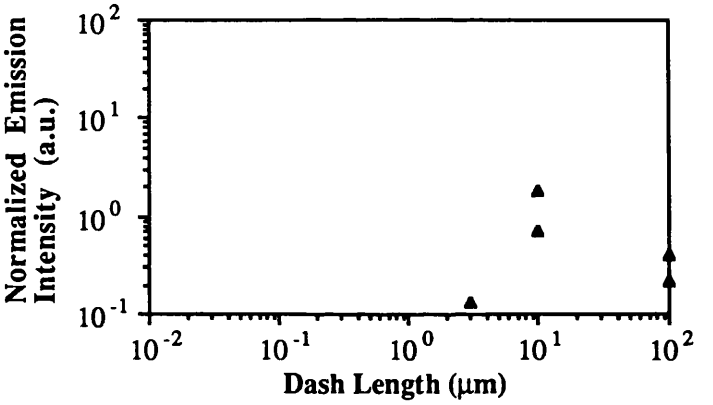


Figure (7.18dii): 6 nm well of 10 μm wide dashes of Dash 6

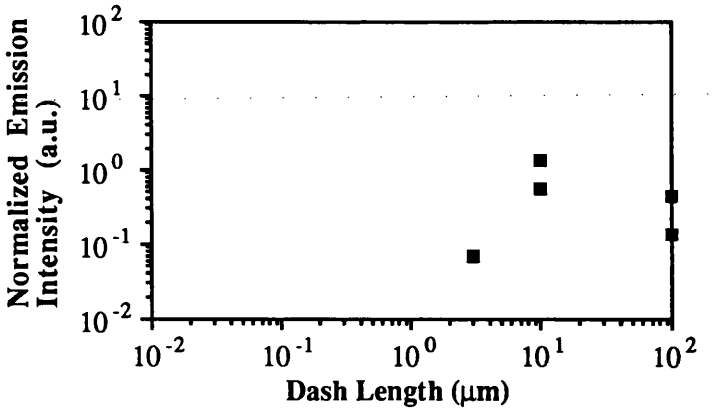


Figure (7.18diii): 8 nm well of 10 μm wide dashes Dash 6

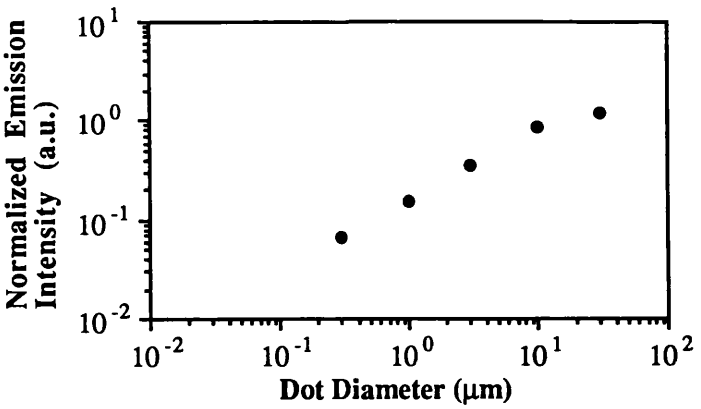


Figure (7.18ei): 4 nm well of dots of Dash Sample 6

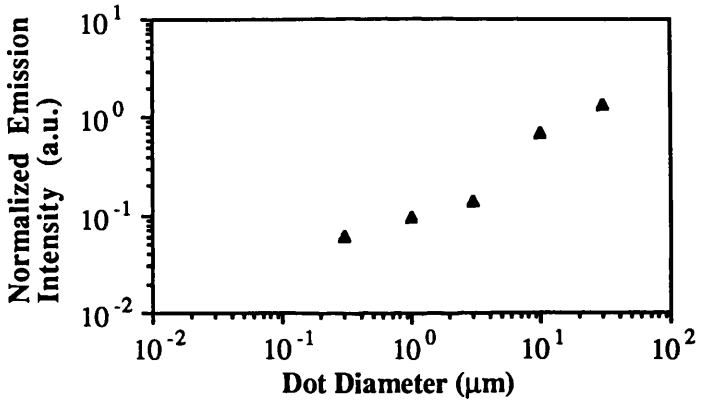


Figure (7.18eii): 6 nm well of dots of Dash 6

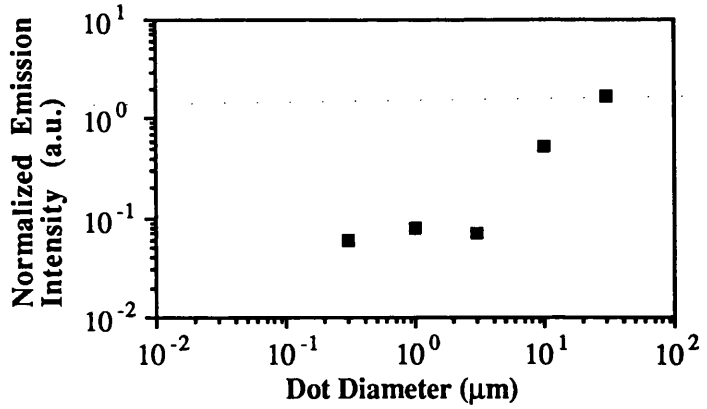


Figure (7.18eiii): 8 nm well of dots of Dash Sample 6

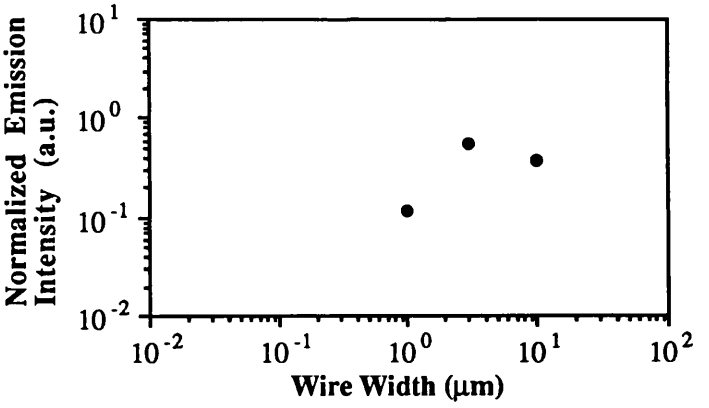


Figure (7.18ei): 4 nm well of wires of Dash Sample 6

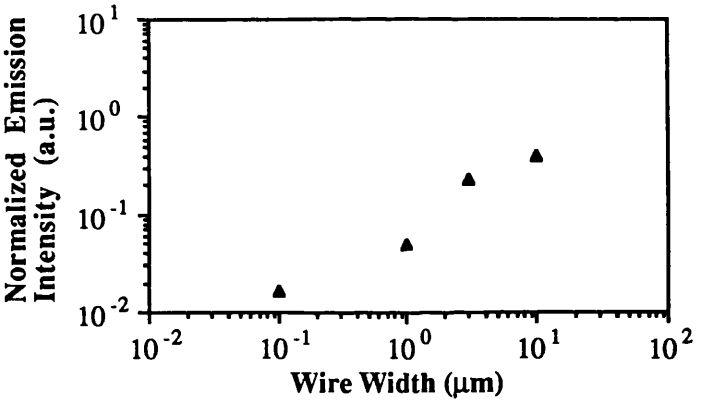


Figure (7.18eii): 6 nm well of wires of Dash Sample 6

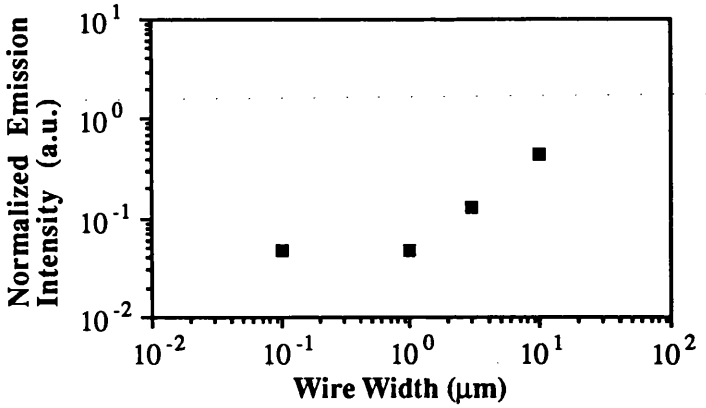


Figure (7.18eiii): 8 nm well of wires of Dash Sample 6

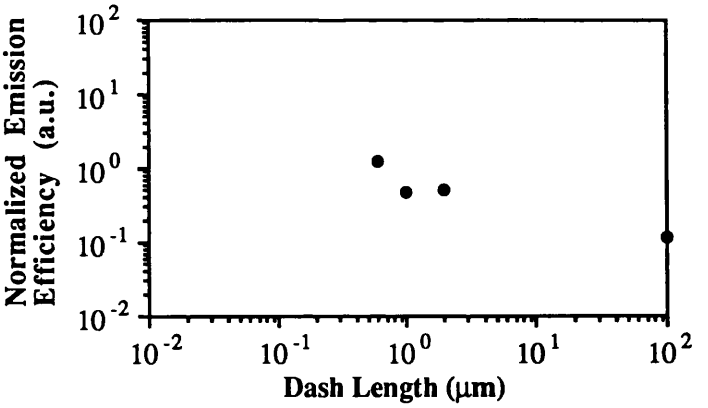


Figure (7.19i): 4 nm well of Dash Sample 7

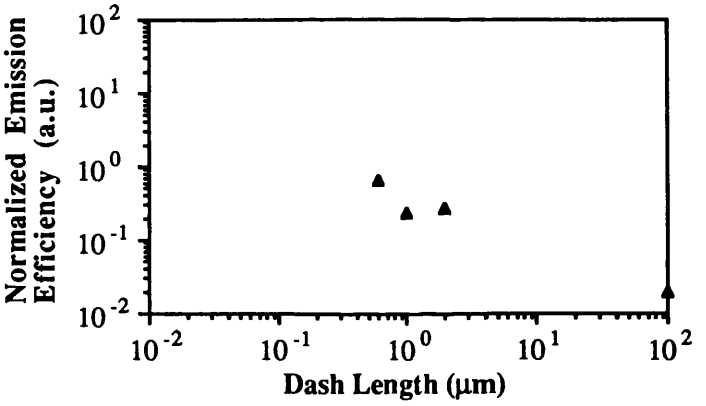


Figure (7.19ii): 6 nm well of Dash Sample 7

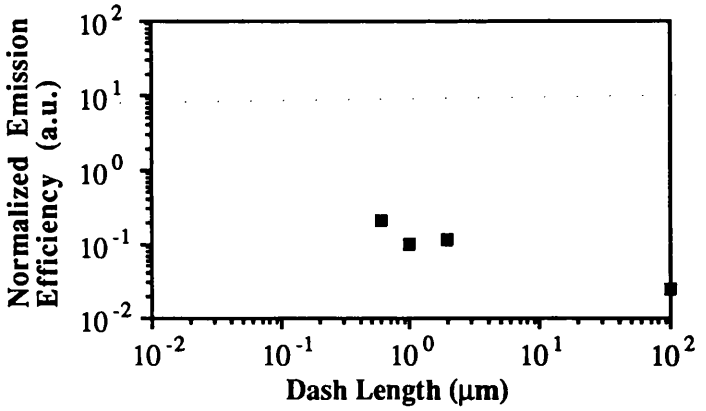


Figure (7.19iii): 8 nm well of Dash Sample 7

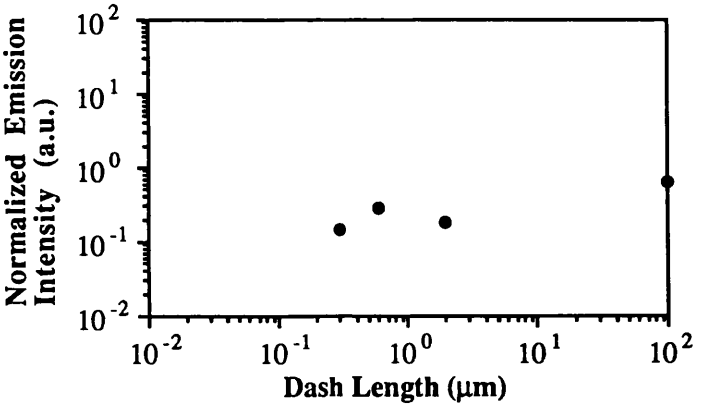


Figure (7.20i): 4 nm well of Dash Sample 8

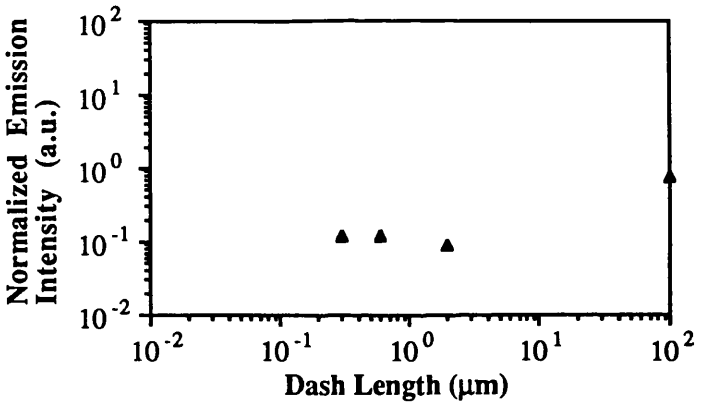


Figure (7.20ii): 6 nm well of Dash Sample 8

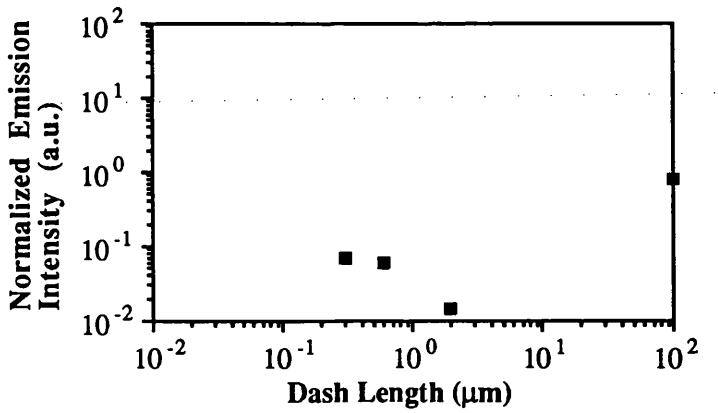


Figure (7.20iii): 8 nm well of Dash Sample 8

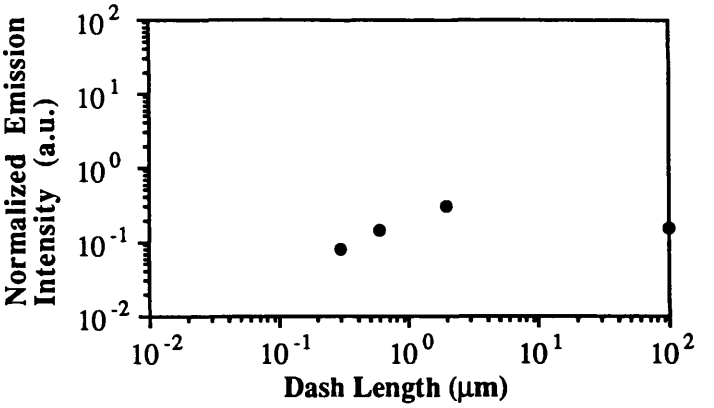


Figure (7.21i): 4 nm well of Dash Sample 9

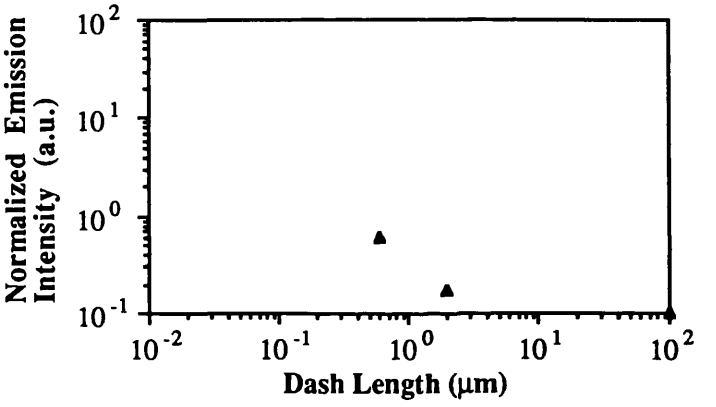


Figure (7.21ii): 6 nm well of Dash Sample 9

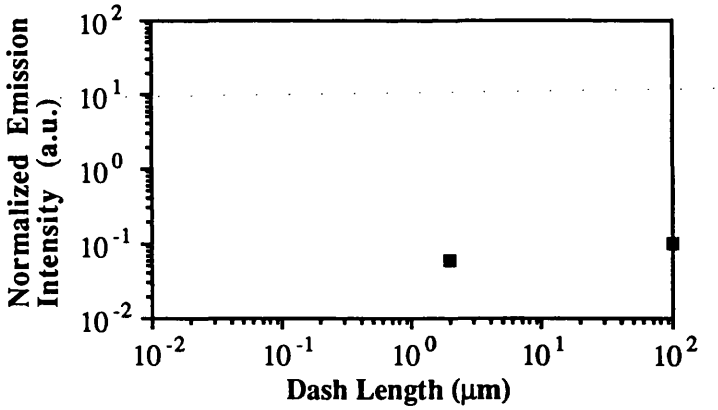


Figure (7.21iii): 8 nm well of Dash Sample 9

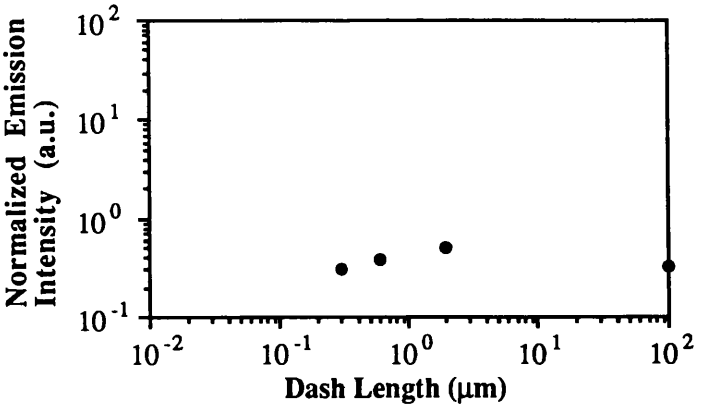


Figure (7.22i): 4 nm well of Dash Sample 10

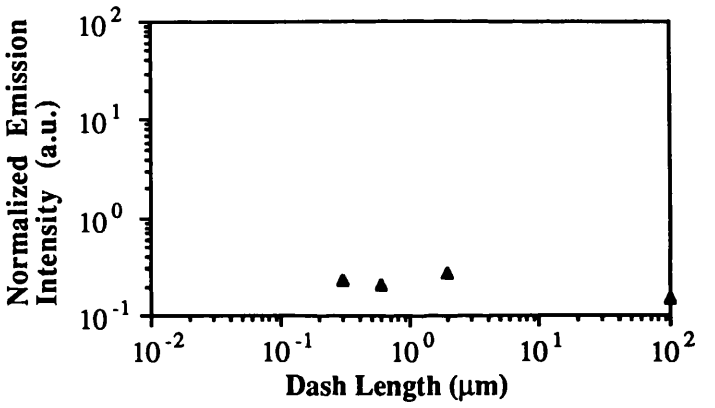


Figure (7.22ii): 6 nm well of Dash Sample 10

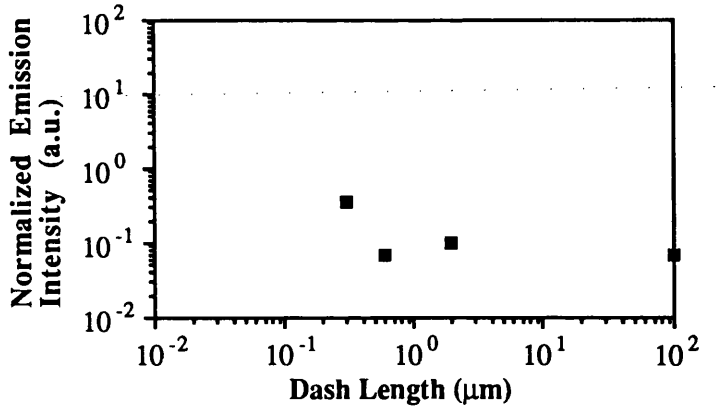


Figure (7.22iii): 8 nm well of Dash Sample 10

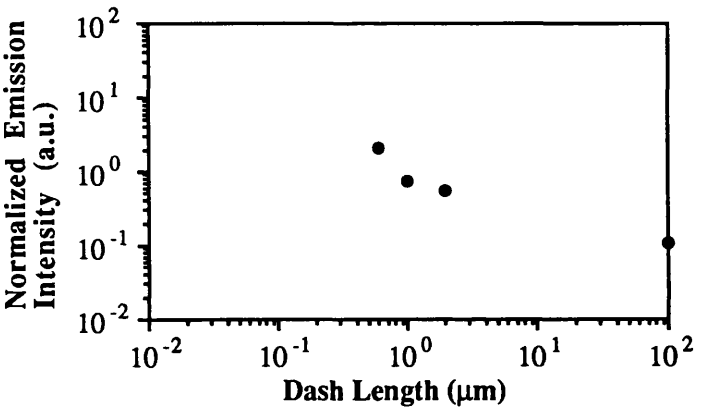


Figure (7.23i): 4 nm well of Dash Sample 11

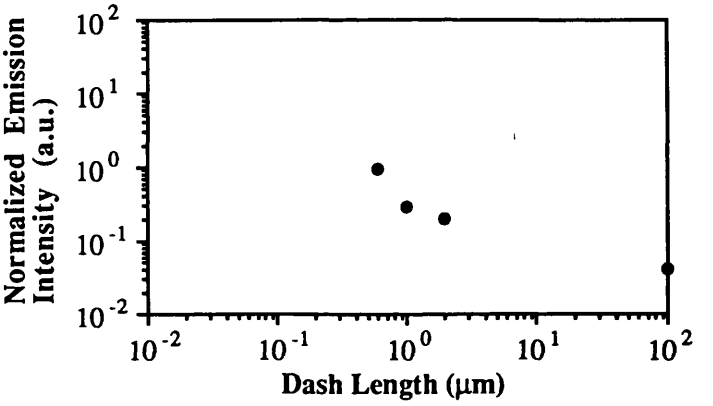


Figure (7.23ii): 6 nm well of Dash Sample 11

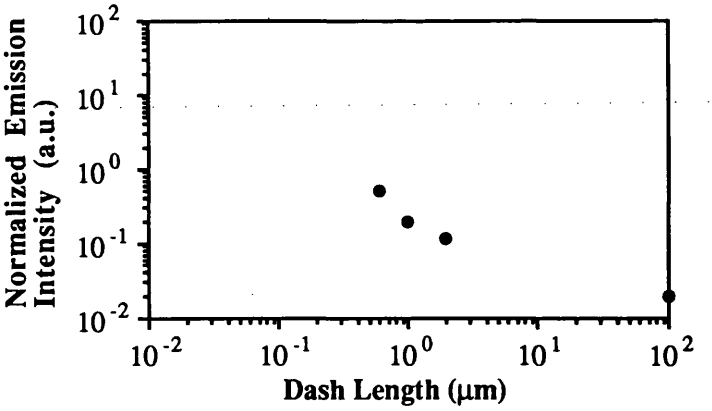


Figure (7.23iii): 8 nm well of Dash Sample 11

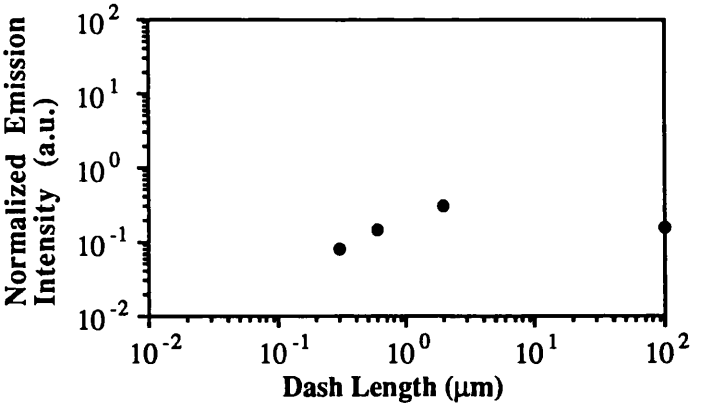


Figure (7.24i): 4 nm well of Dash Sample 12

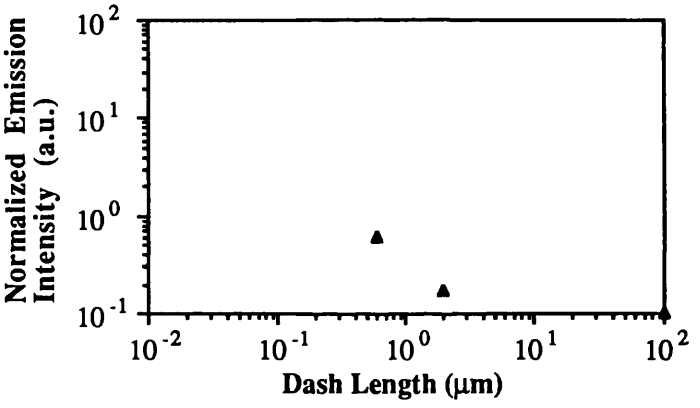


Figure (7.24ii): 6 nm well of Dash Sample 12

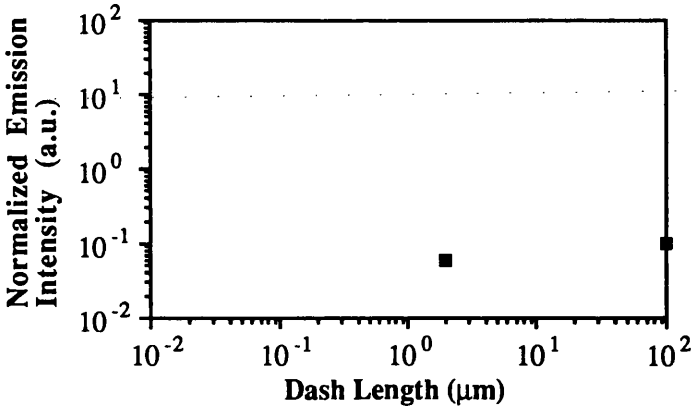


Figure (7.24iii): 8 nm well of Dash Sample 12

### 7.7.4 Discussion of Structure Spectra

Photoluminescence spectra typical of the structures characterized are given in Figures (7.25-7.30). The spectra illustrate the difference in behaviour between the A1995A material, grown by MOCVD, used for the structures in Figure (7.27), and the A315 and B33 material, grown by MBE, used for the structures in the spectra in Figures (7.25, 7.26) and (7.28-7.30) respectively. The MBE material structures exhibit a sharp reduction in intensity, whereas the structures fabricated on MOCVD material maintain their luminescence to the smallest structures.

The maintenance of the luminescence to small structures in the MOCVD material may perhaps be due to the luminescence arising from bound-exciton transitions. This is examined further in the temperature dependence discussion in Section (7.8).

The prominent peak dominating the emission of the smallest structures in Figures (7.25) and (7.26) is due to the excitation of the superlattice emission of the etched-back material.

### 7.7.5 Quantum Well Transition Energy Measurement

As the structure size is reduced, and the quantum confinement régime is approached, the ground state energies of the electrons and holes will increase, resulting in a blue-shift of the quantum well emission.

For quantum effects to be observable, the structure size must be comparable with the 2-D exciton diameter, and thus must be of the order of 30 nm. The fabrication procedure used could not approach this size limit, being limited to 60 nm at best, and so one would not expect to observe a blue-shift of the quantum well emission in the structures fabricated.

There has been no discussion of the effect of the postulation of a 'dead layer' surrounding the structures on the quantum confinement in these structures. If the carrier wavefunctions vanish at the inner edge of the 'dead layer', quasi-quantized states would be formed at structure sizes much greater than the maximum required for structures where the wavefunctions vanish at the outer surface. Thus, with a 'dead layer' of 20 nm, the exciton centre-of mass régime could be approached with a structure size of 70 nm.

The free-exciton quantum well peak positions were recorded as a function of structure size, and shown in Figures (7.31) to (7.34). A blue-shift may be observed, both as a function of dot size, and of wire width, which is much greater than the well-width variation across the wafer discussed in Chapter 6. The blue-shift is less likely to be the result of a confinement effect than as a result of the effects of strain introduced during the fabrication process; this is discussed at greater length in Chapter 8. As the structure size is reduced, the emission becomes much weaker, and thus the error in fitting the peak position is increased.

For a more accurate measurement of the blue-shift of the structures, a more sensitive technique such as photoluminescence excitation must be employed, together with measures to reduce the strain introduced into the structures by the etch process.

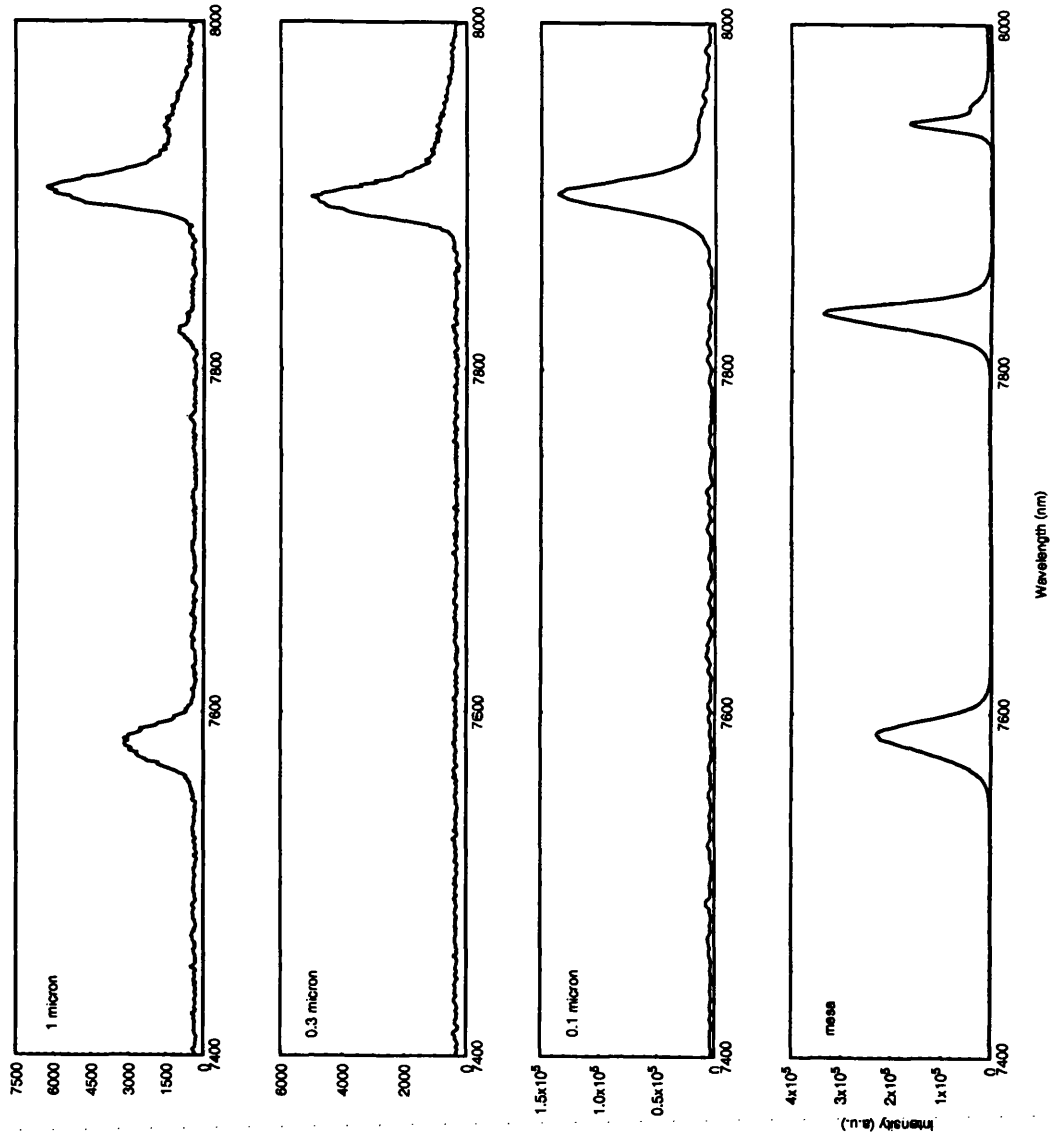


Figure (7.25): Luminescence Spectrum of Dot Sample 1

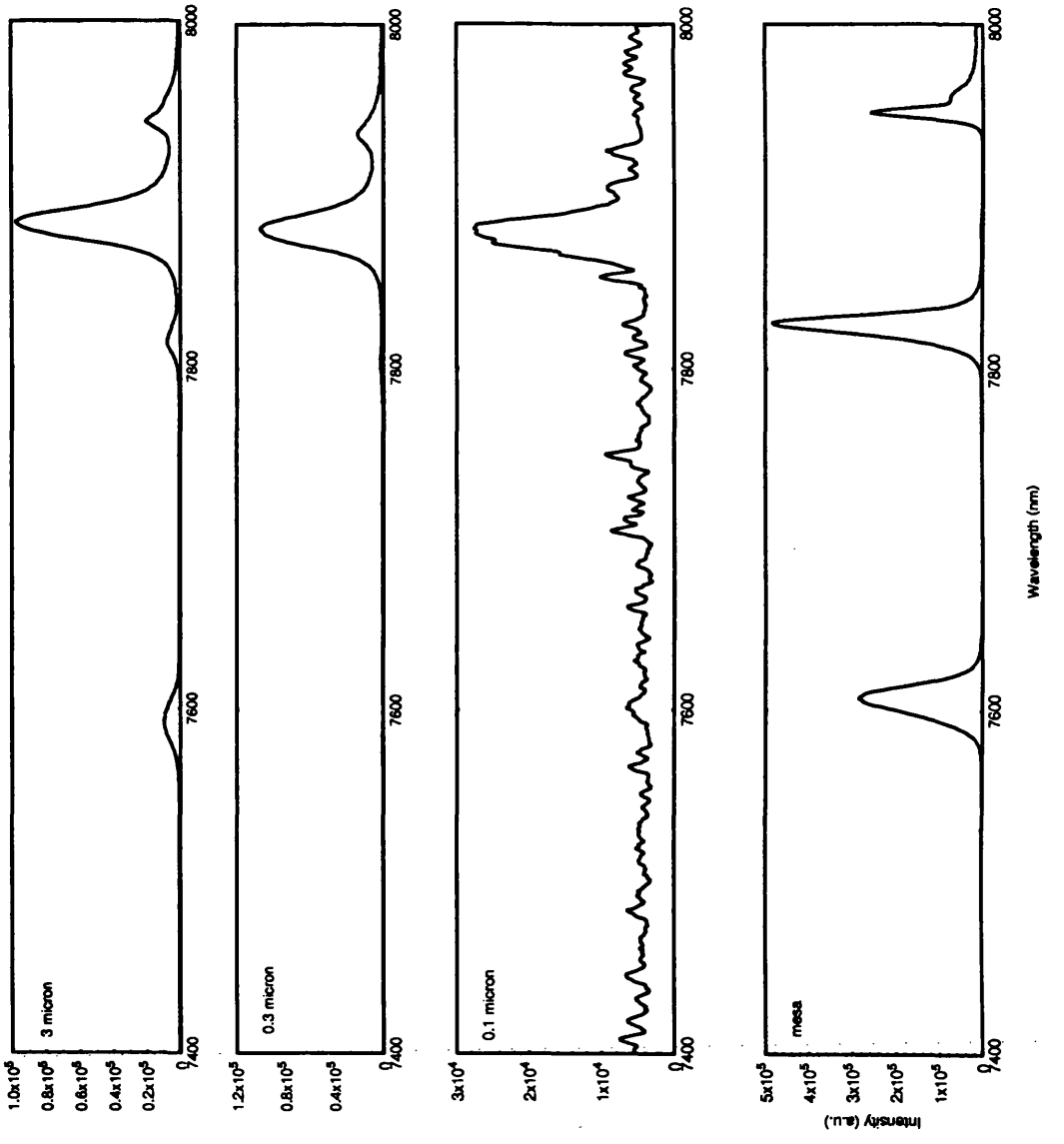


Figure (7.26): Luminescence Spectrum of Wire Sample 1

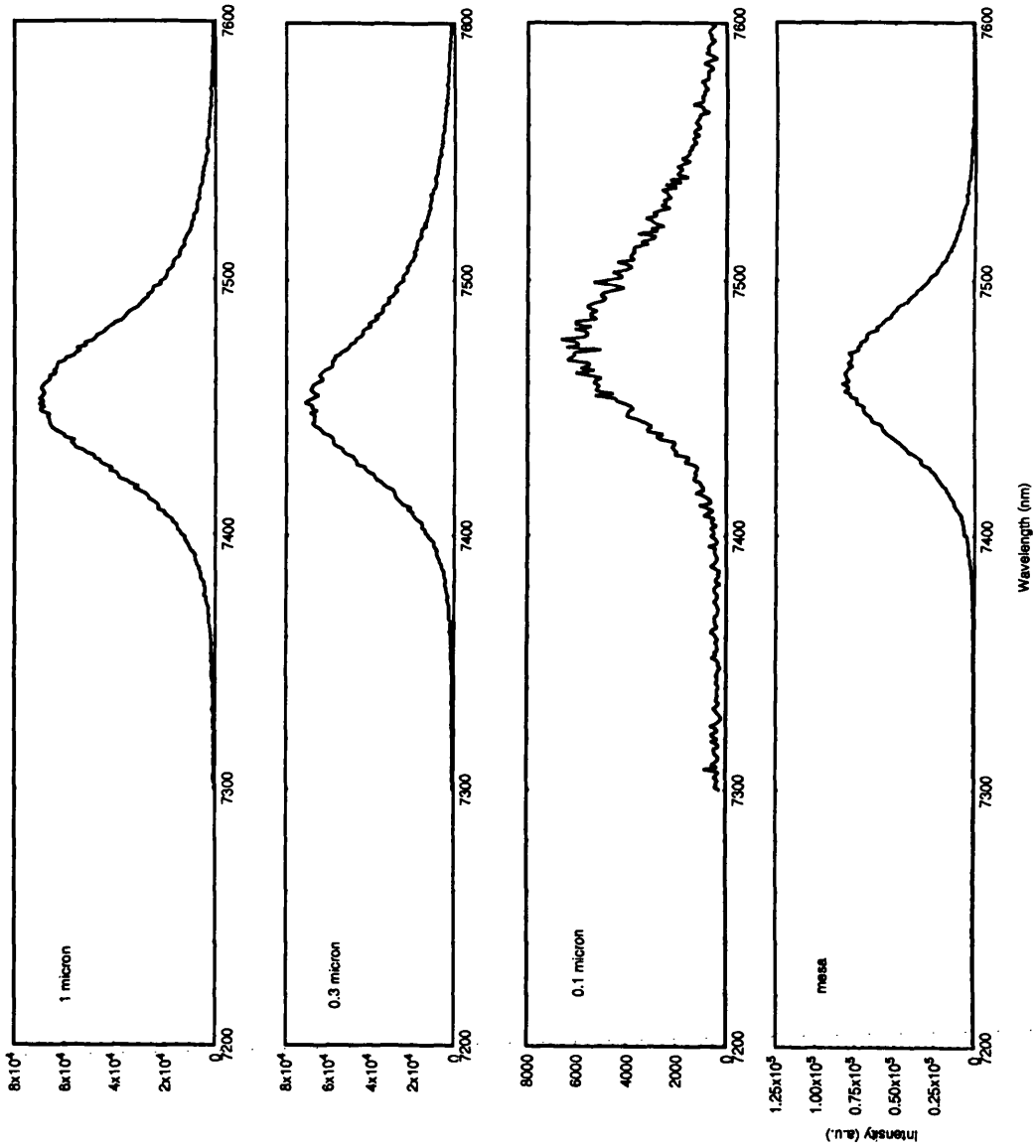


Figure (7.27): Luminescence Spectrum of Wire Sample 4

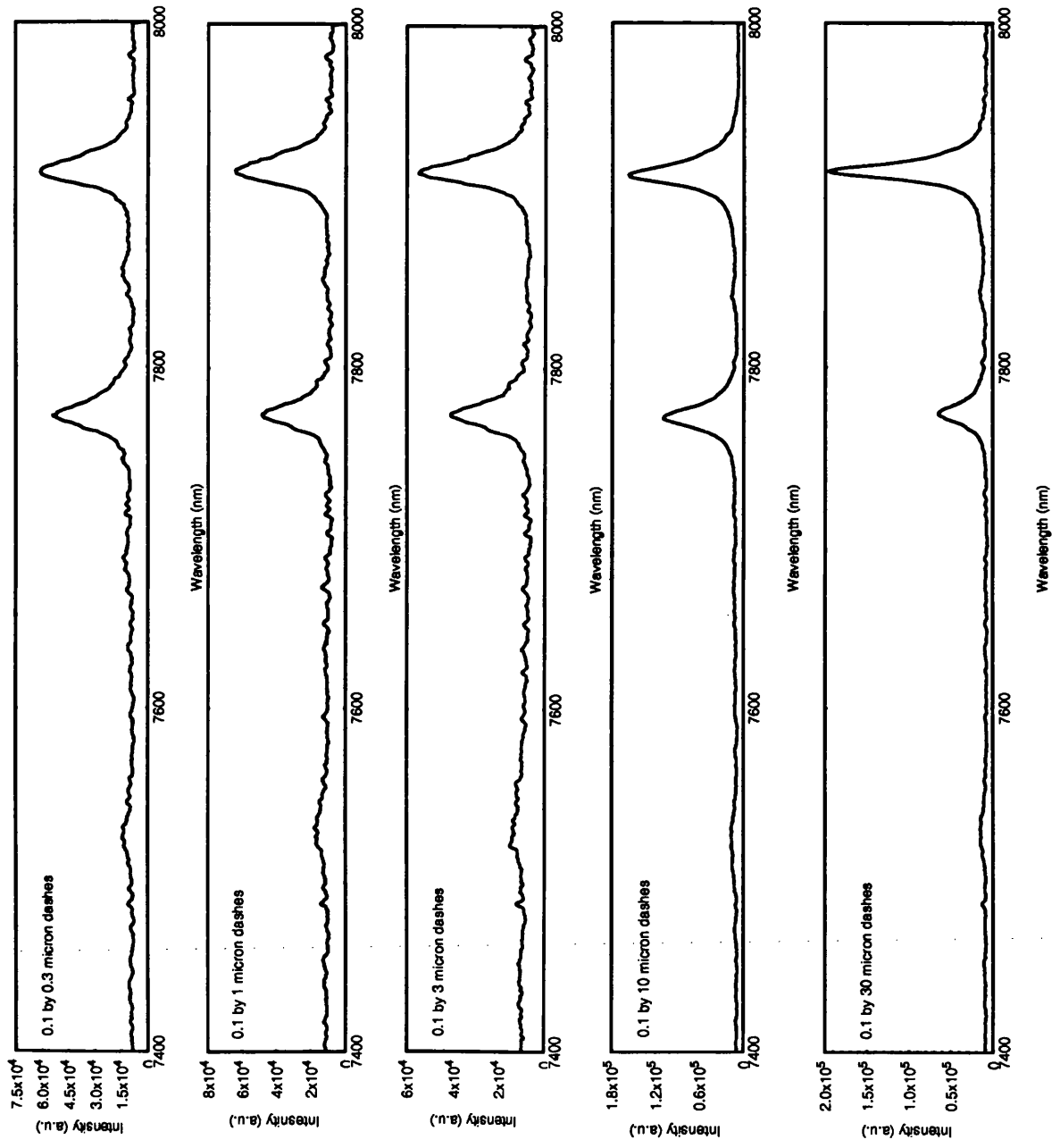


Figure (7.28): Luminescence Spectrum of 0.1 dashes of Dash Sample 6

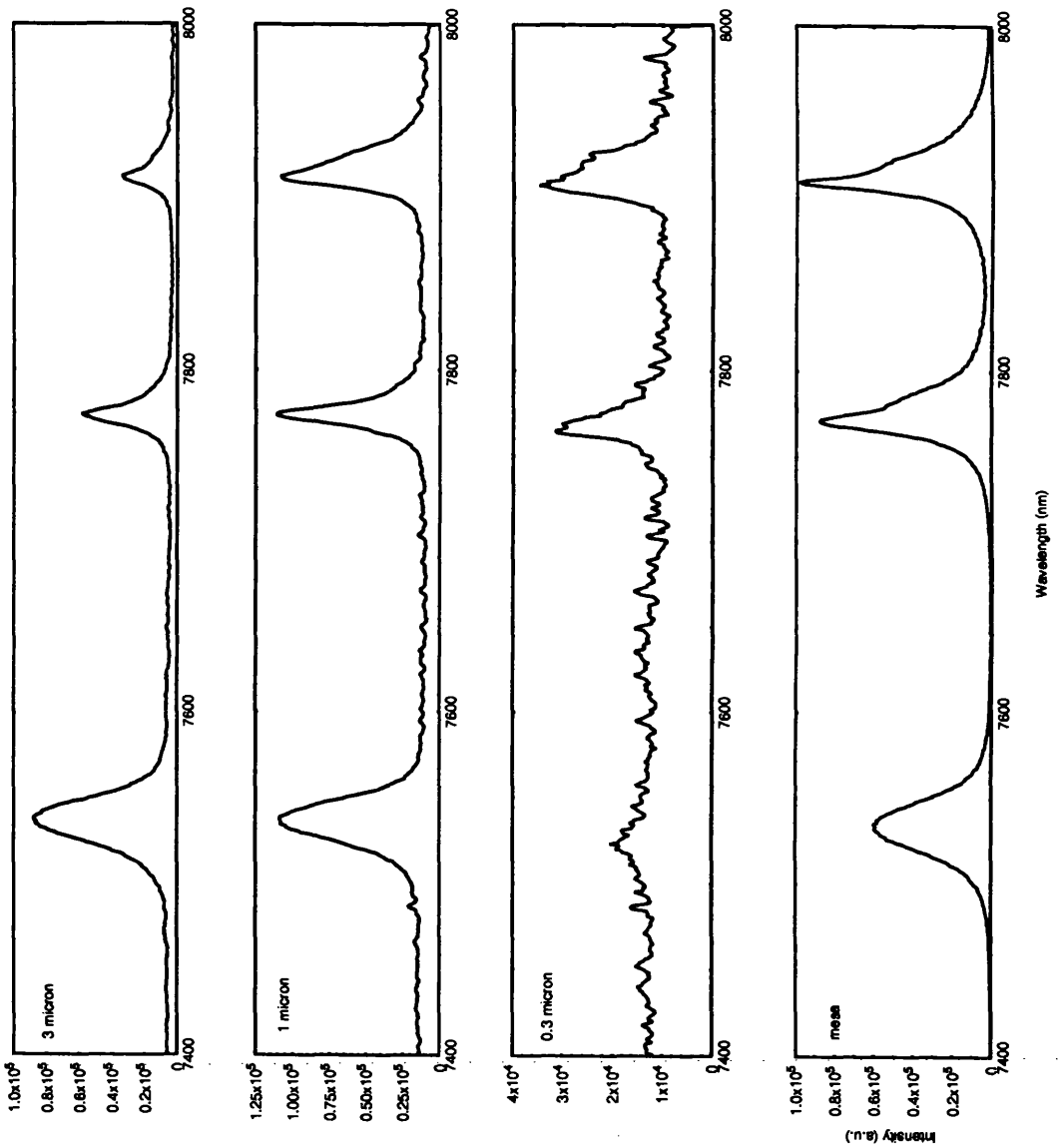


Figure (7.29): Luminescence Spectrum of dots of Dash Sample 6

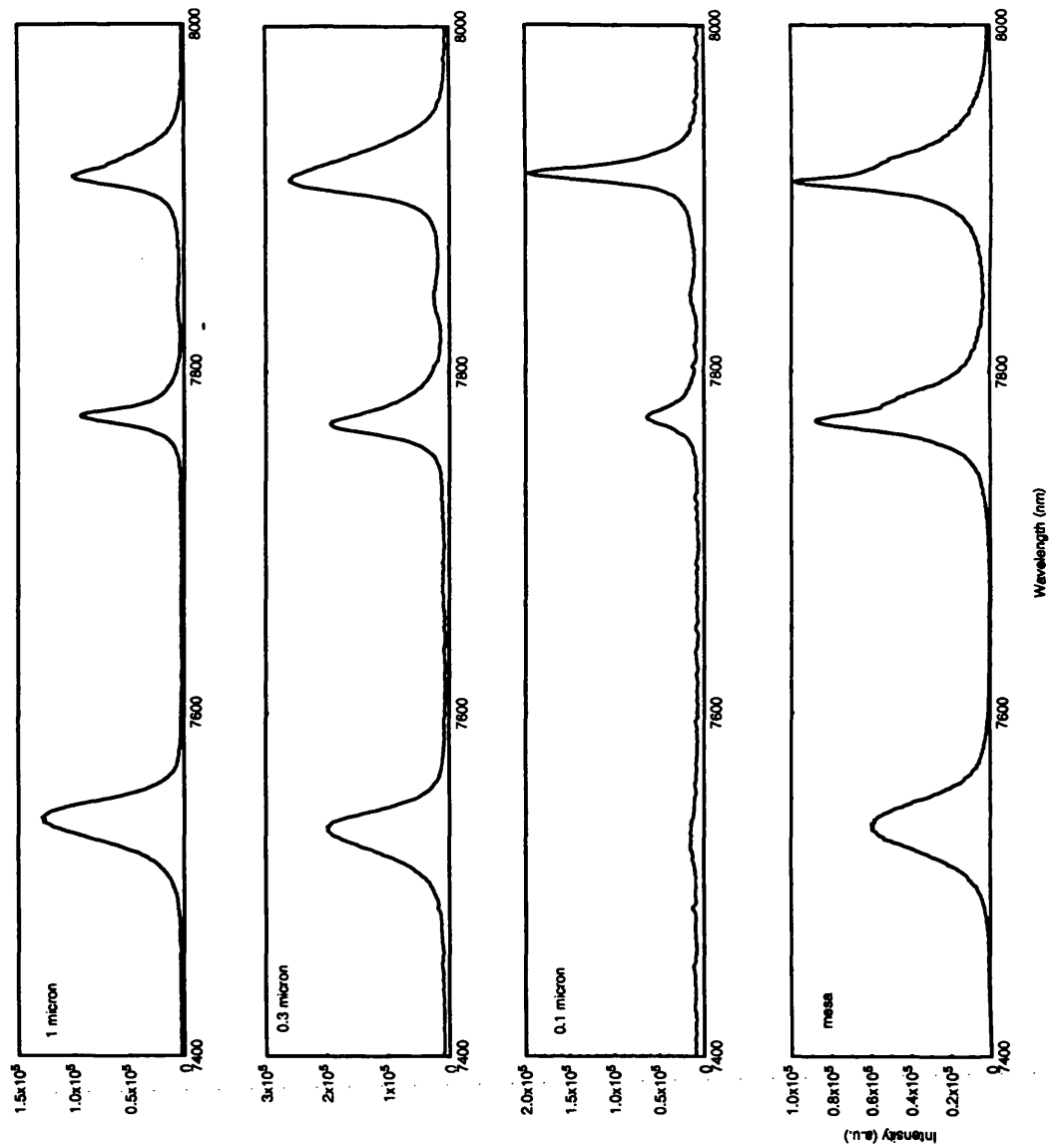


Figure (7.30): Luminescence Spectrum of wires of Dash Sample 6

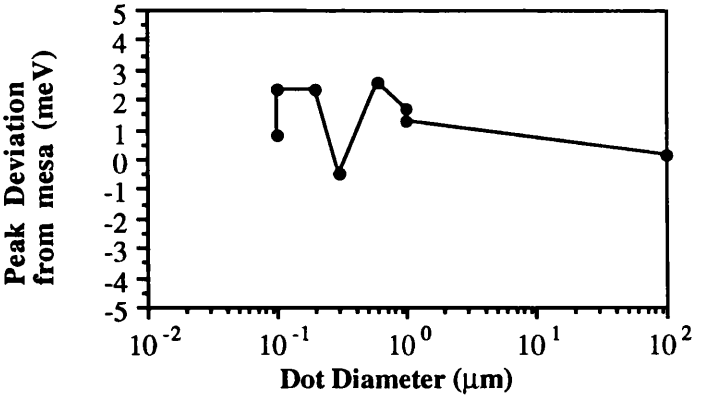


Figure (7.31i): Peak Position Dependence of 4 nm well of Dot Sample 1

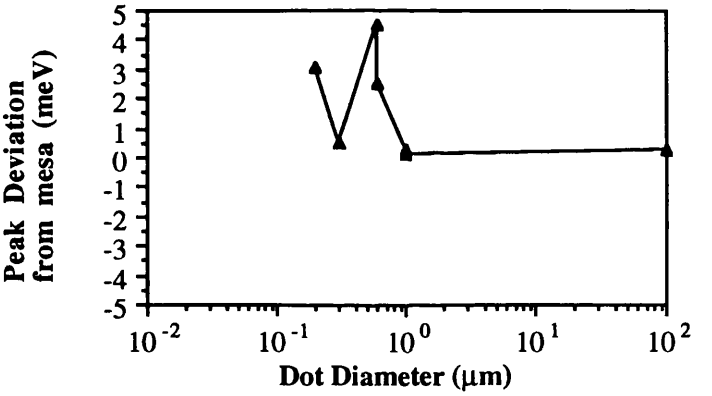


Figure (7.31ii): Peak Position Dependence of 6 nm well of Dot Sample 1

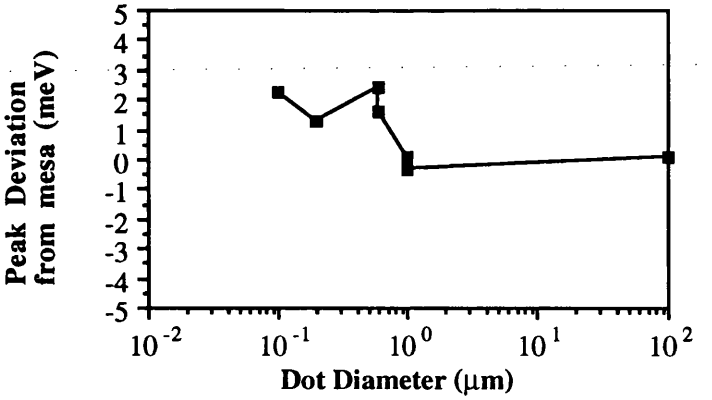


Figure (7.31iii): Peak Position Dependence of 8 nm well of Dot Sample 1

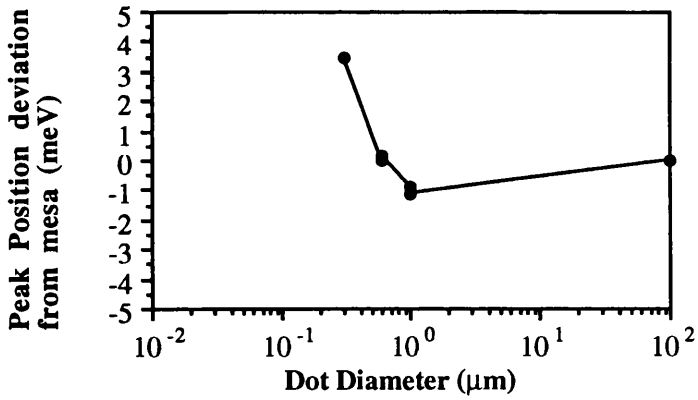


Figure (7.32i): Peak Position Dependence of 4 nm well of Dot Sample 2

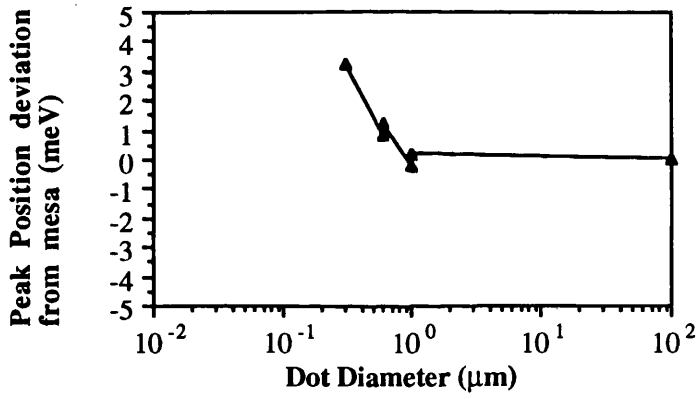


Figure (7.32ii): Peak Position Dependence of 6 nm well of Dot Sample 2

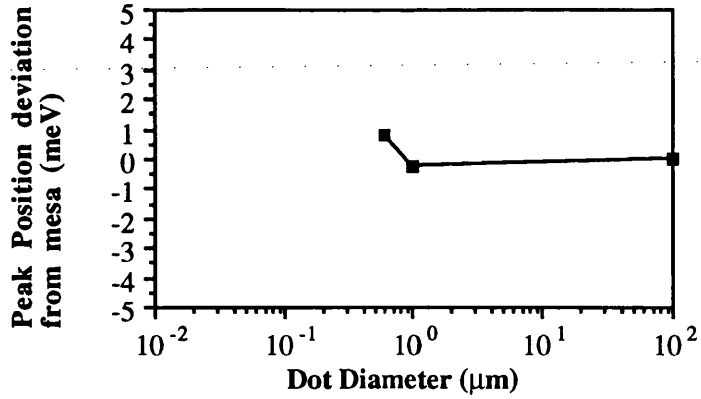


Figure (7.32iii): Peak Position Dependence of 8 nm well of Dot Sample 2

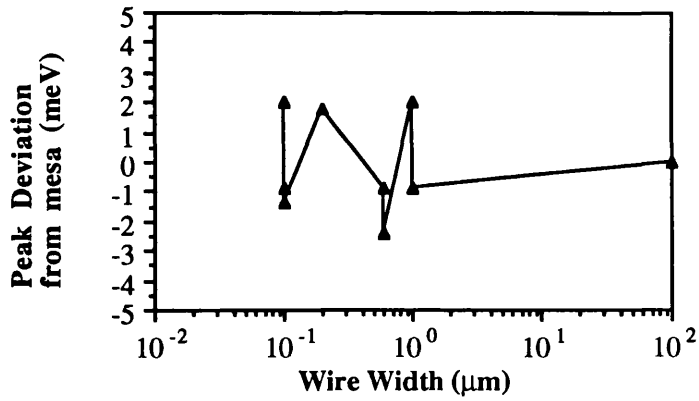


Figure (7.33i): Peak Position Dependence of 6 nm well of Wire Sample 2

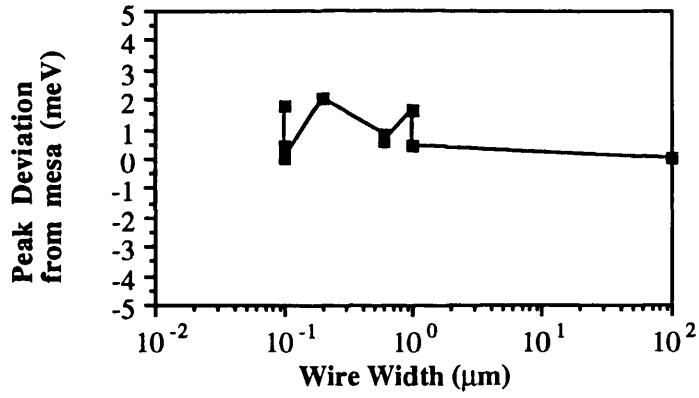


Figure (7.33ii): Peak Position Dependence of 8 nm well of Wire Sample 2

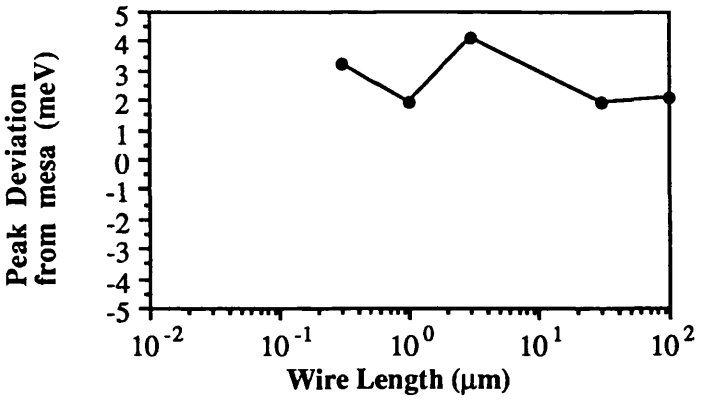


Figure (7.34i): 4 nm well

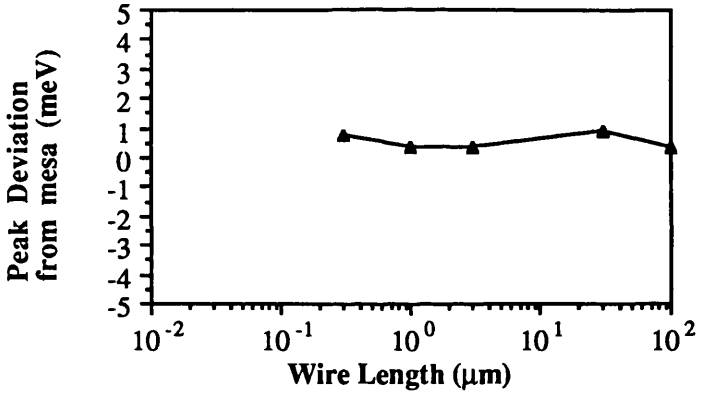


Figure (7.34ii): 6 nm well

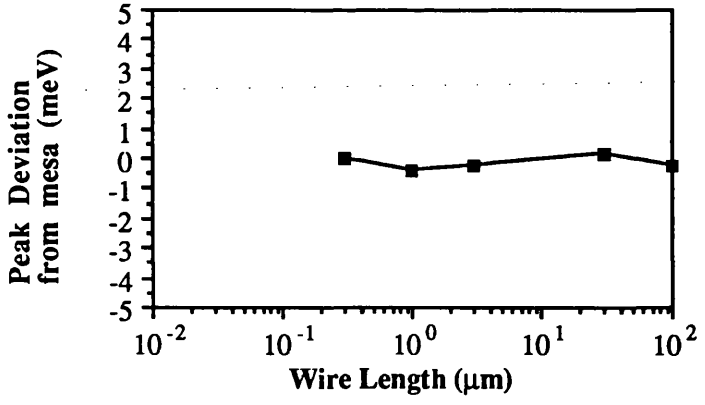


Figure (7.34iii):Peak Position Dependence of 8 nm well of 0.1 μm dashes on Dash 6

## 7.8 Temperature Dependence of Luminescence Intensity

The temperature dependence of the emission intensity from Wire Sample 4 is illustrated in Figure (7.35). As may be observed, the temperature dependence of the emission from the structures approximately follows that of the mesa.

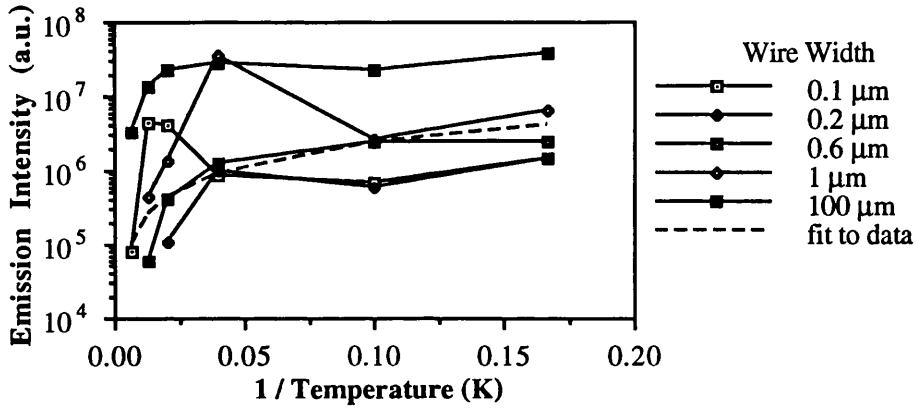


Figure (7.35): Temperature Dependence of the 8 nm well Emission Intensity for Wire Sample 4

As may be observed from the graph, the behaviour of the thinnest wires (0.1 and 0.2 μm) ceases to follow that of the mesa at raised temperatures between 20 and 50 K.

The material from which the structures were fabricated was the MOCVD material A1995A, which showed strong luminescence from the smallest structures at low temperature. The anomalies occur at Arrhenius energies of ~ 2 meV and 4 meV, which are of the order of the binding energy of donor-bound excitons in quantum wells. Investigation of the effect of the temperature on the position of the emission peak, illustrated in Figure (7.36), gives little information on the nature of the transitions, and one may suggest that in the thinnest wires, the emission is dominated by bound-exciton emission in this poor material, but the bound-exciton transitions are less important in the material grown by MBE. There is little evidence, however, for this hypothesis.

Thus a significant contribution to the emission of the smallest structures in poor material is due to bound-exciton transitions, and in higher purity material, such as that of Sample Dash 6, the emission will be dominated by free exciton transitions, giving a consistent reduction in the relative emission intensity with the reduction in structure size.

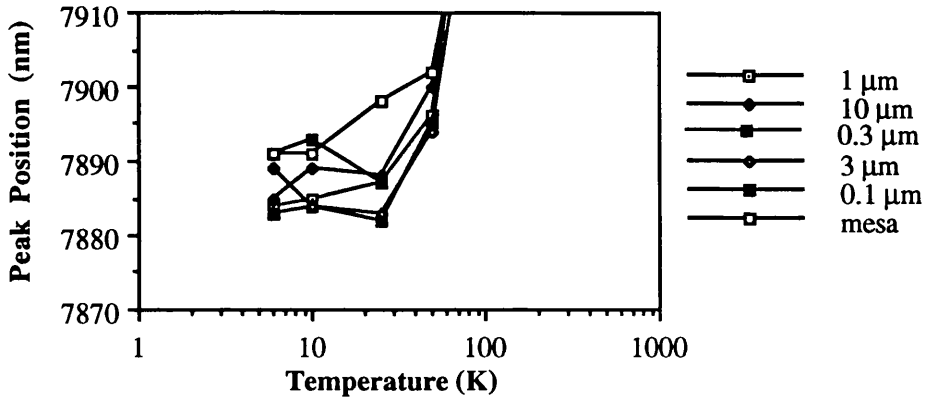


Figure (7.36): Temperature Dependence of the 8 nm well Peak Position for Wire Sample 4

## 7.9 Summary

Measurements of the radiative emission efficiency of small structures characterized by photoluminescence have yielded data which appear contradictory at first inspection.

Further examination of these results, by comparison with data on the original starting material, together with some data on the temperature dependence of structures which show particularly strong luminescence from small structures at low temperature, suggests that, in quantum well material characterized by a broad emission peaks and poor well uniformity in peak position and intensity, the material is dominated by bound exciton transitions, and these are weakly affected by the the size of the structure or nature of the surface.

In material which has good quantum well uniformity, and narrow emission peaks, has a lower contribution from bound-exciton luminescence, and thus demonstrates a reduction in luminescence efficiency as the structure size is reduced, from the effects of surface recombination.

The samples on which structures show such intrinsic emission are used to derive models for the behaviour of low temperature luminescence from small structures in Chapter 8.

# Chapter 8: Modelling of Results

## 8.1 Introduction

The purpose of this chapter is to present theoretical models of the emission intensity behaviour of wires, dots, and dashes in order to explain the experimental data.

In this section, the results from the characterization of the structures obtained in Chapter 7 are compared with the behaviour of several relevant numerical models.

In the 'Surface Effect' model, discussed in Section 3.3.1, the intensity of the radiative recombination in the quantum well structures is dependent on the effect of the recombination at the surface of the structures, which is assumed to be the dominant non-radiative recombination path. Numerical values for the behaviour of the model are obtained in both Cartesian and cylindrical polar coordinate systems, representing the wire and dot symmetries respectively.

In contrast, the 'Intrinsic' model developed by Benisty et al. (1991), discussed in Section 3.3.2, predicts a size dependence of the normalized emission intensity arising from the inhibition of acoustic-phonon scattering in quantum confined structures. The reduced phonon scattering prevents the thermalization of the carriers to the n=1 exciton levels, and thus as the confinement increases, the radiative emission from these levels decreases.

In the final model considered here, the 'Trap Distribution' model, the normalized emission intensity is dependent on the distribution of non-radiative recombination centres, with a finite carrier capture radius, and the effect of a large array of small identical structures with a large filling factor is to reduce the impact of the non-radiative recombination on the normalized emission when compared to that from a control mesa.

In the following sub-sections, the applicability and implications of each model is considered, and the fundamental assumptions emphasized.

## 8.2 Modelling of the Surface Recombination

In this model, one assumes a uniform generation of carriers across the structure concerned, that these carriers diffuse across the structure with a diffusion constant D, and that they recombine either radiatively, by one transition with a time constant $\tau$, or non-radiatively through surface recombination at the external surfaces.

This surface recombination can be characterized by a *Surface Recombination Velocity* S, which is assumed to be constant for a particular surface at a particular time, but the actual value of which will be dependent on the fabrication procedure followed, will most likely vary from material to material, and may vary with the ambient.

At low temperature, in a patterned quantum well, the carriers rapidly form excitons after their generation by, for example, a laser beam, and the radiative recombination may be taken to be that of the

n=1 hh exciton, although the dependence of the model on the choice of $\tau$ is negligible. The recombination of the carriers at the quantum well interfaces is neglected, as S is much lower for these surfaces [Aspnes, 1983].

The use of macroscopic concepts such as surface recombination velocity S and diffusion constant D dictates that this model in this form is only applicable in the centre-of-mass exciton confinement régime.

If one solves the diffusion equation with a constant generation of carriers c, carrier diffusion constant D, and bulk lifetime $\tau$, we have, in the steady state with $\partial n/\partial t = 0$

$$D\nabla^2 n - \frac{n}{\tau} + c = 0 \qquad \{8.1\}$$

### 8.2.1 Solution in the Cartesian Coordinate System

The most appropriate coordinate system for the symmetry of a wire is the rectangular coordinate system, and in this system, the General Solution is:

$$n = A(e^{kx} + e^{-kx}) \qquad \{8.2\}$$

which yields:

$$k = \frac{1}{\sqrt{D\tau}} \qquad \{8.3\}$$

One can take a particular integral of $c\tau$, giving a sufficient solution as:

$$n = c\tau + A(e^{kx} + e^{-kx}) \qquad \{8.4\}$$

The boundary condition is:

$$Sn = -D\frac{\partial n}{\partial x}\bigg|_{x=\pm W/2} \qquad \{8.5\}$$

giving the normalized total number of carriers as:

$$N_{norm} = 1 - \frac{2S\sinh\left(\frac{kW}{2}\right)}{SkW\cosh\left(\frac{kW}{2}\right) + Dk^2W\sinh\left(\frac{kW}{2}\right)} \qquad \{8.6\}$$

This is the expression for a wire in which the width occupied by the carriers is the same as the geometrical width of the wire. A number of authors have found that a better fit to their data may be obtained by assuming that the fabrication process has created a 'dead layer' of optically inactive material on etched surfaces, (see section 3.3.1) and so the 'live' width of the wire available for carriers, 2A, must be reduced by this layer $W_d$ on either side.

If one defines L = 1/k,

$$N_{norm} = 1 - \frac{\frac{SL^2}{AD}\sinh\left(\frac{A}{L}\right)}{\frac{SL}{D}\cosh\left(\frac{A}{L}\right) + \sinh\left(\frac{A}{L}\right)} \qquad \{8.7\}$$

This is the same expression as that derived by Forchel et al. (1990), except for a change in notation:

$$\frac{I(W)}{I(W \to \infty)} = 1 - \frac{\frac{SL^2}{AD}\sinh\left(\frac{A}{L}\right)}{\frac{SL}{D}\cosh\left(\frac{A}{L}\right) + \sinh\left(\frac{A}{L}\right)} \qquad \{8.8\}$$

This is the expression for the normalized emission for a single 2-D wire of infinite length. Further details are given in Appendix A.4. To extend this expression to an array of fabricated wires, one assumes that the length of the wires is greater than the diffusion length 1/k, in order to neglect the effect of the end surfaces. When a large number of wires is considered, the wire emission will vary in S and $W_d$, thus giving an increase in the scatter of the recorded intensities.

Modelling the equation above to obtain the exciton population as a function of wire width for a series of values of the surface recombination velocity S, (Figure (8.1)) and the diffusion constant D, (Figure (8.2)) yields the results shown below.

The most critical parameter in the calculation is the thickness of the 'dead layer', which is process dependent. The calculation is weakly dependent on the carrier diffusion constant.

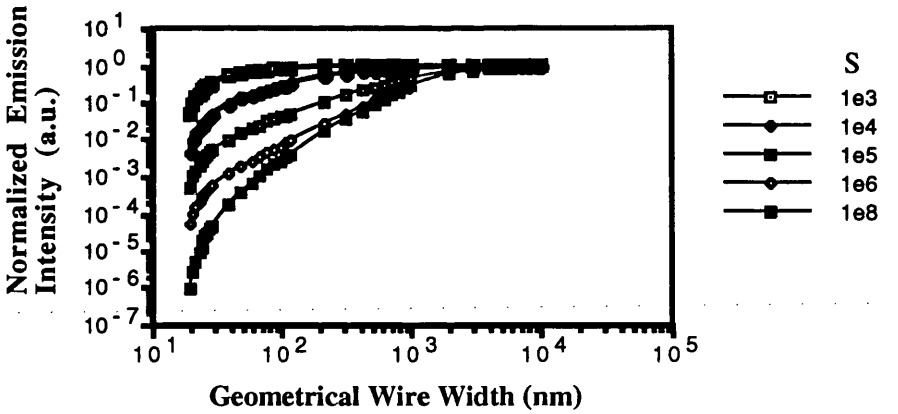


Figure (8.1): Normalized Emission Efficiency Dependence of Wires on the Surface Recombination Velocity S (cm $s^{-1}$), from Equation {8.8}

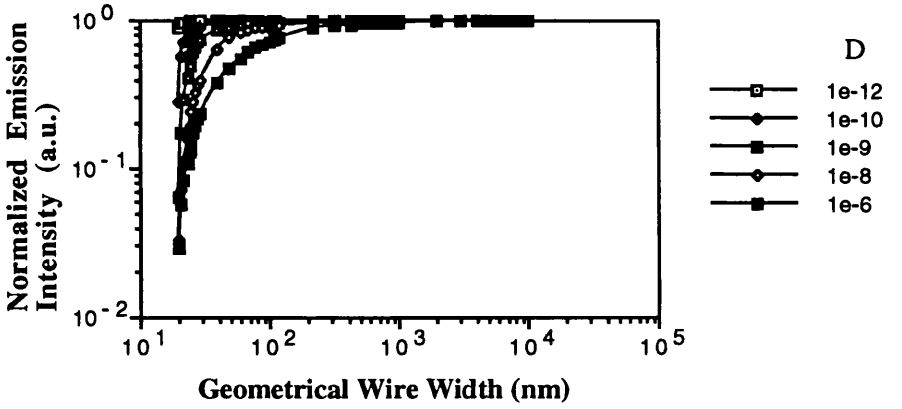


Figure (8.2): Normalized Emission Efficiency Dependence of Wires on the carrier diffusion constant D ($m^2\ s^{-1}$), from Equation {8.8}

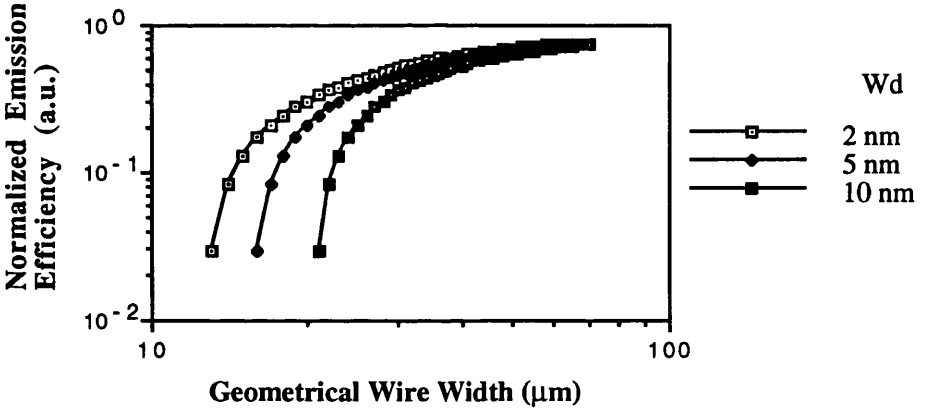


Figure (8.3): Normalized Emission Efficiency Dependence of Wires on the Dead Layer Thickness $W_d$ (nm), from Equation {8.8}

### 8.2.2 Solution of the Diffusion Equation in the Cylindrical Polar Coordinate System

Because of the cylindrical symmetry of a dot, one can solve the diffusion equation in cylindrical polar coordinates. The General Solution in this coordinate system is:

$$\nabla^2\psi - k^2\psi = 0 \qquad \psi_{m\gamma} = \begin{Bmatrix} I_m(\gamma\rho) \\ K_m(\gamma\rho) \end{Bmatrix} \begin{Bmatrix} \cos(m\phi) \\ \sin(m\phi) \end{Bmatrix} \begin{Bmatrix} e^{-\gamma z} \\ e^{\gamma z} \end{Bmatrix} \qquad \gamma^2 = \left|\alpha^2 + k^2\right| \tag{8.8}$$

where: $\alpha$ separation constant

I, K modified cylindrical Bessel functions.

If x<<1, one may expand the functions and neglect smaller contributions, as the series falls off rapidly due to the factorial functions.

Assuming angular symmetry, the solution consists of modified Bessel functions, subject to the boundary conditions:

i) n is finite at the origin

ii) the recombination at the surface r = R is $\underline{S}.\underline{n}$

$$\Rightarrow Sn = -D\left.\frac{\partial n}{\partial r}\right|_{r=R} \tag{8.9}$$

The general solution gives $k^2 = 1 / D\tau$.

Imposing the boundary conditions, and neglecting powers of kR greater than 2, gives the integrated exciton population as:

$$N_{norm} \approx \frac{\frac{R}{2S\tau} + \left(\frac{(kR)^2}{8}\right)}{\left(1 + \frac{R}{2S\tau} + \frac{(kR)^2}{4}\right)} \tag{8.10}$$

This is the same result as that obtained by Clausen et al. (1989), except for the typographic error in the original reference. Further details are given in Appendix A.4.

One may extend the model in a similar to way to that of the wires by inclusion of a 'dead layer', $R_d$.

$$A = R - R_d \tag{8.11}$$

$$N_{norm} \approx \frac{\frac{A}{2S\tau} + \left(\frac{(kA)^2}{8}\right)}{\left(1 + \frac{A}{2S\tau} + \frac{(kA)^2}{4}\right)} \tag{8.12}$$

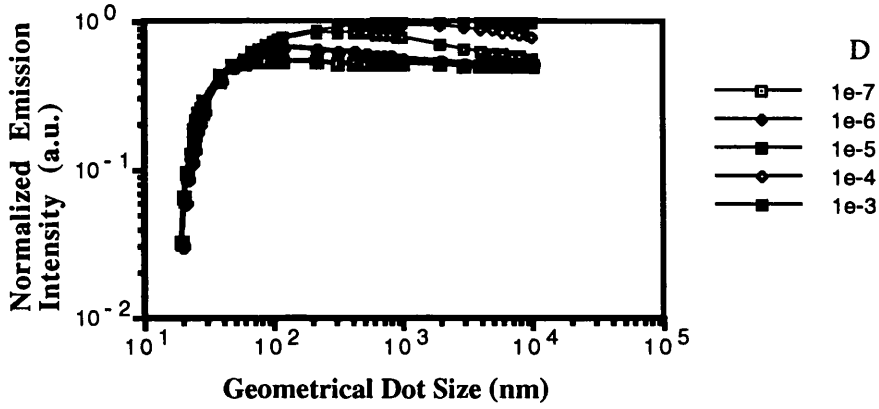


Figure (8.4): Normalized Emission Efficiency Dependence of Dots on the carrier diffusion constant D ($m^2 s^{-1}$), from Equation {8.12}

The expression for the normalized emission efficiency for dots given in Equation {8.12} shows a similar dependence on dot radius as on wire width, for the cases where kR >> 1. The dot efficiency dependence deviates greatly from the wire dependence for small D, shown in Figure (8.4), and saturates for large R at a value of 0.5 rather than 1. This is due to the neglect of terms in kR of order greater than two, which become significant for small D.

### 8.2.3 Comparison of Emission Intensities From Dots and Wires

When one compares the normalized emission efficiency for dots and wires of similar dimensions (the wire width being equal to the dot diameter), with the same values for D, S, and $W_d$, and for which kR << 1, one observes a similar behaviour (see Figure (8.5) overleaf), but the dots have a normalized emission efficiency lower than that of the wires, although within an order of magnitude of the wire efficiency.

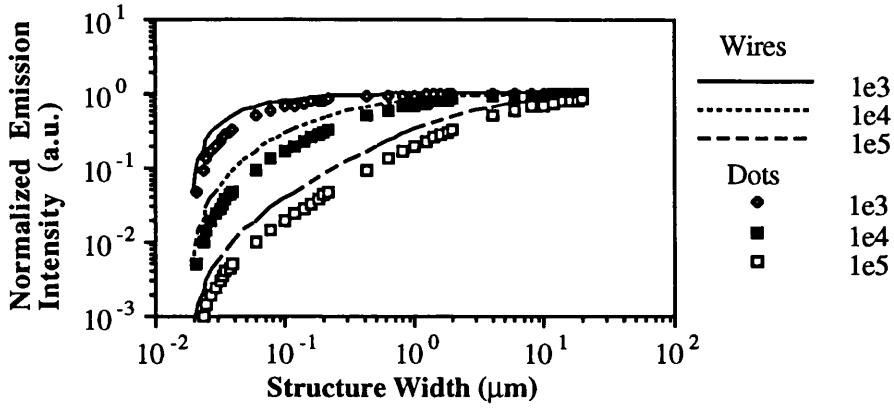


Figure (8.5): Comparison of the Dependence on S (cm $s^{-1}$) of the Normalized Emission Efficiency of Dots and Wires Derived from Equations {8.8} and {8.12}

One would expect, however, that this small difference in behaviour would only be significant if one could neglect variations in S and $W_d$, which would have a much larger impact on the normalized emission efficiency.

### 8.2.4 Fit of Theory to Data

A number of authors have reported data on the values of the surface recombination velocity, diffusion constant, and 'dead layer' thickness. The available data for GaAs are summarized overleaf in Table (8.1).

| Author | S ($cms^{-1}$) | notes |
|---|---|---|
| Clausen et al. 1989 | $10^6$ to $10^{10}$ | $BCl_3$ / Ar |
| Izrael et al. 1990 | $1.3 \times 10^5$ | $SiCl_4$ RIE |
| Maile et al. 1988, 1990 | $4 \times 10^5$ | Ar IBE, $CCl_2F_2$ RIE |
| Wang et al. 1992 | $1 \times 10^5$ | $SiCl_4$ RIE |
| Hamao et al. 1991 | $8 \times 10^6$ | $Cl_2$ RIBE |
| Forchel et al. 1988 | $5 \times 10^5$ | $CCl_2F_2$ RIE |
| Forchel et al. 1990 | $6.5 \times 10^6$ | Ar IBE, $CCl_2F_2$ RIE |
| Aspnes et al. 1983 | $10^4 - 10^7$ | bulk surfaces |
| Korinfskiĭ et al. 1985 | $10^5 - 10^7$ | " |
| Nelson et al. 1980 | $10^4 - 10^6$ | " |
| Hoffman et al. 1978 | $5 \times 10^5$ | " |

Table (8.1): Values of the Surface Recombination Velocity S ($cms^{-1}$) for GaAs free surfaces

| Author | $\mu$ ($cm^2V^{-1}s^{-1}$) | D ($cm^2s^{-1}$) |
|---|---|---|
| Hillmer et al. 1990 | $1 \times 10^4$ | $\approx 5$ @ 6 K |

Table (8.2): Extrapolated Value of the 6 K Diffusivity D ($cm^2\ s^{-1}$) calculated from exciton mobility in a GaAs 10 nm well

| Author | D ($cm^2s^{-1}$) | Temperature (K) |
|---|---|---|
| Clausen et al. 1989 | 2.5 | 20 |
| Izrael et al. 1990 | - | - |
| Maile et al. 1988, 1990 | 0.4 | 2 |
| Wang et al. 1992 | 2.5 | 5 |
| Hamao et al. 1991 | 20 | 293 |
| Forchel et al. 1988 | 3.6 | 2 |
| Forchel et al. 1990 | 2.63 | 4 |

Table (8.3): Values of the exciton Diffusivity D ($cm^2\ s^{-1}$) in GaAs quantum wells

| Author | $W_d$ (nm) | Etch Technique |
|---|---|---|
| Clausen et al. 1989 | 40-100 | $BCl_3$ / Ar |
| Maile et al. 1988, 1990 | 100 | Ar IBE, $CCl_2F_2$ RIE |
| Wang et al. 1993 | 30 | $SiCl_4$ RIE |
| Forchel et al. 1988 | 130 | $CCl_2F_2$ RIE |
| Forchel et al. 1990 | 65 | Ar IBE, $CCl_2F_2$ RIE |

Table (8.4): Values of the Dead Layer Thickness assumed by authors using the Surface Recombination Model

The luminescence intensity is found to be insensitive to the surface recombination velocity when the dot is smaller than the exciton diffusion length of ~1 μm. Measurements of S at low temperature suggest values of S between $10^5$ to $10^7$ $cms^{-1}$. Consensus values of the parameters cluster around the values of S at $10^6$ $cms^{-1}$ , D at 5 $cm^2s^{-1}$ and $W_d$ at most at 100 nm, although $W_d$ is heavily process-dependent. These values are used in Chapter 9 to compare the experimental data with the model predictions.

### 8.2.5 Validity of the Surface Recombination Model

The surface recombination model is valid in systems where the non-radiative recombination in a quasi-2-D system is dominated by the recombination at the surface, and the carriers are laterally confined in a system which is larger than the exciton centre-of-mass confinement régime above 100 nm.

Although the model has gained much support in the literature, it relies a set of empirical parameters which are not well known for an etched quantum well system. The exciton diffusion constant D is dependent on the roughness of the quantum well interfaces, and the surface recombination velocity for an etched GaAs surface depends on the ambient and the etch process used, and can vary by up to three orders of magnitude. The 'dead-layer' $W_d$ is an empirical value used by a number of authors to fit their data. Given the number of free-parameters, it is thus difficult to determine the behaviour of the structures independent of the material and etch process used.

## 8.3 Trap Distribution Modelling

### 8.3.1 Assumptions

If one assumes that the most significant non-radiative recombination path is assisted by trapping of carriers on centres in the quantum well, the radiative emission efficiency of structures comparable in size to the diffusion length of the carriers will show a dependence on the aspect ratio of the structures.

This is due to the combined effects of carrier diffusive transport and the scaling of the true structure area to form an effective area coverage.

In order to quantify this effect on the structure, the effective 'live' area was calculated for structures of differing aspect ratio as a function of the number of trapping centres. The general process was as follows. A trap was created at a random position within the total area of the structure array, which included both the structure and the etched space between the structures (see Figures (8.6) and (8.7)). If the trap lay within the structure, all carriers within one diffusion length of the trap were assumed to have recombined non-radiatively instantaneously. The remaining carriers were then assumed to recombine radiatively. The proportion of radiative to non-radiative transitions was then calculated by the ratio of area within one diffusion length to the area of the structure as a whole.

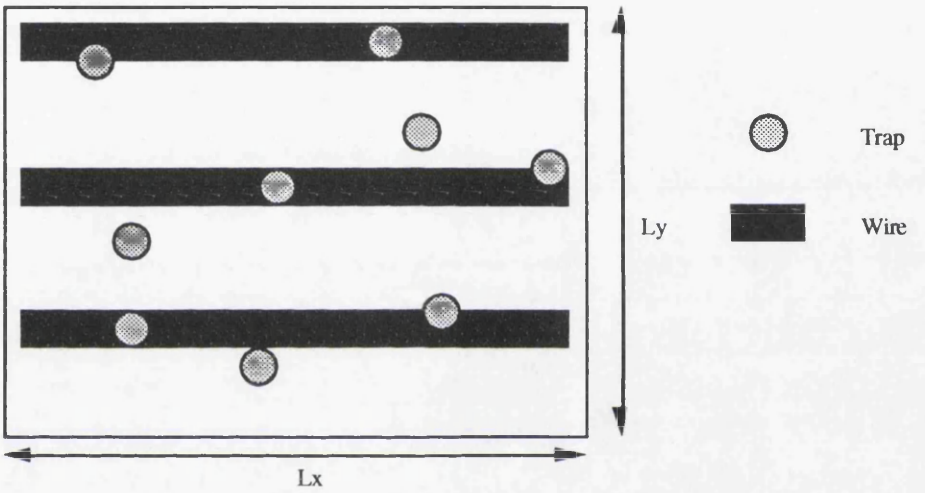


Figure (8.6): Trap Distribution Model: Wires

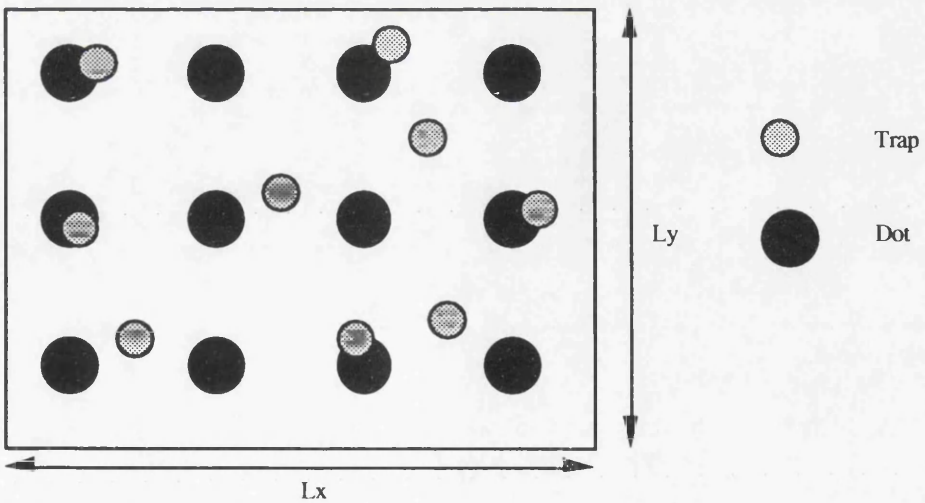


Figure (8.7): Trap Distribution Model: Dots

The process was repeated consecutively for a set number of traps, and the whole process was repeated to simulate an array of identical structures. The radiative efficiency, defined as the area of radiatively combining carriers to the area of non-radiatively combining carriers, was thus calculated as a function of trap density, structure shape and size, and diffusion length.

### 8.3.2 Results for a constant concentration of Traps

The program was written in Pascal using a Turbo Pascal 6.0 compiler running on a 80386 PC with co-processor.

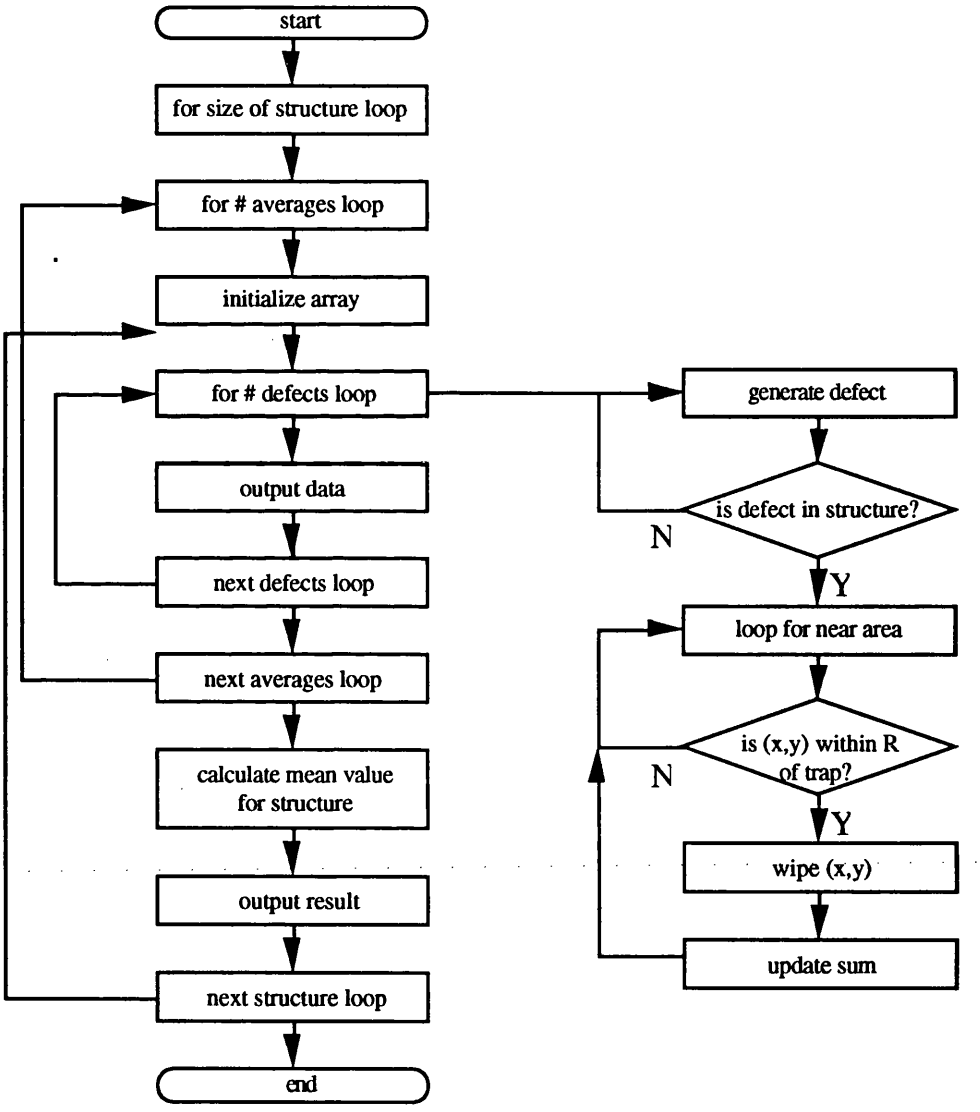


Figure (8.8): Flowchart of the Trap Distribution Model

It consists of a series of loops (see Figure (8.8)), which vary, in this order, the diffusion length, the length of the structure, the width of the structure, the number of identical structures modelled, and the number of traps. The program is listed in Appendix A.5. Due to restrictions on the memory organisation, the maximum number of elements in the array corresponding to the actual structure was limited to 10 000, and for convenience the number of identical structures and maximum number of traps were varied to maximize efficiency of the time. The diffusion lengths were chosen to allow a suitable range whilst attempting to avoid features arising from the coincidence of the dimensions. The mean values of the results for each group of identical structures were calculated and stored on file, each data-file occupied approximately 4K of disc space, and the time requirement varied from a few minutes for the smallest structures to many hours for the largest structures.

When limited to the low-defect régime, the data showed an increase of relative emission efficiency as the structure dimensions were reduced, and, for a given structure width, as the length was reduced, the relative emission efficiency increased. This was most noticeable for the narrowest structures, as can be seen in Figures (8.9,8.10).

For a fixed array of 10 000 elements, if one takes an array element to be 0.1 μm, this gives a two-dimensional trap concentration of 1400 traps per 100 $\mu m^2$, which is 1.4 x $10^{13}$ $m^{-2}$. This is equivalent to a bulk trap concentration of 5 x $10^{13}$ $cm^{-3}$.

Measurements of the peak electron mobilities at low temperature in n-GaAs grown without intentional doping by molecular beam epitaxy at Glasgow University have yielded measurements of the free electron concentration as low as 3 x $10^{13}$ $cm^{-3}$ [Stanley et al., 1991]. The free electron concentration is the difference between the concentration of residual donors and that of of residual acceptors, and assuming this to be within an order of magnitude of the concentration of residual impurities leads to a value of the residual impurity concentration of $10^{14}$ $cm^{-3}$.

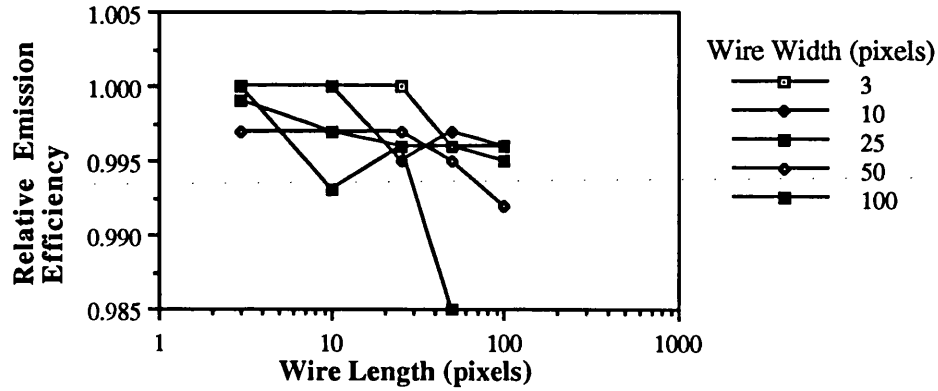


Figure (8.9):- Radiative Efficiency vs. Wire Length for 1000 traps

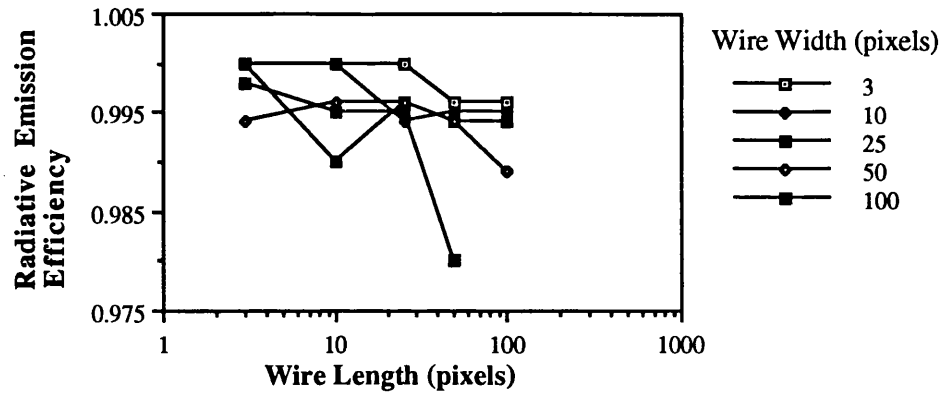


Figure (8.10) Radiative Efficiency vs. Wire Length for 1400 traps

Thus, assuming that the residual trap concentration is of the same order as the residual impurity concentration, the trap concentration is of the order of $10^{14}$ $cm^{-3}$. For this trap concentration, the relative emission efficiency for a 10 μm by 10 μm box structure is 97.5 % of that of a 10 μm by 0.3 μm wire.

These calculations indicate that assuming a trap concentration of the order of $10^{14}$ $cm^{-3}$, the relative emission efficiency increases by a small percentage as the filling factor is increased. This result is insufficient to match the dramatic variation in emission efficiency observed.

The main residual acceptor in the GaAs grown by the MBE group at Glasgow is carbon, with silicon as the main donor. Smaller concentrations of sulphur and selenium are also present [Stanley et al., 1991].

### 8.3.3 Validity of the Trap Distribution Model

The trap-distribution model fails to give a dramatic reduction in the luminescence emission efficiency, and thus its effect may be neglected for the structure system investigated in this data as it is much smaller than the inaccuracies in the experimental procedure.

In addition, the number and distribution of the optically active traps in quantum wells are not well known, complicating the calculation of the impact on the radiative emission efficiency.

## 8.4 Intrinsic 'Bottleneck' Modelling

The behaviour of the radiative efficiency of quantum box luminescence is tentatively explained in a model produced by Benisty et al. [Benisty et al., 1991]. In this model, the poor radiative efficiency is explained as an intrinsic effect due to the decreased relaxation rate in zero-dimensional systems in the 100-

200 nm size range, and in quantum dashes, or 'pseudo-wires', the onset of the decay in radiative efficiency occurs for a much smaller dash width than for the same dot diameter. See section (3.3.2).

In the model presented by Benisty et al., the steady state occupation probabilities of a set of electron states are obtained by successively iterating the transitions between the states to obtain a stable solution. The fraction of the electrons which decay radiatively is then calculated as a function of dot diameter for both GaAs and $In_{0.47}Ga_{0.53}As$ wells; the difference between the materials taken to be in the effective mass.

The transitions between the states are taken to be due to a size-dependent LA-phonon emission; the transitions which remove carriers are a radiating path of fixed lifetime $\tau_R$=1.6 ns, or a non-radiative decay path of fixed decay rate $\tau_{NR}$=10 ns, and carrier capture is included by enforcing a top level occupancy of 0.5.

The model is based on the lateral E(l,m,n) energy levels of the n=1 sub-band of an infinite square well of dimensions $L_x$,$L_y$,$L_z$ where:

$$L_x, L_y > L_z \qquad \{8.13\}$$

and:

$$E \propto \left[\frac{l^2}{L_x^2} + \frac{m^2}{L_y^2}\right] \qquad \{8.14\}$$

For a fuller discussion see [Benisty et al., 1991].

The results of the simulation are illustrated for dots at 4 K in Figure (8.11). The radiative efficiency drops dramatically below 200 nm, and is relatively insensitive to variations of several orders of magnitude in the adjustable parameters ($\tau_R$ and $\tau_{NR}$), due to the rapid reduction in relaxation rate.

This model was further extended in the paper to consider a quantum dash or 'pseudo-wire' of dimensions $L_x$ and $L_y = 10\,L_x$. The change in aspect ratio in the quantum dash ('pseudo-wire') delays the drop in radiative efficiency to smaller dimensions, and thus for a set of dashes of the same width, one would expect a decrease in radiative efficiency as the dash length is reduced, if this intrinsic effect were the dominant factor in the radiative efficiency size dependence.

### 8.4.1 Validity of the 'Bottleneck' Model

The 'bottleneck' model is valid in a régime where the confinement energy from the lateral dimensions of the structure is comparable with the LA-phonon separation. This requires a structure size of around 100 nm for GaAs for the onset of the reduction in luminescence efficiency.

The model has no free parameters for a given material system, and there is little direct experimental evidence for the model so far.

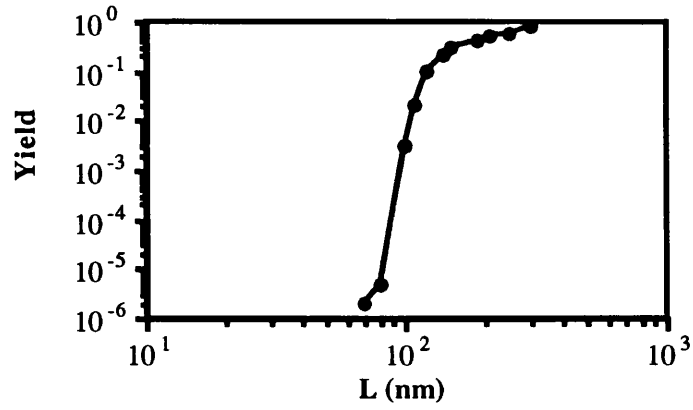


Figure (8.11): 'Intrinsic' Model of Luminescence Yield as a function of square dot side L for a GaAs quantum well

## 8.5 Strain-Dependent Recombination

### 8.5.1 Strain in Etched Quantum Structures

Recent work by Qiang et al. (1993) has shown that significant residual strain is present in etched dot structures characterized by room temperature photoreflectance.

The strain is explained as due to the relaxation after structure etching of wells strained by the mismatch of lattice constant with those of the barriers. Although the GaAs quantum well layers are approximately lattice-matched to the AlGaAs barriers, especially at the growth temperature, reduction of the crystal temperature from the growth temperature (around 900 K) to 6 K, results in a residual strain in the material from the difference in lattice constants, and exacerbated by the difference in the thermal expansivities of the GaAs and the AlGaAs. As the thermal properties of GaAs and AlGaAs are very similar, the strain is expected to be small, but is nevertheless significant.

This has little effect in quantum well material, but when small structures are fabricated in the quantum well material, the removal, by etching, of material surrounding the structures allows the relaxation of the strain at the edges of the structures. This relaxation results in a shallow well being developed in the structure; the size of the well depends on the quantum well material, the etch process used, the exposure to ambient, and on the size of the structure.

As the structure size is reduced, the compressive strain in the structure is released, resulting in a stress potential gradient at the surface of the structure. Calculations of the residual compressive strain in the biggest structures give maximum values of strain $\varepsilon$ of the order of $5 \times 10^{-4}$, which results in potentials of the order of several meV.

At room temperature in the GaAs / $Al_{0.3}Ga_{0.7}As$ system, there is a lattice mismatch of approximately 0.04 %. The coefficients of linear expansion of GaAs and AlAs at room temperature are 5.4 x $10^{-6}$ $K^{-1}$ and 4.8 x $10^{-6}$ $K^{-1}$, and thus at low temperatures the mismatch will be greater. In addition, in the GaAs / AlGaAs structures, the well is completely etched through, increasing the well depth over that achieved by etching through a stressor layer only.

Prolonged etching of GaAs in the reactive ion etch process is believed to promote gallium loss from the sidewalls, resulting in a excess of arsenic on the sidewalls [Foad et al., (1990)]. This contamination is exacerbated by the growth of arsenic and gallium oxides under exposure to the ambient. These contaminants will give an ambient-dependent surface behaviour, which will complicate the material-dependent lateral potentials.

### 8.5.2 Strain Localization in Etched Quantum Structures

The quantum wells in the dot, wire and dash structures will be subject to a lateral localizing potential well compared with the quantum well material. This potential well arises from the residual strain between the GaAs and AlGaAs layers

Calculation of the lateral potential well would require an involved finite element analysis; an approximation can be achieved by extrapolating the results of Kash et al. (1989), on the effect of InGaAsP overlayers on InP, to the GaAs / AlGaAs material system. In that paper, biaxial strain was deliberately introduced into the structure, by growing an overlayer which differed in lattice constant from that of the quantum well by 0.04 %. The wires and dots fabricated by this strain confinement method were of 200 nm and 400 nm, and the potential well resulting from the stress confinement for the 400 nm wires was calculated to be 3.7 meV, and measured to be 7 meV.

The deformation potential derived from the GaAs / AlGaAs system above was of the order of several meV, comparable with the well depth calculated by Kash et al. above.

As a result of the shallow confinement from the strain relaxation, one would expect the carriers to be inhibited from reaching the surfaces, and thus a reduction in overall non-radiative recombination rate.

In addition, because the relaxation will depend on the size of the stressor and stressed material, one would expect the shape and depth of the potential well to be dependent on the size of the structure.

One can thus derive some qualitative results for the effect of strain potentials on surface recombination.

### 8.5.3 Solutions to the Strain Potential Well

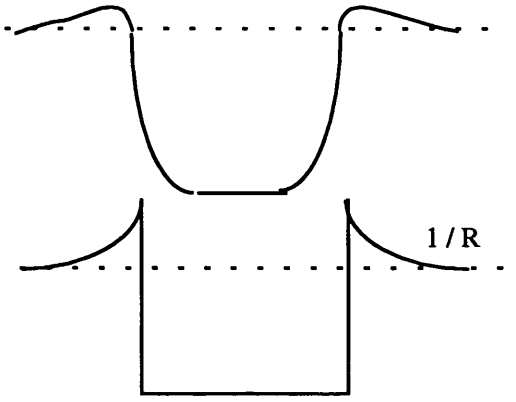


Figure (8.12): Schematic of Stress Potential (top) and (1/R) barrier approximation (below)

The actual form of the barrier is not significant, and actual barrier thickness is assumed to be approximately constant for all the structures. The variation between structures will be in the separation between the barriers resulting from the difference in structure size. This barrier separation variation will result in a variation in the electron ground state energy, and also in the transit time of the carriers confined in this shallow well.

Due to the slow variation in the potential well, one can approximate the tunneling through the potential barriers by a Wentzel-Kramers-Brillouin model similar to that used for nuclear α-decay or the field emission of electrons [French and Taylor, 1978].

The Wentzel-Kramers-Brillouin model [Schiff, 1968] is applicable for the approximate solution of quantum mechanical problems where the potential changes so slowly that the momentum of the particle is constant over many wavelengths.

The penetrability T of a barrier V(x) for a particle of energy E from $x_1$ to $x_2$ is given by:

$$T \approx \exp\left\{-2\int_{x_1}^{x_2}\frac{\sqrt{2m[V(x)-E]}}{\hbar}\,dx\right\} \qquad \{8.15\}$$

The decay constant γ, equal to the reciprocal of the lifetime τ for the state, for a carrier confined to a radius R and with velocity $v_1$ by barriers of penetrability T is given by:

$$\gamma = \frac{1}{\tau} = \frac{v_1}{2R}\,T \qquad \{8.16\}$$

In the application of the WKB method to this problem, we can differentiate two régimes:

#### 8.5.3.1 Quantum-confined régime

In this case, one has to calculate the effect of the lateral quantization energy level on the barrier penetrability. This has been calculated in a similar problem for α-decay of nuclei.

In the solution to the nuclear α-decay problem, the potential was modelled as a spherical quantum well of radius R and of height $V_0$, with the barrier potential decaying inversely with the radius. The α particle escapes with an energy E, and so the problem was solved in terms of the barrier penetrability as a function of the carrier energy E.

For the qualitative results we are interested in, the energy dependence of the structure can be assumed to have a potential inversely dependent on the structures radius. This gives a negligible barrier penetrability at large R, which is not very realistic, but at small R the barrier penetrability rises to a peak at values of R around 10 nm, for a barrier height of 10 meV and an effective mass of 0.067 $m_e$, and then falls slowly again as R is further reduced.

For very small structures, the carriers can tunnel through the barriers arising from the relief by etching of the stress sustained due to the differing thermal properties of the alloys in the material, and so the surface recombination becomes very significant.

#### 8.5.3.2 Large-dimension régime

In this régime, the carrier energy variation is negligible and so the barrier penetration is effectively constant. In these structures, the tunneling decay constant γ is inversely dependent on the structure size, due to the carrier transit time. The carrier velocity is approximately independent of R, and so the lifetime is linearly proportional to the structure dimension R. For non-radiative recombination at the surface, the carriers have to tunnel through the stress barrier, and so one would expect an increase in the surface recombination as the structure dimensions are reduced. This régime applies so long as the quantization energy variation is insignificant with the barrier energy (~ 10 meV), which applies until we enter the quantized régime with structures of order 100 nm in size.

Thus, for these large structures, the non-radiative recombination ($R_{NR}$) varies inversely as the transit time τ for the carriers:

$$R_{NR} \propto 1 / \tau \qquad \{8.17\}$$

or, the non-radiative recombination ($R_{NR}$) varies with structure size (L) as:

$$R_{NR} \propto L \qquad \{8.18\}$$

which means that the radiative recombination rate (R) varies linearly with the structure dimension:

$$R \propto L \qquad \{8.19\}$$

### 8.5.4 Validity of the Strain-Dependent Recombination Model

The lateral confinement in the Strain-Dependent Recombination Model should be observable as a red-shift in the confined luminescence emission of the order of several meV. This, however, cannot be observed unambiguously due to the variation in peak position with position on the wafer, which is of the same order.

The Strain-Dependent Recombination Model is complicated due to the lack of knowledge of the potential, and the non-radiative recombination of the etched GaAs surface at low temperature. In addition, the nature of the etched surface is not well understood; complications include the disruption of the crystal structure from stoichiometric loss and contamination of the etch wall with oxides of gallium and arsenic. Both these changes affect the band-gap and contribute to strain in the well layer.

Most important of all, there is no evidence for a difference in the behaviour of the dots, dashes, and wires, as might be expected from the difference in stress-relief in these structures of different aspect ratio.

## 8.6 Summary of Modelling

The surface recombination model is strongly dependent on empirical values for the surface recombination velocity and diffusivity, which are not well known for the particular material structures in the temperature range of interest. With the free parameters of the surface recombination velocity S, the diffusivity D and the fitting parameter of the 'dead layer' $W_d$, one can fit the efficiency dependence. Values for these parameters when the model is fitted to our data are derived in Chapter 9. In the case of wires, there is a decrease in radiative efficiency for meaningful values of these parameters, although in the case of dots the model is not analytical for meaningful values of the parameters.

The trap distribution model is a qualitative model of the effect of a random distribution of traps on the radiative efficiency of arrays of dots, wires and dashes. The model, is sensitive to the aspect ratio of a quantum dash, but predicts at most a few percent difference in the values of relative emission efficiency of the wires and dots. As designed, there is a decrease in radiative efficiency as the trap concentration is increased, but there is also a more dramatic reduction in the radiative efficiency of the dashes and wires as the trap concentration is increased. For a given dash width, the radiative efficiency falls off as the length is increased; the decrease is most significant, however, for the widest dashes.

The intrinsic mechanism model is relatively insensitive to the adjustable parameters, and predicts a dramatic difference between the behaviour of dots and wires, with the wires having a greater radiative efficiency.

In the Strain-Dependent Recombination Model, the large structures fabricated in this project are expected to show behaviour in the large-dimension régime, where the non-radiative recombination is inversely dependent on the structure dimension. The small structure régime shows a rapid decrease in intensity; this will complicate the debate on the relative importance of surface recombination versus 'intrinsic' effects for non-radiative recombination.

The comparison of the experimental data of this project with these models is discussed in the next chapter.

# Chapter 9: Data Analysis

## 9.1 Summary of Results

### 9.1.1 Samples with a Variation in a Single Dimension

These samples consist of a set of structures with a single varying parameter; in the case of dots it is the dot diameter, for wires it is the wire width, and for the dashes it is the dash length.

The case of varying both dash width as well as dash length on the same sample is considered in the next section.

#### 9.1.1.1 Dots

| Dot Sample | Figure | Dot Diameter (μm) | Normalized Intensity (a.u.) | Trend of Intensity with dot diameter d |
|---|---|---|---|---|
| 1 | 7.3 | 0.1 to 1 | 0.1 to 10 | Flat, or slight ↑ as d ↓ |
| 2 | 7.4 | 0.1 to 1 | 0.1 to 10 | strongly ↑ as d ↓ |
| 3 | 7.5 | 0.1 to 1 | 0.1 to 10 | weakly ↑ as d ↓ |
| 4 | 7.6 | 0.1 to 1 | 0.1 to 1 | weakly ↑ as d ↓ |

Table (9.1): Summary of Luminescence Intensity Measurements of Dot Samples

The dot diameters were chosen to be 0.1, 0.3 and 1 μm, to allow for duplication of areas on the same sample. Measurements of the normalized emission intensity are concentrated between $10^{-1}$ and $10^{0}$, thus showing no evidence for a dramatic reduction in emission efficiency, but rather that as the dot size is reduced, the general trend of the normalized emission intensity is to increase, sometimes strongly.

Dot samples 1, 2 and 4 were fabricated on MBE material A315, A315, and A365 respectively, and dot sample 3 on MOCVD material A1995A. Little difference can be deduced from the material behaviour. As dot samples 1 and 2 were fabricated on the same material with the same patterns under the same conditions, one can note the large scatter in the methodology as a whole.

#### 9.1.1.2 Wires

| Wire Sample | Figure | Size Range (μm) | Normalized Intensity (a.u.) | Trend of Intensity with wire width d |
|---|---|---|---|---|
| 1 | 7.7 | 0.1 to 1 | 0.01 to 1 | strongly ↓ as d ↓ |
| 2 | 7.8 | 0.1 to 1 | 0.001 to 10 | weakly ↓ as d ↓ |
| 3 | 7.9 | 0.1 to 1 | 0.01 to 1 | strongly ↑ as d ↓ |
| 4 | 7.10 | 0.1 to 1 | 0.001 to 1 | weakly ↓ as d ↓ |
| 5 | 7.11 | 0.1 to 1 | 0.1 to 10 | strongly ↓ as d ↓ |
| 6 | 7.12 | 0.1 to 1 | 0.1 to 10 | weakly ↓ as d ↓ |

Table (9.2): Summary of Luminescence Intensity Measurements of Wire Samples

The wire widths were chosen to be 0.1, 0.3 and 1 μm, to allow for duplication of areas on the same sample, and comparison with the dot structures. The normalized emission intensity is concentrated between $10^{-3}$ and $10^{1}$. As the wire width is reduced, the trend of the normalized emission efficiency is to decrease, and for wire samples 1, 3 and 5, the normalized emission efficiency decreases strongly.

Wire samples 1-3 were fabricated on MBE material A315, samples 5 and 6 on A365, and sample 4 on MOCVD A1995A. The difference in material has no effect on the wire width dependence of the normalized emission efficiency of the wire structures.

#### 9.1.1.3 Dashes of Fixed Width

| Dash Sample | Figure | Dash Width (μm) | Dash Length (μm) | Normalized Intensity (a.u.) | Trend of Intensity with dash length l |
|---|---|---|---|---|---|
| 1 | 7.13 | 0.1 | 0.1 , 1 | 0.01 - 10 | weakly ↓ as l ↓ |
| 2 | 7.14 | 0.1 | 1 | 0.001 - 1 | weakly ↑ as l ↓ |
| 3 | 7.15 | 0.1 | 0.1 , 10 | 0.01 - 1 | weakly ↓ as l ↓ |
| 7 | 7.19 | 0.1 | 0.3, 1, 3 | 0.01 - 1 | flat |
| 8 | 7.20 | 0.6 | 0.6 - 100 | 0.001 - 10 | flat |
| 9 | 7.21 | 0.3 | 0.3 - 100 | 0.01 - 1 | flat |
| 10 | 7.22 | 0.3 | 0.3 - 100 | 0.01 - 1 | flat |
| 11 | 7.23 | 0.3 | 0.3 - 100 | 0.01 - 100 | flat |
| 12 | 7.24 | 0.6 | 0.6 - 100 | 0.01 - 10 | flat |

Table (9.3): Summary of Luminescence Intensity Measurements of Dash Samples

For these dash samples of fixed dash width, there is no dependence on the dash length. As the dash length is always fabricated greater than the dash width, this suggests that the emission is dominated by the smallest dimension, i.e. the dash width, to such an extent that the effect of dash length is negligible.

Dash samples 1-3 were fabricated on MBE B33 material, samples 7-12 on MBE A315 material. No dependence on material is observed.

### 9.1.2 Samples with Variation in Both Dimensions

#### 9.1.2.1 Dashes of Varying Width and Length

| Dash Sample | Figure | Dash Width (μm) | Dash Length (μm) | Normalized Intensity (a.u.) | Trend of Intensity with dash length l |
|---|---|---|---|---|---|
| 4 | 7.16 | 0.1 - 1.2 | 0.4 - 100 | 0.01 - 10 | see Table (9.5) |
| 5 | 7.17 | 0.1 - 30 | 0.1 - 100 | 0.001 - 100 | see Table (9.6) |
| 6 | 7.18 | 0.1 - 30 | 0.1 - 100 | 0.001 - 10 | see Table (9.7) |

Table (9.4): Summary of Luminescence Intensity Dependence on Dash Length for Dash Samples of Varying Width

| Dash Width (μm) | Figure | Dash Length (μm) | Normalized Intensity (a.u.) | Trend of Intensity with dash length l |
|---|---|---|---|---|
| 0.1 | 7.16b | 0.4 - 7 | 0.01 - 10 | weakly ↓ as l ↓ |
| 0.1, 0.4, 0.75, 1.2 | 7.16a | 0.1, 0.4, 0.75, 1.2 | 0.01 - 10 | weakly ↓ as l ↓ |

Table (9.5): Summary of Luminescence Intensity Dependence on Dash Length for Dash Sample 4

| Dash Width (μm) | Figure | Dash Length (μm) | Normalized Intensity (a.u.) | Trend of Intensity with dash length l |
|---|---|---|---|---|
| 0.1 | 7.17a | 0.1 - 100 | 0.001 - 100 | weakly ↓ as l ↓ |
| 0.3 | 7.17b | 0.3 - 100 | 0.001 - 100 | flat |
| 1 | 7.17c | 1 - 100 | 0.001 - 100 | weakly ↓ as l ↓ |
| 3 | 7.17d | 3 -100 | 0.001 - 100 | flat |
| 10 | - | 10, 100 | 0.001 - 100 | weakly ↑ as l ↓ |

Table (9.6): Summary of Luminescence Intensity Dependence on Dash Length for Dash Sample 5

| Dash Width (μm) | Figure | Dash Length (μm) | Normalized Intensity (a.u.) | Trend of Intensity with dash length l |
|---|---|---|---|---|
| 0.1 | 7.18a | 0.1 - 100 | 0.01 - 10 | flat |
| 0.3 | 7.18b | 0.3 - 100 | 0.01 - 10 | flat |
| 1 | 7.18c | 1 - 100 | 0.01 - 10 | flat |
| 10 | 7.18d | 10 , 100 | 0.01 - 10 | weakly ↓ as l ↓ |

Table (9.7): Summary of Luminescence Intensity Dependence on Dash Length for Dash Sample 6

**General Observations**

In these dash samples, both the dash width and the dash length were varied on the same samples, thus giving dots, wires, and intermediate dashes all on the same material and processed at the same time under the same conditions.

As in the case of the dashes of fixed width, there is no dependence on the dash length, as the dash length is greater than the dash width. The wires, as in the single-structure samples, show a decrease in emission efficiency with wire width, but the dots on these samples also show a decrease in emission efficiency with dot diameter, consistent with the results for the other structures on the same samples.

Dash samples 4-6 were also fabricated on MBE B33 material, which was the material which exhibited the best uniormity and brightest quantum well emission.

## 9.2 Discussion of the Data

### 9.2.1 Review of Results

#### 9.2.1.1 Batch Processing of Samples

A number of samples were processed simultaneously in batches, in order to reduce run-to-run fabrication variations, and to reduce the scatter on the data.

When samples were fabricated on the same material with the same patterns under the same conditions, there was still a large scatter in the recorded data, showing that the scatter was not as a result of lack of care in the methodology, but more associated with uncontrollable factors such as material quality and etch behaviour.

#### 9.2.1.2 Material Dependence

In the analysis of Chapter 6, it was found that material B33 had the most favourable material properties for the fabrication of nanostructures of the material assessed. This was due to its narrow free-exciton peak, and small variation in peak intensity and quantum well width across the wafer.

Of the structures tested, it would be expected that structures fabricated on B33 would show the most dependable results, and this corresponds with samples Dash 1-6. Other structures were fabricated on a range of other material, depending on the material available.

#### 9.2.1.3 Single Dimension Varied Samples

For the samples constructed exclusively of dots, the dot emission efficiency is approximately independent of the dot diameter. But for all the wires, and for the dashes, including those dashes which are 'dot-like', fabricated on the mixed samples, the efficiencies show a consistent decrease with the smallest dimension. There is no significant dependence of emission efficiency on dash length for a given dash width, but this is because the dash length is always greater than the dash width.

If one considers initially the behaviour of the wires and dashes, one observes that the emission efficiency is dominated by the smallest dimension. This would seem to indicate that the emission is dominated by recombination at the nearest surfaces, and, for a given dash, the emission is thus approximately independent of the dash length.

#### 9.2.1.4 Both Dimensions Varied Samples

Plotting the emission efficiency as a function of structure size for the dot-like dashes and the wire-like dashes, one observes a very similar behaviour to that of the wires, and the emission appears to be dominated by the smallest dimension.

#### 9.2.1.5 Summary

The structure behaviour appears to depend on the material, and to inhomogeneity in the etch process. For material with good uniformity and narrow linewidth, the dots, dashes and wires exhibit similar behaviour, with a consistent linear decrease in relative emission efficiency with reduction in structure dimension.

The behaviour of the wires is independent of the material, and shows a consistent linear decrease in relative emission efficiency with reduction in structure dimension, in a similar fashion to that of the dashes.

The samples solely of dots were fabricated on poorer material, and appear to be far more vulnerable to damage from the etch processing, and thus give rise to unpredictable results. The dot emission, apparently scaling with the filling factor of the remaining material, may be due to the introduction of traps and the quasi-amorphous nature of the damaged material.

As a result, it was decided to select the data from Dash samples 5 and 6 to be analysed. This was because they offered the widest range of structures, were fabricated on material which showed the best uniformity and brightest emission, and demonstrated consistent results for the dots, wires, and dashes.

### 9.2.2 Comparison of Results with Available Models

#### 9.2.2.1 Surface Model

When comparing the experimental data of Dash samples 5 and 6 with that derived with the model calculations, it was not possible to obtain a good fit between the two sets of data. A slightly different behaviour is observed. For example, in Figure (9.1) below, the data from the 6nm of wire structures on Dash Sample 6 is compared with data from the Surface Recombination Model applied to wires. The data points show a much slower decrease in relative emission efficiency with reducing wire width than the surface recombination model points for the best fit data, where S is $10^6$ $cms^{-1}$ , D is 5 $cm^2s^{-1}$ and $W_d$ is 100 nm, as derived in Chapter 8.

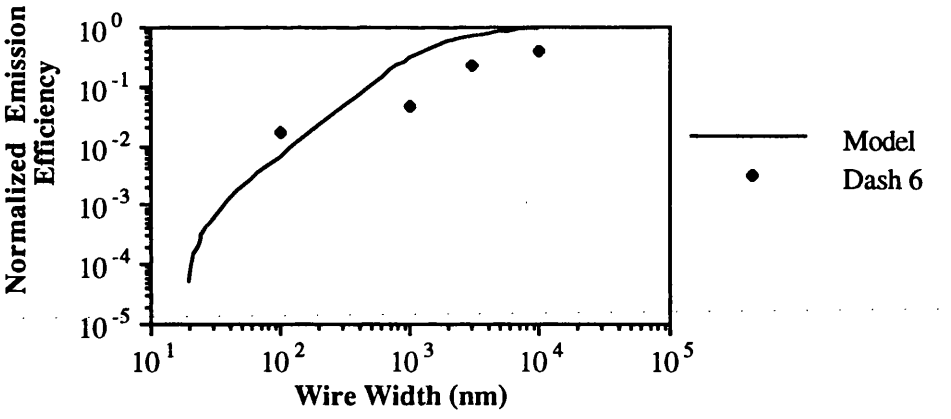


Figure (9.1): Comparison of Luminescence Intensity Dependence on Wire Width for
Dash Sample 6 with data from Equation {8.8}

The errors on the data are large, but a better fit is obtained by using a modification of the surface model, described later in this chapter.

#### 9.2.2.2 Bottleneck Model

Although the 'intrinsic' bottleneck model devised by Benisty et al. (1991), outlined in Chapter 8, suggests a rapid decrease in emission efficiency at small structure size, it suggests a constant behaviour of the emission intensity for the size régime of relevance to the structures fabricated. Thus there was insufficient data to corroborate the 'intrinsic' model.

The comparison is illustrated graphically below, with the experimental results of the 6 K emission efficiency of the 6 nm well of the dot structures of Dash 6, and the calculations of the emission efficiency of a 10 nm GaAs well at 4 K as published by Benisty et al.

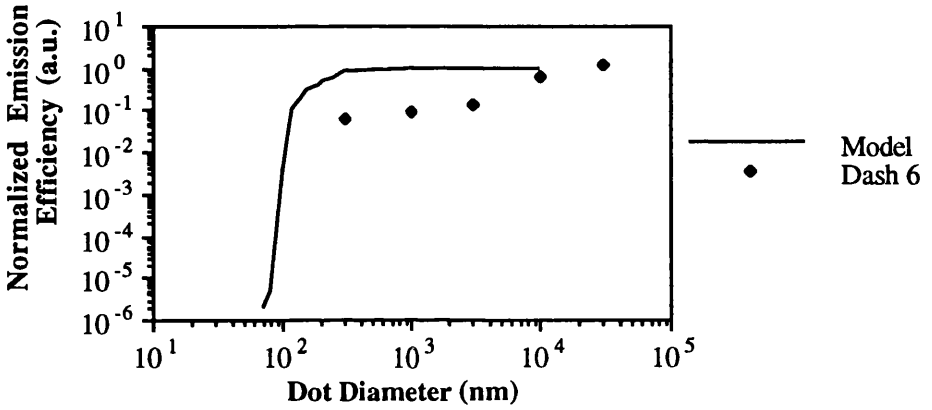


Figure (9.2): Comparison of Luminescence Intensity Dependence on Dot Diameter for Dash Sample 6 with data from Benisty et al. (1991)

The bottleneck model has no free parameters, and yields insufficient decrease in emission efficiency with size to fit the data comfortably in the size régime of interest.

#### 9.2.2.3 Trap Distribution Model

The trap distribution model yields too little variation in relative emission efficiency (a few percent) with structure size to fit the data, which varies in relative emission efficiency by several orders of magnitude.

#### 9.2.2.4 Strain-Dependent Recombination Model

This linear model has no need to invoke quantization in the largest structures, and does not require an absolute specification for the states at the surface. The linear dependence of the emission efficiency on R predicted by the model has a qualitative fit to the wires data from Dash 6.

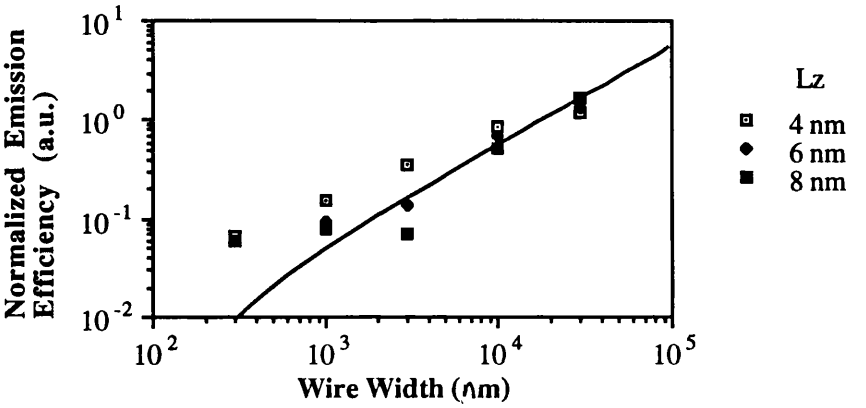


Figure (9.3): Comparison of Luminescence Intensity Dependence on Dot Diameter for Dash Sample 6 with linear fit from Equation {8.19}

### 9.2.3 Fit of models to data

The data of the best samples, as determined by the quality of the starting material, and the consistency of the data, was fitted by the available models.

The data from Dash samples 5 and 6 suggest that the relative emission efficiency is dominated by surface recombination on the smallest dimension, but this is moderated to an extent by the necessity of the electrons to tunnel through a shallow barrier.

This barrier is as a result of the relief, by etching, of the residual strain in the structures from the difference in thermal expansion of the GaAs well and the AlGaAs barriers.

## 9.3 Comparison with Data on Deeply Etched GaAs Structures

Apart from an initial report of an enhanced relative emission efficiency, and several reports of dot relative emission efficiency scaling as material remaining (see Chapter 3) (the scaling of the luminescence efficiency with the area coverage can also be observed in the dot-only samples prepared in this project), most current data reports a significant decrease in relative emission efficiency with reduction in structure dimensions. In general, the decrease is attributed to severe surface recombination in the as-etched state, with the surface recombination mitigated after regrowth.

In general, however, there is a consensus on the severely degrading effect of as-etched surfaces on GaAs quantum well structures, although the precise factors are still to be confirmed, and concentration is being directed towards overgrowth and direct-growth of structures.

## 9.4 Summary of Main Points

- Successful Fabrication of dots and wires down to 0.1 μm in GaAs system
- Successful Fabrication of intermediate structures:- dashes
- Characterization of these structures by low temperature photoluminescence
- Characterization of the starting material quantifies material variation
- Luminescence Efficiencies of Structures subject to wide variation
- Data obtained was consistent with other reports within the research group
- Luminescence Efficiencies data was material and etch-process dependent
- Large scatter on points-limited by material and observation method
- On 'good' material, on structures down to 0.1 μm, the luminescence emission efficiency reduces slowly with the reduction in structure size
- No difference in behaviour between dots, wires, and dashes
- Surface recombination model does not fit the reduction in emission efficiency
- New model proposed: Stress-relief after structure etching localizes carriers in a shallow potential well, inhibiting the surface recombination

# Chapter 10: Conclusions

## 10.1 Position of Current Work in Literature

This work reports for the first time the assesment of dots, wires, and dashes fabricated on the same samples. It enables the measurement of structures fabricated simultaneously, and thus attempts to unite the differing views on the emission efficiency behaviour of dots and wires, showing a consistent new overview.

Serious attempts were made to reduce the sample-to-sample variation by standardizing the production methodology, and by attempting to fabricate samples in batches to allow cross-comparison of samples with different structures.

Two new models were introduced: a 'trap distribution' model was devised to calculate the effect of varying filling factor on the relative emission efficiency. The 'Etch-Stress-Relief' model was designed to calculate the effect of a shallow potential well resulting from the relief of differing thermal expansion by etching on the electrons in the structures.

When fabricated on good quantum well material, as evidenced by high uniformity and a narrow free-exciton quantum well emission, the wires, dots, and dashes showed a consistent decrease in emission efficiency with reducing lateral dimensions. The decrease in emission efficiency is dominated by the smallest lateral dimension, due to the extremely rapid reduction in emission efficiency with size, and so little evidence may be seen of a emission eficiency-dash length dependence.

The data derived was best fitted by the 'Etch-Stress-Relief' model; the lack of a dependence of radiative emission efficiency on dash-length, and the lack of any free parameters, prevent the Benisty 'intrinsic' model fitting the data, and the data did not fit the 'Surface Recombination' model well on its own.

The data provide a useful function in eliminating the search for improved material and processing techniques for the deep-mesa etching route in order to obtain high emission efficiency of small structures; progress must be re-directed towards searching for methods to avoid the creation of free-surfaces in GaAs such as overgrowth and direct-growth.

The fundamental problem tackled in the thesis was that of the irreconcilable results obtained by studying the low-temperature photoluminescence of deep-mesa-etched dot and wire structures in GaAs /AlGaAs quantum wells.

This problem was approached by fabricating intermediate structures, by standardizing the fabrication methodology, and by batch producing the samples.

The results obtained from the processing depend crucially on the material quality. Variations across the material of quantum well width, aluminium content, and trap density give rise to an emission efficiency variation across the wafer, which confuses the emission efficiency variation due to the structure arrays. More accurate control of substrate temperature, the use of $As_2$ cracker sources, and the

understanding of processes giving rise to trap formation could lead to an improved material quality and better understanding of the structure emission efficiency size dependance.

Despite the attempt to reduce the scatter of the results by mass production of identical structures to derive an underlying trend being largely unsuccessful, this approach could be further exploited by fabrication of extremely large arrays of structures on single wafers, using a high-precision large-area electron-beam lithography system, such as a Beamwriter.

As done in this project, care must be taken to ensure uniform etching by performing the etching in small batches of material, but this may be extended to etching whole wafers in order to determine the etch-chamber uniformity precisely.

The tool of low-temperature photoluminescence is of limited use in this context. Investigations by photoluminescence excitation yield higher energy states in the quantum wells, and are less sensitive to impurity transitions. More accurate results would be the measurement of the luminescence from a large number of single structures, such as by cathodoluminescence, to enable a statistical analysis of luminescence efficiency.

More work is needed to determine the effect of etched surfaces on the radiative recombination of quantum structures. The radiative recombination efficiency is intimately dependent on a combination of confinement effects, fabrication effects, and quantum well trap distribution effects.

The following list summarizes some possible ways to improve the investigation of this subject:

1) Wide-area fabrication of structure arrays
2) Batch Production of Samples
3) Better material
4) Further investigation into the etch process
5) Single structure luminescence
6) Surface Studies: Ambient Control
7) Modelling of Contamination-Stressed Surfaces
8) Passivation of Material

# References


Altarelli M., in "Heterojunctions and Semiconductor Superlattices", Allan G., Bastard G., Boccara N., Lannoo M., and Voos M., eds., Springer-Verlag, Berlin, (1986)

Andrews S.R., and Arnot H.E.G., 5th International Conference on Superlattices and Microstructures, Berlin, August 13-16 (1990).

Andrews S.R., Arnot H., Kerr T.M., Rees P.K., and Beaumont S.P., in "Science and Engineering of One- and Zero-Dimensional Semiconductors", Beaumont S.P. and Sotomayor Torres C.M., eds., NATO ASI Series B: Physics **214**, Plenum Press, New York, (1990a)

Antoniadis D.A., Ismail K., and Smith H.I., in "Science and Engineering of One- and Zero-Dimensional Semiconductors", Beaumont S.P. and Sotomayor Torres C.M., eds., NATO ASI Series B: Physics **214**, Plenum Press, New York, (1990)

Arakawa Y., and Sakaki H., Applied Physics Letters **40** 939 (1982)

Arakawa Y., Vahala K., Yariv A., and Lau K., Applied Physics Letters **47** 1142 (1985)

Arnot H. E. G., Ph.D. Thesis, Glasgow University, (1990)

Arnot H., Andrews S.R., and Beaumont S.P., Microelectronic Engineering **9** 365 (1989c)

Arnot H.E.G., Sotomayor Torres C.M., Cusco R., Watt M., Glew R., and Beaumont S.P., in "Quantum wells for Optics and Optoelectronics", Technical Digest Series Vol. 10, Optical Society of America, p. 83, (1989b).

Arnot H.E.G., Watt M., Sotomayor Torres C.M., Glew R., Cusco R., Bates J., and Beaumont S.P., Superlattices and Microstructures **5** (3) 459 (1989)

Aspnes D.E., Kelso S.M., Logan R.A., and R. Bhat, Journal of Applied Physics **60** (2) 754 (1986)

Aspnes D.E., Surface Science **132** 406 (1983)

Aspnes, D.E., "Handbook on Semiconductors", **2**, Moss T.S. ed., North-Holland, Amsterdam, (1980).

Austin E.J., Semiconductor Science and Technology **3** 960 (1988)

Banyai L., Lindberg M., and Koch S.W., Optics Letters **13** (3) 212 (1988)

Barford N.C., "Experimantal Measurements: Precision, Error and Truth", 2nd edition, Chapter 2, John Wiley and Sons, Chichester, (1985)

Bastard G., "Wave Mechanics Applied to Semiconductor Heterostructures", Edition de Physique, Les Ulis, (1988)

Bastard G., and Brum J.A., IEEE Journal of Quantum Electronics **QE-22** (9) 1625 (1986)

Bastard G., Delalande C., Meynadier M.H., Frijlink P.M., and Voos M., Physical Review **B29** (12) 7042 (1984)

Bastard G., Mendez E.E., Chang L.L., and Esaki L., Physical Review **B26** (4) 1974 (1982)

Beaumont S.P. and Sotomayor Torres C.M., eds., "Science and Engineering of One- and Zero-Dimensional Semiconductors", NATO ASI Series B: Physics **214**, Plenum Press, New York, (1990)

Benisty H., Sotomayor Torres C.M. and Weisbuch C., Physical Review **B44** (19) 10945 (1991)

Besser R.S., and Helms C.R., Applied Physics Letters **52** (20) 1709 (1988)

Bhat R., Kapon E., Hwang D., Koza M., and Yun C., Journal of Crystal Growth **93** 850 (1988)

Bhat R., Kapon E., Simhony S., Colas E., Hwang D.M., Stoffel N.G., and Koza M.A., Journal of Crystal Growth **107** 716 (1991)

Bimberg D., Mars D., Miller J.N., Bauer R., and Oertel D., Journal of Vacuum Science and Technology **B4** (4), 1014 (1986)

Birotheau L., Izrael A., Marzin J.Y., Azoulay R., Thierry-Mieg V., and Ladan F.R., Applied Physics Letters **61** (25) 3023 (1992)

Bishop S.G., "Characterization of GaAs by PL and FTIS", in "GaAs Technology" Ferry D.K., ed., **2** Ch. 11 , Howard Sams and Co., (1990)

Bockelmann U., and Bastard G., Physical Review **B42** 8947 (1990)

Brown J.W., and Spector H. N., Physical Review **B35** (6) 3009 (1987)

Brus L., IEEE Journal of Quantum Electronics **QE-22** (9) 1909 (1986)

Bryant G.W., in "Science and Engineering of One- and Zero-Dimensional Semiconductors", (Beaumont S.P. and Sotomayor Torres C.M., eds.), NATO ASI Series B: Physics Vol. 214, Plenum Press, New York, (1990)

Bryant G.W., Physical Review **B29** (12) 6632 (1984)

Bryant G.W., Physical Review **B31** (12) 7812 (1985)

Bryant G.W., Physical Review **B37** (15) 8763 (1988)

Burnham R.D., Streifer W., Paoli T.L., Journal of Crystal Growth **68** 370 (1984)

Cao M., Daste P., Miyamoto Y., Miyake Y., Nogiwa S., Arai S., Furuya K., and Suematsu Y., Electronics Letters **24** (13) 824 (1988)

Capasso F., in "Semiconductors and Semimetals", Willardson R.K. and Beer A.C., eds., **24**, Chapter 6, Academic Press, New York, (1987)

Challis L.J., "Physics in Less Than Three Dimensions", Contemporary Physics **33** (2) 111 (1992)

Chen Y.J., Koteles E.S., Lee J., Chi J.Y., and Elman B.S., SPIE **792** *Quantum Well and Superlattice Physics* 162 (1987)

Cheung R. Thoms S., Beaumont S.P., Doughty G., Law V., and Wilkinson C.D.W., Electronics Letters **23** (16) 857 (1987)

Cheung R. Thoms S., McIntyre I., Wilkinson C.D.W., and Beaumont S.P., Journal of Vacuum Science and Technology **B 6** (6) 1911 (1988)

Chikyow T., and Koguchi N., Applied Physics Letters **61** (20) 2431 (1992)

Chikyow T., and Koguchi N., in Material Research Society Extended Abstracts of Symposium Y: Nanostructures EA-26, US Materials Research Society Fall Conference, Boston, MA, USA, p.43, (1991)

Cho A.Y., and Arthur J.R., Progress in Solid State Chemistry, **10** 157 (1975)

Christen J., Grundsmann M., Kapon E., Colas E., Hwang D.M., and Bimberg D., Applied Physics Letters **61** (1) 67 (1992)

Cibert J., and Petroff P.M., Physical Review **B36** (6) 3243 (1987)

Cibert J., Petroff P.M., Dolan G.J., Pearton S.J., Gossard A.C., and English J.H., Applied Physics Letters **49** (19) 1275 (1986)

Cibert J., Petroff P.M., Dolan G.J., Werder D.J., Pearton S.J., Gossard A.C., and English J.H., Superlattices and Microstructures **3** (1) 35 (1987)

Clausen E.M. Jr., Craighead H.G., Worlock J.M., Harbison J.P., Schiavone L.M., Florez L., and van der Gaag B., Applied Physics Letters **55** (14) 1427 (1989)

Clausen E.M., Kapon E., Tamargo M.C., and Hwang D.M., Applied Physics Letters **56** (8) 776 (1990)

Colas A., Kapon E., Simhony S., Cox H., Bhat R., Kash K., and Lin P., Applied Physics Letters **55** (9) 867 (1989)

Colas E., Clausen E.M. Jr., Kapon E., Hwang D.M., and Simhony S., Applied Physics Letters **57** (23) 2472 (1990a)

Colas E., Simhony S., Kapon E., Bhat R., Hwang D., and Lin P.S.D., Applied Physics Letters **57** (9) 914 (1990b)

Cooper C.B. III, Salimian S., and MacMillan H.F., Applied Physics Letters **51** (26) 2225 (1987)

Cox H., Lin P., Yi-Yan A., Kash K., Seto M., and Bastos P., Applied Physics Letters **55** (3) 472 (1989a)

Cox H., Morais P., Hwang D., Bastos P., Gmitter T., Nazar L., Worlock J., Yablonovitch E., and Hummel S., "InGaAs/InP quantum wells and quantum wires grown by vapor levitation epitaxy using chloride transport" Institute of Physics Conference Series **96** 119 (1989b)

Cox H.M., Lin P.S., Yi-Yan A., Kash K., and Bastos P., Applied Physics Letters **55** (5) 472 (1989c)

Dawson P., Duggan G., Ralph H.I., Woodbridge K., Physical Review **B28** (12) 7381 (1983)

Dawson P., Moore K.J., Duggan G., Ralph H.I., and Foxon C.T.B., Physical Review **B34** (8) 6007 (1986)

Degani M.H., and Hipólito O., Physical Review **B35** (17) 9345 (1987)

Demeester P., van Daele P., and Baets R., Journal of Applied Physics **63** (7) 1988

Demel T., Heitmann D., Grambow P., and Ploog K., Applied Physics Letters **53** (22) 2176 (1988)

Deveaud B., Emery J.Y., Chomette A., Lambert B., and Baudet M., Applied Physics Letters **45** (10) 1078 (1984)

Deveaud B., Regreny A., Emery J.-Y., and Chomette A., Journal of Applied Physics **59** (5) 1633 (1986)

Dingle R., Wiegmann W., and Henry C.H., Physical Review Letters **33** 827 (1974)

Duggan G., Ralph H.I., Moore K.J., Physical Review **B32** (12) 8395 (1985)

Esaki L., and Chang L.L., Physical Review Letters **33** 495 (1974)

Foad M.A., Hefferman S., Chapman J.N., and Wilkinson C.D.W., Institute of Physics Conference Series **122** 293 (1990)

Forchel A., Leier H., Maile B.E., and Germann R., Festkörperprobleme / Advances in Solid State Physics **28**, 99 Vieweg, Braunschweig, (1988).

Forchel A., Maile B.E., Leier H., Mayer G., and German R., in "Science and Engineering of One-and Zero-Dimensional Semiconductors", Beaumont S.P. and Sotomayor Torres C.M., eds., NATO ASI Series B: Physics **214**, Plenum Press, New York, (1990)

Forchel A., Maile B.E., Leier H., Mayer G., and Germann R., "Optical Emission from Quantum Wires", in *Science and Engineering of One- and Zero-Dimensional Semiconductors*, S.P. Beaumont and C.M. Sotomayor Torres eds., NATO ASI Series B: Physics Vol. 214, Plenum Press, New York, (1990)

French A.P., and Taylor E.F., "An Introduction to Quantum Physics", Chapman and Hall, New York, 1978.

Fujiwara K., Kanamoto K., and Tsukuda N., Physical Review **B40** (14) 9698 (1989)

Fujiwara K., Kanamoto K., Tsukuda N., Miyatake H., and Koyama H., Journal of Applied Physics **66** (3) 1488 (1989)

Fukui T., and Saito H., Applied Physics Letters **62** (4) 466 (1989)

Fukui T., Ando S., Tokura Y., and Toriyama T., Applied Physics Letters **58** (18) 2018 (1991)

Gaines J.M., Petroff P.M., Kroemer H., Simes R.J., Geels R.S., and English J.H., Journal of Vacuum Science and Technology **B6** 1378 (1988)

Galeuchet Y., and Roentgen P., "Selective area MOVPE of GaInAs/InP heterostructures on masked and non-planar (100) and {111} substrates", Proceedings of the 5th International Conference on Metal-Organic Vapour Phase Epitaxy, Aachen (1990a)

Galeuchet Y., Roentgen P., and Graf V., Applied Physics Letters **53** (26) 2638 (1988)

Galeuchet Y., Roentgen P., and Graf V., Journal of Applied Physics **68** (2) 560 (1990b)

Galeuchet Y., Rothuizen H., and Roentgen P., Applied Physics Letters, **58** (21) 2423 (1991)

Galeuchet Y.D., Röntgen P., Nilsson S., and Graf V., "Fabrication of buried GaInAs/InP quantum wires by one-step MOVPE growth" in "Science and Engineering of 1- and 0- dimensional semiconductors", Beaumont S.P. and Sotomayor Torres C.M., eds., NATO ASI Series B: Physics **214**, Plenum Press, New York, (1990)

Gay J.G., and Klauder L.T., Physical Review **172** 811 (1968)

Gershoni D., Temkin H., Dolan G.J., Dunsmuir J., Chu S.N.G., and Panish M.B., Applied Physics Letters **53** (1) 995 (1988)

Goñi A.R., Pfeiffer L.N., West K.W., Pinczuk A., Baranger H.V., and Stormer H.L., Applied Physics Letters **61** (16) 1956 (1992)

Gossard A.C., English J.H., Petroff P.M., Cibert J., Dolan G.J., and Pearton S.J., Journal of Crystal Growth **81** 101 (1987)

Greene R.L., Bajaj K. K., and Phelps D.E., Physical Review **B29** (4) 1807 (1984)

Gréus Ch., Forchel A., Straka J., Pieger K., and Emmerling M., Applied Physics Letters **61** (10) 1199 (1992)

Hamamatsu Photonics Photomultiplier Tubes Guide (Jan 1988) p.46

Hamao N., Sugimoto M., Kohmoto S., and Yokoyama H., Applied Physics Letters **59** (12) 1488 (1991)

Hamilton T.D.S., Munro I.H., and Walker G., "Luminescence Instrumentation", p.179, in 'Luminescence Spectroscopy', Lumb M.D., ed., Academic Press, London, (1978)

Hanamura E., Journal de Physique Colloque **49** (6) C2-213 (1988a)

Hanamura E., Physical Review B**38** 1228 (1988b)

Hasegawa H., Ishii H., Sawada T., Saitoh T., Konishi S., Liu Y., and Ohno H., Journal of Vacuum Science and Technology **B6** (4) 1184 (1988)

Hayakawa T., Suyama T., Takahashi K., Kondo M., Yamamoto S., Yano S., and Hijikata T., Applied Physics Letters **47** (9), 952 (1985)

Heitmann D., Kohl M., Grambow P., and Ploog K., in "Science and Engineering of One- and Zero-Dimensional Semiconductors", Beaumont S.P. and Sotomayor Torres C.M., eds., NATO ASI Series B: Physics **214**, Plenum Press, New York, (1990)

Heitmann D., Lage H., Kohl M., Cingolani R., Grambow P., and Ploog K., Institute of Physics Conference Series **123**, 109 (1991)

Hermann M.A., Bimberg D., and Christen J., Journal of Applied Physics **70** (2) R1 (1991)

Hillmer H., Forchel A., Sauer R., and Tu C.W., Physical Review **B42** (5) 3220 (1990)

Hirayama Y., Tarucha S., Suzuki Y., and Okamoto H., Physical Review **37** (5) 2774 (1988)

Hiruma K., Katsuyama T., Ogawa K., Koguchi M., Kakibayashi H., and Morgan G.P., Applied Physics Letters **59** (4) 431 (1991)

Hodes G., Albu-Yaron A., Decker F., and Motisuke P., Physical Review **B36** 4215 (1987)

Hoffman C.A., Jarasiunas K., Gerritsen H.J., and Nurmikko A.V., Applied Physics Letters **33** (6) 536 (1978)

Hong S., and Singh J., Applied Physics Letters **49** (6) 331 (1986)

Hornischer W., Grambow P., Demel T., Bauser E., Heitmann D., von Klitzing K., and Ploog K., Applied Physics Letters **60** (24) 2998 (1992)

Hu E.L., and Howard R.E., Applied Physics Letters **37** (11) 1022 (1980)

Hu E.L., and Howard R.E., Journal of Vacuum Science and Technology **B2** (1) 85 (1984)

Iida S., and Ito K., Journal of the Electrochemical Society **118** 768 (1971)

ISA Jobin-Yvon THR1000 Monochromator Instruction Manual p. 7, April (1985)

Ismail K., Burkhardt M., Smith H.I., Karam N.H., Sekula-Moise P.A., Applied Physics Letters **58** (14) 1539 (1991)

Ives N.A., Stupian G.W., and Leung M.S., Applied Physics Letters **50** (5) 356 (1987)

Izrael A., Sermage B., Marzin J.Y., Ougazzaden A., Azoulay R., Etrillard J., Thierry-Mieg V., and Henry L., Applied Physics Letters **56** (9) 830 (1990)

Izrael A., Sermage B., Marzin J.Y., Ougazzaden A., Azoulay R., Etrillard J., Thierry-Mieg V., and Henry L., Applied Physics Letters **56** (9) 830 (1990)

Jaros M., Reports of Progress in Physics **48** 1091 (1985)

Juang F.-Y., Nashimoto Y., and Bhattacharya P., Journal of Applied Physics **58**(5), 1986 (1985)

Kanbe H., Chavez-Pirson A., Ando H., Saito H., and Fukui T., Applied Physics Letters **58** (25) 2969 (1991)

Kapon E., Hwang D.M., and Bhat R., Physical Review Letters **63** (4) 430 (1989a)

Kapon E., Kash K., Clausen J.M. Jr., Hwang D.M., and Colas E., Applied Physics Letters **60** (4) 477 (1992)

Kapon E., Simhony S., and Hwang D.M., Applied Physics Letters **55** (26) 2715 (1989b)

Kapon E., Tamargo M., and Hwang D., Applied Physics Letters **50** (6) 347 (1987)

Kash K., Bhat R., Mahoney D.D., Lin P.S.D., Scherer A., Worlock J.M., van der Gaag B.P., Koza M., and Grabbe P., Applied Physics Letters **55** (7) 681 (1989)

Kash K., Journal of Luminescence **46** 69 (1990)

Kash K., Scherer A., Worlock J.M., Craighead H.G., Tamargo M.C., Applied Physics Letters **49** (16) 1043 (1986)

Kash K., Worlack J.M., Gozdz A.S., van der Gaag B.P., Harbison J.P., Lin P.S.D., and Florez L.T., Eighth International Conference on Electronic Processes in Two Dimensional Semiconductors, Grenoble, France, 1989, in Surface Science **229**, 245 (1990b)

Kash K., Worlack J.M., Mahoney D.D., Gozdz A.S., van der Gaag B.P., Harbison J.P., Lin P.S.D., and Florez L.T., Surface Science **228** 415 (1990a)

Kash K., Worlock J.M., Craighead H.G., Tamargo M.C., Applied Physics Letters **49** (16) (1986)

Kash K., Worlock J.M., Sturge M.D., Grabbe P., Harbison J.P., Scherer A., and Lin P.S.D., Applied Physics Letters **53** 782 (1988)

Kittel C., "Introduction to Solid State Physics", John Wiley and Sons, 6th Edition, New York, 1986, p. 372.

Klinger R.E., and Greene J.E., Applied Physics Letters **38** (8) 620 (1981)

Koenig H.R., and Maissel L.I., IBM Journal of Research and Development **14** 168 (1970)

Kohl M., Heitmann D., Grambow P., and Ploog K., Physical Review **B37** 10927 (1988)

Kohl M., Heitmann D., Grambow P., and Ploog K., Physical Review **B42** (5) 2941 (1990)

Kohl M., Heitmann D., Grambow P., and Ploog K., Physical Review Letters **63** (19) 2124 (1989)

Kojima K., Mitsunaga K., Kyuma K., Applied Physics Letters **56** (2) 154 (1990)

Korinfskiĭ A.D., and Musatov A.L., Phys. Chem. Mech. Surf. **2** (8) 2455 (1985)

Korinfskiĭ A.D., and Musatov A.L., Physics, Chemistry, and Mechanical Properties of Surfaces **2** (8) 2455 (1985)

Koteles E.S., Elman B.S., Jaggannath C., and Chen Y.J., Applied Physics Letters **49**(21), 1465 (1986)

Kotthaus J., and Merkt U., in "Science and Engineering of One- and Zero-Dimensional Semiconductors", Beaumont S.P. and Sotomayor Torres C.M., eds., NATO ASI Series B: Physics Vol. 214, Plenum Press, New York, (1990)

Kubena R.L., Applied Physics Letters **50** (22) 1589 (1987)

Kuech T.F., Wolford D.J., Potemski R., Bradley J.A., Kelleher K.H., Yan D., Farrell J.P., Lesser P.M.S., and Pollak F.H., Applied Physics Letters **51** (7) 505 (1987)

Lage H., Heitmann D., and Cingolani R., 12th EPS-CMD, Prague, April 1992a

Lage H., Heitmann D., and Cingolani R., to appear in "Optics of Semiconducting Nanostructures", Henneberger F., and Schmitt-Rink S., eds., May (1992b)

Lebens J.A., Tsai C.S., Vahala K.J. and Kuech K.J., Applied Physics Letters **56** (26) 2642 (1990)

Lee J., Koteles E. S., and Vassell M. O., Physical Review **B33**, (8) 5512 (1986)

Lee K.Y., Smith T.P. III, Arnot H., Knoedler C.M., Hong J.M., Kern D.P., and Laux S.E., Journal of Vacuum Science and Technology **B6** (6) 1856 (1988)

Leier H. Forchel A., B.E., Mayer G., Hommel J., Weimann G., Schlapp W., Applied Physics Letters **56** (1) 48 (1990)

Leier H., Forchel A., Maile B., and Weimann G., Microelectronic Engineering **9** 361 (1989)

Maile B.E., Forchel A., Germann R., Menschig A., Meier H.P., and Grützmacher D., Journal of Vacuum Science and Technology **B6** (6) 2308 (1988)

Maile B.E., Forchel A., Germann R., Menschig A., Streubel K., Scholz F., Weimann G., and Schlapp W., Microcircuit Engineering, **6** 163 (1987)

Maile B.E., Forchel A., Germann R., Straka J., Korte L., and Thanner C., Applied Physics Letters **57** (8) 807 (1990)

Many A., Goldstein Y., and Grover N.B., "Semiconductor Surfaces", North Holland, Amsterdam, 1965

Masselink W.T., Chang Y.-C., and Morkoç H., Journal of Vacuum Science and Technology **B2** (3) 376 (1984)

Mayer G., Maile B.E., Germann R., Forchel A., Grambow P., and Meier H.P., Applied Physics Letters **56** (20) 2016 (1990)

Miyamoto Y., Cao M., Shingai Y., Furuya K., Suematsu Y., Ravikumar K.G., and Arai S., Japanese Journal of Applied Physics **26** (4) L225 (1987)

Mogab C.J., "Dry Etching", in 'VLSI Technology', Sze S.M. ed., McGraw Hill, New York, (1983)

Moore K.J., Dawson P., and Foxon C.T., Physical Review **B34** (8) 6022 (1986)

Morgan G.P., Ogawa K., Hiruma K., Kakibayashi H., and Katsuyama T., Solid State Communications **80** (3) 235 (1991)

Nahory R.E. and Shay J.L., Physical Review Letters **21** 1569 (1968)

Nair S.V., Sinha S., and Rustagi K.C., Physical Review **B35** 4098 (1987)

Nakamura Y., Koshiba S., Tsuchiya M., Kano H., and Sakaki H., Applied Physics Letters **59** (6) 700 (1991)

Nelson R.J., Williams J.S., Leamy H.J., Miller B., Casey H.C., Parkinson B.A., and Heller A., Applied Physics Letters **36** (1) 76 (1980)

Notomi M., Naganuma M., Nishida T., Tamamura T., Iwamura H., Nojima S., and Okamoto N., Applied Physics Letters **58** (7) 720 (1991)

Offsey S.D., Woodall J.D., Warren A.C., Kirchner P.D., Chappell T.I., and Pettit T.I., Applied Physics Letters **48** (7) 475 (1986)

Olego D.J., Schachter R., and Baumann J.A., Applied Physics Letters **45** (10) 1127 (1984)

Olego D.J., Schachter R., and Baumann J.A., Journal of Vacuum Science and Technology **B3** (4) 1097 (1985)

Osório F.A.P., Degani M.H., and Hipólito O., Physical Review **B37** (3) 1402 (1988)

Pankove J.I., "Optical Processes in Semiconductors", Dover Publications Inc, New York (1971)

Patillon J.-N., Jay C., Delalande C., Iost M., Andre J.-P., le Coz H., Signles-Frehel M., Vlaeminck O., and Soucail B., Japanese Journal of Applied Physics **30** (2B) L252 (1991)

Pearah P.J., Klem J., Peng C.K., Henderson T., Masselink W.T., Morkoç H., and Reynolds D.C., Applied Physics Letters **47** (2) 166 (1985)

Petroff P., Gossard A., and Wiegmann W., Applied Physics Letters **45** (6) 620 (1984)

Petroff Y., "Handbook on Semiconductors", **2**, Moss T.S., ed., North-Holland, Amsterdam, (1980)

Philips J.C., "Bonds and Bands in Semiconductors", Academic Press, New York (1973)

Pollak F.H., and Glembocki O.J., "Modulation Spectroscopy of Semiconductor Microstructures: An Overview", in SPIE **946** 2 (1988)

Qiang H., Pollak F.H., Sotomayor Torres C.M., Leitch W.E., Kean A.H., Stroscio M.A., Iafrate G.I., and Kim K.W., Applied Physics Letters **61** (12) 1411 (1992)

Qiang H., Pollak F.H., Tang Y.-S., Wang P.D., and Sotomayor Torres C.M., "Characterization of Process-Induced Strains in GaAs / GaAlAs Quantum Dots Using Room Temperature Photoreflectance", in submission to Applied Physics Letters, August (1993)

Randall J.N., Reed M.A., Matyi R.J., and Moore T.M., Journal of Vacuum Science and Technology **B6** (6) 1861 (1988b)

Randall J.N., Reed M.A., Moore T.M., Matyi R.J., and Lee J.W., Journal of Vacuum Science and Technology **B6** (1) 302 (1988a)

Reed M.A., "Quantum Dots", *Scientific American*, **268** (1) 98 (1993)

Reed M.A., "The Quantum Transistor", *Byte*, May (1989)

Reed M.A., Bate R.T., Bradshaw K., Duncan W.M., Frensley W.R., Lee J.W., and Shih H.D., Journal of Vacuum Science and Technology **B4** (1) 358 (1986)

Reed M.A., Randall J.N., Aggarwal R.J., Matyi R.J., Moore T.M., and Wetsel A.E., Physical Review Review Letters **60** (6) 535 (1988)

Reynolds D.C., Bajaj K.K., Litton C.W., Yu P.W., Masselink W.T., Fischer R., and Morkoç H., Physical Review **B29**(12) 7038 (1984)

Ridley B.K., "Quantum Processes in Semiconductors", Oxford University Press, 2nd edition, Oxford (1988), p. 34.

Rodden W.R., PhD Thesis, Glasgow University, (1993)

Rorison J.M., and Herbert D.C., Superlattices and Microstructures **1** (5) 423 (1985)

Rose-Innes A. C., 'Low Temperature Laboratory Techniques', p. 135

Salimian S., and Cooper C.B. III, Journal of Vacuum Science and Technology **B6** (6) 1641 (1988)

Salimian S., Cooper C.B. III, Norton R., and Bacon J., Applied Physics Letters **51** (14) 1083 (1987)

Sanders G.D., and Chang Y.-C., Physical Review **B32** (8) 5517 (1985)

Sandroff C.J., Nottenburg R.N., Bischoff J.-C., and Bhat R., Applied Physics Letters **51** (1) 33 (1987)

Sato M., and Nakamura H., Journal of Vacuum Science and Technology **20** 186 (1982)

Scherer A., Applied Physics Letters **49** (19) 1284 (1986)

Schiff L.I., " Quantum Mechanics", 3rd Edition, McGraw-Hill, New York, (1968)

Schmitt-Rink S., Miller D.A.B., and Chemla D.S., Physical Review **B35** 8113 (1987)

Seaward K.L., Moll N.J., Coulman D.J., and Stickle W.F., Journal of Applied Physics **61** (6) 2358 (1987)

Seraphin, B. O., and N. Bottka, Phys. Rev **139**, A560 (1965)

Shaw D.W., Journal of the Electrochemical Society, **128** (4) 874 (1981)

Singh J., Bajaj K.K., and Chaudhuri S., Applied Physics Letters **44** (8), 805 (1984)

Skromme B.J., Sandroff C.J., Yablonovitch E., and Gmitter T., Applied Physics Letters **51** (24) 2022 (1987)

Smith T.P. III, Arnot H., Hong J.M., Knoedler C.M., Laux S.E., and Smid H., Physical Review Letters **59** 2081 (1987)

Smolinsky G., Chang R.P., and Mayer T.M., Journal of Vacuum Science and Technology **18** (1), 12 (1981)

Sollner T.C.L.G., Goodhue W.D., Tannenwald P.E., Parker C.D., and Pech D.D., Applied Physics Letters **43**, 588 (1983)

Sols F., Macucci M., Ravaioli U., and Hess K., Physical Review Letters **54** 350 (1989)

Sonek G.J., and Ballantyne J.M., Journal of Vacuum Science and Technology **B2** (4) 653 (1984)

Sotomayor Torres C.M., in "Physics of Nanostructures", Davies J.H., and Long A.R., eds., Adam Hilger, Bristol, (1992)

Sotomayor Torres C.M., Wang P.D., Leitch W.E., Benisty H., and Weisbuch C., "Radiative Recombination in GaAs-GaAlAs Wires and Dots", in 'Excitons in Confined Systems', Quadropani A., ed., Institute of Physics, (1991)

Sotomayor Torres C.M., Watt M., Arnot H.E.G., Glew R., Cusco Cornet R., Kerr T.M., Thoms S., and Beaumont S.P., Surface Science **228** 275 (1990a)

Sotomayor Torres C.M., Watt M., Arnot H.E.G., Glew R., Leitch W.E., Kean A.H., Cusco Cornet R., Kerr T.M., Thoms S., Beaumont S.P., Johnson N.P., and Stanley C.R., in "Science and Engineering of One- and Zero-Dimensional Semiconductors", Beaumont S.P. and Sotomayor Torres C.M., eds., NATO ASI Series B: Physics **214**, Plenum Press, New York, (1990b)

Spindt C.J., and Spicer W.E., Applied Physics Letters **55** (16) 1654 (1989)

Spindt C.J., Besser R.S., Cao R., Miyano K., Helms C.R., and Spicer W.E., Applied Physics Letters **54** (12) 1148 (1989)

Stanley C.R., Holland M.C., and Kean A.H., Applied Physics Letters **58** 478 (1991)

Stern M.B., and Liao P.F., Journal of Vacuum Science and Technology **B1**(4) 1053 (1983)

Stern M.B., Applied Physics Letters **45** (4) 410 (1984)

Stradling R.A., and Klipstein P.C., "Growth and Characterization of Semiconductors", Adam Hilger, Bristol (1990), Stukel D.J., and Euwema R.N., Physical Review **188** (3) 1193 (1969)

Sun Y.L., Fischer R., Klein M.V., Morkoç H., and Mendez E.E., Thin Solid Films **112** 213 (1984)

Takagahara T., Physical Review **B36** (17) 9293 (1987)

Takahashi T., Arakawa Y., Nishioka M., and Ikoma T., Applied Physics Letters **60** (1) 69 (1992)

Tan I.-H., Lishan D., Mirin R., Jayaraman V., Yasuda T., Hu E.L., and Bowers J., Applied Physics Letters **59** (15) 1875 (1991)

Tan I.-H., Mirin R., Jayaraman V., Shi S., Hu E.L., and Bowers J., Applied Physics Letters **61** (3) 300 (1992)

Tanaka M. and Sakaki H., Journal of Crystal Growth **81** 153 (1987)

Tarui Y., Komiya Y., Harada Y., Journal of the Electrochemical Society **110** 585 (1963)

Temkin H., Dolan G.J., Panish M.B., and Chu S.N.G., Applied Physics Letters **50** (7) 413 (1987)

Thomas H., Morgan D.V., Thomas B., Aubrey J.E., and Morgan G.B., "Gallium Arsenide for Devices and Integrated Circuits", IEE Electrical & Electronic Materials and Devices Series 3, Peter Peregrinus Ltd, London, (1986)

Thoms S., Journal of Vacuum Science and Technology **B6** (1) 127 (1988)

Tsai C.S., Lebens J.A., Ahn C.C., Nouhi A., and Vahala K.J., Applied Physics Letters **60** (2) 240 (1992)

Tsang W.T., in "Semiconductors and Semimetals", Willardson R.K. and Beer A.C., eds., **24** p. 397, Academic Press, New York, (1987)

Tsuchiya M., Coldren L., Petroff P., Proceedings IOOC Conf. 1989a, Paper 19C1-1, p. 104

Tsuchiya M., Gaines J., Yan R., Simes R., Holtz P., Coldren L., and Petroff P., Physical Review Letters **62** (4) 466 (1989b)

Tsukamoto S., Nagamune Y., Nishioka M., Arakawa Y., Applied Physics Letters **62** (1) 49 (1993)

Vahala K., Arakawa Y., and Yariv A., Applied Physics Letters **50** (7) 365 (1987)

Vahala K., IEEE Journal of Quantum Electronics **24** (3) 523 (1988)

Vermeire G., Buydens L., Vermaerke F., de Dobbelaere P., van Daele P., and Demeester P., "Fabrication and characterisation of AlGaAs/GaAs/InGaAs quantum well wires on corrugated substrates by Metal-Organic Vapour Phase Epitaxy", presented at the 4th European Workshop on MOVPE, Nijmegen, (1991)

Vodjdani N., and Parrens P., Journal of Vacuum Science and Technology **B5** (6) 1591 (1987)

Voillot F., Madhukar A., Kim J.Y., Chen P., Cho N.M., Tang W.C., and Newman P.G., Applied Physics Letters **48** (15) 1009 (1986)

Wallis R.F., and Sébenne C.A., "Handbook on Semiconductors", **2**, North Holland, Amsterdam, (1980)

Wang E.Y., Albers W.A., and Bleil C.E., in proceedings of the International Conference on II-V Semiconducting Componds, Providence, Rhode Island, USA, 1967, W. A. Benjamin Inc., New York, (1968)

Wang P.D., and Sotomayor Torres C.M., "Phonons in Semiconductor Nanostructures", Leburton J.-P., Pascual J., and Sotomayor Torres C.M., eds., Kluwer Academic Publishers, (1993)

Wang P.D., Sotomayor Torres C.M., Benisty H., Weisbuch C., and Beaumont S.P., Applied Physics Letters **61** (8) 946 (1992)

Warnock J, and Awschalom D.D., Physical Review **B32** (8) 5529 (1985)

Watt M., Ph.D. Thesis, Glasgow University, (1988)

Weiner J.S., Danaan G., Pinczuk A., Valladares J., Pfeiffer L.N., and West K., Physical Review Letters **63** (15) 1641 (1989)

Weiner J.S., Danaan G., Pinczuk A., Valladares J., Pfeiffer L.N., and West K., Surface Science **228** 412 (1990)

Weisbuch C., and Vinter B., "Quantum Semiconductor Structures:- Fundamentals and Applications", Academic Press, New York, (1991)

Weisbuch C., Dingle R., Gossard A.C., and Wiegmann W., Solid State Communications **38** 709 (1981)

Weisbuch C., Dingle R., Petroff P.M., Gossard A.C., and Wiegmann W., Applied Physics Letters **38**(11), 840 (1981)

Weisbuch C., Miller R.C., Dingle R., Gossard A.C., and Wiegmann W., Solid State Communication **37** 219 (1981)

Weisbuch C., Sotomayor Torres C.M., and Benisty H., in: "Nanostructures and Mesoscopic Systems", Kirk W. P., and Reed M. A., eds., Academic Press, Boston (1992)

Weman H., Miller M.S., Kroemer H., Petroff P.M., and Merz J.L., in Material Research Society Extended Abstracts of Symposium Y: Nanostructures EA-26, US Materials Research Society Fall Conference, Boston, MA, USA (1991)

Wieder H.H., Surface Science **132** 390 (1983)

Wilson B.A., Miller R.C., Sputz S.K., Harris T.D., Sauer R., Lamont M.G., Tu C.W., and Kopf R.F., Institute of Physics Conference Series **83** 215 (1986)

Wolfe C.M., Holonyak N.Jr., Stillman G.E., "Physical Properties of Semiconductors", Prentice Hall, NJ, 1989

Woodgate G.K., "Elementary Atomic Structure", Oxford University Press, 2nd edition, Oxford, (1980)

Worlock J.M., Kash K., Scherer A., Craighead H.G., Tamargo M.C., Journal of Optical Society **B3** (8) 246 (1986)

Wu W.-Y., Schulman J.N., Tsu T.Y., and Efron U., Applied Physics Letters **51** (10) 710 (1987)

Xie Y., Chen W., Huang Y., Chen Z., Lu Z., Yang G., Gu S., and Zhou J., Surface Science **228** 403 (1990)

Xu Z., Wassermeier M., Li Y.J., and Petroff P.M., Applied Physics Letters **60** (5) 586 (1992)

Xu Z.Y., Kreismanis V.G., and Tang C.L., Applied Physics Letters **43** (5) 416 (1983)

Yablonovitch E., Sandroff C.J., and Gmitter T., Applied Physics Letters **51** (6) 439 (1987)

Yazawa M., Koguchi M., and Hiruma K., Applied Physics Letters **58** (10) 1080 (1991)

Yu S.J., Asahi H., Takizawa J., Asami K., Emura S., Gonda S., Kubo H., Hamaguchi C., and Hirayama Y., Jounal of Vacuum Science and Technology **B9** (5) 2683 (1991)

Zarem H.L., Sercel P.C., Hoenck M.E., Lebens J.A., and Vahala K.J., Applied Physics Letters **54** (26) 2692 (1989)

Zhou P., Jiang H.X., Bannwart R., Solin S.A., and Bai G., Physical Review **B40** (17) 11862 (1989)

# Appendices

## A.1 Fabrication Data

### A.1.1 Final Philips Electron Microscope Process

1) Clean substrate
2) Spin on 15 % BDH resist and bake at 180 °C for 1 hr
3) Expose alignment marks
4) Develop alignment marks in 1:1 MIBK : IPA at 23 °C for 60 s
5) Wet etch in HCl, $H_2O_2$, $H_2O$ for 60 s at 23 °C
6) Clean sample
7) Spin on 8 % HRN at 7000 rpm for 60 s
8) Bake for 1 hr at 120 °C
9) Expose structures
10) Develop in MIBK at 23 °C for 15 s, then IPA for 15 s
11) Repeat step (10).
12) Etch in $SiCl_4$

### A.1.2 Final Jeol Electron Microscope Process

1) Clean substrate
2) Spin on 8 % HRN at 7000 rpm for 60 s
3) Bake for 1 hr at 120 °C
4) Expose structures
5) Develop in MIBK at 23 °C for 15 s, then IPA for 15 s
6) Repeat step (5).
7) Etch in $SiCl_4$

### A.1.3 Electron Microscope Parameters

| Specification | Philips | Jeol |
|---|---|---|
| Potential | 50 keV | 100 keV |
| Minimum Spot Size | 8 nm | ~ 2 nm |
| Stage Accuracy | - | 5 μm |
| Scan Speed | slow | fast |

Table (A1.1) : Specifications of Lithography Microscopes

| | | | | |
|---|---|---|---|---|
| step and repeat command | 0 | 2 | 4 | 2 |
| size of interval box;<br>number of repeats in x and y | X | Y | Nx | Ny |
| exposure data (microcoulombs / $cm^2$) | 0 | EXP | 1 | 0 |
| size and position of element | x1 | x2 | y1 | y2 |
| end of file marker | 0 | 0 | 0 | 0 |

Table (A1.2): Philips PSEM500 Scan File Layout

| | | | |
|---|---|---|---|
| 0 | 15000 | 1 | 0 |
| 0 | 1 | 4 | 2 |
| 20 | 40 | 200 | 100 |
| 1 | 1 | 2 | 2 |
| 0 | 0 | 0 | 0 |

Table (A1.3): Philips PSEM500 Scan File for Medium Sized Structures

| X (mm) | Y (mm) | | | Key number |
|---|---|---|---|---|
| 0.212 | 0.109 | 0 | 0 | 1 |
| 0.212 | 0.128 | 0 | 0 | 2 |
| 0.212 | 0.147 | 0 | 0 | 3 |
| 0.212 | 0.166 | 0 | 0 | 4 |
| 0.212 | 0.185 | 0 | 0 | 5 |
| 0.237 | 0.185 | 0 | 0 | 6 |
| 0.237 | 0.166 | 0 | 0 | 7 |
| 0.237 | 0.147 | 0 | 0 | 8 |
| 0.237 | 0.128 | 0 | 0 | 9 |
| 0.237 | 0.109 | 0 | 0 | 10 |
| 0.262 | 0.109 | 0 | 0 | 11 |
| 0.262 | 0.128 | 0 | 0 | 12 |
| 0.262 | 0.147 | 0 | 0 | 13 |
| 0.262 | 0.166 | 0 | 0 | 14 |
| 0.262 | 0.185 | 0 | 0 | 15 |
| 0.287 | 0.185 | 0 | 0 | 16 |
| 0.287 | 0.166 | 0 | 0 | 17 |
| 0.287 | 0.147 | 0 | 0 | 18 |
| 0.287 | 0.128 | 0 | 0 | 19 |
| 0.287 | 0.109 | 0 | 0 | 20 |

Table (A1.4): Philips PSEM500 Position File

```
ma 5000
dk 1 \bill\dot211
dk 2 \bill\dot125
dk 8 al125
dk 9 al125x
dl
pf dot.pos
```

Table (A1.5): Philips Go File

| Magnification | Frame size (x) | Frame size (y) | Pixel size (x) | Pixel size (y) |
|---|---|---|---|---|
| 80 X | 1.56 mm | 1.18 mm | 380 nm | 289 nm |
| 1250 X | 100 µm | 76 µm | 24.4 nm | 18.5 nm |
| 5000 X | 25 µm | 19 µm | 6.1 nm | 4.64 nm |

Table (A1.6): Philips PSEM500 Frame Parameters

| Spot Size | Beam Current |
|---|---|
| 0.25 μm | ~ 7500 pA |
| 160 Å | ~ 50 pA |
| 80 Å | ~ 20 pA |

Table (A1.7): Philips PSEM500 Spot Mode Parameters

| | | | | |
|---|---|---|---|---|
| exposure data (microcoulombs / $cm^2$) | 0 | EXP | 1 | 0 |
| step and repeat command | 0 | 1 | 4 | 2 |
| size of interval box;<br>number of repeats in x and y | X | Y | Nx | Ny |
| size and position of element | x1 | x2 | y1 | y2 |
| end of file marker | 0 | 0 | 0 | 0 |

Table (A1.8): Jeol Microscope Scan File Layout

| | | | |
|---|---|---|---|
| 0 | 15000 | 1 | 0 |
| 0 | 1 | 4 | 2 |
| 20 | 40 | 200 | 100 |
| 1 | 1 | 2 | 2 |
| 0 | 0 | 0 | 0 |

Table (A1.9): Jeol Microscope Scan File for Medium Sized Structures

| Magnification | Frame size (x) | Frame size (y) | Pixel size (x) | Pixel size (y) |
|---|---|---|---|---|
| 1200 X | 137 μm | 113 μm | 33.4 nm | 27.9 nm |

Table (A1.10): Jeol Microscope Frame 'Small 2' Parameters

| Spot Mode | Spot Size (nm) | Beam Current (pA) | |
|---|---|---|---|
| | | Aperture 2 | Aperture 3 |
| small 6 | 8 | 860 | 210 |

Table (A1.11): Jeol Microscope Spot Mode Parameters

```
{dot pattern}
{Bill Leitch}
{10/7/91}
sampleo;                                                    |   sets frame origin
uses small 6;                                               |   sets frame size
filelist                                                    |   defines scan files
        jaae
        jdde
        jeea
        jbbe
        jdde
        jeea
        jaae
        jcce
        jjjb;
GetBeamCurrents;                                            |   reads beam current
focusalign 4.000 4.000   2   2 ;                            |   establishes focusses

mover  0.820  0.184 q;   scanfile  1 small 6 M2 L=1 N=1 R=0.00;|  scans file 1 at position 1
...                                                         |   with spotsize small 6

...
...
mover  3.180  3.016 q;   scanfile  8 small 6 M2 L=1 N=1 R=0.00;

mover  2.000  3.800 q;   scanfile  9 small 6 M1 L=1 N=1 R=0.00;

movea 0 0;
```

Table (A1.12) : Jeol Electron Microscope Job file

### A.1.4 Jeol Electron Microscope Job File (Full)

```
{dot pattern}
{Bill Leitch}
{10/7/91}
sampleo;
uses small 6;
filelist
    jaae
    jdde
    jeea
    jbbe
    jdde
    jeea
    jaae
    jcce
    jjjb;
GetBeamCurrents;
focusalign 4.000 4.000   2   2 ;

mover  0.820  0.184 q;   scanfile   1 small 6 M2 L=1 N=1 R=0.00;
mover  0.938  0.184 q;   scanfile   1 small 6 M2 L=1 N=1 R=0.00;
mover  1.062  0.184 q;   scanfile   1 small 6 M2 L=1 N=1 R=0.00;
mover  1.180  0.184 q;   scanfile   1 small 6 M2 L=1 N=1 R=0.00;
mover  0.820  0.326 q;   scanfile   1 small 6 M2 L=1 N=1 R=0.00;
mover  0.938  0.326 q;   scanfile   1 small 6 M2 L=1 N=1 R=0.00;
mover  1.062  0.326 q;   scanfile   1 small 6 M2 L=1 N=1 R=0.00;
mover  1.180  0.326 q;   scanfile   1 small 6 M2 L=1 N=1 R=0.00;
mover  0.820  0.474 q;   scanfile   1 small 6 M2 L=1 N=1 R=0.00;
mover  0.938  0.474 q;   scanfile   1 small 6 M2 L=1 N=1 R=0.00;
mover  1.062  0.474 q;   scanfile   1 small 6 M2 L=1 N=1 R=0.00;
mover  1.180  0.474 q;   scanfile   1 small 6 M2 L=1 N=1 R=0.00;
mover  0.820  0.616 q;   scanfile   1 small 6 M2 L=1 N=1 R=0.00;
mover  0.938  0.616 q;   scanfile   1 small 6 M2 L=1 N=1 R=0.00;
mover  1.062  0.616 q;   scanfile   1 small 6 M2 L=1 N=1 R=0.00;
mover  1.180  0.616 q;   scanfile   1 small 6 M2 L=1 N=1 R=0.00;

mover  2.820  0.184 q;   scanfile   2 small 6 M2 L=1 N=1 R=0.00;
mover  2.938  0.184 q;   scanfile   2 small 6 M2 L=1 N=1 R=0.00;
mover  3.062  0.184 q;   scanfile   2 small 6 M2 L=1 N=1 R=0.00;
mover  3.180  0.184 q;   scanfile   2 small 6 M2 L=1 N=1 R=0.00;
mover  2.820  0.326 q;   scanfile   2 small 6 M2 L=1 N=1 R=0.00;
mover  2.938  0.326 q;   scanfile   2 small 6 M2 L=1 N=1 R=0.00;
mover  3.062  0.326 q;   scanfile   2 small 6 M2 L=1 N=1 R=0.00;
mover  3.180  0.326 q;   scanfile   2 small 6 M2 L=1 N=1 R=0.00;
mover  2.820  0.474 q;   scanfile   2 small 6 M2 L=1 N=1 R=0.00;
mover  2.938  0.474 q;   scanfile   2 small 6 M2 L=1 N=1 R=0.00;
mover  3.062  0.474 q;   scanfile   2 small 6 M2 L=1 N=1 R=0.00;
mover  3.180  0.474 q;   scanfile   2 small 6 M2 L=1 N=1 R=0.00;
mover  2.820  0.616 q;   scanfile   2 small 6 M2 L=1 N=1 R=0.00;
mover  2.938  0.616 q;   scanfile   2 small 6 M2 L=1 N=1 R=0.00;
mover  3.062  0.616 q;   scanfile   2 small 6 M2 L=1 N=1 R=0.00;
mover  3.180  0.616 q;   scanfile   2 small 6 M2 L=1 N=1 R=0.00;

mover  0.820  0.984 q;   scanfile   3 small 6 M2 L=1 N=1 R=0.00;
mover  0.938  0.984 q;   scanfile   3 small 6 M2 L=1 N=1 R=0.00;
mover  1.062  0.984 q;   scanfile   3 small 6 M2 L=1 N=1 R=0.00;
mover  1.180  0.984 q;   scanfile   3 small 6 M2 L=1 N=1 R=0.00;
mover  0.820  1.126 q;   scanfile   3 small 6 M2 L=1 N=1 R=0.00;
mover  0.938  1.126 q;   scanfile   3 small 6 M2 L=1 N=1 R=0.00;
mover  1.062  1.126 q;   scanfile   3 small 6 M2 L=1 N=1 R=0.00;
mover  1.180  1.126 q;   scanfile   3 small 6 M2 L=1 N=1 R=0.00;
mover  0.820  1.274 q;   scanfile   3 small 6 M2 L=1 N=1 R=0.00;
```

```
mover  0.938  1.274 q;   scanfile  3 small 6 M2 L=1 N=1 R=0.00;
mover  1.062  1.274 q;   scanfile  3 small 6 M2 L=1 N=1 R=0.00;
mover  1.180  1.274 q;   scanfile  3 small 6 M2 L=1 N=1 R=0.00;
mover  0.820  1.416 q;   scanfile  3 small 6 M2 L=1 N=1 R=0.00;
mover  0.938  1.416 q;   scanfile  3 small 6 M2 L=1 N=1 R=0.00;
mover  1.062  1.416 q;   scanfile  3 small 6 M2 L=1 N=1 R=0.00;
mover  1.180  1.416 q;   scanfile  3 small 6 M2 L=1 N=1 R=0.00;

mover  2.820  0.984 q;   scanfile  4 small 6 M2 L=1 N=1 R=0.00;
mover  2.938  0.984 q;   scanfile  4 small 6 M2 L=1 N=1 R=0.00;
mover  3.062  0.984 q;   scanfile  4 small 6 M2 L=1 N=1 R=0.00;
mover  3.180  0.984 q;   scanfile  4 small 6 M2 L=1 N=1 R=0.00;
mover  2.820  1.126 q;   scanfile  4 small 6 M2 L=1 N=1 R=0.00;
mover  2.938  1.126 q;   scanfile  4 small 6 M2 L=1 N=1 R=0.00;
mover  3.062  1.126 q;   scanfile  4 small 6 M2 L=1 N=1 R=0.00;
mover  3.180  1.126 q;   scanfile  4 small 6 M2 L=1 N=1 R=0.00;
mover  2.820  1.274 q;   scanfile  4 small 6 M2 L=1 N=1 R=0.00;
mover  2.938  1.274 q;   scanfile  4 small 6 M2 L=1 N=1 R=0.00;
mover  3.062  1.274 q;   scanfile  4 small 6 M2 L=1 N=1 R=0.00;
mover  3.180  1.274 q;   scanfile  4 small 6 M2 L=1 N=1 R=0.00;
mover  2.820  1.416 q;   scanfile  4 small 6 M2 L=1 N=1 R=0.00;
mover  2.938  1.416 q;   scanfile  4 small 6 M2 L=1 N=1 R=0.00;
mover  3.062  1.416 q;   scanfile  4 small 6 M2 L=1 N=1 R=0.00;
mover  3.180  1.416 q;   scanfile  4 small 6 M2 L=1 N=1 R=0.00;

mover  0.820  1.784 q;   scanfile  5 small 6 M2 L=1 N=1 R=0.00;
mover  0.938  1.784 q;   scanfile  5 small 6 M2 L=1 N=1 R=0.00;
mover  1.062  1.784 q;   scanfile  5 small 6 M2 L=1 N=1 R=0.00;
mover  1.180  1.784 q;   scanfile  5 small 6 M2 L=1 N=1 R=0.00;
mover  0.820  1.926 q;   scanfile  5 small 6 M2 L=1 N=1 R=0.00;
mover  0.938  1.926 q;   scanfile  5 small 6 M2 L=1 N=1 R=0.00;
mover  1.062  1.926 q;   scanfile  5 small 6 M2 L=1 N=1 R=0.00;
mover  1.180  1.926 q;   scanfile  5 small 6 M2 L=1 N=1 R=0.00;
mover  0.820  2.074 q;   scanfile  5 small 6 M2 L=1 N=1 R=0.00;
mover  0.938  2.074 q;   scanfile  5 small 6 M2 L=1 N=1 R=0.00;
mover  1.062  2.074 q;   scanfile  5 small 6 M2 L=1 N=1 R=0.00;
mover  1.180  2.074 q;   scanfile  5 small 6 M2 L=1 N=1 R=0.00;
mover  0.820  2.216 q;   scanfile  5 small 6 M2 L=1 N=1 R=0.00;
mover  0.938  2.216 q;   scanfile  5 small 6 M2 L=1 N=1 R=0.00;
mover  1.062  2.216 q;   scanfile  5 small 6 M2 L=1 N=1 R=0.00;
mover  1.180  2.216 q;   scanfile  5 small 6 M2 L=1 N=1 R=0.00;

mover  2.820  1.784 q;   scanfile  6 small 6 M2 L=1 N=1 R=0.00;
mover  2.938  1.784 q;   scanfile  6 small 6 M2 L=1 N=1 R=0.00;
mover  3.062  1.784 q;   scanfile  6 small 6 M2 L=1 N=1 R=0.00;
mover  3.180  1.784 q;   scanfile  6 small 6 M2 L=1 N=1 R=0.00;
mover  2.820  1.926 q;   scanfile  6 small 6 M2 L=1 N=1 R=0.00;
mover  2.938  1.926 q;   scanfile  6 small 6 M2 L=1 N=1 R=0.00;
mover  3.062  1.926 q;   scanfile  6 small 6 M2 L=1 N=1 R=0.00;
mover  3.180  1.926 q;   scanfile  6 small 6 M2 L=1 N=1 R=0.00;
mover  2.820  2.074 q;   scanfile  6 small 6 M2 L=1 N=1 R=0.00;
mover  2.938  2.074 q;   scanfile  6 small 6 M2 L=1 N=1 R=0.00;
mover  3.062  2.074 q;   scanfile  6 small 6 M2 L=1 N=1 R=0.00;
mover  3.180  2.074 q;   scanfile  6 small 6 M2 L=1 N=1 R=0.00;
mover  2.820  2.216 q;   scanfile  6 small 6 M2 L=1 N=1 R=0.00;
mover  2.938  2.216 q;   scanfile  6 small 6 M2 L=1 N=1 R=0.00;
mover  3.062  2.216 q;   scanfile  6 small 6 M2 L=1 N=1 R=0.00;
mover  3.180  2.216 q;   scanfile  6 small 6 M2 L=1 N=1 R=0.00;

mover  0.820  2.584 q;   scanfile  7 small 6 M2 L=1 N=1 R=0.00;
mover  0.938  2.584 q;   scanfile  7 small 6 M2 L=1 N=1 R=0.00;
mover  1.062  2.584 q;   scanfile  7 small 6 M2 L=1 N=1 R=0.00;
mover  1.180  2.584 q;   scanfile  7 small 6 M2 L=1 N=1 R=0.00;
mover  0.820  2.726 q;   scanfile  7 small 6 M2 L=1 N=1 R=0.00;
mover  0.938  2.726 q;   scanfile  7 small 6 M2 L=1 N=1 R=0.00;
mover  1.062  2.726 q;   scanfile  7 small 6 M2 L=1 N=1 R=0.00;
mover  1.180  2.726 q;   scanfile  7 small 6 M2 L=1 N=1 R=0.00;
```

```
mover  0.820  2.874 q;   scanfile  7 small 6 M2 L=1 N=1 R=0.00;
mover  0.938  2.874 q;   scanfile  7 small 6 M2 L=1 N=1 R=0.00;
mover  1.062  2.874 q;   scanfile  7 small 6 M2 L=1 N=1 R=0.00;
mover  1.180  2.874 q;   scanfile  7 small 6 M2 L=1 N=1 R=0.00;
mover  0.820  3.016 q;   scanfile  7 small 6 M2 L=1 N=1 R=0.00;
mover  0.938  3.016 q;   scanfile  7 small 6 M2 L=1 N=1 R=0.00;
mover  1.062  3.016 q;   scanfile  7 small 6 M2 L=1 N=1 R=0.00;
mover  1.180  3.016 q;   scanfile  7 small 6 M2 L=1 N=1 R=0.00;

mover  2.820  2.584 q;   scanfile  8 small 6 M2 L=1 N=1 R=0.00;
mover  2.938  2.584 q;   scanfile  8 small 6 M2 L=1 N=1 R=0.00;
mover  3.062  2.584 q;   scanfile  8 small 6 M2 L=1 N=1 R=0.00;
mover  3.180  2.584 q;   scanfile  8 small 6 M2 L=1 N=1 R=0.00;
mover  2.820  2.726 q;   scanfile  8 small 6 M2 L=1 N=1 R=0.00;
mover  2.938  2.726 q;   scanfile  8 small 6 M2 L=1 N=1 R=0.00;
mover  3.062  2.726 q;   scanfile  8 small 6 M2 L=1 N=1 R=0.00;
mover  3.180  2.726 q;   scanfile  8 small 6 M2 L=1 N=1 R=0.00;
mover  2.820  2.874 q;   scanfile  8 small 6 M2 L=1 N=1 R=0.00;
mover  2.938  2.874 q;   scanfile  8 small 6 M2 L=1 N=1 R=0.00;
mover  3.062  2.874 q;   scanfile  8 small 6 M2 L=1 N=1 R=0.00;
mover  3.180  2.874 q;   scanfile  8 small 6 M2 L=1 N=1 R=0.00;
mover  2.820  3.016 q;   scanfile  8 small 6 M2 L=1 N=1 R=0.00;
mover  2.938  3.016 q;   scanfile  8 small 6 M2 L=1 N=1 R=0.00;
mover  3.062  3.016 q;   scanfile  8 small 6 M2 L=1 N=1 R=0.00;
mover  3.180  3.016 q;   scanfile  8 small 6 M2 L=1 N=1 R=0.00;

mover  2.000  3.800 q;   scanfile  9 small 6 M1 L=1 N=1 R=0.00;

movea 0 0;
```

## A.2 Structure Of Prism File

| | |
|---|---|
| 1 | # of regions |
| 695 | start position |
| 1251 | # of points |
| 0.0343725 | step increment |
| 14901 | min intensity |
| 156184 | max intensity |
| 1 | - |
| -999.999 | start marker |
| 15973 | data |
| 14981 | data |
| 14901 | data |
| 14916 | |
| 14964 | |
| 14903 | |
| 15004 | |
| ... | |
| ... | |
| ... | |
| 15094 | |
| 15090 | |
| 15135 | |
| 15101 | |
| 15137 | |
| 15093 | |
| 15086 | data |
| 15144 | data |
| 3 | end marker |
| U1000 | spectrometer |
| FALSE | - |
| CTS/SEC | y axis label |
| A | x axis label (Å) |
| PMT | detector 1 |
| POWER METER | detector 2 |
| WEL | user name |
| 0 | |
| 0 | |
| 0 | |
| 0 | |
| 0 | |
| 0 | |
| 0 | |
| 0 | |
| 0 | |
| 0 | |
| 0 | |
| 0 | |
| 0 | |
| 0 | |
| 0 | |
| 0 | |
| 0 | |
| 0 | |
| 1800 | grating gr/mm |
| 1200 | - |
| 1 | # of scans in file |

| | |
|---|---|
| -10 | code for Å |
| 10 | - |
| 1024 | - |
| 1 | count time (s) |
| 0 | - |
| 0 | |
| 0 | |
| 0 | |
| 0 | |
| 2E-1 | |
| 0 | |
| 0 | |
| 0 | |
| 0 | |
| 0 | |
| 2E-1 | |
| 0 | |
| 0 | |
| 0 | |
| 0 | |
| 0 | |
| 2E-1 | |
| 0 | |
| 0 | |
| 0 | |
| 0 | |
| 0 | |
| 2E-1 | |
| 0 | |
| 0 | |
| 0 | |
| 0 | |
| 0 | |
| 01/29/91 | acquisition date |
| 18:09:13 | start time |
| 18:32:19 | end time |
| 13.08 | included angle |
| 10 | - |
| 2000 | focal length (mm) |
| 200 | - |
| 487.986 | laser line (nm) |
| -1000 | - |
| 0 | |
| 0 | |
| 0 | |
| 0 | |
| 0 | |
| TRUE | |
| TRUE | |
| FALSE | |
| TRUE | |
| TRUE | |
| 2 | |
| 0 | |
| 0 | |
| 0 | |
| 0 | |
| 0 | |
| 0 | |
| 0 | |
| FALSE | |

```
FALSE
FALSE
FALSE
FALSE
FALSE
0
-1
32767
-                    laser characteristic
-                    from power meter
-
-
-
-
-                    peak storage start
-                    peak storage end
-                    user entries...
-                    ...
-                    ...
-                    ...
-
-
-
-                    comments
```

## A.3 Photoluminescence Characterization

### A.3.1 Selected Quantum Well Material Data

All materials were initially characterized at 6 K, and at 12 mW on the 488 nm line of an Ar ion laser

#### A.3.1.1 Glasgow University MBE B33

**Growth Conditions**

| Layer (from substrate) | Nominal Thickness | Substrate Temperature |
|---|---|---|
| 25 period superlattice | - | 625 °C |
| GaAs buffer | 0.5 μm | 625-685 °C |
| AlGaAs x=0.3 | 80 nm | 685 °C |
| GaAs QW | 8 nm | 685 °C |
| AlGaAs x=0.3 | 20 nm | 685 °C |
| GaAs QW | 6 nm | 685 °C |
| AlGaAs x=0.3 | 20 nm | 685 °C |
| GaAs QW | 4 nm | 685 °C |
| AlGaAs x=0.3 | 20 nm | 685 °C |
| GaAs | 10 nm | 685 °C |

| Superlattice | Thickness per period | Substrate Temperature |
|---|---|---|
| GaAs | 5 monolayers | 625 °C |
| AlAs | 5 monolayers | 625 °C |

Table (A3.11): Growth Parameters for Glasgow B33

**Summary of Data**

| Well Width (nm) ± 0.2 nm | λ (eV) | Γ (meV) ± 14 % | Intensity (a.u.) ± 31 % |
|---|---|---|---|
| 8.3 | 1.568 | 1.6 | $1 \times 10^5$ |
| | 1.569 | 1.4 | $2 \times 10^5$ |
| 5.8 | 1.597 | 1.6 | $1 \times 10^5$ |
| | 1.595 | 2.4 | $6 \times 10^4$ |
| 4.0 | 1.646 | 3.2 | $6 \times 10^4$ |

Table (A3.12): Photoluminescence data from Glasgow B33 (5 measurements)

### A.3.1.2 Glasgow University MBE A275

**Growth Conditions**

| Layer (from substrate) | Nominal Thickness | Substrate Temperature |
|---|---|---|
| GaAs buffer layer | 2 μm | 650 °C |
| AlGaAs x=0.3 | 80 nm | 800 °C |
| GaAs QW | 10 nm | 800 °C |
| AlGaAs x=0.3 | 20 nm | 800 °C |
| GaAs QW | 7 nm | 800 °C |
| AlGaAs x=0.3 | 20 nm | 800 °C |
| GaAs QW | 4 nm | 800 °C |
| AlGaAs x=0.3 | 20 nm | 800 °C |
| GaAs | 10 nm | 800 °C |

Table (A3.13): Growth Parameters for Glasgow A275

**Summary of Data**

| Well Width (nm) | λ (eV) | Γ (meV) | Intensity (a.u.) |
|---|---|---|---|
| 9.4 | 1.558 | 5.1 | $1.1 \times 10^5$ |
| 6.5 | 1.5892 | 5.9 | $1.4 \times 10^5$ |
| 3.3 | 1.668 | 6.7 | $7.5 \times 10^4$ |

Table (A3.14): Photoluminescence data from Glasgow A275 (1 measurement)

### A.3.1.3 Glasgow University MBE A315

**Growth Conditions**

| Layer (from substrate) | Nominal Thickness | Substrate Temperature |
|---|---|---|
| 25 period superlattice | - | 725 °C |
| GaAs buffer | 0.5 μm | " |
| AlGaAs x=0.3 | 80 nm | " |
| GaAs QW | 8 nm | " |
| AlGaAs x=0.3 | 20 nm | " |
| GaAs QW | 6 nm | " |
| AlGaAs x=0.3 | 20 nm | " |
| GaAs QW | 4 nm | " |
| AlGaAs x=0.3 | 20 nm | " |
| GaAs | 10 nm | " |

| Superlattice | Thickness per period | Substrate Temperature |
|---|---|---|
| GaAs | 5 ML | 725 °C |
| AlGaAs x=0.3 | 5 ML | " |

Table (A3.15): Growth Parameters for Glasgow A315

**Summary of Data**

| Well Width (nm) | λ (eV) | Γ (meV) | Intensity (a.u.) |
|---|---|---|---|
| 9.3 | 1.562 | 3.0 | $1.7 \times 10^2$ |
| 9.0 | 1.565 | 1.2 | $1.9 \times 10^2$ |
| 6.6 | 1.588 | 2.0 | $1.8 \times 10^3$ |
| 4.5 | 1.637 | 3.3 | $1.0 \times 10^3$ |

Table (A3.16): Photoluminescence data from Glasgow A315
(1 measurement)

### A.3.1.4 Glasgow University MBE A362

**Growth Conditions**

| Layer (from substrate) | Nominal Thickness | Substrate Temperature |
|---|---|---|
| 24 period superlattice | - | 630 °C |
| GaAs | 1 μm | " |
| AlGaAs | 20 nm | " |
| AlAs | 3 ML | " |
| GaAs QW | 8 nm | " |
| AlAs | 3 ML | " |
| AlGaAs | 20 nm | " |
| GaAs | 4 nm | " |

| Superlattice | Thickness per period | Substrate Temperature |
|---|---|---|
| GaAs | 3 monolayers | 630 °C |
| AlAs | 5 monolayers | " |

Table (A3.17): Growth Parameters for Glasgow A362

**Summary of Data**

| Well Width (nm) | λ (eV) | Γ (meV) | Intensity (a.u.) |
|---|---|---|---|
| 6.7 (Nom 8 ) | 1.587 | 3.1 | $4.8 \times 10^3$ |
| Feature | | | |
| GaAs | 1.496 | 5.1 | $1.6 \times 10^3$ |
| GaAs | 1.517 | 1.2 | $1.8 \times 10^4$ |
| GaAs | 1.519 | 1.2 | $5.2 \times 10^4$ |

Table (A3.18): Photoluminescence data from Glasgow A362
(1 measurement)

**A.3.1.5 Glasgow University MBE A363**

**Growth Conditions**

| Layer (from substrate) | Nominal Thickness | Substrate Temperature |
|---|---|---|
| 24 period superlattice | - | 630 °C |
| GaAs | 1 μm | " |
| AlGaAs | 20 nm | " |
| AlAs | 3 ML | " |
| GaAs QW | 6 nm | " |
| AlAs | 3 ML | " |
| AlGaAs | 20 nm | " |
| GaAs | 4 nm | " |

| Superlattice | Thickness per period | Substrate Temperature |
|---|---|---|
| GaAs | 3 monolayers | 630 °C |
| AlAs | 5 monolayers | " |

Table (A3.19): Growth Parameters for Glasgow A363

5 s Growth Interruption on top surface with $As_2$ off.

**Summary of Data**

| Well Width (nm) | λ (eV) | Γ (meV) | Intensity (a.u.) |
|---|---|---|---|
| 4.6 (Nom 6) | 1.631 | 3.5 | $2.8 \times 10^3$ |
| Feature | | | |
| GaAs | 1.520 | 3.1 | $2.5 \times 10^2$ |

Table (A3.20): Photoluminescence data from Glasgow A363 (1 measurement)

### A.3.1.6 Glasgow University MBE A364

**Growth Conditions**

| Layer (from substrate) | Nominal Thickness | Substrate Temperature |
|---|---|---|
| 24 period superlattice | - | 630 °C |
| GaAs | 1 μm | " |
| AlGaAs | 20 nm | " |
| AlAs | 3 ML | " |
| GaAs QW | 4 nm | " |
| AlAs | 3 ML | " |
| AlGaAs | 20 nm | " |
| GaAs | 4 nm | " |

| Superlattice | Thickness per period | Substrate Temperature |
|---|---|---|
| GaAs | 3 monolayers | 630 °C |
| AlAs | 5 monolayers | " |

Table (A3.21): Growth Parameters for Glasgow A364

5 s Growth Interruption on top surface with $As_2$ off.

**Summary of Data**

| Well Width (nm) | λ (eV) | Γ (meV) | Intensity (a.u.) |
|---|---|---|---|
| (Nom 20) | 1.520 | 1.0 | $3 \times 10^5$ |
| Feature | | | |
| GaAs | 1.497 | 5.1 | $5 \times 10^3$ |
| GaAs | 1.518 | 1.5 | $6 \times 10^4$ |

Table (A3.22): Photoluminescence data from Glasgow A364 (1 measurement)

### A.3.1.7 Glasgow University MBE A365

**Growth Conditions**

| Layer (from substrate) | Nominal Thickness | Substrate Temperature |
|---|---|---|
| 24 period superlattice | - | 630 °C |
| GaAs | 1 μm | " |
| AlGaAs | 20 nm | " |
| AlAs | 3 ML | " |
| GaAs QW | 20 nm | " |
| AlAs | 3 ML | " |
| AlGaAs | 20 nm | " |
| GaAs | 4 nm | " |

| Superlattice | Thickness per period | Substrate Temperature |
|---|---|---|
| GaAs | 3 monolayers | 630 °C |
| AlAs | 5 monolayers | " |

Table (A3.23): Growth Parameters for Glasgow A365

5 s Growth Interruption on top surface with $As_2$ off.

**Summary of Data**

| Well Width (nm) | λ (eV) | Γ (meV) | Intensity (a.u.) |
|---|---|---|---|
| (Nom 13) | 1.527 | 2.3 | $1.2 \times 10^5$ |
| Feature | | | |
| GaAs | 1.496 | 5.9 | $1 \times 10^3$ |
| GaAs | 1.517 | 1.8 | $1.5 \times 10^3$ |
| GaAs | 1.5186 | 1.1 | $5.8 \times 10^4$ |

Table (A3.24): Photoluminescence data from A365
(1 measurement)

### A.3.1.8 STL Material A1995A

**Growth Conditions**

No information was available on the growth conditions or structure of material A1995A other than that it was an undoped multiple quantum well GaAs / AlGaAs structure grown by metal-organic vapour phase epitaxy.

**Summary of Data**

| Well Width (nm) | λ (eV) | Γ (meV) | Intensity (a.u.) |
|---|---|---|---|
| 3.7 | 1.660 | 11.7 | $1.8 \times 10^4$ |
| 8.3 | 1.572 | 12.2 | $4.1 \times 10^4$ |

Table (A3.25): Photoluminescence data from STL A1995A

### A.3.2 Parameters for Structure Photoluminescence

Dot Sample 1

| | |
|---|---|
| Material: | A315 |
| Power: | 1.57 mW |
| Temperature: | 6 K |

Dot Sample 2

| | |
|---|---|
| Material: | A315 |
| Power: | 1 mW |
| Temperature: | 6 K |

Dot Sample 3

| | |
|---|---|
| Material: | A1995A |
| Power: | 16 mW |
| Temperature: | 6 K |

Dot Sample 4

| | |
|---|---|
| Material: | A365 |
| Power: | 1 mW |
| Temperature: | 6 K |

Wire Sample 1

| | |
|---|---|
| Material: | A315 |
| Power: | 53 μW |
| Temperature: | 6 K |

Wire Sample 2

| | |
|---|---|
| Material: | A315 |
| Power: | 53 μW |
| Temperature: | 6 K |

Wire Sample 3

| | |
|---|---|
| Material: | A315 |
| Power: | 1 mW |
| Temperature: | 6 K |

Wire Sample 4

| | |
|---|---|
| Material: | A1995A |
| Power: | 16 mW |
| Temperature: | 6 K |

Wire Sample 5

| | |
|---|---|
| Material: | A365 |
| Power: | 1 mW |
| Temperature: | 6 K |

Wire Sample 6

| | |
|---|---|
| Material: | A365 |
| Power: | 1 mW |
| Temperature: | 6 K |

Dash Sample 1

| | |
|---|---|
| Material: | B33 |
| Power: | 100 mW |
| Temperature: | 6 K |

Dash Sample 2

| | |
|---|---|
| Material: | B33 |
| Power: | 100 mW |
| Temperature: | 6 K |

Dash Sample 3

| | |
|---|---|
| Material: | B33 |
| Power: | 100 mW |
| Temperature: | 6 K |

Dash Sample 4

| | |
|---|---|
| Material: | B33 |
| Power: | 12 mW |
| Temperature: | 6 K |

Dash Sample 5

| | |
|---|---|
| Material: | B33 |
| Power: | 12 mW |
| Temperature: | 6 K |

Dash Sample 6

| | |
|---|---|
| Material: | B33 |
| Power: | 12 mW |
| Temperature: | 6 K |

Dash Sample 7

| | |
|---|---|
| Material: | A315 |
| Power: | 1 mW |
| Temperature: | 6 K |

## Dash Sample 8

| | |
|---|---|
| Material: | A315 |
| Power: | 1 mW |
| Temperature: | 6 K |

## Dash Sample 9

| | |
|---|---|
| Material: | A315 |
| Power: | 1 mW |
| Temperature: | 6 K |

## Dash Sample 10

| | |
|---|---|
| Material: | A315 |
| Power: | 1 mW |
| Temperature: | 6 K |

## Dash Sample 11

| | |
|---|---|
| Material: | A315 |
| Power: | 1 mW |
| Temperature: | 6 K |

## A.4 Surface Model

### A.4.1 Rectangular Coordinate System

If one solves the diffusion equation with a constant generation of carriers c, carrier diffusion constant D,and bulk lifetime $\tau$,we have, in the steady state with $\partial n/\partial t = 0$

$$D\nabla^2 n - \frac{n}{\tau} + c = 0 \qquad \{A.1\}$$

The most appropriate coordinate system for the symmetry of a wire is the rectangular coordinate system, and in this syatem, the General Solution is:

$$n = A(e^{kx} + e^{-kx}) \qquad \{A.2\}$$

which yields:

$$k = \frac{1}{\sqrt{D\tau}} \qquad \{A.3\}$$

One can take a particular integral of $c\tau$, giving a sufficient solution as:

$$n = c\tau + A(e^{kx} + e^{-kx}) \qquad \{A.4\}$$

The boundary condition is:

$$Sn = -D\frac{\partial n}{\partial x}\bigg|_{x=\pm W/2} \qquad \{A.5\}$$

$$-D\frac{\partial n}{\partial x} = -DAk(e^{kx} - e^{-kx}) \qquad \{A.6\}$$

$$A = \frac{-Sc\tau}{S(e^{kW/2} + e^{-kW/2}) + Dk(e^{kW/2} - e^{-kW/2})} \qquad \{A.7\}$$

$$n = c\tau - \frac{Sc\tau(e^{kx} + e^{-kx})}{S(e^{kW/2} + e^{-kW/2}) + Dk(e^{kW/2} - e^{-kW/2})} \qquad \{A.8\}$$

$$N = \int_{-W/2}^{W/2} n\, dx \qquad \{A.9\}$$

$$N = \int_{-W/2}^{W/2} \left\{ c\tau - \frac{Sc\tau(e^{kx} + e^{-kx})}{S(e^{kW/2} + e^{-kW/2}) + Dk(e^{kW/2} - e^{-kW/2})} \right\} dx \qquad \{A.10\}$$

$$N_{norm} = N / c\tau \qquad \{A.11\}$$

$$N_{norm} = 1 - \frac{2\,S(e^{W/2} - e^{-W/2})}{SkW(e^{kW/2} + e^{-kW/2}) + Dk^2 W(e^{kW/2} - e^{-kW/2})} \qquad \{A.12\}$$

thus one obtains:

$$N_{norm} = 1 - \frac{2\,S \sinh\left(\frac{kW}{2}\right)}{SkW \cosh\left(\frac{kW}{2}\right) + Dk^2 W \sinh\left(\frac{kW}{2}\right)} \qquad \{A.13\}$$

If one defines a 'dead layer' $W_d$ where:

$2A = W - 2W_d$

or

$$A = W/2 - W_d \qquad \{A.14\}$$

$$N_{norm} = 1 - \frac{S \sinh(kA)}{SkA \cosh(kA) + Dk^2 A \sinh(kA)} \qquad \{A.15\}$$

or

$$N_{norm} = 1 - \frac{\frac{S}{Dk^2 A} \sinh(kA)}{\frac{S}{Dk} \cosh(kA) + \sinh(kA)} \qquad \{A.16\}$$

or, defining $L = 1/k$, one obtains:

$$N_{norm} = 1 - \frac{\frac{SL^2}{AD} \sinh\left(\frac{A}{L}\right)}{\frac{SL}{D} \cosh\left(\frac{A}{L}\right) + \sinh\left(\frac{A}{L}\right)} \qquad \{A.17\}$$

### A.4.2 Cylindrical Polar Coordinates

Because of the cylindrical symmetry of a dot, one can solve the diffusion equation in cylindrical polar coordinates. The General Solution in this coordinate syatem is:

$$\nabla^2\psi - k^2\psi = 0 \qquad \psi_{m\gamma} = \begin{Bmatrix} I_m(\gamma\rho) \\ K_m(\gamma\rho) \end{Bmatrix} \begin{Bmatrix} \cos(m\phi) \\ \sin(m\phi) \end{Bmatrix} \begin{Bmatrix} e^{-\gamma z} \\ e^{\gamma z} \end{Bmatrix} \qquad \gamma^2 = \left|\alpha^2 + k^2\right| \qquad \{A.18\}$$

where: $\alpha$ separation constant

I,K modified cylindrical Bessel functions.

Modified Bessel functions may be expressed as infinite series:

$$I_\nu(x) = \sum_{s=0}^{\infty} \frac{1}{s!\,(s+\nu)!}\left(\frac{x}{2}\right)^{2s+\nu} \qquad \{A.19\}$$

$$K_\nu(x) = \frac{\pi}{2}\frac{I_{-\nu}(x) - I_\nu(x)}{\sin(\nu\pi)} \qquad \{A.20\}$$

and so one may expand the functions and neglect smaller contributions if x<<1, as the series falls off rapidly due to the factorial functions.

Assuming angular symmetry, the solution consists of modified Bessel functions, subject to the boundary conditions:

i) n is finite at the origin

ii) the recombination at the surface r=R is $\underline{S}.\underline{n}$

$$\Rightarrow Sn = -D\frac{\partial n}{\partial r}\bigg|_{r=R} \qquad \{A.21\}$$

In cylindrical coordinates, the radial dependence of the Laplacian is:

$$\nabla^2 n = \frac{1}{r}\frac{\partial}{\partial r}\left(r\frac{\partial n}{\partial r}\right) \qquad \{A.22\}$$

The boundary conditions can be satisfied with a single solution of the form

$$n = c\tau + AI_0(kr) \qquad \{A.23\}$$

The boundary condition is:

$$Sc\tau + S\,AI_0(kr) = -DA\frac{\partial(I_0(kr))}{\partial r} \qquad \{A.24\}$$

The integrated exciton population across the disc of well material is:

$$N = \int_{r=0}^{R} \left( c\tau + A\left\{ 1 + \frac{(kr)^2}{4} + .. \right\} \right) 2\pi r dr \qquad \{A.25\}$$

$$N = \pi c \tau R^2 + \pi A R^2 + A\pi \frac{k^2 R^4}{8} + .. \qquad \{A.26\}$$

$$A = \frac{-Sc\tau}{\{SI_0(kR) + DI'_0(kR)\}} \qquad \{A.27\}$$

$$N = \pi c \tau R^2 + \frac{-S\tau c\left( \pi R^2 + \pi \frac{k^2 R^4}{8} + .. \right)}{\left\{ S\left( 1 + \frac{(kR)^2}{4} + ... \right) + D\frac{k^2 R}{2}\left( 1 + \frac{k^2 R^2}{8} + .. \right) \right\}} \qquad \{A.28\}$$

$$\frac{N}{\pi c \tau R^2} = 1 - \frac{\left( 1 + \frac{k^2 R^2}{8} + .. \right)}{\left\{ \left( 1 + \frac{(kR)^2}{4} + ... \right) + \frac{Dk^2 R}{2S}\left( 1 + \frac{k^2 R^2}{8} + ... \right) \right\}} \qquad \{A.29\}$$

As the General Solution gives $k^2 = 1/D\tau$,

$$\frac{N}{\pi c \tau R^2} = 1 - \frac{\left( 1 + \frac{k^2 R^2}{8} + .. \right)}{\left\{ \left( 1 + \frac{(kR)^2}{4} + ... \right) + \frac{R}{2S\tau}\left( 1 + \frac{k^2 R^2}{8} + .. \right) \right\}} \qquad \{A.30\}$$

$$N_{norm} = \frac{\left\{ \frac{R}{2S\tau}\left( 1 + \frac{k^2 R^2}{8} + .. \right) \right\} + \left\{ \left( \frac{(kR)^2}{4} + ... \right) - \left( \frac{k^2 R^2}{8} + .. \right) \right\}}{\left\{ \left( 1 + \frac{(kR)^2}{4} + .. \right) + \frac{R}{2S\tau}\left( 1 + \frac{k^2 R^2}{8} + .. \right) \right\}} \qquad \{A.31\}$$

Neglecting powers of kR greater than 2 gives:

$$N_{norm} \approx \frac{\frac{R}{2S\tau} + \left(\frac{(kR)^2}{8}\right)}{\left(1 + \frac{R}{2S\tau} + \frac{(kR)^2}{4}\right)} \qquad \{A.32\}$$

This is the same result as that obtained by Clausen et al. (1989), except for the typographic error in the printing of the expression above.

One may extend the model in a similar to way to that of the wires by inclusion of a 'dead layer', $R_d$.

$$A = R\text{-}Rd \qquad \{A.33\}$$

$$N_{norm} \approx \frac{\frac{A}{2S\tau} + \left(\frac{(kA)^2}{8}\right)}{\left(1 + \frac{A}{2S\tau} + \frac{(kA)^2}{4}\right)}. \qquad \{A.34\}$$

## A.5 Trap Distribution Model Program

```
program model(input,output);

{$N+I-}

{program to model the effect of defect distribution on the radiative efficiency of quantum dots and wires by
diffusive transport}

{William E. Leitch 31/10/92}


uses crt;

const
        sizestor1       :       array[1..5] of integer = (3,10,25,50,100);
                                                                {structure sizes}
        sizestor2       :       array[1..3] of integer = (1,3,10);
                                                                {lambda sizes}
        ff              :       array[1..5] of integer = (4,3,2,2,1);
                                                                {filling factors}
        stp             :       integer         =       200;    {number of defects / 100}

var
        intarray        :       array[1..100,1..100] of Boolean;        {structure}
        resultarray     :       array[1..100,1..100] of single;         {matrix of results}
        outarray        :       array[1..100,1..2]   of single;         {matrix to file}
        dev             :       real;                                   {stan dev calc}
        XS,YS           :       integer;                                {box size}
        sum             :       real;                                   {running active area}
        sumtot          :       real;                                   {max pos active area}
        percent         :       real;                                   { sum / sumtot}
        x,y,z           :       integer;                                {defect position}
        results         :       text;                                   {output file}
        KPflag          :       Boolean;                                {key pressed flag}
        Xct,Yct         :       integer;                                {size of structure}
        Nav,Ndef        :       integer;                                {numbers of defects
                                                                        and averages}
        resfilnam       :       string;                                 {output filename}
        lam             :       integer;                                {diffusion length}
        filpath         :       string;                                 {directory path}
        Ndefmax         :       integer;                                {number of defects}
        Navmax          :       integer;                                {number of averages}
        xff             :       integer;                                {x filling factor}
        yff             :       integer;                                {y filling factor}
        rpts            :       integer;                                {# rpts in str arr}
        xrpt            :       integer;                                {# rpts in x}
        yrpt            :       integer;                                {# rpts in y}
{.....}
```

```
procedure procnumgen;

{generates defect position ranging over structure plus filling factor}

begin
        randomize;
        x:=random(XS*xff)+1;
        y:=random(YS*yff)+1;
        z:=random(rpts)+1;
end;

{.....}

procedure procwipe;

{wipes all array positions within one diffusion length of the defect
 position}

var
        c           :       real;                   {running separation variable}
        xx,yy       :       integer;                {running wipe coords}
        X1,Y1       :       integer;                {minimum diffusion coords}
        X2,Y2       :       integer;                {maximum diffusion coords}
        flg         :       Boolean;                {flag}

begin
        writeln('hit');
        for xx:=1 to XS do
        for yy:=1 to YS do
        begin
        c:=(xx-x)*(xx-x)+(yy-y)*(yy-y);
        if (c<lam*lam) or (c=lam*lam) then
        begin
        flg:=intarray[xx,yy];
        if flg=true then
        begin
        intarray[xx,yy]:=false;
        sum:=sum-1;
        end;
        end;
        end;
end;

{.....}

procedure procrun;

{main work: generates defect position, wipes, and repeats for the required
 number of defects}

begin
        for Ndef:=1 to Ndefmax do
        begin
        procnumgen;
        if ( (x<XS) and (y<YS) and (z=1) ) then procwipe;
        percent:=sum/sumtot;
        if ( ( Ndef MOD stp ) = 0 ) then
        resultarray[Nav, ( Ndef DIV stp ) ]:=percent;
        end;
end;
```

```
{.....}

procedure procclrint;

{sets all intarray positions to true}

var
        xx,yy           :                                       integer;

begin
        for xx:=1 to 100 do for yy:=1 to 100 do intarray[xx,yy]:=true;

end;

{.....}

procedure procclrres;

{sets all resultarray positions to zero}

var
        xx,yy           :                                       integer;

begin
        for xx:=1 to 100 do for yy:=1 to 100 do resultarray[xx,yy]:=0;

end;

{.....}

procedure prockeypres;

{flags a key pressed}

begin
        KPflag:=true; writeln('Abort Key Pressed');
end;

{.....}

procedure procfilinit;

{sets up input file}

var
        Xctstr,Yctstr,lamstr            :                       string;

begin
        Str(Xct,Xctstr); Str(Yct,Yctstr); Str(lam,lamstr);
        resfilnam:='x'+Xctstr+'y'+Yctstr+'l'+lamstr; chdir(filpath);
        if IOresult<>0 then
        begin
        mkdir(filpath); chdir(filpath);
        end;
        Assign(results,resfilnam);
        Rewrite(results);
        Close(results);
end;
```

```
{.....}

procedure procaverage;

{generates an array for each structure and defect number}

begin
        writeln('procaverage');
        for Nav:=1 to Navmax do
        begin
        if Keypressed then prockeypres;
        sumtot:=XS*YS; sum:=sumtot;
        if (KPflag=true) then Exit;
        procclrint;
        procrun;
        end;
end;

{.....}

procedure procstor;

{dumps data to file}

var
        xx,yy :                 integer;                                {running variables}

begin
        writeln('procstor');
        assign(results,resfilnam);
        rewrite(results);
        writeln(results,'Defect Distribution Model');
        writeln(results); writeln(results); writeln(results,'XS=',XS,'      ','YS=',YS,'lam=',lam);
        writeln(results,'xrpt=',xrpt,' ','yrpt=',yrpt,' ','rpts=',rpts); writeln(results);writeln(results);
        writeln(results,'Ndef':10,'%':10,'err':10); writeln(results);
        for yy:=1 to ( Ndefmax DIV stp ) do outarray[yy,1]:=0;
        for yy:=1 to ( Ndefmax DIV stp ) do outarray[yy,2]:=0;
        for yy:=1 to ( Ndefmax DIV stp ) do
        begin
        for xx:=1 to Navmax do
        begin
        outarray[yy,1]:=outarray[yy,1]+resultarray[xx,yy];
        end;
        outarray[yy,1]:=outarray[yy,1]/Navmax;
        end;
        for yy:=1 to ( Ndefmax DIV stp ) do
        begin
        for xx:=1 to Navmax do
        begin
        dev:=resultarray[xx,yy]-outarray[yy,1];
        outarray[yy,2]:=outarray[yy,2]+((dev*dev)/Navmax);
        end;
        end;
        for yy:=1 to ( Ndefmax DIV stp ) do
        begin
        writeln(results,( yy*stp ):10,outarray[yy,1]:10:3,outarray[yy,2]:10:3);
        end;
        close(results);
end;
```

```
{.....}

procedure procupdate;

{keeps screen informed of current status}

begin
        writeln('XS=',XS,'    ','YS=',YS,'   ');
        writeln;
        writeln('Nav=',Nav,'          ','lam=',lam);
        writeln;
end;

{.....}

procedure procsizevar;

{varies size of structure}

begin
        for Xct:=1 to 5 do
        begin
        for Yct:=1 to 5 do
        begin
        writeln('procsizevar',Xct:10,Yct:10);
        XS:=sizestor1[Xct];
        YS:=sizestor1[Yct];
        xff:=ff[Xct];
        yff:=ff[Yct];
        xrpt:=( 100 DIV (XS*xff) );
        yrpt:=( 100 DIV (YS*yff) );
        rpts:= xrpt * yrpt;
        Navmax:= ( 100 DIV rpts );
        writeln('initializing file');
        procfilinit;
        writeln('file initialization complete');
        procaverage;
        writeln('procaverage complete');
        procstor;
        writeln('procstor complete');
        procupdate;
        if (KPflag=true) then Exit;
        procclrres;
        end;
        end;
end;
```

```
{*********************************************************************}

{       MAIN BODY       }

begin
        Ndefmax:=100*stp;
        clrscr;
        lam:=sizestor2[1;
        KPflag:=false;
        filpath:='d:\bill\model1';
        procsizevar;
end.
```

GLASGOW
UNIVERSITY
LIBRARY